Delft University of Technology

Climate-Optimal Aircraft Design and Fleet Allocation
Evaluating the Impact of Sustainable Aviation Fuels

Proesmans, P.

DOI
10.4233/uuid:295a037d-02ef-4bb9-bd4e-c6e346f0fefa

Publication date
2024

Document Version
Final published version

Citation (APA)
Proesmans, P. (2024). *Climate-Optimal Aircraft Design and Fleet Allocation: Evaluating the Impact of Sustainable Aviation Fuels*. [Dissertation (TU Delft), Delft University of Technology]. https://doi.org/10.4233/uuid:295a037d-02ef-4bb9-bd4e-c6e346f0fefa

Important note
To cite this publication, please use the final published version (if applicable).
Please check the document version above.

Copyright
Other than for strictly personal use, it is not permitted to download, forward or distribute the text or part of it, without the consent of the author(s) and/or copyright holder(s), unless the work is under an open content license such as Creative Commons.

Takedown policy
Please contact us and provide details if you believe this document breaches copyrights.
We will remove access to the work immediately and investigate your claim.

This work is downloaded from Delft University of Technology.
For technical reasons the number of authors shown on this cover page is limited to a maximum of 10.

CLIMATE-OPTIMAL AIRCRAFT DESIGN AND FLEET ALLOCATION

EVALUATING THE IMPACT OF SUSTAINABLE AVIATION FUELS

CLIMATE-OPTIMAL AIRCRAFT DESIGN AND FLEET ALLOCATION

EVALUATING THE IMPACT OF SUSTAINABLE AVIATION FUELS

Dissertation

for the purpose of obtaining the degree of doctor
at Delft University of Technology
by the authority of Rector Magnificus prof.dr.ir. T.H.J.J. van der Hagen,
chair of the Board for Doctorates,
to be defended publicly on
Thursday 26 September 2024 at 15:00 o'clock

by

Pieter-Jan PROESMANS

Master of Science in Aerospace Engineering,
Delft University of Technology, the Netherlands
born in Brasschaat, Belgium.

This dissertation is approved by the promotors.

Composition of the doctoral committee:

Rector Magnificus	chairperson
Dr. ir. R. Vos	Delft University of Technology, *promotor*
Prof. dr. ir. L.L.M. Veldhuis	Delft University of Technology, *promotor*
Independent members:	
Prof. dr. ir. S.P. Hoogendoorn	Delft University of Technology
Prof. Dr.-Ing. V. Gollnick	Hamburg University of Technology, Germany
Prof. dr. R.E. Perez	Royal Military College of Canada
Dr. C. Jouannet	Linköping University, Sweden
Dr. S. Delbecq	ISAE-SUPAERO, France
Prof. dr. S.J. Watson	Delft University of Technology, *reserve member*

This research was funded by the European Union's Clean Sky 2 Thematic Topics program (H2020-EU.3.4.5.10.) with grant agreement number 865300 (GLOWOPT project).

Keywords: conceptual aircraft design, MDAO, aviation climate impact, liquid hydrogen, sustainable aviation fuels, fleet allocation
Printed by: Gildeprint

Front & Back: Designed by Pieter-Jan Proesmans.

Copyright © 2024 by P. Proesmans

ISBN 978-94-6366-899-6

An electronic version of this dissertation is available at
`http://repository.tudelft.nl/`.

As you set out for Ithaka
hope your road is a long one,
full of adventure, full of discovery.

Konstantinos Petrou Kaváfis

SUMMARY

Research into aviation-induced global warming highlights the critical contribution of non-CO_2 effects caused by NO_x emissions, water vapor emissions, and contrail formation. Whereas the CO_2 emissions and effects scale directly with the fuel consumption, this is not the case for non-CO_2 effects. The non-CO_2 effects depend on the location, have varying lifetimes, and do not purely scale with aircraft fuel burn. Additionally, research has indicated that minimizing these non-CO_2 effects does not necessarily align with classic design objectives, such as cost, mass, or energy consumption.

Therefore, these aspects have to be considered in the conceptual evaluation and optimization of new aircraft and fuels. The objective of this research is *to study the potential of aircraft design optimization and fleet allocation to minimize the global warming impact while observing the change in energy consumption and financial costs for the operator, considering various technologies and fuels.* This study employs a multidisciplinary and multi-objective approach to explore the conceptual design space of aircraft by performing optimizations aiming at climate impact minimization. The aircraft design space is defined in terms of airframe, engine, and mission variables. Since the latter can influence the flight speed and block time, such climate-optimal aircraft operations must be studied further. Therefore, an additional level is added to the multidisciplinary design analysis and optimization (MDAO) framework to include fleet allocation.

A linear temperature response model is included in the MDAO framework to estimate the climate impact. Based on a multi-year scenario of emissions, this climate model estimates the radiative forcing and temperature due to emissions of CO_2, NO_x (short-term O_3 formation, depletion of CH_4 and primary mode ozone), water vapor, soot, and sulfate, and the formation of persistent contrails. The combined temperature response of all these species is evaluated over 100 years and translated into the average temperature response (ATR_{100}) metric. This metric is the objective function in aircraft design optimizations, along with operating costs and energy consumption.

The first step of the research is the optimization of medium-range, kerosene-powered aircraft to achieve a minimum ATR_{100} compared to an aircraft optimized for minimum cash operating cost (direct operating cost minus depreciation, navigation, and financing fees). This optimization showed that the ATR_{100} can be reduced up to 64% at a cash operating cost penalty of 17%, showing that these objectives are conflicting. This reduction in ATR_{100} targets the radiative impact of contrails and short-term ozone (due to NO_x emissions). Contrail formation is eliminated in this case by flying lower (6.0 to 7.6 km), so the conditions for persistent contrail formation are not met. The lower cruise altitude also reduces the radiative impact of short-term ozone. Additionally, the engine overall pressure ratio (OPR) is lowered to reduce the NO_x emission index and total NO_x emissions at the cost of engine overall efficiency. The climate-optimal aircraft also features a lower cruise Mach number (0.5 to 0.6) to maintain a near-optimal lift-to-drag ratio.

Since turboprop engines can offer higher propulsive efficiency at this cruise Mach number regime, propeller-based aircraft are considered a suitable alternatives to further reduce ATR_{100} by targeting the CO_2 emissions, also in the medium-range category. At a propeller efficiency of 88%, which is higher than currently available technology, the ATR_{100} can be reduced up to 71%, depending on the set block time constraint. A sensitivity analysis indicates that a turboprop aircraft provides improved climate impact compared to a climate-optimal turbofan aircraft when a propeller efficiency higher than 75% is achieved.

Multi-objective optimization of the operating cost and climate impact shows that by targeting contrails, a significant reduction in ATR_{100} of 53% (medium-range, kerosene) can be achieved at a limited cost increase of 1%. This highlights the potential of flying at lower cruise altitudes and avoiding contrail formation. Nonetheless, all these climate-optimized kerosene aircraft still have a significant impact due to the CO_2 emissions.

Therefore, in the second step of the research, liquid hydrogen and drop-in sustainable aviation fuels (SAF) are examined to reduce the climate impact further. Besides their potential to completely or partially cut CO_2 emissions, these fuels offer benefits in terms of non-CO_2 effects. In particular, the contrail impact can be reduced due to the reduced soot emissions. However, this effect is partially offset in the case of hydrogen combustion due to the increased probability of contrail formation.

A cost-optimized, medium-range hydrogen aircraft can achieve a 73% reduction in ATR_{100} at a 28% cost increase, while climate-optimized designs can attain a 99% reduction at a 39% cost increase. This cost increase is mainly caused by the higher fuel price compared to kerosene and partially due to an energy penalty due to the cryogenic tank integration, although this is category-dependent. Employing a mixture of 50% SAF and 50% fossil kerosene, the ATR_{100} can be reduced between 47% and 83% for the cost- and climate-optimal medium-range aircraft, respectively. This climate impact reduction is accompanied by a cost increase of 4% to 21%. The SAF-powered aircraft's design characteristics are similar to those of the kerosene aircraft.

The third element of the presented research focuses on the consequences of aircraft design changes on aircraft operations. The reduced flight speed increases the mission block times and reduces productivity and scheduling problems. Additionally, the increased operating cost of climate-optimal aircraft, liquid hydrogen, and SAF are expected to decrease the profit margin on flights. The aircraft are grouped per optimization objective and fuel type, each containing regional, medium-, and long-range aircraft types, to investigate these effects. Each of the nine fleets (three objectives × three fuels) is allocated on a network through dynamic programming to maximize the network profit and compared to the cost-optimal kerosene fleet.

This analysis shows that a fleet of climate-optimal aircraft leads to a 55% decrease in climate impact at a 24% loss in network profit. The climate-optimal kerosene fleet needs 21% more aircraft to reach this maximum possible profit. This is caused by the lowered productivity of the aircraft. The 21% increase in fleet size is lower than the expected increase from analysis based on a simple productivity constraint at the aircraft level because such constraint does not account for specific scheduling problems and the fact that some routes become unprofitable. This highlights the importance of evaluating such optimized aircraft concepts at the network level.

The fleet allocation of hydrogen aircraft highlights that the climate-optimal hydrogen aircraft offer the lowest climate impact at a profit penalty of 35%. While medium-range hydrogen aircraft are competitive, in particular, the long-range, climate-optimal hydrogen performs significantly worse than its kerosene and SAF counterparts due to increased flight time, energy consumption, and fuel price. The SAF-powered fleet provides Pareto-optimal solutions in terms of profit and climate impact between the kerosene and hydrogen solutions. SAF-powered fleets can reduce the climate impact between 47% and 78%, at profit decreases between 3% and 27%. Although these results provide helpful conceptual insights for several stakeholders in the aviation industry, further analyses on different networks must confirm the conclusions' robustness.

This research focuses on the global warming effect due to aviation. Nevertheless, this is only one aspect of sustainable aviation. Conceptual analyses show that climate-optimal aircraft perform better than cost-optimal aircraft in terms of local and global air quality. The reduced engine OPR reduces the emission of NO_x, a precursor for harmful $PM_{2.5}$ and ozone formation. Considering the noise levels of climate-optimal aircraft, it is concluded that the different engine cycles may lead to higher noise levels at take-off and departure, while airframe noise is expected to be similar to cost-optimal aircraft. However, the noise of climate-optimal aircraft is only assessed qualitatively, and further research is required in this area.

The climate impact assessment in the current research carries uncertainty since not all climate effects are yet fully understood and since the linear temperature response model offers lower fidelity than more advanced global climate models, for example. An uncertainty analysis highlights a significant standard deviation of 6.4 mK for an ATR_{100} reduction of 15 mK for climate-optimal, medium-range, kerosene aircraft. The uncertainty in contrail radiative forcing estimates is the largest contributor to the overall uncertainty in climate impact reduction. Although the uncertainty in terms of ATR_{100} reduction reaches its maximum for climate-optimal aircraft, it is argued that the uncertainty in absolute climate impact is actually smaller for these aircraft due to a reduction in uncertain, non-CO_2 effects.

Adding air quality and noise disciplines to the MDAO framework is helpful to create a more insightful sustainability report of the optimized aircraft. In terms of problem formulation, it interesting to use the results from the fleet allocation to simultaneously optimize the payload and range requirements of the aircraft, in particular for hydrogen aircraft. In terms of technologies, it is highly recommended that propeller-based propulsion and contrail avoidance technologies be studied further. The climate-optimal aircraft can benefit from advanced turboprop technology to reduce energy consumption and operating costs. Technologies or procedures that eliminate contrails can offer a considerable ATR_{100} reduction at a potentially limited cost increase while also reducing uncertainty.

SAMENVATTING

Onderzoek naar opwarming van de aarde door de luchtvaart benadrukt de belangrijke bijdrage van niet-CO_2 effecten, veroorzaakt door de uitstoot van NO_x, waterdamp en de vorming van condenssporen (vliegtuigstrepen, condensatiestrepen of contrails). Terwijl de CO_2 emissies en effecten direct schalen met het brandstofverbruik, is dit niet het geval voor de niet-CO_2 effecten. De niet-CO_2 effecten zijn afhankelijk van de locatie, hebben een variërende levensduur en schalen niet enkel met het brandstofverbruik van het vliegtuig. Bovendien toont onderzoek dat het minimaliseren van deze niet-CO_2 effecten niet noodzakelijkerwijs overeenkomt met klassieke ontwerpdoelstellingen.

Daarom moeten deze aspecten worden meegenomen bij de conceptuele evaluatie en optimalisatie van nieuwe vliegtuigen en brandstoffen. Het doel van dit onderzoek is *om het potentieel te bestuderen van de optimalisatie van vliegtuigontwerpen en vloottoewijzing om de impact op de opwarming van de aarde te minimaliseren en tegelijkertijd de verandering in energieverbruik en financiële kosten te observeren, rekening houdend met verschillende technologieën en brandstoffen.* Deze studie maakt gebruik van een multidisciplinaire en multi-objectieve benadering om de conceptuele ontwerpruimte van vliegtuigen te verkennen door optimalisaties uit te voeren die gericht zijn op het minimaliseren van de impact op het klimaat. De ontwerpruimte van vliegtuigen wordt gedefinieerd in termen van de vliegtuigstructuur-, motor- en missievariabelen. Aangezien deze laatste de vliegsnelheid en de missie tijd kunnen beïnvloeden, moeten dergelijke klimaatoptimale vliegtuigoperaties verder worden onderzocht. Daarom wordt er een extra niveau toegevoegd aan het Multidisciplinaire Ontwerpanalyse en Optimalisatie (MDAO) kader om vloottoewijzing op te nemen.

In het MDAO-kader is een lineair temperatuurresponsmodel opgenomen om de gevolgen voor het klimaat in te schatten. Op basis van een meerjarig emissiescenario bepaalt dit klimaatmodel de stralingsforcering als gevolg van emissies van CO_2, NO_x (vorming van kortdurende O_3, depletie van CH_4 en primaire ozon), waterdamp, roet en sulfaat, en de vorming van aanhoudende condenssporen. De gecombineerde respons van al deze soorten wordt geëvalueerd over een periode van 100 jaar en vertaald in de gemiddelde temperatuurrespons (ATR_{100}). Dit prestatiegetal is de doelfunctie in de optimalisaties van vliegtuigontwerpen, samen met de operationele kosten en het energieverbruik.

De eerste stap van het onderzoek is de optimalisatie van middellange afstandsvliegtuigen op kerosine om ATR_{100} te minimaliseren en deze vliegtuigen te vergelijken kostoptimale vliegtuig (directe bedrijfskosten zonder afschrijvingen, navigatie en financieringskosten). Deze optimalisatie toont aan dat de ATR_{100} tot 64% kunnen worden verlaagd met een verhoging van 17% in operationele kosten, waaruit blijkt dat deze twee doelstellingen tegenstrijdig zijn. Deze reductie van de ATR_{100} is gericht op de stralingseffecten van condenssporen en kortdurende ozon (als gevolg van de uitstoot van NO_x). De vorming van condenssporen wordt in dit geval geëlimineerd door lager te vliegen (6.0 tot 7.6 km), zodat niet langer aan de voorwaarden voor de vorming van aanhoudende condenssporen wordt voldaan. De lagere kruishoogte vermindert ook de stralingsimpact van ozon op korte termijn. Daarnaast wordt de totale drukverhouding (OPR) van de motor verlaagd om de NO_x-emissie-index en de totale NO_x-emissies te verlagen ten koste van de totale efficiëntie van de motor. Het klimaatoptimale vliegtuig heeft ook een lager Mach-getal in de kruisvlucht (0.5 tot 0.6) om een vrijwel optimaal glijgetal te behouden.

Aangezien turboschroefmotoren (turboprops) een hoger voortstuwingsrendement kunnen bieden rond dit Mach-getal, worden turboschroefvliegtuigen beschouwd als een geschikt alternatief om ATR_{100} verder te verlagen, ook op de middellange afstand. Bij een schroefrendement van 88%, wat hoger is dan de huidige beschikbare technologie, kan de klimaat impact tot 71% worden verminderd, afhankelijk van de ingestelde vliegtijd. Een gevoeligheidsanalyse geeft aan dat een turbopropvliegtuig een betere impact heeft op het klimaat in vergelijking met een klimaatoptimaal turbofanvliegtuig wanneer een schroefrendement van meer dan 75 % wordt bereikt.

Multi-objectieve optimalisatie van de operationele kosten en de impact op het klimaat laat zien dat door condenssporen aan te pakken een significante reductie van 53% (middellange afstand, kerosine) kan worden bereikt tegen een beperkte kostenstijging van 1%. Dit benadrukt het potentieel van vliegen op lagere vlieghoogtes en het vermijden van condenssporen. De klimaatoptimale kerosinevliegtuigen hebben nog steeds een aanzienlijke impact door de uitstoot van CO_2.

Daarom worden in de tweede stap van het onderzoek vloeibare waterstof en drop-in duurzame vliegtuigbrandstoffen (SAF) onderzocht om de gevolgen voor het klimaat verder te beperken. Naast hun potentieel om de uitstoot van het CO_2 geheel of gedeeltelijk terug te dringen, bieden deze brandstoffen ook voordelen op het gebied van andere niet-CO_2 effecten. De verminderde roetuitstoot kan de impact van condenssporen verlagen. Dit effect wordt echter gedeeltelijk tenietgedaan in het geval van waterstofverbranding vanwege de grotere kans op vorming van condenssporen.

Een kostenoptimaal waterstofvliegtuig voor de middellange afstand kan een vermindering van ATR_{100} van 73% bereiken bij een kostenstijging van 28%, terwijl klimaatoptimale ontwerpen een vermindering van 99% kunnen bereiken bij een kostenstijging van 39%. Deze kostenstijging wordt voornamelijk veroorzaakt door de hogere brandstofprijs in vergelijking met kerosine en gedeeltelijk door een hoger energieverbruik door de integratie van de cryogene tank, hoewel dit afhankelijk is van de categorie. Met een mengsel van 50% SAF en 50 % fossiele kerosine kan de klimaatimpact tussen 47 % en 83 % worden verminderd voor respectievelijk de kostenoptimale en de klimaatoptimale middellangeafstandsvliegtuigen. Deze vermindering van de klimaatimpact gaat gepaard met een kostenstijging van 4% tot 21%. De ontwerpkenmerken van het vliegtuig met SAF-motor zijn vergelijkbaar met die van het vliegtuig met kerosinemotor.

Het derde element van het onderzoek richt zich op de gevolgen voor de vluchtuitvoering. De verminderde vliegsnelheid verhoogt de bloktijden van missies, vermindert de productiviteit en zorgt voor planningsproblemen. Bovendien wordt verwacht dat de hogere bedrijfskosten van klimaatoptimale vliegtuigen, vloeibare waterstof en SAF de winstmarge op vluchten zullen verlagen. De vliegtuigen zijn gegroepeerd per optimalisatiedoelstelling en brandstoftype, zodat elke groep regionale, middellange- en langeafstandsvliegtuigtypes bevat. Elk van de negen vloten (drie doelstellingen × drie brandstoffen) wordt via dynamisch programmeren toegewezen aan een netwerk om de netwerkwinst te maximaliseren en vergeleken met de kostenoptimale kerosinevloot.

Deze analyse laat zien dat een vloot van klimaatoptimale vliegtuigen leidt tot een afname van 55% in klimaatimpact bij een verlies van 24% in netwerkwinst. De klimaatoptimale kerosinevloot heeft 21% meer vliegtuigen nodig om deze maximale winst te behalen. Dit wordt veroorzaakt door de lagere productiviteit van de vliegtuigen. De toename van de vlootomvang met 21% is lager dan de verwachte toename op basis van een analyse die uitgaat van een eenvoudige productiviteitsbeperking op vliegtuigniveau, omdat een dergelijke beperking geen rekening houdt met specifieke roosterproblemen en het feit dat sommige routes onrendabel worden. Dit benadrukt het belang van het evalueren van dergelijke geoptimaliseerde vliegtuigconcepten op netwerkniveau.

De vloottoewijzing van waterstofvliegtuigen laat zien dat de klimaatoptimale waterstofvliegtuigen de laagste klimaatimpact hebben tegen een winstverlies van 35%. Terwijl waterstofvliegtuigen voor de middellange afstand competitief zijn, presteert vooral het klimaatoptimale waterstofvliegtuig voor de lange afstand opmerkelijk slechter dan de kerosine en SAF tegenhangers door de langere vluchttijd, het hogere energieverbruik en de hogere brandstofprijs. SAF-vloten kunnen de klimaatimpact tussen 47% en 78% verminderen, bij winstdalingen tussen 3% en 27%. Hoewel deze resultaten nuttige inzichten bieden, moeten verdere analyses op verschillende netwerken de robuustheid van de conclusies bevestigen.

Dit onderzoek richt zich op het broeikaseffect als gevolg van de luchtvaart. Toch is dit slechts één aspect van duurzame luchtvaart. Conceptuele analyses tonen aan dat klimaatoptimale vliegtuigen beter presteren op het gebied van lokale en mondiale luchtkwaliteit. De lage OPR van de motor vermindert de uitstoot van NO_x, een precursor voor schadelijk fijnstof en ozon. Met betrekking tot de geluidsniveaus van klimaatoptimale vliegtuigen wordt geconcludeerd dat de verschillende motorcycli kunnen leiden tot hogere geluidsniveaus bij het opstijgen en vertrekken, terwijl het geluid van de vliegtuigstructuur naar verwachting vergelijkbaar zal zijn. Het geluid van klimaatoptimale vliegtuigen is echter alleen kwalitatief beoordeeld en er is verder onderzoek nodig.

De beoordeling van de klimaat impact in het huidige onderzoek is onzeker omdat niet alle klimaateffecten volledig bekend zijn en omdat het lineaire model minder betrouwbaar is dan meer geavanceerde klimaatmodellen. Een onzekerheidsanalyse wijst op een standaardafwijking van 6.4 mK voor een ATR_{100} reductie van 15 mK voor klimaatoptimale, middellange afstand, kerosinevliegtuigen. De onzekerheid in de stralingsforcering van de condenssporen draagt het meeste bij aan de totale onzekerheid. Hetwordt gesteld dat de onzekerheid in absolute klimaatimpact voor deze klimaatoptimale vliegtuigen kleiner is door een vermindering in onzekere, niet-CO_2 effecten.

Het toevoegen van de luchtkwaliteit en geluid aan het MDAO-raamwerk is nuttig om een meer inzichtelijk duurzaamheidsrapport te maken. Op het gebied van probleemformulering is het interessant om de resultaten van de vloottoewijzing te gebruiken om tegelijkertijd het laadvermogen en het bereik van de vliegtuigen te optimaliseren, in het bijzonder voor waterstofvliegtuigen. Verder kunnen klimaatoptimale vliegtuigen profiteren van geavanceerde turboschroeftechnologie om het energieverbruik en de bedrijfskosten te verlagen. Technologieën of procedures die condenssporen elimineren kunnen een aanzienlijke reductie van de klimaat impact opleveren tegen een beperkte kostenstijging, terwijl ook de onzekerheid wordt verminderd.

CONTENTS

Summary vii

Samenvatting xi

Nomenclature xix

1 Introduction 1
- 1.1 Global Warming Impact of Aviation . . . 3
- 1.2 Selecting the Aircraft Design Objective(s) . . . 4
- 1.3 Integration into Airline Operations . . . 6
- 1.4 Research Objective and Questions . . . 7
- 1.5 Research Scope and Limitations . . . 8
  - 1.5.1 Aircraft Design and Network Model Levels . . . 8
  - 1.5.2 Aircraft Configuration and Propulsion System Selection . . . 10
  - 1.5.3 System and Lifecycle Boundaries . . . 10
- 1.6 Outline of Dissertation . . . 11

2 Aviation Emissions and Climate Effects 13
- 2.1 Earth's Radiation Budget and Global Warming . . . 14
- 2.2 Aviation's Contribution to Global Warming . . . 17
  - 2.2.1 Carbon Dioxide . . . 17
  - 2.2.2 Nitrogen Oxides . . . 17
  - 2.2.3 Water Vapor . . . 20
  - 2.2.4 Aerosols . . . 20
  - 2.2.5 Contrails and Contrail Cirrus. . . . 21
  - 2.2.6 Total Impact of Aviation . . . 23
- 2.3 Metric Selection and Integration into Aircraft Design Optimization . . . 23
- 2.4 Consequences of Global Warming . . . 25

3 Kerosene, Medium-Range Aircraft Design Optimization 27
- 3.1 Problem Formulation and Methods . . . 29
  - 3.1.1 Optimization Problem Formulation . . . 30
  - 3.1.2 Design and Analysis Methods . . . 33
- 3.2 Verification of Analysis and Design Methods . . . 47
  - 3.2.1 Turbofan Performance Verification . . . 47
  - 3.2.2 Aircraft Synthesis Verification . . . 47
- 3.3 Results and Discussion . . . 51
  - 3.3.1 Future Fleet Scenario Definition . . . 52
  - 3.3.2 Single-Objective Optimization Results . . . 53
  - 3.3.3 Multi-Objective Optimization Results . . . 58
  - 3.3.4 Comparison with Literature . . . 58

3.4 Conclusions . . . 59

4 Turboprop, Medium-Range Aircraft Design Optimization 61
4.1 Problem Formulation and Methods . . . 63
4.1.1 Optimization Problem Formulation . . . 63
4.1.2 Design and Analysis Methods . . . 66
4.2 Verification of Analysis and Design Methods . . . 70
4.2.1 Turboprop Performance Module . . . 70
4.2.2 Aircraft Synthesis Verification . . . 71
4.3 Results and Discussion . . . 72
4.3.1 Optimization Results . . . 74
4.3.2 Comparison with Turbofan Aircraft . . . 77
4.3.3 Block Time Constraint . . . 78
4.4 Sensitivity Analysis . . . 80
4.5 Conclusions . . . 82

5 Hydrogen, Medium-Range Aircraft Design Optimization 83
5.1 Problem Formulation and Methods . . . 85
5.1.1 Optimization Problem Formulation . . . 85
5.1.2 Design and Analysis Methods . . . 88
5.2 Verification and Validation . . . 102
5.3 Results and Discussion . . . 104
5.3.1 Optimized Aircraft Solutions . . . 104
5.3.2 Comparison between Kerosene and Hydrogen Aircraft . . . 109
5.4 Sensitivities and Uncertainties . . . 112
5.4.1 Hydrogen Technology Uncertainty . . . 112
5.4.2 Climate Model Uncertainty . . . 113
5.4.3 Cost Model Uncertainty . . . 114
5.5 Conclusions . . . 115

6 Comparison of Future Aviation Fuels for Three Aircraft Categories 117
6.1 Problem Formulation and Methods . . . 119
6.1.1 Optimization Problem Definition . . . 119
6.1.2 Design and Analysis Methods . . . 120
6.1.3 Top Level Requirements and Future Fleet Scenarios . . . 126
6.2 Validation of Design Methods . . . 128
6.3 Results and Discussion . . . 129
6.3.1 Regional Aircraft . . . 129
6.3.2 Medium-Range Aircraft . . . 133
6.3.3 Long-Range Aircraft . . . 140
6.3.4 Multi-Objective Solutions . . . 143
6.3.5 Sensitivity to SAF Types and Mixtures . . . 144
6.4 Conclusions . . . 146

7 Fleet Allocation and Network-Level Analysis 147
- 7.1 Multidisciplinary, Multilevel Setup and Methods . . . 149
  - 7.1.1 Multidisciplinary, Multilevel Problem Definition and Setup . . . 149
  - 7.1.2 Fleet Allocation Approach . . . 152
  - 7.1.3 Operating Cost Analysis . . . 156
  - 7.1.4 Climate Impact Assessment . . . 157
- 7.2 Cost-Optimal Reference Case and Verification . . . 159
  - 7.2.1 Reference Network Data and Cost-Optimal Aircraft . . . 159
  - 7.2.2 Verification . . . 161
- 7.3 Results and Discussion . . . 164
  - 7.3.1 Allocation of Climate-Optimal, Kerosene Aircraft . . . 164
  - 7.3.2 Introduction of Future Aviation Fuels . . . 167
  - 7.3.3 Reducing the Design Range of Large Passenger Aircraft . . . 174
- 7.4 Conclusions. . . . 176

8 Discussion on Sustainability Aspects and Climate Impact Uncertainties 179
- 8.1 Air Quality . . . 181
  - 8.1.1 Local Air Quality . . . 182
  - 8.1.2 Global Air Quality . . . 183
  - 8.1.3 Air Quality Impact of Alternative Fuels . . . 186
- 8.2 Noise . . . 186
- 8.3 Life Cycle Impact of Future Aviation Fuels . . . 188
- 8.4 Economics . . . 189
- 8.5 Uncertainty Quantification and Robust Design . . . 195
  - 8.5.1 Uncertainty Analysis of Climate Impact Model. . . . 195
  - 8.5.2 Uncertainty of Future Aviation Fuels . . . 201

9 Conclusions and Recommendations 203
- 9.1 Conclusions. . . . 203
  - 9.1.1 Climate-Optimal, Kerosene Aircraft Design . . . 204
  - 9.1.2 Impact of Liquid Hydrogen and drop-in SAF . . . 205
  - 9.1.3 Fleet Allocation of ATR_{100}-Optimal Aircraft and Fuels . . . 208
- 9.2 Recommendations . . . 210

A Data for Verification and Validation 213
- A.1 Data for Propulsion Discipline Verification and Validation . . . 213
- A.2 Data for Aircraft Synthesis Verification . . . 214

B Geometry Creation Methods 217
- B.1 Fuselage . . . 217
- B.2 Wing Planform . . . 218
- B.3 Empennage Planform and Wing Placement. . . . 219
- B.4 Nacelles. . . . 221

C Optimization Approach and Convergence Information **223**
C.1 Single-Objective, Kerosene . . . 223
C.2 Medium-Range, Hydrogen Aircraft . . . 224
C.2.1 Single-Objective Optimization . . . 224
C.2.2 Multi-Objective Optimization . . . 224
C.3 Multi-Objective Fuel Comparison . . . 225

D Engine Design Discussion **231**

E Optimized Aircraft Data **235**
E.1 Characteristics of Optimized Aircraft . . . 235
E.2 Inputs for Fleet Allocation . . . 235

F Demand and Allocation of Reference Network **243**

G Simple Ticket Price Estimation **249**

H Aircraft Design Code Setup **251**
H.1 Synthesis and Optimization Setup . . . 251
H.2 Discipline Setup . . . 255
H.3 Data Structure . . . 256

Bibliography **259**

Acknowledgments **281**

Curriculum Vitæ **283**

List of Publications **285**

NOMENCLATURE

Latin Symbols

A = Aspect ratio [-] or cross-sectional area [m^2]
b = Wing span [m]
c = Chord length [m] or climb rate [m/s]
$\bar{c}$ = Length of mean aerodynamic chord [m]
c_p = Isobaric specific heat [J/(kg K)]
C = Cost [USD per hour, km, or trip]
C_L = Aircraft lift coefficient [-]
C_D = Aircraft drag coefficient [-]
C_{D_0} = Zero-lift drag coefficient [-]
C_{D_w} = Wave drag coefficient [-]
C_{ops} = Operating costs [USD/(seat $\cdot$ nmi) or USD]
d = Diameter [m]
D = Aircraft drag force [N]
e = Oswald efficiency factor [-]
E_i = Emission of species i [kg]
EI_i = Emission index of species i [kg/kg]
F = Objective function
f_{PR} = Payload-range envelope function
g = Gravitational acceleration [m/s^2]
$\mathbf{g}$ = Inequality constraint vector
h = Altitude or specific enthalpy [m, ft or J/kg]
l = Length [m]
L = Aircraft lift force [N]
k = Aircraft type index [-]
m = Mass [kg]
$\dot{m}$ = Mass flow [kg/s]
M = Mach number [-]
M_i = Molar mass of species i [g/kmol]
N = Integer number or amount [-]
p = Pressure [N/m^2]
P = Power or price [W or USD]
$\mathscr{P}$ = Range parameter [-]
p^i = Partial pressure of species i [N/m^2]
r = Range [km]
R = Gas constant [J/(kg K)]
R_h = Range-equivalent fuel calorific value ($R_h = \text{LHV}/g$) [km]
S = Wing surface area [m^2]
t = Time [hours or years]

T = Thrust [kN] or temperature [K]
t/c = Chord thickness [-]
$\mathrm{U}_{\mathrm{ann}}$ = Annual utilization [hours/year]
v = Velocity [m/s]
V = Volume [m^3]
$\bar{V}$ = Volume coefficient [-]
W = Weight [kN]
x = Absolute, longitudinal coordinate [m]
$\mathbf{x}$ = Design vector

Greek Symbols
γ = Ratio of specific heats [-]
ΔT = Surface temperature change [K]
η_{grav} = Gravimetric index [-]
η_{ov} = Overall propulsion efficiency [-]
$\eta_{\mathrm{pol},i}$ = Polytropic efficiency of component i [-]
λ = Wing taper ratio [-]
$\Lambda_{0.25}$ = Wing quarter-chord sweep angle [deg]
ξ = Longitudinal coordinate relative to MAC [-]
Π = Pressure ratio [-]
ρ = Density [kg/m^3]
ϕ = Temperature-dependent fraction of entropy [J/(kg K)]
χ_i = Concentration of species i [ppmv]

Sub- and superscripts
0 = Sea-level condition or initial value
0.25 = Measured at quarter-chord
AC = Evaluated for one aircraft
amb = Ambient condition
ann = Annually
app = Approach condition
bl = Block mission parameter
core = Core flow
CO = Climb-out condition
cr = Cruise condition
eng = Engine
f = Flight index
fe = Fixed equipment
FG = Fuselage group
fleet = Evaluated for the entire fleet
fuel = Fuel
fus = Fuselage
harm = Harmonic
ht = Horizontal tail
L = Lower bound
nac = Nacelle

ov = Overall
ref = Reference scenario
root = Measured at the wing root
s = Static condition
t = Total condition
tip = Measured at the wing tip
TO = Take-off condition
U = Upper bound
vt = Vertical tail
w = Wing
WG = Wing group
$*$ = Optimal solution
∞ = Freestream condition

Acronyms
AOGCM = Atmosphere-ocean general circulation model
ATR = Average temperature response [K]
ASK = Available seat kilometer [km]
BPR = Bypass ratio [-]
c.g. = Center of gravity
COC = Cash operating cost [USD]
DOC = Direct operating cost [USD]
ERF = Effective radiative forcing [W/m^2]
far = Fuel-to-air mass flow ratio [-]
GCM = Global climate model
GEOM = Geometry
GWP = Global warming potential [-]
GTP = Global temperature potential [-]
HPC = High-pressure compressor
HPT = High-pressure turbine
IOC = Indirect operating cost [USD]
LCC = Life cycle costs [USD]
LH2 = Liquid hydrogen
LHV = Lower heating value of fuel [J/kg]
LPC = Low-pressure compressor
LPT = Low-pressure turbine
LR = Long range
LTOT = Landing and take-off time [hrs]
MAC = Mean aerodynamic chord
MDAO = Multidisciplinary design analysis and optimization
MILP = Mixed-integer linear programming
MLM = Maximum landing mass [kg]
MO = Multi-objective (in terms of COC and ATR_{100})
MTOM = Maximum take-off mass [kg]
MZFM = Maximum zero fuel mass [kg]
OEI = One engine inoperative

OEM = Operating empty mass [kg]
OPR = Overall pressure ratio [-]
REG = Regional
RF = Radiative forcing [W/m^2]
RPK = Revenue passenger kilometer [km]
RQ = Research question
SAF = Sustainable aviation fuel
SEC = Specific energy consumption [MJ/(N s)]
SMR = Small/medium range
TAT = Turn-around time [hrs]
TET = Turbine entry temperature [K]
TLAR = Top-level aircraft requirement
TOA = Top of the atmosphere
TOP = Take-off parameter [N/m^2]
TSFC = Thrust-specific fuel consumption [kg/(N s)]
XDSM = Extended design structure matrix

Chemical & Particle Symbols
BC = Black carbon
CO = Carbon monoxide
CO_2 = Carbon dioxide
C_xH_y = Hydrocarbons
H_2 = Hydrogen
H_2O = Water
CH_4 = Methane
N_2 = Nitrogen
NO_x = Nitrogen oxides
O_3 = Ozone
OC = Organic compounds
$PM_{2.5}$ = Particulate matter with a diameter of less than 2.5 micrometers
PMO = Primary mode ozone
nvPM = Non-volatile particulate matter
vPm = Volatile particulate matter
SO_x = Sulphur oxides

1

INTRODUCTION

RECENT reporting on climate change discusses the already observed impact due to anthropogenic global warming [1]. The observed impacts include more frequent and more intense weather events, a loss of biodiversity on land and in the water, and a negative influence on the physical and mental health of humans. In summary, the increase in the average temperature of the Earth's atmosphere will undoubtedly lead to economic and non-economic losses in future decades if the radiative forcing due to human activity is not reduced and if we do not adapt quickly enough to the changing climate.

The fact that aviation contributes to human-induced global warming is well established [2, 3]. Lee et al. estimated that in 2011, aviation caused approximately 3.5% of the anthropogenic effective radiative forcing. This contribution is a result of fossil-fuel combustion needed to propel the aircraft. This combustion leads to the emission of gases, which through several pathways cause a radiative imbalance in the atmosphere resulting in a net warming effect. Out of this 3.5% contribution, approximately 66% is attributed to effects not related to carbon dioxide (i.e., non-CO_2 effects) [3].

While this 3.5% contribution of aviation may appear small in the overall picture, reducing it to 0% or maintaining the same level is challenging for the aviation transport sector. If we examine the past trends in Figure 1.1, we see that the fuel burn per revenue passenger kilometer (RPK) has dropped drastically since 1960. Nevertheless, the total achieved RPK has also increased significantly. In the past, this strong growth was caused by reduced operating costs, an increase in the liberalization of international aviation, and higher per capita incomes in developed countries [4]. Considering both the fall in fuel burn per RPK and the increase in total RPK, the result is a net increase in absolute CO_2 emissions. It is important to note that this analysis does not account for the non-CO_2 effects of fossil-fuel combustion.

It is estimated that this demand for commercial air transport will continue to increase at 4 to 5% annually for the next two decades [9, 10]. This growth is related to a decrease in flight costs [11]. Without further technological, operational, and/or policy developments, the net effect of aviation on global warming will continue to grow. The result of a scenario study highlighting this effect is presented in Figure 1.2.

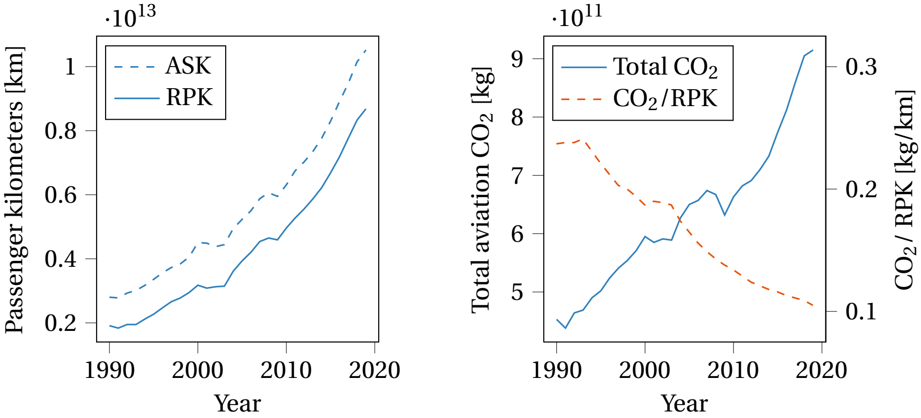

(a) Available seat kilometers [5] and revenue passenger kilometers [6, 7]

(b) Total CO_2 emissions and CO_2 emissions per revenue passenger kilometer [7]

Figure 1.1: Global airline traffic and aviation transport efficiency (CO_2 emissions per revenue passenger kilometer) from 1990 to 2019 (adapted from [8])

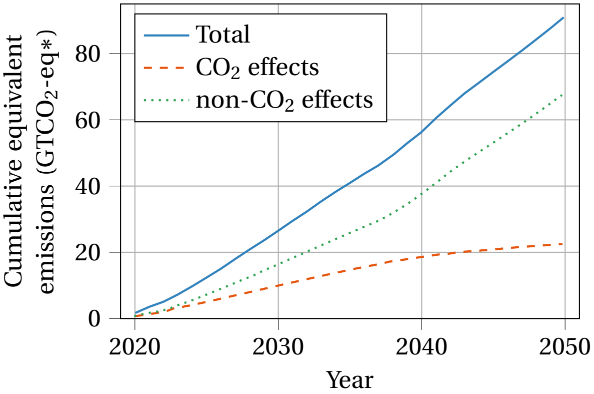

Figure 1.2: Cumulative emission in GtCO$_2$-eq∗ for future technology scenario (adapted from Figure 9.7 in Reference [12], scenario C without contrail strategy). This metric converts the impact of all climate species to equivalent CO_2 emissions based on the calculation of the global warming potential * (GWP*), which instead of the absolute emissions, considers the variation in emission rate for short-lived species [12, Appendix A].

This net warming effect will in the long term have detrimental consequences for nature and humanity. It is clear that there are economic and non-economic drivers to make aviation sustainable. However, the path to achieving sustainable, commercial air transport is not clear yet. The formulation of the way forward is complicated by several factors, such as non-CO_2 climate effects, conflicting design objectives, and the integration into operational networks. The following three sections dive deeper into these aspects and highlight the need for further analysis and a system-of-systems evaluation, in particular when considering alternative fuels.

1.1. GLOBAL WARMING IMPACT OF AVIATION

Sustainable aviation entails multiple aspects, including global warming, air quality, noise, and economy. The work in this dissertation focuses on the first pillar, which is also referred to as climate impact. In the past and at the time of writing, aviation contributes to global warming as a result of the combustion of fossil fuels (kerosene or Jet A1) in flight to provide propulsion and power to the aircraft and its systems. Considering the operational stage in an aircraft lifecycle, the combustion of fossil fuel changes the composition and physical processes in the atmosphere, leading to a radiative imbalance, also known as radiative forcing (RF), which in turn results in an increase in mean surface temperature (ΔT). More elaborate background information is provided in Chapter 2.

Fossil-fuel combustion at altitude leads to net positive radiative forcing through several pathways [13]. Figure 1.3 summarizes these pathways. Through complete and ideal combustion of kerosene, the engine emits carbon dioxide (CO_2) and water vapor (H_2O). However, the combustion process in aero engines is not perfect and, as a consequence, other species are emitted as well. Nitrogen oxides (NO_x), consisting of NO and NO_2, are formed near the flame region and in the post-flame gases [14]. Additional incomplete combustion products are soot, also known as black carbon (BC), unburned hydrocarbons (UHC or HC), carbon monoxide (CO), and sulfur oxides (SO_x). Finally, due to the emission of water vapor and aerosols into the dry and cold ambient flight conditions, condensation trails or *contrails* are formed under certain atmospheric conditions. The contrails can further evolve into contrail cirrus and/or interact with natural clouds.

As introduced above, the resulting climate impacts are often categorized as CO_2 and non-CO_2 effects. The formation of CO_2 emissions and the consequences on the atmosphere are well understood and are not particular to aviation. The total mass of CO_2 emissions is linearly related to the mass of kerosene burned. Hence, more fuel-efficient engines, lighter airframes, and/or reduced aerodynamic drag lead directly to reduced CO_2-related climate impact. This global warming effect is long-term, spanning centuries, and independent of emission location [16].

However, the radiative forcing and temperature change due to non-CO_2 species is not purely dependent on fuel consumption. First, the impact due to NO_x, H_2O, and contrails is strongly dependent on the altitude, latitude, and longitude of the emission or formation [16]. The altitude of lowest climate impact does not necessarily match the fuel-optimal altitude which would automatically minimize the CO_2 impact. Second, the emission index of NO_x increases with increasing pressure and temperature at the inlet of the combustor [14], and therefore engine overall pressure ratio (OPR). This parameter also greatly influences the engine's thermal efficiency, which drives fuel consumption and total emissions. Hence, to minimize NO_x effects with current technology, one has to find a balance between minimizing the emission index and fuel consumption. Third, the overall efficiency of a turbofan engine performs a role in the contrail formation criterion, with higher efficiencies increasing the probability of formation [17]. Finally, the non-CO_2 effects typically have a shorter lifespan than the response due to CO_2 emissions.

In conclusion, the total climate impact of an aircraft or fleet is dependent on the engine cycle parameters, the location of emission, and the considered time scale. Especially when considering novel fuels such as liquid hydrogen (LH2) or drop-in, sustainable aviation fuels (SAF), it becomes even more important to account for the non-CO_2

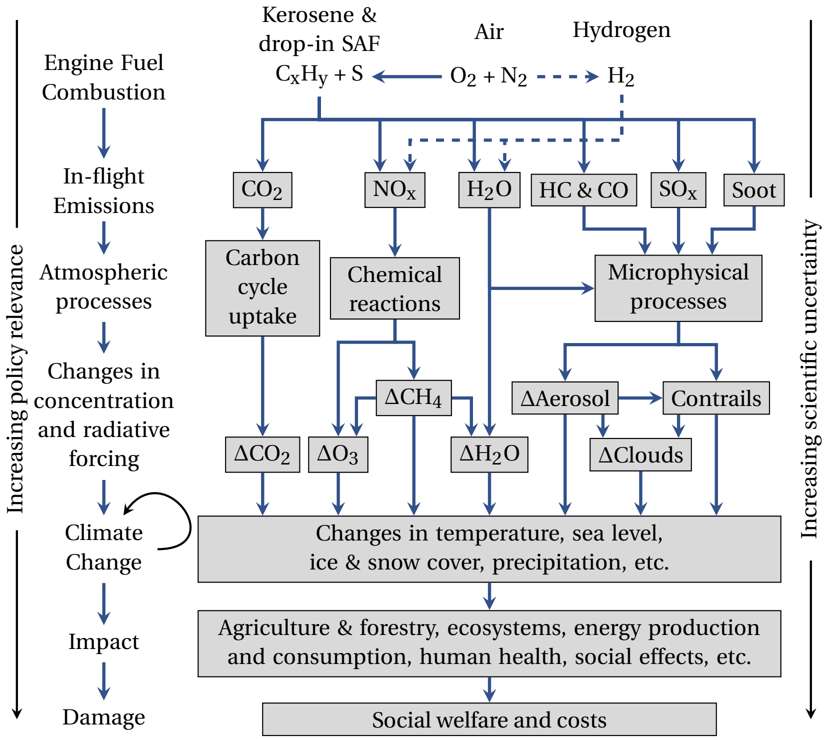
Increasing policy relevance
Engine Fuel Combustion
In-flight Emissions
Atmospheric processes
Changes in concentration and radiative forcing
Climate Change
Impact
Damage
Kerosene & drop-in SAF
C_xH_y + S
Air
$O_2 + N_2$
Hydrogen
H_2
CO_2
NO_x
H_2O
HC & CO
SO_x
Soot
Carbon cycle uptake
Chemical reactions
Microphysical processes
ΔCH_4
ΔAerosol
Contrails
ΔCO_2
ΔO_3
ΔH_2O
ΔClouds
Changes in temperature, sea level, ice & snow cover, precipitation, etc.
Agriculture & forestry, ecosystems, energy production and consumption, human health, social effects, etc.
Social welfare and costs
Increasing scientific uncertainty

Figure 1.3: Pathways from aviation in-flight emissions to climate impact and societal damages (adapted from References[13, 15, 3])

effects. When designing the next generation of aircraft, the design process should reflect these interactions between aircraft and engine design, operating conditions, fuel selection, and climate science. This highlights the need for multidisciplinary design analysis and optimization (MDAO).

Additionally, due to the emission-location dependencies and the formation of contrails mentioned above, the total emissions mass cannot be used as a design objective. Traditional design objectives, such as fuel consumption, operating costs, or maximum take-off mass (MTOM), do not necessarily lead to a climate-optimal aircraft design or fleet due to the non-linear relation between climate impact and fuel burn. This means that existing aircraft and engine design trends have to be updated, considering the conflicting objectives.

1.2. Selecting the Aircraft Design Objective(s)

By including the climate impact assessment in the multidisciplinary design workflow, a climate impact metric can be incorporated in the optimization of new aircraft concepts. The metric can be selected as the objective function, or a limit can be imposed on the climate impact. Ideally, the climate impact is the objective since this results in the most sustainable aircraft solution. The choice of climate impact metric is elaborated upon in Chapter 2.

However, a climate impact objective beyond the emissions was only introduced into aircraft optimization studies rather recently [18, 19, 20]. Examples of typical aircraft design objectives are fuel consumption, operating empty mass (OEM), maximum take-off mass (MTOM), direct operating costs (DOC), or lifecycle costs (LCC) [21]. These classical objectives can also be conflicting. For example, although a correlation exists between the fuel consumption and direct operating costs due to fuel cost, the optimal cruise Mach number for minimal fuel burn is typically lower than the optimal Mach number for minimal DOC [22, 23]. This offset in optimal cruise Mach number is caused by cost components which vary with block time, such as pilot and crew costs. Figure 1.4 provides an example of the trade-off between the cost objective and fuel objective. Note that these studies made assumptions concerning the ratio between time-related and fuel-related costs, captured in the cost index. The cruise Mach number that the airline selects for its operations may be different from the minima found in these studies considering other operational requirements.

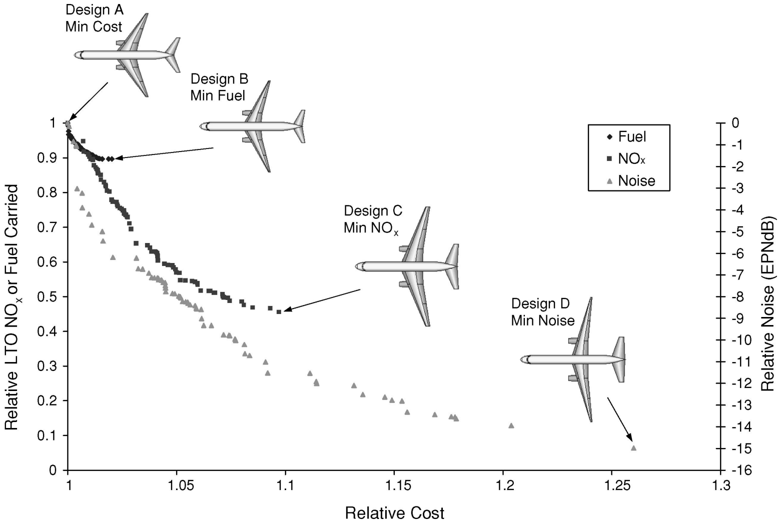

Figure 1.4: Pareto fronts showing the trade-off between cost, fuel, NO$_x$, and noise objectives [22]

Design objectives such as DOC and MTOM are directly related to fuel burn. Therefore, these single-objective solutions are often positioned closely together in the design and objective spaces. This is for example shown in Figure 1.4, where the fuel- and cost-optimal solutions are more similar than for example the aircraft optimized for minimum NO$_x$ or noise. In the climate impact objective, this correlation with fuel burn is still present since the emissions of CO$_2$, NO$_x$, and H$_2$O scale directly with fuel burn. In particular, the impact due to CO$_2$ scales directly with fuel burn since the emission index is constant for a given fuel type and since the position of emission does not matter.

However, as discussed above, the non-CO$_2$ effects are also dependent on other factors and do not directly relate to fuel consumption. Due to a mix of positive and negative correlations with fuel burn, climate-optimal design solutions are different from fuel- and cost-optimal aircraft [24, 20]. However, since these two aspects also perform an important role in future aircraft design and selection, it is advised to consider all three objectives simultaneously through multi-objective optimization.

When looking at potential future aviation fuels, this multi-objective approach is important since one has to ensure that the design variables of future aircraft are chosen such that for a targeted reduction in climate impact, the fuel type and design point minimize the cost and/or energy consumption. Alternatively, for a limited increase in cost, what aircraft design and which fuel type offer the largest reduction in climate impact? By considering all figures of merit in the assessment of alternative fuels, we can ensure we select the Pareto-optimal combination of design variables and fuel type.

In conclusion, the design solutions obtained through different objectives, in particular a climate impact objective, can be significantly different from the classical solutions. Therefore, the way they will be integrated into an operational fleet has to be evaluated. This highlights the need for a multi-level approach, as discussed in the following section.

1.3. INTEGRATION INTO AIRLINE OPERATIONS

Mission design variables, such as cruise Mach number, also influence the aircraft operations in a route network. Especially aircraft which fly slower may reduce the productivity, meaning that the aircraft have to be allocated differently, that more aircraft have to be introduced into the fleet to ensure a high enough frequency, and/or that aircraft have to transport more passengers in a single flight. Therefore, the analysis of climate-optimal aircraft should monitor the fleet-level climate impact, energy consumption, operating costs, and number of operational aircraft.

Over the past decade, optimization methods have been developed to support simultaneous aircraft design and fleet allocation. Jansen and Perez [25, 26, 27] proposed a method to optimize aircraft families and their allocation in different markets, showing that a reduction in fuel burn, operating cost, and acquisition cost can be achieved. This requires solving optimizations at multiple levels. Typically a nonlinear aircraft design optimization is combined with a (mixed-integer) linear programming (MILP) or dynamic programming approach for fleet allocation.

Moolchandani et al. [28] combined aircraft design with MILP to assess the environmental impact of new technologies, mainly focusing on CO_2 emissions. Hwang et al. [29] proposed a modular adjoint approach to solve such combined problems, resulting in fleet profit gains. Also, probabilities and uncertainties in aircraft technologies and forecasts can be taken into account [30]. Govindaraju, Davendralingam, and Crossley [31] employed a multi-level approach to study potential fuel burn savings under operational uncertainty.

However, these studies focused on optimization objectives which are closely related to fuel burn, energy consumption and/or operating costs. Therefore, it is of interest to study how the fleet composition and allocation change when the climate impact objective is employed. Such analysis can yield insight into how many more additional "slow-flying" would be required to meet the same network demand as cost-optimal aircraft. Or, how should the top-level aircraft requirements (payload and range) be adapted to limit the number of new aircraft?

Additionally, when studying alternative fuels such as liquid hydrogen and drop-in SAF, it is important to note that the availability of these fuel types in the near future is a key challenge [32]. Furthermore, in the case of hydrogen, the spacious cryogenic tanks introduce a penalty on the in-flight energy consumption due to a higher operating empty mass (OEM) and increased drag [33]. Therefore, key questions are how to optimally allocate these fuels in a fleet and what the corresponding top-level aircraft requirements are. This can lead to the creation of *multi-fuel fleets*.

1.4. RESEARCH OBJECTIVE AND QUESTIONS

The previous sections highlighted the interest to have multi-objective design trends which indicate how to achieve a reduction in the climate impact of aircraft while studying the trade-off with other objectives such as energy consumption and/or operating cost. Considering the need to decarbonize the industry, such trends should also be derived for alternative fuels such as liquid hydrogen and drop-in SAF. Additionally, it would be helpful to have insights into the effects of integrating climate-optimal aircraft into an operational network. Hence, to obtain such trends, a multidisciplinary, multi-objective, and multilevel approach has to be taken.

Therefore, the research objective of this dissertation is

to study the potential of aircraft design optimization and fleet allocation to minimize the global warming impact, while observing the change in energy consumption and financial costs for the operator, considering various technologies and fuels.

To achieve this research objective, two steps are taken: first, the climate impact and the relation to other objectives are assessed at the aircraft or system level. This allows us to develop the necessary models and verify them before moving to step two, the fleet-level assessment. In this step, the insights from the aircraft design optimizations are employed in a system-of-systems setup. The research questions related to the aircraft-level analysis are:

RQ1 Which set of aircraft and engine design variables minimizes the global warming impact and cash operating cost of one kerosene-powered turbofan aircraft for a given set of top-level aircraft requirements (TLARs) and a specified mission?

RQ2 What are the differences in operating cost, mission fuel, and climate impact between optimized propeller-powered aircraft and a turbofan-powered aircraft optimized for the same objectives, TLARs, and mission?

RQ3 For a hydrogen-powered, turbofan aircraft with the same top-level requirements and mission as in RQ1:

  (a) Which set of airframe, engine and mission design variables minimizes the global warming impact and cash operating cost?

  (b) What is the difference in climate impact, cash operating cost and other flight performance-related parameters when compared to the kerosene baseline?

RQ4 For turbofan aircraft powered by a 50-50 mix of drop-in SAF (HEFA) and fossil kerosene, with the same top-level requirements and mission as in RQ1:

   (a) Which set of airframe, engine and mission variables minimizes the global warming impact and cash operating cost?
   (b) What is the difference in climate impact, cash operating cost and other flight performance-related parameters when compared to the kerosene and liquid hydrogen aircraft?

RQ5 How does the trade-off between climate impact and operating cost vary between aircraft categories, considering kerosene, liquid hydrogen, and drop-in SAF?

Based on the aircraft-level assessments studied in the previous questions, the (near) climate-optimal solutions can be allocated in a route network. This yields insight into how to integrate these aircraft should be allocated and evaluate the impact at the fleet level. The results from the fleet-level assessment can in turn be employed to update aircraft design in terms of design variables and top-level requirements such as harmonic range and maximum structural payload. This system-of-systems approach is applied to answer the following two research questions:

RQ6 Considering an available network demand and fixed yield per passenger kilometer, what is the optimal fleet diversity and allocation of climate-minimal, kerosene aircraft in an airline network to maximize the profit?

RQ7 Considering the same network demand as in RQ6, what is the optimal fleet diversity and allocation of liquid hydrogen or drop-in SAF aircraft in an airline network to maximize the profit?

The answers to the above questions will provide insights to aircraft designers, airlines, and policymakers about design trades for reduced climate impact, the associated trade-off with other objectives, and the integration of such aircraft into operational networks. Such insights may in turn be used to make decisions to realize sustainable aviation.

1.5. RESEARCH SCOPE AND LIMITATIONS

Although the above questions aim at multiple levels of assessment, boundaries to the aircraft and fleet systems have to be imposed. Additionally, the analyses are multidisciplinary in nature, which captures the interactions between different disciplines but imposes constraints on the level of detail in which each aspect is treated. This level of detail is constrained to limit the computational workload in the MDAO and to reduce the number of detailed assumptions, leading to more uncertainty. This section provides an overview of the imposed boundaries on the system-of-systems approach, the level of design detail, and the assessed technologies.

1.5.1. AIRCRAFT DESIGN AND NETWORK MODEL LEVELS

The aircraft design and development cycle consists of several stages, from conceptual design to service engineering, as indicated in Figure 1.5 [34]. With each step, the designer gains more detailed knowledge about the aircraft, leading to more accurate information about its mass, performance, and geometry. Although this level of detail increases throughout the development stages, most in-service costs are fixed through decisions made in the conceptual and preliminary design stages [35].

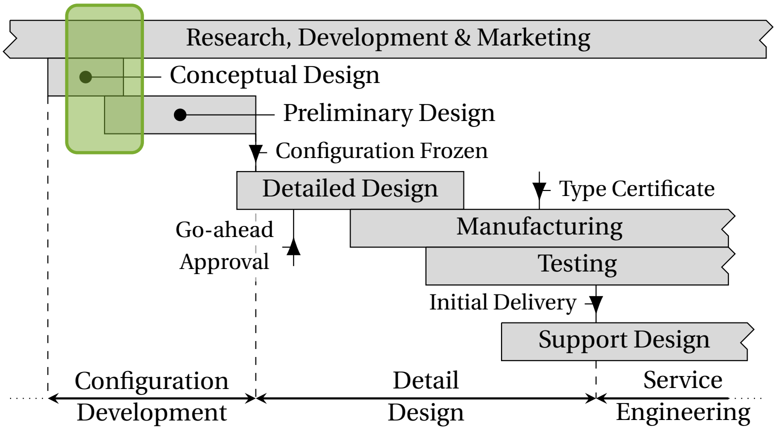
Research, Development & Marketing
Conceptual Design
Preliminary Design
Configuration Frozen
Detailed Design
Type Certificate
Go-ahead
Approval
Manufacturing
Testing
Initial Delivery
Support Design
Configuration Development
Detail Design
Service Engineering

Figure 1.5: Aircraft design and development stages (adapted from Torenbeek [34]). The green box indicates the design level considered in this dissertation.

In this research project, the aircraft and engines are developed at a conceptual and early-preliminary level of detail, as indicated by the green box in Figure 1.5. Before initiating the MDAO, the concept configuration and engine technology are fixed, as described in the next section. The assessment of the airframe is done at a conceptual level, relying on semi-empirical rules, Class-II methods, and a simplified three-view of the geometry. The analysis of the propulsion system involves a 1D thermodynamic, physics-based analysis which is sensitive to engine design variables and operating conditions.

The reason for selecting this conceptual design level is twofold. First, this approach limits the complexity of the methods and hence the computational cost of the aircraft design and optimization iterations. This low computational cost is required to execute the multi-objective optimizations in a timely manner. The conceptual methods also reduce the code implementation time. Second, extreme levels of detail in the structural or aerodynamic analyses would introduce more unknowns into the framework and therefore more uncertainties, without necessarily leading to more insight into how the climate impact drives high-level aircraft variables and top-level requirements.

Considering the fleet allocation and network modeling, a fixed network demand is assumed which is expressed as the number of passengers (or payload) per unit of time between given city pairs. For this constant demand, the change in the number of aircraft required and the change in their allocation for different objectives is of interest. This information can be used to derive updated top-level aircraft requirements and to provide information for a complete lifecycle analysis of an aircraft type. Nevertheless, it is outside the scope of this thesis to consider how the design objectives drive specific scheduling and maintenance decisions on an hourly or daily basis. Additionally, the feedback effect the fleet allocation or operating cost may have on the network demand is not considered.

1.5.2. AIRCRAFT CONFIGURATION AND PROPULSION SYSTEM SELECTION

Although novel aircraft concepts are proposed to replace current aircraft, this study focuses on the classical tube-and-wing configuration. The reason is twofold: first, the focus on tube-and-wing aircraft allow the usage of semi-empirical relations in the design process, whereas completely new configurations would require more physics-based analysis work. Such detailed analysis would require a higher computational effort and draw the focus away from the holistic analysis proposed above. Additionally, novel configurations would introduce more uncertainty in the outcome. Therefore, it is recommended to first develop the design trends for well-known configurations, clearly document the causes which drive these trends, and use these to support the design of other configurations. Climate impact evaluations of certain novel concepts, such as the Flying-V [36, 37] or AHEAD blended wing body [38], have been carried out in dedicated projects.

Alongside aircraft design changes, technology improvements, and the combustion of novel fuels, several research projects have investigated radical new propulsion systems [39, 40, 41, 42]. Examples include hybrid and fully electric propulsion, where propulsion power is partially or fully provided by electricity coming from batteries on board the aircraft. Additionally, there is also the option to convert hydrogen into electric power onboard by employing fuel cells.

These technologies offer a significant reduction in the in-flight contribution to global warming. Fully-electric aircraft do not emit any species at all in flight, bringing the net impact of flight to zero. This also means that there is no air pollution. Hybrid-electric aircraft, depending on the fuel and energy split, still emit the species discussed in Section 1.1, although at lower quantities. Nevertheless, Yin, Grewe, and Gierens showed that for hybrid-electric aircraft, the temperature threshold for contrail formation is lower, meaning that such aircraft will not form contrails at relatively low altitudes where conventional aircraft may already produce contrails [43]. Hydrogen-powered fuel-cell systems do not emit CO_2 or NO_x, but produce water vapor emissions and therefore exhibit a higher frequency of contrail formation [44]. However, it is expected that such contrails have a shorter lifetime.

Although the climate impact evaluation and optimization of such concepts is of interest for future aircraft, these concepts are outside the scope of the research work presented in this dissertation. The reason for this is twofold: first, other recent research projects have already provided insights into the design [41, 42], costs and climate impact of these technologies [43, 45, 46]. Second, the batteries or fuel-cell systems required to support such powertrains have been shown to introduce a high mass penalty, limiting their application in the short term to regional networks. Therefore, the focus in this work lies on short-, medium-, and long-range aircraft.

1.5.3. SYSTEM AND LIFECYCLE BOUNDARIES

Although the research proposed herein considers a system-of-systems approach, certain boundaries have to be imposed to scope the analyses and optimizations. The climate impact will be computed based on the in-flight emissions and contrail formation during the operational life of the aircraft. Emissions from other aircraft lifecycle phasesare not included in this dissertation. Also, the emissions related to the production of fuels are not accounted for in the climate impact analysis. Nevertheless, the current aircraft-level analysis can serve as input to more all-encompassing studies.

Considering the network model, the demand between origin-destination pairs is assumed to be constant and independent of the aircraft operating cost. It is possible that in the future, network and airline markets may change depending on the aircraft which become available. Additionally, the fleet allocation assumes an unlimited supply of liquid hydrogen and drop-in SAF at all considered airports. In reality, not all airports may be offer these fuels which will impose limits on the operations of aircraft powered by these fuels. However, the supply chain of liquid hydrogen and drop-in SAF is outside the scope of the current dissertation.

1.6. OUTLINE OF DISSERTATION

This dissertation aims at providing answers to the research questions introduced in Figure 1.6. First, Chapter 2 provides background information about the current scientific understanding of global warming due to aviation. The chapter touches briefly on the underlying chemical and meteorological effects and serves as a starting point for the climate modeling applied in the subsequent chapters.

Chapter 3 starts with the formulation of the general, multi-objective optimization problem and the description of the multidisciplinary aircraft design and optimization framework used throughout the research. Additionally, this framework is validated with existing engine and aircraft data. The optimization problem is then solved in Chapter 3 for a medium-range, narrow-body aircraft powered by fossil kerosene.

Based on the results of this baseline case, two technology pathways are explored. First, the performance of propeller-powered, medium-range aircraft is studied in Chapter 4, comparing the climate impact, energy consumption, and operating cost to those of the turbofan counterpart. The second pathway is to introduce novel fuels into the aircraft and fleet. Therefore, Chapter 5 studies the optimization of medium-range aircraft. The MDAO workflow is adapted to account for the tank integration into the fuselage and the climate impact as a result of hydrogen combustion. Additionally, the Pareto-optimal hydrogen designs are compared to the multi-objective solutions from Chapter 3. In Chapter 6, this analysis is extended for drop-in, sustainable aviation fuel mixtures (with fossil kerosene) and different aircraft categories. In this chapter, conclusions are drawn concerning the Pareto-optimality of different fuel applications.

The analyses and optimization in Chapters 3 to 6 provide mainly an aircraft-level assessment. In Chapter 7, a system-of-systems approach is presented to assess the aircraft design changes together with the impact on the fleet allocation considering a given network demand. This chapter discusses how the design changes impact the network profit and revenue passenger kilometers (RPKs) transported, among other metrics.

Chapter 8 brings the findings from the research together and discusses them in the context of sustainable aviation. Other sustainability aspects, such as air quality, aircraft community noise, and economics are touched upon in this chapter. Furthermore, the uncertainties due to the climate model are quantified in Chapter 8, which leads to design for robustness through robust multidisciplinary design optimization (RMDO). Chapter 9 summarizes the most important conclusions of the dissertation and identifies recommendations for further research.

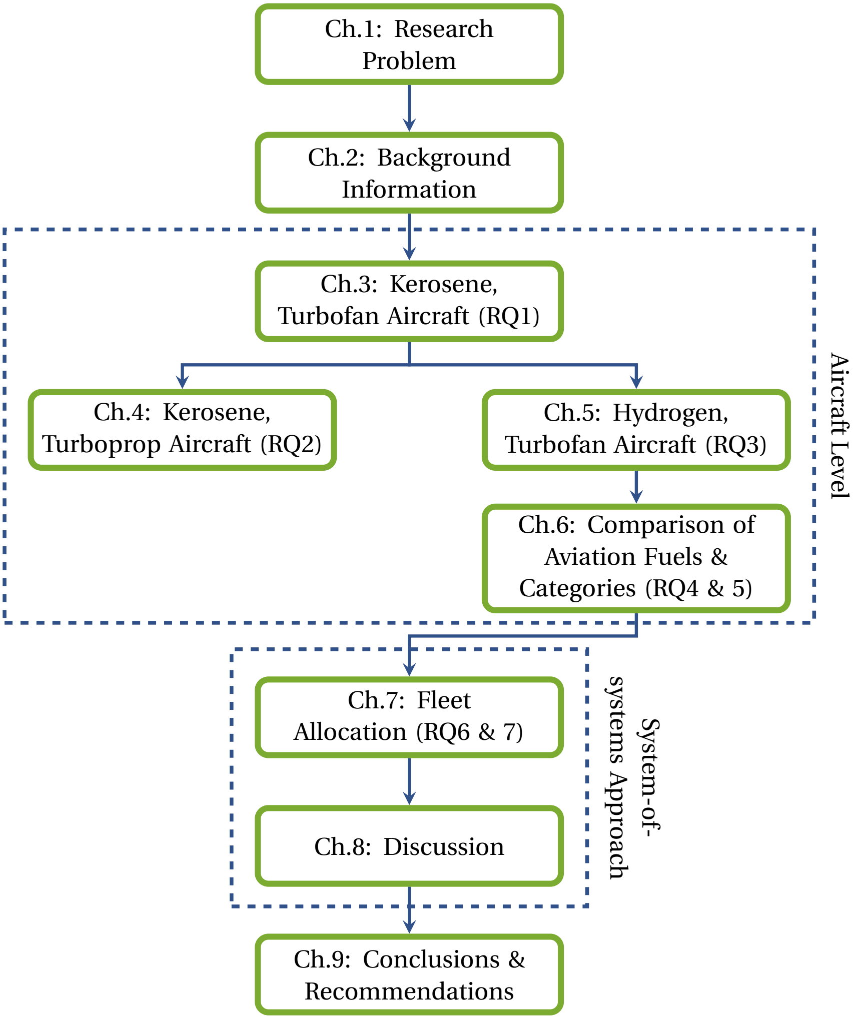
Ch.1: Research Problem
Ch.2: Background Information
Ch.3: Kerosene, Turbofan Aircraft (RQ1)
Ch.4: Kerosene, Turboprop Aircraft (RQ2)
Ch.5: Hydrogen, Turbofan Aircraft (RQ3)
Ch.6: Comparison of Aviation Fuels & Categories (RQ4 & 5)
Aircraft Level
Ch.7: Fleet Allocation (RQ6 & 7)
Ch.8: Discussion
System-of-systems Approach
Ch.9: Conclusions & Recommendations

Figure 1.6: Dissertation structure

2

AVIATION EMISSIONS AND CLIMATE EFFECTS

This chapter discusses the influence of aviation on the Earth radiation budget and its contribution to global warming. Furthermore, an overview of the observed and expected impact due to climate change is provided.

Carbon dioxide is a natural greenhouse gas whose emission from fossil fuels directly leads to global warming. The atmospheric CO_2 *concentration decreases again through the carbon cycle, but this process spans from several years to millennia. Similarly, water vapor emissions directly contribute to the enhanced greenhouse effect, although the* H_2O *vapor perturbation lifetime is limited to several months in the troposphere. Nitrogen oxides (NO and* NO_2*) are formed through non-ideal combustion with air, which chemically react when emitted at the upper troposphere and lower stratosphere. As a consequence, short-term ozone is formed, causing a warming effect, while atmospheric methane is depleted. The latter reaction also depletes primary-mode ozone and stratospheric water vapor, resulting in a cooling effect. Nevertheless, the net effect of* NO_x *emissions of aviation leads to warming. Due to the combustion of kerosene, aerosols are also created, mainly soot and sulfate, which have a direct radiative impact, interact with natural cirrus, and perform a role in contrail formation. Emitting hot and humid air leads to persistent contrail formation under certain atmospheric circumstances. These contrails can lead to contrail cirrus and interact with natural clouds. Although the impact due to contrails depends on many factors, the net radiative forcing is estimated to be positive. Considering all of these aviation-induced changes to the climate, the net impact is warming.*

Together with other sectors, aviation thus contributes to global warming. At the time of writing, temperature changes and their impact on weather events, such as storms and droughts, have been observed. This anthropogenic warming is expected to lead to sea-level rises, reduced availability of fresh water, food insecurity, damage to ecosystems, and a negative influence on human health. Although difficult to quantify, these effects will have economic and social consequences.

THIS chapter aims to provide a state-of-the-art overview of how aviation leads to global warming according to Figure 1.3 on Page 4. First, a general introduction to global warming is presented in Section 2.1. Second, Section 2.2 focuses on how aviation contributes to a change in the Earth's radiative budget and the characteristics of each climate species. Subsequently, Section 2.3 discusses how the climate impact is quantified in the current study and how it is integrated into aircraft design optimization. Finally, Section 2.4 summarizes the currently observed and expected global impacts due to global warming. This chapter provides background material to aid in the modeling of the climate impact and reflecting on the results in the subsequent chapters. Nevertheless, for a more detailed discussion on the individual climate effects, the reader is referred to the provided references. Additionally, climate science is rapidly evolving, leading to improved confidence and agreement levels. Hence, staying up to date with the latest insights is essential.

2.1. EARTH'S RADIATION BUDGET AND GLOBAL WARMING

The weather and climate, which is defined as the average weather condition [47], is driven by the Earth's radiation budget [48]. This radiation budget accounts for the Earth system's absorption, reflection, and emittance of radiation. Figure 2.1 illustrates these principles and the role of the atmosphere. The sun at the center of the solar system provides the primary source of incoming radiation. The sun produces energy as a result of nuclear fusion and emits this energy as radiation. A small part of this radiation reaches the Earth system, which includes the atmosphere. From this small part, a fraction is reflected by clouds, atmospheric molecules, and the Earth's surface [49]. The remainder is absorbed by the Earth's surface. At the same time, the Earth's surface emits thermal radiation into space that balance the incoming energy [49].

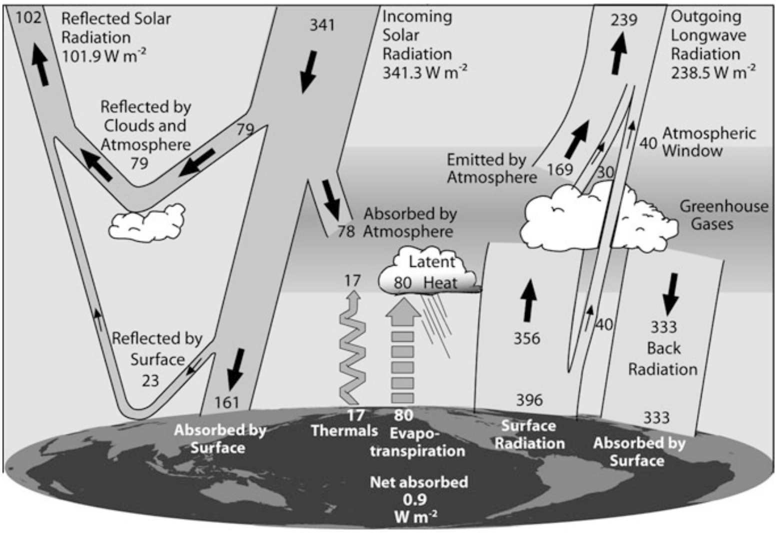
102
Reflected Solar Radiation 101.9 W m-2
341
Incoming Solar Radiation 341.3 W m-2
239
Outgoing Longwave Radiation 238.5 W m-2
Reflected by Clouds and Atmosphere 79
79
40 Atmospheric Window
Emitted by Atmosphere
169
30
Greenhouse Gases
Absorbed by 78 Atmosphere
Latent 80 Heat
17
356
40
333 Back Radiation
Reflected by Surface 23
161
396
333
Absorbed by Surface
17 Thermals
80 Evapo-transpiration
Surface Radiation
Absorbed by Surface
Net absorbed 0.9 W m-2

Figure 2.1: Earth's global annual mean energy budget from March 2000 to March 2004. Image by K. E. Trenbeth, National Center for Atmospheric Research, Boulder, Colorado, USA

The atmosphere performs an important role in this radiation budget, as shown in Figure 2.1. Although oxygen and nitrogen make up most of the atmosphere in terms of concentration, these gases do not perform a role in the absorption or emittance of longwave radiation from the Earth's surface as they are infrared inactive. As indicated on the right hand side in Figure 2.1, the atmosphere contains greenhouse gases that interact with the outgoing radiation. The greenhouse gases carbon dioxide (CO_2), methane (CH_4), water vapor (H_2O), ozone (O_3), and nitrous oxide (N_2O) are naturally present in the atmosphere [49]. Each of these gases occurs in different concentrations and has different radiative properties. Therefore, the gases interact with different radiation wavelengths [49]. Furthermore, while the methane concentration may be lower than the one of carbon dioxide, the greenhouse effect of a molecule of methane is 7.5 times higher than for carbon dioxide [49], indicating that using concentrations of gases as a metric for global warming does not yield a complete picture.

These greenhouse gases absorb a fraction of the outgoing thermal radiation, which means this energy is not emitted into space. As a consequence, this absorption naturally traps heat, and therefore, an average surface temperature of approximately 15°C (288.15 K) is obtained. The processes described above are natural, and they are known as the *the natural greenhouse effect* [49] since they do not involve warming induced by human activities. It is important to note that, next to radiation, convection and mixing also perform essential roles in heat transfer within the atmosphere, and the temperature decreases with increasing altitude. Additionally, clouds affect the radiative balance by reflecting incoming radiation and absorbing and emitting Earth's thermal radiation.

Problems in the radiation budget start to occur when human activities alter the composition of greenhouse gases in the atmosphere. In the past two centuries, and in particular, in the past decades, additional carbon dioxide and methane from fossil sources have entered the atmosphere. Also, human-made greenhouse gases (sulfur hexafluoride [SF6], hydrofluorocarbons [HFCs], chlorofluorocarbons [CFCs], and perfluorocarbons [PFCs]) have been introduced into the atmosphere. These gases have their own radiative properties and lead to ozone depletion.

Human activities change the atmosphere's composition compared to its natural state [49]. Aviation also induces changes to the atmospheric composition and cloudiness through several pathways, as discussed in Section 2.2. An increase in greenhouse gas concentrations enforces the above-mentioned effect, namely the absorption of Earth's thermal radiation without any changes to the incoming radiation. The surface and lower atmosphere warm up to maintain the balance. This warming is also called the *enhanced greenhouse effect* [49].

Research has identified another source of long-term global heating, namely trough waste heat from energy production [50, 51, 52], sometimes referred to as anthropogenic heat flux [53]. Although the relative contribution to the overall warming is initially estimated to be small [52], the contribution of this warming mechanism may increase in the future as greenhouse gas emissions decrease, but the need for energy production grows [1]. Although it is important to be aware of this mechanism, further consideration of the potential heating through waste heat is outside the scope of the current research.

---

[1] URL `https://aeon.co/essays/theres-a-deeper-problem-hiding-beneath-global-warming` accessed on 22 February 2024

This enhanced greenhouse effect, which leads to surface warming, also has other consequences which have a heating or cooling effect. These consequences are often referred to as *feedbacks in the climate system* or *Earth system feedbacks*. In Figure 1.3, this feedback is illustrated by the arrow loop originating from the climate change level. These feedback mechanisms can be positive, leading to a warming effect, or negative, resulting in cooling. Table 2.1 provides an overview of these feedback mechanisms. The most prominent positive feedback mechanisms are the increase in water vapor (also a greenhouse gas) and a reduction in albedo due to ice and snow melting. The largest negative feedback loop is the Planck feedback, accounting for the increased outgoing radiation due to increased temperature. The latest research indicates that the net feedback effect is negative (i.e., cooling), although uncertainty is present due to the effect of global-warming on clouds [54]. The net feedback parameters also depend on the global temperature and considered time scale.

Table 2.1: Overview of feedbacks in the climate system [54]

Positive (Warming)	Negative (Cooling)
Water vapor	Planck
Carbon cycle	Carbon Cycle
Cloud-radiation	
Ice-albedo	
Gas release	

The difference in radiation budget and the warming effect is often quantified by the *radiative forcing* metric, which measures the “change in average net radiation at the top of the troposphere” (Houghton, 1997, page 22) and is expressed in terms of power per unit area ($\mathrm{W m^{-2}}$ or $\mathrm{mW m^{-2}}$). A positive radiative forcing corresponds to a warming effect where the incoming radiation is higher than the outgoing radiation. Oppositely, negative radiative forcing results in a cooling effect. The radiative forcing is computed for a change in concentration with respect to pre-industrial times, typically 1750.

However, several definitions of radiative forcing exist, and the Intergovernmental Panel on Climate Change (IPCC) often uses the stratosphere-adjusted radiative forcing at the top of the troposphere, i.e., the tropopause [3]. However, several considerations apply to this parameter, such as the applicability for heterogenous climate species. These considerations are considered outside the scope of this section. Recently, the IPCC [54] and aviation climate impact analyses [3] have used the *effective radiative forcing* (ERF) as a metric for the global mean temperature response. The ERF measures “the change in the net downward radiative flux at the TOA [top of the atmosphere] . . . after the system has adjusted to the perturbation but excluding the radiative response to changes in surface temperature” (IPCC, 2021, page 941). This means that the ERF metric takes into account TOA energy balance differences due to changes in the stratospheric and tropospheric temperature, cloudiness, and water vapor. However, flux changes due to changing ground surface air temperature are not included in ERF.

The change in the Earth's radiation budget thus leads to changes in global surface temperature. The consequences of this temperature increase are discussed further in Section 2.4.

2.2. AVIATION'S CONTRIBUTION TO GLOBAL WARMING

This section focuses on how each of the emitted species in Figure 1.3 on Page 4 results in global warming. The pathways are typically classified into CO_2 and non-CO_2 effects. For each species, its emission and formation, behavior in the atmosphere, lifetime, and radiative effects are discussed to help understand the design changes in the following chapters. The following sections also discuss the relative impact of each of these pathways to the total aviation climate impact. Recent research (from 2021) [3] estimated that this net aviation impact measured by ERF was +100.9 $\mathrm{mW/m^2}$ in 2018.

2.2.1. CARBON DIOXIDE

Carbon dioxide (CO_2) is formed due to the combustion of fuels which are based on carbon-hydrogen bonds (C_xH_y). One kilogram of kerosene fuel results in approximately 3.16 kilograms of carbon dioxide. This ratio is known as the emission index. Ideally all carbon atoms in the combustion process are bonded to two oxygen atoms during complete combustion.

When CO_2 is emitted into the atmosphere, it mixes with other gases but does not chemically react with them. This makes CO_2 a well-mixed gas and makes its climate impact independent of the location, altitude, or time of emission. CO_2 emitted from fossil fuels enters the global carbon cycle [49]. At first, this increases the atmospheric CO_2 concentration. Through the carbon cycle, CO_2 is removed from the atmosphere through several pathways: biosphere uptake (plants and trees, on land and in the ocean), ocean uptake, and land or soil uptake [49]. Each of these uptake processes has a different lifetime, ranging from years to centuries and even thousands of years. As a result, the emitted CO_2 is a long-lived gas whose effects remain noticeable for centuries.

As discussed in Section 2.1, the human-induced increase of greenhouse gases, such as CO_2, leads to a warming effect by absorbing thermal radiation from the Earth. Lee et al. [3] estimated that aviation-induced CO_2 emissions have to lead an effective radiative forcing of +34.3 $\mathrm{mW/m^2}$ in 2018.

Depending on the combustion technology and conditions, carbon monoxide is also formed in smaller amounts due to incomplete combustion. Nonetheless, the impact of this emission due to aviation on global warming is expected to be negligible compared to the other processes treated in this section [55].

2.2.2. NITROGEN OXIDES

Nitrogen oxides, which comprise both NO and NO_2, result from non-ideal combustion due to the presence of nitrogen (N_2) in the ingested air. This means that NO_x is not only formed in the case of fossil kerosene but also when drop-in SAF or hydrogen is combusted. An exception is the use of fuel cells to extract electric power from hydrogen. The following four different mechanisms lead to nitric oxide (NO) formation in the gas turbine combustion processes [14, Chapter 9]:

1. Thermal NO: This endothermic process oxidizes the atmospheric nitrogen in the flame and post-flame gases at high temperatures (≥ 1800-1850 K [14, 56]). The Zeldovich mechanism lies at the foundation of this formation process, leading to nitric oxide (NO) which can later oxidize to NO_2. This process highly depends on temperature, pressure, equivalence ratio, and residence time.

2. Prompt NO: In low-temperature and fuel-rich regions of the flame, early in the combustion process, when nitrogen reacts with hydrocarbons (CH). This reaction leads to HCN and N, of which the N will oxidize to form NO_x [56].

3. Nitrous oxide: This reaction is similar to the thermal NO_x formation process but occurs at lower temperatures [56] and features the production of N_2O. This N_2O subsequently oxidizes and leads to NO_x.

4. Fuel NO: a fourth mechanism which can lead to NO_x emissions is due to nitrogen content in the fuel, or *fuel-bound nitrogen*. In the combustion process, this nitrogen can react to form NO_x. However, kerosene contains limited trace amounts of fuel-bound nitrogen [55, Section 7.8]. Therefore, this formation mechanism is not relevant to the fuels considered in this dissertation.

The NO oxidizes to NO_2 in post-flame regions. NO_x captures both compounds in one term. The relative contribution of the first three mechanisms changes according to the combustion conditions [14].

Different from CO_2, the emission index of NO_x, EI_{NO_x}, is not constant but depends on the combustion technology and the conditions (i.e., pressure, temperature, humidity, and fuel-to-air ratio) in the combustion process. As a result, the total amount of NO_x emitted depends on the fuel flow and the emission index. These two factors conflict in the case of increasing engine overall pressure ratio (OPR) [57, 58]. The high pressure and temperature in the combustor increase the formation of NO_x. At the same time, a high OPR also increases the engine's thermal efficiency reducing the fuel consumption and CO_2 emissions.

Since the emission index depends on combustion technology and conditions, the prediction is non-trivial. Several methods exist to estimate EI_{NO_x}, with varying complexity and fidelity. Chandrasekaran and Guha [59] provide an overview of correlation-based, $P_3 - T_3$, fuel flow, simplified physics-based, and high fidelity simulations. In the subsequent chapters, a $P_3 - T_3$ method is used, as discussed in Section 3.1.2.

NO_x is not a greenhouse in itself but indirectly influences greenhouse gas concentrations in the atmosphere, which will, in turn, affect the radiative forcing and global warming. Available research has identified the following four pathways through which aircraft NO_x emissions at altitude affect ozone, methane, and stratospheric water vapor content:

1. Formation of short-term ozone (O_3) which causes a warming effect: O_3 is naturally present in the atmosphere. This compound is produced, destroyed, and transferred in the troposphere and stratosphere by means of various processes [55]. Figure 2.2 illustrates the chemical processes involved in ozone creation in the troposphere. The NO_x concentration performs an important role in the rate

of O_3 production through reaction with HO_2: $HO_2 + NO \longrightarrow OH + NO_2$, on the right side of Figure 2.2. The NO_2 subsequently undergoes photolysis, resulting in atomic oxygen (O) which reacts with oxygen (O_2) to produce ozone. A complete set of chemical reactions can be found in References [55, Section 2.1.2] and [60, Table 3]. The increase in ozone concentration will subsequently lead to an enhanced greenhouse effect. The radiative effect of this pathway depends on the emission altitude [60] and is relatively short-lived, on the order of months [61].

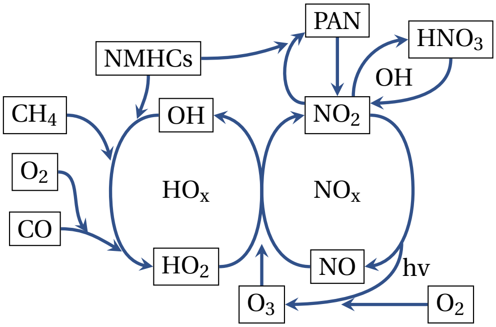

Figure 2.2: Tropospheric chemical mechanism leading to ozone (NMHC = non-methane hydrocarbons, PAN = peroxi-acetyl-nitrate, hv represents photolysis process through sunlight), adapted from Grewe [62]

2. Depletion of methane (CH_4), leading to a cooling effect: As can be seen in Figure 2.2, NO_x also performs a role in the production hydroxyl radical (OH). Hydroxyl reacts with methane (CH_4) reducing the lifetime and atmospheric concentration of CH_4 [63]. Since methane is a greenhouse gas with a higher efficacy than CO_2, its depletion leads to a cooling effect. Notably, the methane lifetime change is transient [64], which also influences the following two effects on primary mode ozone and stratospheric water vapor. The depletion is a long-term effect (approximately 11 to 12 years) due to the changing lifetime of methane. Additionally, the radiative effect varies with emission location and altitude [63, 60].

3. Depletion of long-term, primary-mode ozone (PMO), which results in a cooling effect: Since methane is a precursor of ozone, the depletion of methane discussed above also causes a decrease in background or primary-mode ozone [61, 64]. Unlike the first ozone effect, this process is long-lived, according to the methane response, and also results in cooling due to the removal of the greenhouse gas, although this cooling effect is smaller than that of methane depletion.

4. Decrease in stratospheric water vapor content, which causes a cooling effect: Via natural processes, methane enters the stratosphere and is oxidized, resulting in CO_2 and water vapor [65, 64]. However, due to the reduction in methane discussed in item 2, less stratospheric water vapor is produced. Since water vapor is a greenhouse gas, this reduction also leads to a cooling effect, although the magnitude of this effect is estimated to be smaller than the methane and PMO effects [3].

Based on the current understanding, it is expected that aviation-induced NO_x emissions so far have led to a net warming effect [3]. This effect amounts to approximately $+17.5\,\mathrm{mW/m^2}$ in effective radiative forcing [3], which is approximately 17% of the total net aviation ERF.

2.2.3. WATER VAPOR

Similar to carbon dioxide, water (H_2O) is produced in the ideal combustion process of kerosene, and it exits the engine as water vapor. The emission index of water vapor is constant and approximately 1.26 kg/kg for kerosene. Therefore, the total H_2O emissions scale with fuel burn. The emitted water vapor increases the atmospheric water vapor concentration and leads to contrail formation, as discussed in Section 2.2.5. This section focuses on the impact of water vapor as a greenhouse gas.

Since water vapor is a greenhouse gas, it can absorb thermal radiation from the Earth and enhance the greenhouse effect. However, in contrast to carbon dioxide, the atmospheric lifetime of water vapor depends on the emission altitude. The water vapor emitted into the troposphere or lower stratosphere by aircraft, for example, is quickly washed out by precipitation (the hydrological cycle) within one to two weeks and does therefore not accumulate [55]. This process makes the effect of water vapor due to aircraft in the troposphere short-lived. Recent research from 2021 estimates that the climate impact due to subsonic-aircraft water vapor emissions is relatively small compared to the contributions of CO_2, NO_x, and contrails [3], amounting to approximately 2% of the net total effective radiative forcing.

If water vapor is emitted into the stratosphere, which is dry and has a slow turnover of air, the residence time will be longer (on the order of months [66] or years for very high altitudes [15-30 km][67]) and the build-up of water vapor will be higher. This can make water vapor the largest contributor to the climate impact of potential supersonic [66] and hydrogen-powered hypersonic fleets [67], although other chemical reactions perform a role in the latter case.

The current research is limited to high-subsonic and low-transonic aircraft emitting water vapor in the troposphere and lower stratosphere, up to 12 km. This upper altitude bound limits the maximum water vapor perturbation lifetime to approximately 1 month according to Figure 6a in Reference [66]. Therefore, including the short-term effects of water vapor is sufficient.

2.2.4. AEROSOLS

Non-ideal combustion of kerosene leads to the emission of aerosols, which are airborne solid particles or liquid droplets. In the atmosphere and when considering aero engine emissions, aerosols are also often referred to as particulate matter. Soot is the primary non-volatile particulate matter (nvPM) emitted from kerosene-powered turbofan engines. It comprises black carbon (BC, elemental carbon, or EC) and organic compounds (OC). This mixture is created due to hydrogen oxidization in the fuel-rich, turbulent region of the flame, leading to particles with a high carbon content [68]. Since aromatic hydrocarbons have a higher hydrogen-to-carbon ratio, fuels with more aromatics lead to higher soot formation. Additionally, the combustion technology and process influence the formation of soot [69]. The smoke number in engine tests measures the amount of soot and varies with engine thrust settings [70].

Also, volatile particulate matter (vPM) is emitted. However, vPM is created in the exhaust plume or ambient air as a consequence of emitted precursors [69]. One of the sources is sulfur content in the fuel, which causes the emission of SO_2 and, in smaller amounts, H_2SO_4 [3]. Through oxidation in the atmosphere, sulfate aerosols (SO_4^-) are created. Also, NO_x emissions lead to particulate matter in the form of nitrate (NO_3^-). The latter process is particularly important for pollution and not for global warming.

Aerosols influence global warming through the following two pathways [3, 63]:

1. Direct radiation interaction:
    - Soot absorbs shortwave radiation, leading to a net warming effect.
    - Sulfates reflect incoming radiation causing a cooling effect, similar to when volcanoes erupt [49].
2. Interaction with natural clouds:
    - Soot can influence nucleation in clouds, leading to a cooling or small warming effect. This process carries high uncertainty.
    - Sulfates can also act as condensation nuclei for liquid clouds and cause nucleation for ice clouds. This promotes albedo and leads to cooling, although this effect is possibly the opposite for high-altitude clouds [55, Section 1.3.4].

The net effective radiative forcing of aerosol-radiation processes is approximately $-6.5\,\mathrm{mW/m^2}$ in 2018 [3], resulting in cooling. The radiative forcing due to the aerosol-cloud interaction is often not added to the current aviation-induced global warming budgets due to the lack of best estimates [11]. The effects induced by aerosols are short-lived, on the order of days to one week, since the lifetime of aerosols is short. Also, unburnt hydrocarbons (HC or UHC) are emitted by the engine and can form new particles or interact with existing aerosols [63], although no consequences for global warming have been identified at the time of writing.

2.2.5. CONTRAILS AND CONTRAIL CIRRUS

Condensation trails, commonly known as *contrails*, form behind aero engines when the hot and humid exhaust flow mixes with the colder and drier ambient air, which is also drawn in from the wing vortices [71, 72]. In the mixing process, the temperature and humidity of the exhaust gases decrease while the air becomes saturated with respect to liquid water. As a result, droplets form, which, under the right conditions, are supercooled and freeze, i.e. form crystals. If ice supersaturation is achieved, these ice crystals can persist. The term *persistent contrails* is used in this case.

This process of ice crystal formation relies on aerosols to act as nuclei. Soot (nvPM) can act as nuclei for kerosene-powered engines. Nevertheless, in the absence of particles from the engine exhaust, there are enough aerosols in the ambient to act as nuclei. Therefore, other fuels, such as SAF or hydrogen, with fewer or no soot particles, can produce contrails. Nevertheless, the properties of these contrails are different. The number and size of the ice particles dictate their lifetime and resulting radiative forcing [73]. Sections 5.1.2 and 6.1.2 (Pages 88 and 120) explain how these differences are accounted for in the presented studies. The ice crystal formation process occurs during the *jet phase* of contrail formation, which takes on the order of five to ten seconds.

Subsequently, the *vortex phase* starts in which the vortices from the wing tips interfere with the trails of ice crystals. The trails roll up with the vortices, and the contrails start to descend. This process, which also involves ice microphysics, depends on many factors, such as relative humidity, temperature, ambient turbulence, initial crystal size and number, and aircraft type. With higher aircraft mass and higher circulation, the downwash and therefore contrail downward motion (typically between 200 and 600 m) increases [71, 74]. During this phase of two to four minutes, the number of ice crystals decreases due to adiabatic heating. Note that in recent research, the vortex phase is split up into the *vortex* and *dissipation regimes* [72, 75].

The final phase is the *dispersion* or *diffusion phase*, which can last from a couple of minutes to a couple of hours. In this phase, vertical wind shear may interact with the vertically-distributed contrail and spread the contrails horizontally. This leads to contrail cirrus. Additionally, or depending on the location, the contrails may interact with other contrails or natural cirrus. However, this process is highly dependent on the weather. Since the total lifetime is not expected to exceed a couple of hours, the global warming impact is considered to be short-lived.

Contrails and contrail cirrus do not alter the concentration of greenhouse gases but instead affect the radiation budget by reflecting incoming shortwave solar radiation (albedo) and the absorption of outgoing, longwave radiation. Schumann et al. [76] studied the sensitivity of the net radiative forcing (longwave absorption minus shortwave reflection) with respect to contrail temperature, optical depth, crystal size and habit, solar zenith angle and the presence of other cirrus. A strong dependence on particle habit and zenith angle was found. The latter parameter also causes the impact of contrails to vary throughout the day, with a larger cooling effect at the surface during the day (high zenith angles) [77], as well as seasonally [78]. Additionally, the radiative forcing is sensitive to the cruise altitude of the aircraft [79], as discussed further in Section 3.1.2.

Considering that contrails and contrail cirrus can have both cooling and warming effects, depending on the time of day, season, and particle characteristics, the net radiative effect is expected to be warming. According to Lee et al. [3], the effective radiative forcing due to contrail cirrus amounted to $+57.4\,\mathrm{mW/m^2}$ in 2018, with a 90% likelihood between +17 and $+98\,\mathrm{mW/m^2}$. This average is approximately 1.7 times as high as the CO_2 effect. Additionally, not all flights contribute to this effect since the contrail formation conditions are not met in all flights. Teoh et al. [78] estimated that in the North-Atlantic region, approximately 12% of the flights lead to 80% of the forcing due to contrails. Research by Burkhardt and Kärcher [80] focused on contrail cirrus and the interaction with natural cirrus found that the radiative impact of contrail cirrus is potentially nine times as high that of line-shaped contrails.

Taking all of the above considerations and sensitivities into account, it is clear that the prediction of the radiative impact due to contrails is complicated. At the time of writing, the impact of contrails and contrail cirrus carries the largest uncertainty [80] of all contributions discussed in this section. The impact of this uncertainty on the results of studies presented in this dissertation is discussed in Section 8.5.

2.2.6. TOTAL IMPACT OF AVIATION

Considering all of the above effects, aviation has a net warming effect of approximately +101 mW/m^2 in 2018, measured in effective radiative forcing [3]. The contribution of CO_2 to this net total impact is (only) 34%, indicating the significance of non-CO_2 effects. The relative contribution of aviation in 2018 to total anthropogenic warming is not available at the time of writing. However, the ERF was 80.4 mW/m^2 in 2011, which amounts to approximately 3.5% of the total, global warming.

2.3. METRIC SELECTION AND INTEGRATION INTO AIRCRAFT DESIGN OPTIMIZATION

The overview in the previous section uses effective radiative forcing as a climate metric. However, when evaluating new aircraft designs or technologies, radiative forcing is not the best indicator [81]. The absolute emissions in kg cannot be used as a metric either since they do not consider the dependence of the impact on location, altitude, and time. Additionally, contrails cannot be expressed in this format. Ideally, the climate impact can be evaluated in monetary terms to perform cost-benefit analyses of different mitigation and adaptation technologies and strategies. However, making the step from temperature to a monetary value increases the uncertainty even further, as will become evident from the discussion in the subsequent section.

Aircraft design and technology evaluation requires an all-encompassing metric that considers both CO_2 and non-CO_2 effects. This condition is satisfied when using ERF. However, measure of temperature is a more relevant indicator of climate impact than (effective) radiative forcing, as indicated by the relative position in Figure 1.3. The change in temperature is also considered to be more intuitive. Therefore, also metrics based on radiative forcing, such as the global warming potential (GWP), are not preferred.

Additionally, the chosen metric should ideally not be a “snapshot” at a given time instance but rather provide an impact evaluation independent of the considered year or time horizon. An evaluation at a selected time instance may give particular importance to either short- or long-term effects, while both timescales be considered. For this reason, this study does not use the global temperature potential (GTP) or the value of radiative forcing at a given time instance. For a complete overview and detailed comparison of the available climate metrics, the reader is referred to References [24] and [81].

Considering all of the above aspects, the average temperature response (ATR) has been selected as a climate metric in previous aircraft design studies [24, 20] and is recommended to evaluate aircraft design and aviation policies [81]. The average temperature response is defined as the averaged integral of the temperature response ΔT over a given time horizon H:

$$\mathrm{ATR}_H = \frac{1}{H}\int_0^H \Delta T(t)\,\mathrm{d}t \tag{2.1}$$

where the time t is expressed in terms of years. There is no fixed guideline defining the length of period H, so it can be set to 20, 50, 100, or even 500 years, for example. To evaluate $\Delta T(t)$, often a multi-year fuel or operational scenario is defined. Hence, it is important to ensure that H at least covers this scenario, and allows for enough time to account for long-term effects, such as caused by CO_2 emissions.

In the next chapters, the objective function of the aircraft design optimizations is ATR_{100} which considers a period of 100 years to analyze an operational scenario of 85 years where a new aircraft type is introduced and retired (Section 3.3.1), or a scenario of 35 years assuming constant fleet operations (Section 7.1.4). To compute this objective, the temperature response has to be determined as a function of the aircraft design variables (Chapters 3 to 6) and fleet operations (Chapter 7).

In the current study, a linearized temperature response model is employed to calculate ΔT for a given aircraft or fleet, based on inputs from a mission analysis including a 1D-thermodynamic engine performance evaluation. This temperature response model and the other disciplines are elaborated upon in Section 3.1.2 and are further developed in the subsequent chapters. The linear temperature response model introduced by Schwartz Dallara, Kroo, and Waitz [24] is taken as a starting point and updated to

- include the Schmidt-Appleman criterion for contrail formation,
- respond to changes in engine design variables, and
- conceptually evaluate the climate impact of hydrogen.

The implemented linear temperature response model captures the climate effects due to CO_2, H_2O, NO_x, soot and sulfate emissions and contrail formation, as discussed above. For CO_2, the change in atmospheric concentration is computed before calculating the radiative forcing. For the other emission species, an averaged radiative forcing per unit of emissions is assumed, skipping the concentration change computation. To include the effect of contrails, first the formation of contrails is verified using the Schmidt-Appleman criterion, after which a fixed radiative forcing per length of persistent contrail is applied. The radiative impacts of NO_x effects and contrails are assumed to be a function of the emission and formation altitude.

This modeling approach allows to capture the first-order impact of aircraft-level design changes on ATR_{100}. Nevertheless, the linear temperature response model offers less fidelity than global climate models (GCMs) or atmosphere-ocean general circulation models (AOGCMs) [82]. Such advanced methods include models of the fluid dynamics and chemistry, with possibly three-dimensional spacial discretization. Compared to such methods, the current linear temperature response model has several limitations:

- The linear temperature model only captures the variation with altitude, not latitude or longitude. Therefore, the varying altitude of the tropopause and the effect on non-CO_2 effects is not captured. In essence, the linear temperature response offers a annually- and globally-averaged insights into the climate effects.
- The perturbation lifetime of water vapor is assumed to be independent of the emitted altitude. This assumption is only valid for flights in the troposphere and lower stratosphere. Therefore, an upper bound is imposed accordingly on the considered cruise altitude.
- The radiative impact of persistent contrails is assumed to be fixed for each fuel type and independent of the latitude, longitude, time and season of formation, and emitted particulate matter.

Further modeling details and assumptions are discussed in the following chapters.

Although the linear temperature response model makes simplifying assumptions, it has a lower computational cost than GCMs or AOGCMs [82] while still being sensitive to airframe, engine, and mission design variables. This makes the linear temperature response model suitable for the conceptual multidisciplinary and multi-objective optimizations in the following chapters. Nonetheless, it is important to aware of the limitations of the employed model and higher fidelity analyses are recommended to accurately predict the temperature response and ATR_{100} metric.

2.4. CONSEQUENCES OF GLOBAL WARMING

The increase in global surface temperature has far-reaching consequences for nature and humanity. These consequences are covered in the *Impact* and *Damage* levels in Figure 1.3. A doubling of the carbon dioxide concentration results in approximately a 2.5°C increase in the average global surface temperature [49]. If this warming level continues to rise, the consequences will become larger with possibly irreversible effects [83]. This section provides an overview of the impacts and damages due to global warming, highlighting the need to research climate impact mitigation for aviation. Additionally, the complexity supports the decision to choose the temperature response as a metric rather than trying to express aviation-induced warming in terms of a monetary unit.

Weather and Climate Changes The increase in radiative forcing and warming also affect other characteristics of the atmosphere. Both thermodynamic properties and dynamic processes are expected to change and affect each other [84]. Important changes, among others, are the difference in heat capacity between land and the ocean, leading to larger temperature gradients, the increase in atmospheric water vapor content, and the variation of lapse rate. Overall, global warming is expected to lead to more frequent and more intense extreme weather and climate events. The following changes to phenomena are expected [84], with varying likelihood in different regions:

- Temperature: more frequent hot days and nights on land, increased frequency and intensity of heatwaves, fewer or less intense cold days and spells
- Droughts: increased frequency and intensity in some regions
- Rainfall: increased frequency, intensity, and amount of heavy precipitation events
- Storms: more intense and more frequent storms, such as tropical cyclones
- Compound events: higher frequency of heatwaves combined with drought

Sea and Ocean Level One of the most considerable impacts of global warming is the rise in sea level. Several contributions are identified [49, 85], with the largest being thermal expansion (or *thermosteric sea level change*), melting of glaciers, and changes in the volume of the Antarctic and Greenland ice sheets. Note that sea level changes can also vary locally. The level increase poses a threat to people living in coastal areas, low-lying islands, and regions below sea level. An example of such a critical location is the Tuvalu island group in the South Pacific, where the sea level in 2023 is approximately 0.15 m higher than 30 years earlier [2]. This led to a pact with Australia offering climate refuge to Tuvalu inhabitants [3]. In other countries or regions, mitigation actions, such as reinforced or higher dykes, might have to be implemented.

Availability of Fresh Water Global warming will impact the availability of fresh water through increased evaporation, as a result of higher surface temperature, and through reduced rainfall in certain regions [49]. The amount of run-off can also vary seasonally and regionally. Overall, the shifts in water availability lead to desertification and land degradation. Ultimately, this will affect agriculture, people's livelihood, and ecosystems.

Agriculture and Food Supply The variation in temperature and precipitation will require different approaches to farming. In particular, the absence of water for irrigation can cause issues for the agriculture sector and, therefore, the food supply chain. Ocean warming can also impact the fishing industry. Although the choice of crops can be updated according to the conditions and new technologies will be implemented, these consequences can lead to regional food insecurity and reduced water access [86].

Damage to Ecosystems Variations in the climate can cause issues for ecosystems since animals or plants may not be able to migrate or adapt quickly enough to the changing environment. This can also lead to increased competition between species and/or susceptibility to diseases. A positive (i.e., warming) feedback loop may cause a further increase in atmospheric carbon dioxide through the deteriorating health of forests, deforestation, and forest fires. Furthermore, damage to natural ecosystems, both on land and in the oceans, can cause a loss in biodiversity.

Impact on Human Health The previous two aspects, combined with increased heat and pollution, affect human health. Extreme heat events have already increased human mortality and morbidity [86]. Diseases through food and water, as well as between animals and humans, occur more frequently and spread to new regions [49]. These are the most direct effects due to higher surface temperatures. However, indirect effects can also impact human health. The more frequent and more intense weather events can lead to trauma and mental health issues if limited or no support is present.

Economic Impact Economic damages have already been observed in specific sectors, such as agriculture, fishing, energy, and tourism [86]. This can lead to a decrease in social equity, which can, in turn, make some people or groups even more vulnerable to climate change. Considering the above consequences of global warming, the impact and damages would preferably be expressed in terms of a monetary unit. Nevertheless, such approach carries a lot of uncertainty due to the different timescales, regional effects, economic assumptions, and political situations involved.

---

[2] URL `https://sealevel.nasa.gov/news/265/nasa-un-partnership-gauges-sea-level-threat-to-tuvalu` accessed on 27 November 2023

[3] URL `https://www.bbc.com/news/world-australia-67340907` accessed on 27 November 2023

3

KEROSENE, MEDIUM-RANGE AIRCRAFT DESIGN OPTIMIZATION

This chapter presents a method to assess the performance of turbofan, kerosene aircraft designed for minimum direct operating cost and aircraft designed for minimum global warming impact. The method comprises a multidisciplinary aircraft optimization algorithm capable of changing wing, engine, and mission design variables while including constraints on flight and field performance, as well as technology limits. The presented methods use traditional Class-I methods augmented with dedicated Class-II models to increase the sensitivity of the performance indicators to relevant design variables. The global warming impact is measured through the average temperature response caused by several emission species, including CO_2 *and* NO_x*, and contrail formation, over a period of one hundred years. The analysis routines are verified against public data or higher-order methods. The design algorithm is subsequently applied to a single-aisle, medium-range aircraft, demonstrating that a 57% reduction in average temperature response can be achieved compared to an aircraft optimized for minimal direct operating costs. This reduction is realized by flying at a cruise altitude of 7.6 km and at Mach 0.60, while lowering the engine overall pressure ratio to approximately 37. However, to compensate for the lower productivity, resulting from the lower cruise Mach number, it is estimated that 13% more climate-optimized aircraft are required to fulfill a given demand in air travel.*

Parts of this chapter have been published in Journal of Aircraft, **59**, 5, 2022, Proesmans and Vos [87].

As briefly discussed in Chapter 1, previous studies have revealed that the objective of minimizing the global warming impact, from an aircraft design perspective, does not align with the objective of minimizing direct operating costs (DOC) [22, 19, 88]. Even when the minimization of fuel consumption is considered as the overall design objective, this still does not result in an airframe and engine combination that has a minimal impact on global warming due to non-CO_2 effects [89].

In Reference [22], Antoine and Kroo carry out a multi-objective optimization of both aircraft and engine design variables for four individual design objectives: minimal DOC, minimal fuel burn, minimal NO_x emissions, and minimal noise. In their research, the climate impact of an aircraft is assessed by the emissions (in kg or lb) of CO_2 over the entire flight as well as the NO_x emissions in the landing and take-off (LTO) cycle. These two cost functions are considered individually since it is assumed that NO_x emissions in cruise are insignificant with respect to the emissions of CO_2 (and CO and SO_2) in cruise. A similar approach is taken by Henderson, Martins, and Perez [23] and Chai, Yu, and Wang [90]. Although the NO_x emissions in LTO are of interest and ICAO regulations are imposed, this measure does not account for the effect of NO_x at high altitudes due to its influence on short-term ozone (O_3) creation and long-term methane (CH_4) and ozone depletion. Such indirect effects on global warming, and other effects such as contrail formation and contrail cirrus, have to be determined through more advanced climate models and more comprehensive metrics. Examples of the latter are the average temperature response (ATR) [19, 88, 91] and the global warming potential (GWP) [92].

Later studies by Dallara and Kroo [88] and Koch [20] included more advanced models and metrics in aircraft optimization routines. The former adopted a linearized climate model with altitude variations, providing an average climate response with limited computational power, while the latter employed the more detailed AirClim model by Grewe and Stenke [66]. Although the numerical results of these studies cannot be compared directly, the trends in aircraft design parameters appear to be similar. For example, when changing the design objective from the minimization of DOC to the minimization of the average temperature response, it can be observed that the wing aspect ratio increases, the wing becomes less swept back, the cruise Mach number reduces, and the cruise altitude is lowered. While only operational changes, such as a different cruise altitude and Mach number, can already reduce the climate impact of the original aircraft, the financial cost rise can be limited by an optimized redesign.

The studies by Koch, Dallara and Kroo can be further extended by including more turbofan design variables such as overall pressure ratio (OPR) and turbine entry temperature (TET). Research conducted in NASA's Environmentally Responsible Aviation (ERA) project, among others, has explored the influence of a higher OPR and increased bypass ratio (BPR) on the fuel burn, LTO NO_x and noise [93]. Although it was shown that such engine cycle modifications can yield a significant reduction in fuel burn (33 to 45% for a large, single-aisle aircraft), they may have an adverse effect on non-CO_2 climate effects. Raising the OPR and TET, for example, increases the formation of thermal NO_x [58], although the emission index of NO_x in LTO and cruise can be further reduced through future combustor technologies [94]. Additionally, increasing the bypass ratio of turbofan engines increases the probability of contrail formation [17]. This demonstrates minimum fuel burn, again, does not necessarily align with minimizing climate impact.

Although flying lower and slower may be one effective measure to reduce the climate impact of an aircraft design, it increases the mission block time. For a constant travel demand, this productivity loss has to be covered by carrying more passengers per flight or by increasing the number of aircraft in the fleet. Several research projects have highlighted the importance of a complete fleet-level analysis in the assessment of new technologies and have proposed advanced modeling frameworks [95, 96, 97] in which the aircraft flight profiles have to be simulated [98]. Research by Moolchandani et al. and Jimenez, Pfaender, and Mavris employed fleet-level models to assess the environmental impact of future technologies considered in the ERA project [99, 100]. It was concluded that the introduction of ERA technologies can lower the fleet-total fuel burn sufficiently to sustain carbon-neutral operational growth in the future, according to the goals set worldwide, although a discussion of non-CO_2 climate effects is not included.

Building upon these observations from previous research, this chapter focuses on answering research question one from Section 1.4: which set of aircraft and engine design variables minimizes the global warming impact and cash operating cost of one kerosene-powered turbofan aircraft for a given set of top-level aircraft requirements and a specified mission?

To answer this question, a design method is proposed capable of capturing the interrelated effects of all relevant disciplines. Furthermore, the temporal effects of CO_2, NO_x, and induced cloudiness have to be assessed employing one comprehensive metric. In this assessment, the assumptions and limitations from Section 1.5 apply.

While it is recognized that operational changes and trajectory optimizations can further reduce the fuel burn [101, 102] and ATR [103], such improved operational schemes are outside the scope of the current study. Nevertheless, it is recommended to perform a simultaneous optimization of the aircraft design and operations to minimize the climate impact, including non-CO_2 effects, in the future employing similar approaches as taken in previous studies [99, 104].

The chapter is structured as follows. Section 3.1 defines the optimization problem and elaborates on the multidisciplinary design methodology. All the relevant analysis methods are explained in this section. Subsequently, validation of the analysis methods is performed in Section 3.2 along with the verification of the design methodology. Section 3.3 presents the results of the optimization study tailored towards a medium-range, single-aisle aircraft and answers the research question. Finally, the most important conclusions are gathered in Section 3.4 along with recommendations for further studies.

3.1. PROBLEM FORMULATION AND METHODS

To answer the research question proposed in the introduction, a multidisciplinary design and optimization routine is developed. This section discusses the working principles of the multidisciplinary design optimization framework. Section 3.1.1 focuses on the definition of the optimization problem and the overall strategy, followed by Section 3.1.2 which discusses the methods of the individual analyses and design disciplines in more detail.

3.1.1. OPTIMIZATION PROBLEM FORMULATION

One can optimize an aircraft design to achieve minimal average temperature response (ATR), minimal cash operating costs (COC or C_{ops}), or minimal mission fuel burn (m_{fuel}). The latter objective relates directly to the in-flight energy consumption. To study the difference between the three design objectives, a single-objective optimization problem is defined as follows:

$$\begin{aligned}
\underset{\mathbf{x}}{\text{minimize}} \quad & F(\mathbf{x}) = \text{ATR}_{100}(\mathbf{x}) \;\text{ or }\; C_{\text{ops,fleet}}(\mathbf{x}) \;\text{ or }\; m_{\text{fuel,fleet}}(\mathbf{x}) \\
\text{subject to} \quad & W/S \leq \frac{1}{2}\rho_0 \left(\frac{v_{\text{app}}}{1.23}\right)^2 C_{L_{\max}}, \\
& b \leq b_{\max}, \\
& \text{TET}_{\text{TO}} \leq \text{TET}_{\text{TO, max}}, \\
& C_{L_{\text{cr}}} \leq \frac{C_{L_{\text{buffet}}}}{1.3} = \frac{0.86 \cdot \cos\Lambda_{0.25}}{1.3}, \\
& C_{L_{\max}} \leq 2.8 \cdot \cos\Lambda_{0.25}, \\
& C_{L_{\max}} \leq 2.8 \cdot \cos\Lambda_{0.25}, \\
& x_i^L \leq x_i \leq x_i^U \qquad\qquad \text{for } i = 1, 2, \ldots, 10
\end{aligned} \tag{3.1}$$

Since the climate impact is assessed for a complete fleet, the costs, and fuel usage are evaluated in a similar manner, denoted by the fleet subscript. The design vector $\mathbf{x}$ contains the variables related to the airframe, engine, and mission. Table 3.1 provides a summary of these variables and their lower ($\mathbf{x}^L$) and upper ($\mathbf{x}^U$) bounds. For the airframe, the aspect ratio (A), wing loading (W/S), and maximum lift coefficient ($C_{L_{\max}}$) are used as the prime design variables, where the maximum lift coefficient is related to the design of the high-lift devices. The engine design is governed by the bypass ratio, the pressure ratios of the individual compressors (Π_i), as well as the turbine entry temperature (TET). The latter is the temperature at the intersection between the combustor and the first turbine stage, without the addition of cooling flow. The mission design variables comprise the cruise Mach number (M_{cr}) and the cruise altitude (h_{cr}).

The optimization definition in Equation (3.1) includes five constraints. The first one imposes a limit on the wing loading due to the required minimum approach speed V_{app} given the selected $C_{L_{\max}}$. The single-aisle, medium-range jet aircraft of interest is considered to belong to ICAO aircraft approach category C, resulting in an approach speed of approximately 135 to 140 kts (69 to 72 m/s). In this study, the approach speed is set to 70 m/s. A constraint is introduced for the maximum turbine entry temperature at take-off. $\text{TET}_{\text{TO, max}}$ is assumed to be 2000 K according to the insights by Mattingly, Heiser, and Pratt [105, Chapter 4]. The third constraint dictates a maximum wing span. For the aircraft category under consideration, this limit is set to 36 m [106].

The fourth constraint restricts the aircraft lift coefficient in cruise conditions due to buffet onset. The lift coefficient at which buffet occurs, for a given sweep angle, is estimated from the buffet onset boundaries provided by Obert [107]. Finally, a constraint is added to limit the maximum achievable lift coefficient. As discussed by Obert [107], $C_{L_{\max}}$ decreases with increasing quarter-chord wing sweep angle according to a linear relation with the cosine of this angle. A value of 2.8 relates to the maximum lift coefficient

Table 3.1: Design variables used in the optimization process and their respective bounds

Variable	**Description [Unit]**	**Lower Bound (x^L)**	**Upper Bound (x^U)**
W/S	Wing loading [kN/m^2]	3.00	7.00
A	Aspect ratio [-]	5.00	12.0
$C_{L\max}$	Maximum lift coefficient [-]	2.00	2.80
BPR	Bypass ratio [-]	4.00	11.0
Π_{fan}	Fan pressure ratio [-]	1.30	1.80
Π_{LPC}	LPC pressure ratio [-]	1.30	1.80
Π_{HPC}	HPC pressure ratio [-]	10.0	20.0
TET	Turbine entry temperature [K]	1100	1700
h_{cr}	Initial cruise altitude [km]	6.00	12.0
M_{cr}	Cruise Mach number [-]	0.60	0.80

attainable at zero quarter-chord sweep angle. The latter two constraints are plotted in Figure 3.1. Other flight and field performance constraints are considered in the Class-I sizing module (Section 3.1.2).

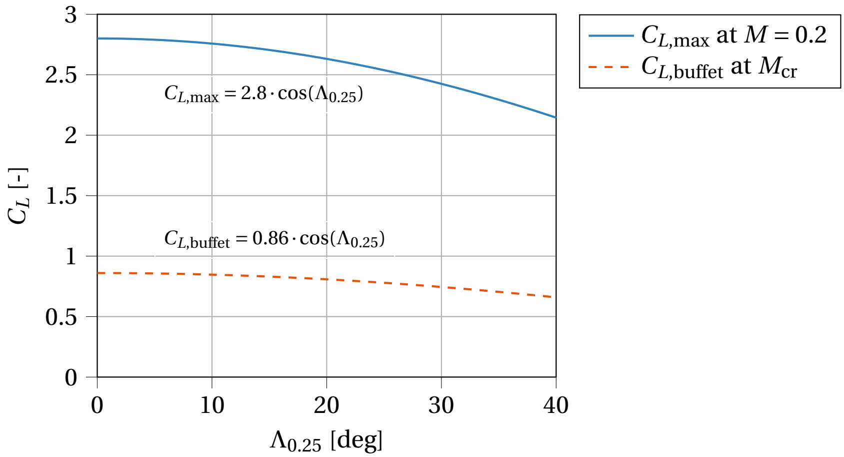

Figure 3.1: Constraints on $C_{L_{\max}}$ and $C_{L_{\text{buffet}}}$ (based upon data from Reference [107])

The structure of the design and optimization approach is presented in Figure 3.2 in the format of an extended design structure matrix (XDSM), as introduced by Lambe and Martins [108]. The airframe and propulsion disciplines both consist of several design modules as shown in Figures 3.3 and 3.4. A multiple-discipline feasible (MDF) scheme with Gauss-Seidel procedure is implemented for this problem. The next section describes the methods and assumptions of the modules on the diagonal of the XDSM. The optimization is solved in a three-step approach: first, a design of experiments is carried out. Second, a global search approach is used. Finally, the result is refined with the Nelder-Mead algorithm using a termination tolerance of 1.0×10^{-4}. Appendices C.1 and H further describe the optimization setup and code implementation, respectively.

In this MDAO framework, the optimizer and converger modules are separated. The inner convergence loop ensures that the airplane, defined by the design variables set by the optimizer, is consistent in terms of operating empty mass (OEM) and maximum take-off mass (MTOM). Three convergence criteria apply to the aircraft design convergence. First, a minimum of 7 iterations has to be performed. Second, the iterations stop after 30 iterations, indicating that the design is not converging within a reasonable amount of iterations. Finally, the change in OEM compared to the previous iteration has to be smaller than 0.1%, which, in practice, is always reached before the maximum number of iterations during the optimization run.

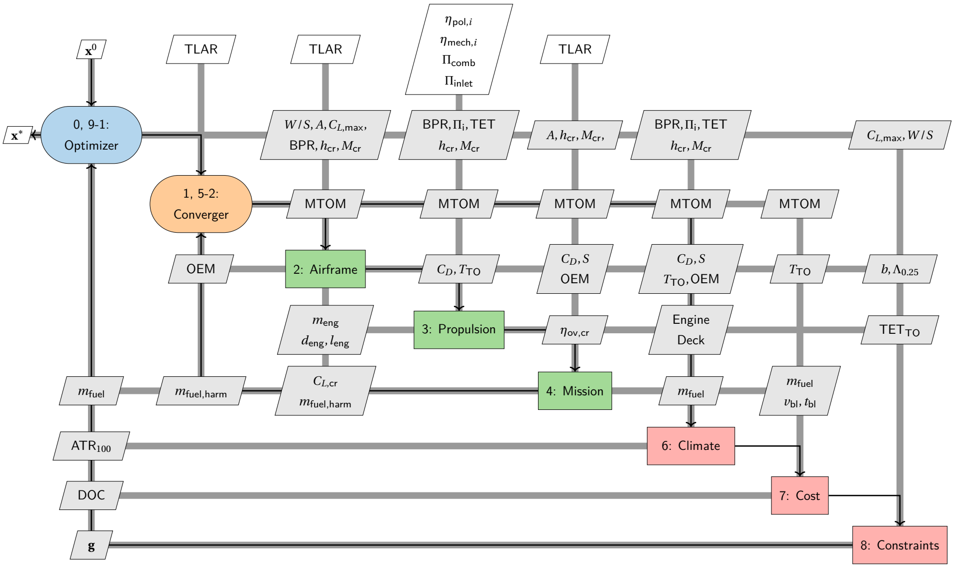
$\mathbf{x}^0$
TLAR
TLAR
$\eta_{\text{pol},i}$, $\eta_{\text{mech},i}$, Π_{comb}, Π_{inlet}
TLAR
$\mathbf{x}^*$
0, 9-1: Optimizer
$W/S, A, C_{L,\max}$, BPR, $h_{\text{cr}}, M_{\text{cr}}$
BPR, Π_i, TET, $h_{\text{cr}}, M_{\text{cr}}$
$A, h_{\text{cr}}, M_{\text{cr}}$,
BPR, Π_i, TET, $h_{\text{cr}}, M_{\text{cr}}$
$C_{L,\max}, W/S$
1, 5-2: Converger
MTOM
MTOM
MTOM
MTOM
MTOM
OEM
2: Airframe
C_D, T_{TO}
C_D, S, OEM
C_D, S, T_{TO}, OEM
T_{TO}
$b, \Lambda_{0.25}$
m_{eng}, $d_{\text{eng}}, l_{\text{eng}}$
3: Propulsion
$\eta_{\text{ov,cr}}$
Engine Deck
TET_{TO}
m_{fuel}
$m_{\text{fuel,harm}}$
$C_{L,\text{cr}}$, $m_{\text{fuel,harm}}$
4: Mission
m_{fuel}
m_{fuel}, $v_{\text{bl}}, t_{\text{bl}}$
ATR_{100}
6: Climate
DOC
7: Cost
$\mathbf{g}$
8: Constraints

Figure 3.2: Extended design structure matrix showing the multidisciplinary design workflow

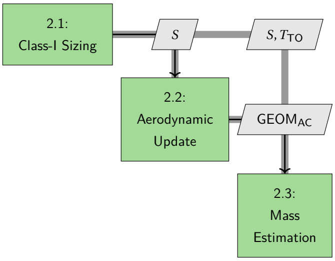
2.1: Class-I Sizing
S
S, T_{TO}
2.2: Aerodynamic Update
GEOM_{AC}
2.3: Mass Estimation

Figure 3.3: Airframe design and analysis workflow (step 2 of workflow in Figure 3.2)

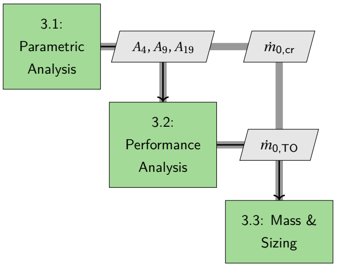
3.1: Parametric Analysis
A_4, A_9, A_{19}
$\dot{m}_{0,\text{cr}}$
3.2: Performance Analysis
$\dot{m}_{0,\text{TO}}$
3.3: Mass & Sizing

Figure 3.4: Propulsion design and analysis workflow (step 3 of workflow in Figure 3.2)

3.1.2. DESIGN AND ANALYSIS METHODS

As introduced above, answering the research question requires a multidisciplinary approach to capture the interrelated effects of design choices. In this subsection, the methods and assumptions of these disciplines are discussed in detail.

CLASS-I SIZING

Based on the inputs of aspect ratio, wing loading, maximum lift coefficient, cruise altitude, and Mach number, a preliminary sizing study is performed to size the wing area (S) and the sea-level take-off thrust (T_{TO}). The sea-level thrust-to-weight ratio is computed as the maximum required for the following three performance conditions:

1. take-off distance (included through the take-off parameter TOP),
2. cruise Mach number (M_{cr}) at the beginning of cruise, and
3. the second-segment climb gradient (c/V) in one-engine-inoperative condition.

These constraints on T_{TO}/W are captured in the following equation:

$$\begin{aligned}\frac{T_{\mathrm{TO}}}{W} = \max\Bigg\{ & \frac{W/S}{\mathrm{TOP}}\frac{1}{C_{L_{\mathrm{TO}}}}, \\ & \left(\frac{\rho_0}{\rho_{\mathrm{cr}}}\right)^{\frac{3}{4}}\left[\frac{C_{D_0}\frac{1}{2}\gamma p_{\mathrm{cr}}M_{\mathrm{cr}}^2}{(W/S)_{\mathrm{cr}}} + \frac{(W/S)_{\mathrm{cr}}}{\pi A e\frac{1}{2}p_{\mathrm{cr}}\gamma M_{\mathrm{cr}}^2}\right], \\ & \frac{N_{\mathrm{eng}}}{N_{\mathrm{eng}}-1}\left(\frac{c}{v}+2\sqrt{\frac{C_{D_0}}{\pi A e}}\right)\Bigg\}\end{aligned} \tag{3.2}$$

Here, the acronym TOP is the take-off parameter, which correlates to the take-off distance [109]. The TOP value is assumed to be equal to the take-off field length s_{TOFL} (in feet) divided by 37.5 lbs/ft^2 for turbofan aircraft certified by EASA CS-25 or FAR Part 25 [109, Chapter 3]. $C_{L_{\mathrm{TO}}}$ is the take-off lift coefficient which is assumed to be related to the maximum lift coefficient according to $C_{L_{\mathrm{TO}}} = C_{L_{\mathrm{max,TO}}}/1.21 = \left(C_{L_{\mathrm{max}}} - 0.3\right)/1.21$. The value of 0.3 is derived from the different take-off and landing flap settings.

$(W/S)_{\mathrm{cr}}$ is the wing loading at the start of the cruise phase. Furthermore, C_{D_0} and e are the zero-lift drag coefficient and Oswald factor, respectively. The parameter γ is the ratio of specific heats and N_{eng} is the number of engines. The symbols ρ_{cr} and p_{cr} represent the density and pressure at cruise altitude respectively. These values are dependent on the cruise altitude h_{cr}, which is a design variable in this study. Hence, the pressure and density in Equation (3.2) are adapted according to the relations of the International Standard Atmosphere model in Table 3.2 as a function of the cruise altitude set by the optimizer.

AERODYNAMICS

The aerodynamic module computes the drag polar of the airplane as a function of its geometry. The geometry is influenced directly by the selected design variables and payload requirements. The creation of the geometry is summarized in Appendix B. The aerodynamic discipline provides an update to the estimated drag polar, which, in turn, is employed in the propulsion discipline and mission analysis. Furthermore, this polar is also

Table 3.2: Calculation of temperature, pressure and density as a function of the selected cruise altitude h_{cr} (in meter) according to the International Standard Atmosphere (ISA) model ($g = 9.81\,\mathrm{m/s^2}$, $R = 287\,\mathrm{J/(kg\,K)}$)

Parameter [Unit]	**Troposphere** ($0 \leq h_{\mathrm{cr}} \leq 11\,\mathrm{km}$)	**Stratosphere** ($11 < h_{\mathrm{cr}} \leq 20\,\mathrm{km}$)
Temperature T_{cr} [K]	$288.15 - 0.0065 \cdot h_{\mathrm{cr}}$	216.65
Pressure p_{cr} [N/m^2]	$101325\,(T_{\mathrm{cr}}/288.15)^{-g/(0.0065R)}$	$101325 \cdot e^{-g(h_{\mathrm{cr}}-11000)/(216.65R)}$
Density ρ_{cr} [kg/m^3]	$p_{\mathrm{cr}}/\,(R \cdot T_{\mathrm{cr}})$	$p_{\mathrm{cr}}/\,(R \cdot T_{\mathrm{cr}})$

fed back to the Class-I sizing module to re-evaluate the thrust-to-weight ratio according to Equation (3.2).

The drag estimation methods are set up according to the techniques laid out by Obert [110]. The following quadratic drag polar is assumed:

$$C_D = C_{D_0} + \beta \cdot C_L^2 \tag{3.3}$$

for which two constants have to be computed specific to the design variables. The β constant is dependent on the wing aspect ratio A and the Oswald factor e. Obert proposes the following relation to determine β, based on statistical analysis [110]:

$$\beta = \frac{1}{\pi A e} \approx \frac{1.05}{\pi A} + 0.007 \tag{3.4}$$

By capturing the Oswald factor this way, other wing planform parameters such as sweep angle, taper ratio, and twist, are not direct inputs to induced drag model. However, this statistical model is built upon data of existing aircraft [110] and thus includes the effects of these parameters. To ensure consistency between the statistical model and the wing parameters computed through the methods in Appendix B, the sweep angle and taper estimates are verified for several of the aircraft on which Equation (3.4) is based. Additionally, due to the conceptual approach in this study, there is some design freedom to possible achieve the desired induced drag through airfoil and twist angle selection.

The first term of Equation (3.3), C_{D_0}, constituting of friction, profile, and excrescence drag, is assumed to be independent of the lift coefficient. C_{D_0} can be calculated by adding the sum of the minimum pressure drag of all aircraft components, and the drag contributions due to aircraft size-dependent (control surface gaps, doors, etc.) and aircraft size-independent (antennas, sensors, etc.) excrescences or protuberances:

$$C_{D_0} = \sum C_{D_{p,\mathrm{min}}} + \Delta C_{D_{\mathrm{E,I}}} + \Delta C_{D_{\mathrm{E,II}}} \tag{3.5}$$

$C_{D_{p,\mathrm{min}}}$ of each component is computed according to the flat plate analogy, including shape and compressibility corrections. Aircraft size-dependent excrescence drag ($\Delta C_{D_{\mathrm{E,I}}}$) is taken to be 1.5% of the total profile drag, $\sum C_{D_{p,\mathrm{min}}}$, assuming hydraulically smooth control surfaces. The size-independent contribution ($\Delta C_{D_{\mathrm{E,II}}}$) is presumed to be equal to $0.035/S$, where S is the wing reference area.

To obtain the drag polars in landing and take-off configurations, constant contributions are added to C_{D_0} and e to account for the extension of the flaps and the landing gear. In the take-off configuration, contributions of 0.015 and 0.05 [109] are added to C_{D_0} and e, respectively. In the landing phase, C_{D_0} and e are assumed to be approximately 0.085 and 0.10 higher [109] than the nominal values, respectively.

MASS ESTIMATION

To capture the effect of design choices on the operating empty mass of the aircraft, a Class-II mass estimation is implemented. The mass estimation is performed according to the methods presented in Appendices C and D of the book by Torenbeek [34]. These semi-empirical and statistical methods allow the prediction of the weight of individual structural groups (i.e. wing, fuselage, empennage, undercarriage, and propulsion) as well as the mass of airframe equipment and operational items.

As can be seen from previous research into global warming impact reduction, the wing aspect ratio is increased in several instances [19, 88, 90, 92] to lower the induced drag. However, this design change can have a dramatic effect on the wing weight, although this penalty may be lessened by increasing the wing thickness and/or decreasing the wing sweep. The employed methods are sensitive to the aspect ratio, nevertheless, the result may be inaccurate for high aspect-ratio values since limited or no reference data is available for such slender wings. Therefore, the aspect ratio is limited to 12.

The structural mass of the fuselage is calculated similarly employing a combination of statistical and empirical relationships. However, this mass remains (approximately) constant throughout the optimization since the fuselage geometry is independent of the chosen design variables.

Since the wing geometry and location affect the geometry of the empennage, the mass of the horizontal and vertical tails is updated throughout the optimizations. This mass prediction is dependent on the respective tail surface and sweep angle, which are updated according to assumed volume coefficients and the main wing sweep angle in this chapter. Appendix B.3 provides more information about the empennage design assumptions. The mass of the undercarriage varies according to the maximum take-off mass of the aircraft, while in all cases it is assumed that the landing gear is retractable and is located in a low-wing configuration.

As will be further elaborated in the next section, the mass of the engines is updated according to the required size (i.e. mass flow), bypass ratio, and overall pressure ratio. Also, the impact of high-bypass-ratio engines on nacelle mass is included in the weight assessment of the propulsion group. Furthermore, a forecast of the airframe services and equipment weight is included. The mass of this group is assumed to be equal to a fraction of the maximum take-off mass (MTOM). This fraction is dependent on the aircraft category and design range. For the medium-range, narrow-body under consideration here, a fraction of 12% is assumed. The mass of the operating items is assumed to be equal to 6.5% of the MTOM in this chapter.

The OEM estimate from this discipline is fed forward to the propulsion discipline, the mission analysis, and the subsequent aircraft iteration to update the wing surface area. Furthermore, to ensure that a consistent mass is adopted in all design modules, the operating empty mass has to converge to complete the convergence loop (1, 5-2) in the design framework of Figure 3.2.

PROPULSION

In the current aircraft configuration, propulsion is provided by two turbofan engines installed on the wing. Each engine features a two-spool architecture with separate exhausts. Five key design variables are selected for the turbofan cycle, being the bypass ratio (BPR), fan pressure ratio (Π_{Fan}, $p_{T21}/p_{T2} = p_{T13}/p_{T2}$), low-pressure compressor ratio (Π_{LPC}, p_{T25}/p_{T21}), the pressure ratio of the high-pressure compressor (Π_{HPC}, p_{T3}/p_{T25}), and the total turbine entry temperature (TET or T_{T4}). Figure 3.5 shows the layout of the engine and the station numbers.

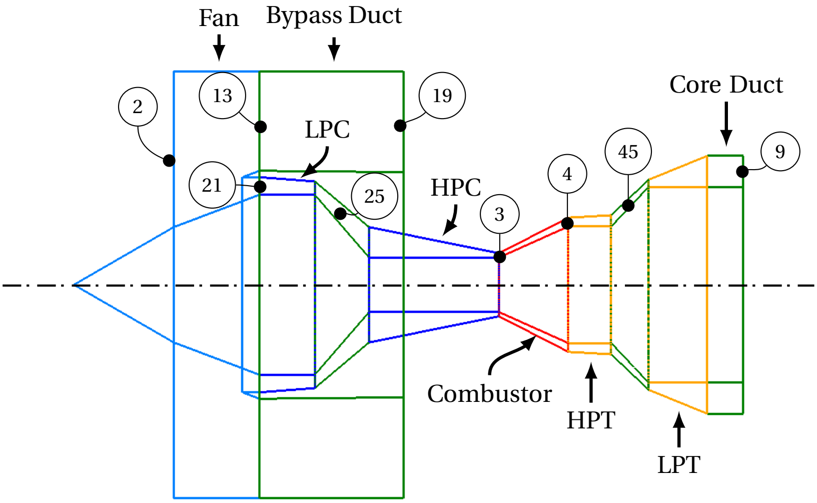

Figure 3.5: Longitudinal section of turbofan engine flowpath with station numbers (adapted from Reference [111])

Additional variables required by the discipline are component polytropic efficiencies, mechanical efficiencies, and inlet and combustor pressure losses. These parameters are related to the technology level and are assumed constant throughout the optimization. Example values of the latter parameters are included in Appendix A.1 for the verification case. In the aircraft design verification (Section 3.2.2) and the optimizations (Section 3.3) in this chapter, the performance parameters from Table A.3 are used.

Based on the cruise drag polar and cruise conditions, the thermodynamic cycle is determined by the parametric analysis module of Figure 3.4. Subsequently, off-design analysis can be carried out to find the required fuel flow for a given thrust at key points in the mission. Both the on-design and off-design point analyses are executed employing the strategies laid out by Mattingly, Heiser, and Pratt [105], and the variable specific heat model for air and kerosene-air mixtures introduced by Walsh and Fletcher [112].

Several simplifying assumptions, such as constant component efficiencies, are made in the models to limit computational cost and eliminate the need for component maps in this early design stage. Additionally, cooling flows, bleed air, and power extraction are neglected in the current case study for the sake of simplicity. By excluding these three elements, the approach may underestimate of the ingested mass flow, engine mass, nacelle dimensions, and drag. This loss in accuracy is accepted since the verification cases in Section 3.2 show limited deviations.

The results from the thermodynamic analyses are utilized in the third module of the workflow in Figure 3.4 to estimate the fan diameter and bare engine mass, which are required by the other disciplines to update the drag and structural masses accordingly. The fan diameter is calculated by assuming an axial Mach number of 0.6 at the fan inlet face and a hub-to-tip ratio of 0.3 for the local cross-section, taking into account the spinner. The mass of a single turbofan engine is estimated using the following relation [113]:

$$m_{\text{eng}}[\text{lbs}] = a \cdot \left(\frac{\dot{m}_{\text{core,TO}}[\text{lb/s}]}{100} \right)^{b} \cdot \left(\frac{\Pi_{\text{core,TO}}}{40} \right)^{c} \tag{3.6}$$

where a, b and c are polynomial functions of the bypass ratio. This formulation, which is based on simulations by the more advanced weight estimation software WATE++ [113, 114], allows capturing mass penalties due to high bypass ratios and high pressure ratios, while only a limited number of inputs is required.

The engine design can have a strong effect on the absolute emissions, as well as the NO_x emission index, as discussed in Section 1.1. While high pressure ratios and temperatures typically lead to reduced fuel consumption and thus low(er) CO_2 emissions, they also increase the production of thermal NO_x [58]. The production of NO_x is also influenced by the detailed combustor design, which is not captured by the current design vector and is out of scope for the current study. From a thermodynamic perspective, the bypass ratio can further improve fuel consumption, although sufficiently high pressure ratios and temperatures are required to power the large fan [22], worsening NO_x emissions. Finally, increased overall propulsive efficiency due to increased bypass ratio or OPR is expected to lead to more frequent contrail formation, possibly at higher ambient temperatures [17] and thus at lower altitudes. Hence, balancing the fuel consumption and CO_2 production against the effects of NO_x and contrails is important.

MISSION ANALYSIS

The aircraft is sized for a standard design mission for which the mission profile is shown in Figure 3.6. Reserve fuel is accounted for by including a diversion range to another airport (approximately 460 km or 250 nmi) and a loiter phase of 35 minutes. In step 4 of the framework presented in Figure 3.2, the lost-range method [115] is employed to determine the fuel mass which is required to iterate upon the MTOM and OEM.

The lost-range method computes the mission-fuel mass ($m_{\text{fuel, mission}}$) to take-off mass (m_{TO}) ratio for the standard mission from the cruise range (r_{cr}), altitude (h_{cr}), lift-to-drag ratio ($(L/D)_{\text{cr}}$) and engine overall efficiency ($\eta_{\text{ov, cr}}$) according to the following equations:

$$\begin{gathered} \frac{m_{\text{fuel, mission}}}{m_{\text{TO}}} = \frac{r_{\text{cr}}/R_{\text{H}}}{\mathscr{P} + (1/2)\cdot r_{\text{cr}}/R_{\text{H}}} + \frac{h_{\text{cr, eq}}}{0.7\cdot\eta_{\text{ov, cr}}\cdot R_{\text{H}}} + \frac{0.0025}{\eta_{\text{ov, cr}}} \\ \text{where } R_{\text{H}} = \frac{\text{LHV}}{g},\ \mathscr{P} = \eta_{\text{ov, cr}}\cdot\left(\frac{L}{D}\right)_{\text{cr}},\ h_{\text{cr, eq}} = h_{\text{cr}} + \frac{v_{\text{cr}}^2}{2\cdot g} \end{gathered} \tag{3.7}$$

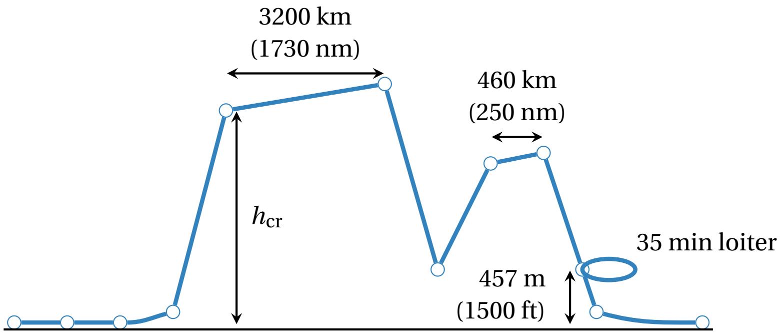

Figure 3.6: Mission profile (flown distance versus altitude) under consideration

The three terms in Equation (3.7) consider different flight phases: the first term determines the fuel spent during the cruise phase. The second part accounts for the fuel required to take off and climb to the cruise altitude, where $h_{\text{cr, eq}}$ combines the altitude increase and the acceleration to cruise speed. The factor $0.7 \cdot \eta_{\text{ov, cr}}$ approximates the engine efficiency during the climb phase. The last term adds a minor contribution to model in-flight maneuvering. Two terms can be included to account for a given diversion range (r_{div}) and a loiter phase of t_{hold} hours [115]:

$$\left(\frac{\Delta m_{\text{fuel}}}{m_{\text{fuel, mission}}}\right)_{\text{div}} = 1.20 \cdot \frac{r_{\text{div}}}{r_{\text{harm}}} \tag{3.8}$$

$$\left(\frac{\Delta m_{\text{fuel}}}{m_{\text{fuel, mission}}}\right)_{\text{hold}} = 0.20 \cdot t_{\text{hold}} \cdot \frac{R_{\text{H}}}{r_{\text{harm}}} \cdot \left(1 - \frac{m_{\text{fuel, mission}}}{m_{\text{TO}}}\right) \tag{3.9}$$

In the above equations, r_{harm} is the harmonic range of the aircraft, defined at maximum structural payload. This leads to the following estimate of the total fuel mass required for one trip, as a fraction of the take-off mass:

$$\left(\frac{m_{\text{fuel}}}{m_{\text{TO}}}\right)_{\text{total}} = \frac{m_{\text{fuel, mission}}}{m_{\text{TO}}} \cdot \left[1 + \left(\frac{\Delta m_{\text{fuel}}}{m_{\text{fuel, mission}}}\right)_{\text{div}} + \left(\frac{\Delta m_{\text{fuel}}}{m_{\text{fuel, mission}}}\right)_{\text{hold}}\right] \tag{3.10}$$

Together with the MTOM estimation from the previous iteration, the required fuel mass can be calculated. This fuel mass is added to OEM estimation and the payload mass to obtain an updated value for the MTOM. Since this lost-range approach is completely analytical, it can be executed efficiently in the synthesis loop.

However, a more detailed mission analysis is required for the climate impact assessment. This is because the emission index of NO_x depends on the engine pressure ratio, combustor inlet temperature and relative humidity, which vary with the operation conditions. Additionally, the formation of contrails is dependent on the ambient temperature. Also, the radiative forcing of these non-CO_2 species is sensitive to the flight altitude.

Therefore, in the climate impact assessment module, the mission is simulated numerically by applying basic flight mechanics rules and by analyzing the engine's off-design performance for discrete time steps. Since this mission assessment approach is more time consuming than the lost-range method, it is only called once in every objective function evaluation rather than in every design iteration.

In the global warming impact evaluation, the accumulated emissions over this design mission and the altitude of emission are employed to assess the radiative forcing and the average temperature response. Although this provides insight into the climate burden of the aircraft on this specific mission, it has to be noted that this is not fully representative of an aircraft operated more flexibly in a fleet. The analysis in Chapter 7 includes different missions in the cost and climate assessment.

GLOBAL WARMING IMPACT EVALUATION

The assessment of the climate impact of an aircraft is a nontrivial task. Ideally, the societal costs and damages due to emissions would be calculated and compared to operating costs to make a cost-benefit analysis. However, due to large uncertainties, it is almost impossible to evaluate these costs and damages accurately in a conceptual design stage. Therefore, a suitable climate metric has to be selected. To make an insightful evaluation, Grewe and Dahlmann [116] suggested a five-step process to define the impact valuation and avoid misconceptions.

Firstly, the question to be answered has to be clarified. In this study, the objective is to compare the climate impact of aircraft optimized for different objectives (fuel, cost, and climate impact). Secondly, the reference aircraft is a non-optimized, yet consistent aircraft design which also serves as a starting point for the optimizations. Thirdly, an emission scenario is to be defined. It is decided to count the emissions over the entire operational lifecycle of a new aircraft to be introduced in 2020. This hypothetical aircraft is assumed to be produced for a period of 30 years, while its operational lifetime is assumed to be 35 years (ignoring potential airframe losses). Accordingly, the maximum fleet size will occur in the years 2050 to 2055. Section 3.3 discusses this fleet scenario definition and productivity constraint in further detail.

Grewe and Dahlmann discuss several climate metrics which are available and their features. In this research, the average temperature response (ATR) is selected as the metric representing global warming impact since it captures the effect of emissions on the surface temperature change (ΔT) while limiting the influence of the time horizon on the result. The average temperature response is computed as follows for a period of H years:

$$\mathrm{ATR}_H = \frac{1}{H}\int_0^H \Delta T(t)\,\mathrm{d}t \tag{3.11}$$

Note that in this section the time variable t is expressed in years and t_0 represents the initial year of the considered period, e.g. 2020. As a final step of the proposed process, the time horizon H of 100 years is imposed because it provides a balanced assessment between long-lived emissions ($\mathrm{CO_2}$) and short-lived forcing effects (such as $\mathrm{NO_x}$ and contrail formation) [20]. Thus the final metric is ATR_{100}, which requires the computation of ΔT for each year in the selected time horizon. The temperature change can be computed as follows [66, 117]:

$$\Delta T(t) = \int_{t_0}^{t} G_T(t-t')\cdot \mathrm{RF}^*(t')\,\mathrm{d}t' \quad \text{with} \quad G_T(t) = \frac{2.246}{36.8}\mathrm{e}^{-t/36.8} \tag{3.12}$$

RF^* in Equation (3.12) is the normalized radiative forcing. This parameter is equal to one for a doubling in atmospheric carbon dioxide concentration compared to pre-industrial times. The actual radiative forcing corresponding to a doubling of this concentration, $\mathrm{RF}_{2\times\mathrm{CO}_2}$, is taken to be 3.7 W/m^2 [118]. The normalized radiative forcing in Equation (3.12) is the summed value of several species:

$$\mathrm{RF}^*(t) = \sum_{i}^{\text{all species}} \mathrm{RF}^*{}_i(t) = \sum_{i}^{\text{all species}} \left[\mathrm{Eff}_i \cdot \frac{\mathrm{RF}_i(t)}{\mathrm{RF}_{2\times\mathrm{CO}_2}}\right] \tag{3.13}$$

for $i = \mathrm{CO_2}, \mathrm{NO_x\text{-}CH_4}, \mathrm{NO_x\text{-}O_{3L}}, \mathrm{NO_x\text{-}O_{3S}}, \mathrm{H_2O}, \mathrm{SO_4}$, soot, and contrails

The factor Eff_i is the efficacy of a given element, which is equal to the ratio between the climate sensitivity of this species and the climate sensitivity of CO_2 [66]. Table 3.3 provides values for these efficacy and sensitivity parameters. To capture the effects of all these species, a linearised temperature response model is developed (module 6 in Figure 3.2), based on methods from literature. The subsequent paragraphs elaborate on the implemented methods per species which translate the emissions (in kg) into the normalized radiative forcing, and subsequently into the approximate temperature change.

Table 3.3: Climate sensitivities (λ_i) and efficacies (Eff_i) for species under consideration [119, 24, 118]

	CO_2	CH_4	O_3	H_2O	SO_4	Soot	Contrails
λ_i [K/(W/m^2)]	0.73	0.86	1.00	0.83	0.66	0.51	0.43
Eff_i	1.00	1.18	1.37	1.14	0.90	0.70	0.59

Carbon Dioxide The emission of carbon dioxide is directly related to the combustion of fossil fuels, with an emission index of approximately 3.16 kg/kg for kerosene. Carbon dioxide is a greenhouse gas with a long lifetime which makes the effects independent of the emission location. An increase in the atmospheric concentration of this species results in a warming effect. The methods introduced by Sausen and Schumann [117] provide an approach to estimate the temperature change due to CO_2 emissions. From the emissions in a given year, the change in atmospheric CO_2 concentration, denoted by $\Delta\chi_{\mathrm{CO}_2}$, can be computed. This change is given by the following convolution integral:

$$\Delta\chi_{\mathrm{CO}_2}(t) = \int_{t_0}^{t} G_{\chi_{\mathrm{CO}_2}}\left(t-t'\right)\cdot E_{\mathrm{CO}_2}\left(t'\right)\mathrm{d}t' \quad \text{with} \quad G_{\chi_{\mathrm{CO}_2}}(t) = \sum_{i=1}^{5} \alpha_i \cdot \mathrm{e}^{-\mathrm{t}/\tau_\mathrm{i}} \tag{3.14}$$

where E_{CO_2} represents the absolute CO_2 emissions (in kg or Tg) in year t. Table 3.4 provides the α_i coefficients and perturbation lifetimes τ_i for the impulse response function $G_{\chi_{\mathrm{CO}_2}}$. Equation (3.14) does not depend on the emission altitude since CO_2 does not react with other atmospheric compounds and, consequently, is a well-mixed gas.

If the concentration change $\Delta\chi_{\mathrm{CO}_2}$ is known, the normalized radiative forcing can be obtained from the ratio between the updated concentration and the background concentration, $\chi_{\mathrm{CO_2},0}$, which is assumed to be equal to 380 ppmv:

$$\mathrm{RF}^*(t) = \frac{1}{\ln 2} \cdot \ln\left(\frac{\chi_{\mathrm{CO_2},0} + \Delta\chi_{\mathrm{CO_2}}(t)}{\chi_{\mathrm{CO_2},0}}\right) \tag{3.15}$$

Table 3.4: Coefficients of impulse response function $G_{\chi_{\mathrm{CO_2}}}$ in Equation (3.14) [117]

i	**1**	**2**	**3**	**4**	**5**
α_i	0.067	0.1135	0.152	0.0970	0.041
τ_i	∞	313.8	79.8	18.8	1.7

Nitrogen Oxides Although $\mathrm{NO_x}$ is not a greenhouse gas itself, it causes several indirect effects which are expected to have a net warming effect [2, 63]. However, unlike carbon dioxide, the emission index is not constant but rather dependent on the engine operating condition and combustor technology. There are several options to approximate the emission index, either through an analytical expression [22, 88], through fuel-flow methods [20], or higher fidelity simulations [59]. In this research, the analytical expression from Schwartz Dallara [82] is employed:

$$\mathrm{EI}_{\mathrm{NO_x}} = 0.0986 \cdot \left(\frac{p_{T3}}{101325}\right)^{0.4} \cdot e^{T_{T3}/194.4 - H_0/53.2} \tag{3.16}$$

where p_{T3} and T_{T3} are the pressure and temperature ahead of the engine combustor, and H_0 is specific humidity. Equation (3.16) can be evaluated at every point in the mission profile from an off-design analysis of the turbofan engine and provides the actual emission of $\mathrm{NO_x}$ through multiplication with the fuel flow $\dot{m}_{\mathrm{fuel}}$.

On a long-term basis, $\mathrm{NO_x}$ depletes atmospheric methane ($\mathrm{CH_4}$) and long-lived (or primary mode) ozone ($\mathrm{O_{3L}}$), which are both greenhouse gases. The depletion of these agents results in a cooling effect. The radiative forcing of these effects can be modeled according to [24]:

$$\begin{gathered} \mathrm{RF}_i(t,h) = s_i(h) \int_{t_0}^{t} G_i\left(t - t'\right) \cdot E_{\mathrm{NO_x}}\left(t'\right) \mathrm{d}t' \\ \text{with } G_i(t) = A_i \cdot \mathrm{e}^{-\mathrm{t}/\tau_\mathrm{n}} \text{ for } i = \mathrm{CH_4}, \mathrm{O_{3L}} \end{gathered} \tag{3.17}$$

In this equation, the coefficient A_i is assumed to be equal to -5.16×10^{-13} (W/m^2) / kg$_{\mathrm{NO_x}}$ and -1.21×10^{-13} (W/m^2) / kg$_{\mathrm{NO_x}}$ for methane and long-lived ozone, respectively. The perturbation lifetime τ_n is set to 12 years. $s_i(h)$ is a forcing factor, as defined in Reference [24], to account for the altitude variation of $\mathrm{NO_x}$ and contrail effects.

The most prominent warming effect of $\mathrm{NO_x}$ emissions is the formation of short-lived ozone in the troposphere and lower stratosphere. Since this is a short-lived effect, no convolution integral with response function is required, but a simpler method can be applied:

$$\mathrm{RF}_{\mathrm{NO_x\text{-}O_{3S}}}(t,h) = s_{\mathrm{NO_x\text{-}O_{3S}}}(h) \cdot \left(\frac{\mathrm{RF_{ref}}}{E_{\mathrm{ref}}}\right)_{\mathrm{NO_x\text{-}O_{3S}}} \cdot E_{\mathrm{NO_x}}(t) \tag{3.18}$$

Similar to Equation (3.17), here a forcing factor $s(h)$ is included to simulate the altitude dependency of the radiative effects. The constant $\mathrm{RF_{ref}}/E_{\mathrm{ref}}$ represents the radiative forcing due to $\mathrm{NO_x}$-$\mathrm{O_{3S}}$ per unit of $\mathrm{NO_x}$ emission. It is assumed to be equal to 1.01×10^{-11} ($\mathrm{W/m^2}$) / $\mathrm{kg_{NO_x}}$, although a large uncertainty is present.

This assessment of $\mathrm{NO_x}$ depends on certain simplifying assumptions. Firstly, the changing lifetime of methane, due to its depletion, is not taken into account [64]. This can be considered a steady-state assumption. Finally, while also the geographic location of emissions performs a role, it is not taken into account in this analysis.

Water, Soot, and Sulfate In the combustion process, other short-lived species are formed such as water vapor, and aerosols such as soot (black carbon) and sulfate. To compute the absolute emissions of these species, constant emission indices are assumed: $\mathrm{EI_{H_2O}} = 1.26$ kg/kg, $\mathrm{EI_{SO_4}} = 2.0 \times 10^{-4}$ kg/kg and $\mathrm{EI_{soot}} = 4.0 \times 10^{-5}$ kg/kg [24]. The impact of these species is modeled in a similar manner to the short-lived ozone production discussed above. However, for these species the altitude dependency factor is omitted, resulting in the following relation [24]:

$$\mathrm{RF}_i(t) = \left(\frac{\mathrm{RF_{ref}}}{E_{\mathrm{ref}}}\right)_i \cdot E_i(t) \text{ for } i = \text{Soot, } \mathrm{H_2O}, \mathrm{SO_4} \tag{3.19}$$

Contrails Because the jet exhaust of the turbofan engines is hot and humid compared to the ambient air, condensation trails may form behind an aircraft. Whether or not contrails indeed develop, can be assessed with the help of the Schmidt-Appleman criterion [17]. This criterion is met if the hot exhaust air reaches saturation with respect to liquid water during the mixing process with the surrounding air. The mixing process is modeled by a mixing line in a diagram of water vapor partial pressure versus ambient temperature, as shown in Figure 3.7. This mixing line can be approximated by a linear relation which depends on the ambient conditions (pressure, temperature, and relative humidity), overall engine efficiency, and the emission index of water.

In Figure 3.7, mixing line 1 represents the mixing process of hot, humid exhaust gases at 11 km of altitude, assuming a relative humidity of 80%. The gases are cooled and pass the saturation point with respect to water, at which point visible contrails are formed. When ambient conditions are reached, at the blue circle marker, the mixture finds itself in between the saturation lines, leading to persistent contrails. If the water vapor pressure were lower than the saturation line with respect to ice, the contrails would soon dissolve after the formation. Mixing line 2 follows from flying at an altitude of 8 km. Since the ambient air pressure and temperature are higher, the slope of the line and the end point are different. In this case, saturation with respect to water is not reached, and no contrails are formed.

Additionally, the formation can only occur when the static ambient temperature lies below the temperature threshold of 235 K (-38 °C). These conditions are not sufficient to ensure that the contrails are persistent. For this to occur, the partial pressure of the

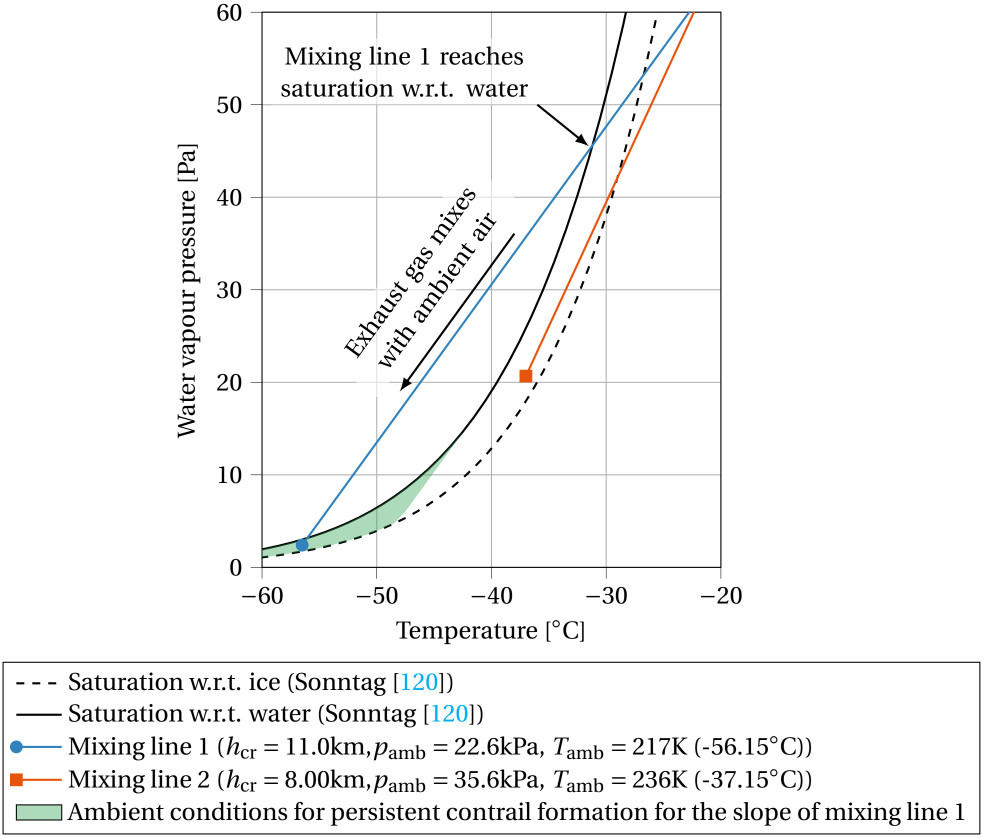

Figure 3.7: Conceptual drawing of exhaust mixing lines in different cruise conditions to illustrate the Schmidt-Appleman criterion ($\eta_{ov} = 0.4$, relative humidity=80%). Mixing line 1 leads to persistent contrail formation whereas no contrails are produced in the case of mixing line 2. (Adapted from Reference [121])

mixed exhaust, which has reached the ambient temperature, should lie in between the thresholds for saturation above liquid water and the saturation level above ice. The formulae provided by Sonntag [120] specify these levels as a function of temperature.

These three criteria are evaluated at every point in the mission analysis, using the international standard atmosphere model to obtain the ambient conditions. The selected cruise altitude and engine design variables are expected to influence the outcome. If all three criteria are met, then that point is marked as a time interval in which persistent contrails appear. At the end of the mission analysis, the total contrail length (in km or nmi) is used to estimate the radiative forcing according to [24]:

$$\mathrm{RF}_{\mathrm{contrails}}(t,h) = s_{\mathrm{contrails}}(h) \cdot \left(\frac{\mathrm{RF}_{\mathrm{ref}}}{L_{\mathrm{ref}}}\right)_{\mathrm{contrails}} \cdot L(t) \tag{3.20}$$

where $s_{\text{contrails}}(h)$ is an altitude-dependent forcing factor, $\left(\frac{\text{RF}_{\text{ref}}}{L_{\text{ref}}}\right)_{\text{contrails}}$ is set to 1.82×10^{-12} $(\text{W/m}^2)/\text{km}$ [3], and $L(t)$ is the accumulated contrail length in year t. According to this formulation, the radiative impact of contrails scales with the distance flown in conditions where persistent contrails form.

It has to be recognized that the contrail assessment method presented in this section is simplified and that uncertainties remain. The radiative forcing of contrails is not a function of emitted particles, thrust levels, or aircraft aerodynamic properties. Section 8.5 provides insight into these uncertainties and the influence on the obtained results. Although the results are sensitive to changes in flight altitude and technology variables, the fact that atmospheric conditions may vary regionally or temporally is not accounted for. Additionally, the dependency of the radiative effects on the geographic location is neglected. Finally, only the impact of linear contrails is analyzed. The formation and effects of contrail cirrus are not considered.

OPERATING COSTS

The total operating cost of an aircraft are often divided into direct and indirect operating costs, according to the ICAO cost categories [122], although different approaches exist to categorize the costs. In this research, the focus lies on a subset of the direct operating cost which is directly influenced through the aircraft design. The impact on indirect operating cost, including airport charges, passenger services, and sales, is not considered in the optimizations. Section 8.4 discusses the impact of changes in direct operating cost on the ticket price.

Although fuel costs constitute a large portion of an aircraft's direct operating costs, other contributions play an important role as well. Reducing the block time (t_{bl}) by increasing the flight speed, for example, decreases the crew costs but may lead to higher fuel costs. Module 7 of Figure 3.2 employs the methods presented by Roskam [35, Chapter 5] to estimate the cash operating costs for a particular aircraft design (USD/(seat · nmi) or USD/(seat · km)) or a complete fleet (in USD).

Two main contributions are included in the analysis. Firstly, the cost related to flight itself is estimated. These comprise fuel and oil costs, crew salaries, and insurance. A fuel price of 1.78 USD/US gallon is assumed, which is approximately equal to the price level in January 2020 before the influence of the Corona pandemic. The following relation determines the fuel and oil costs per seat · nmi:

$$C_{\text{fuel}} = \frac{m_{\text{f,bl}}}{r_{\text{bl}} \cdot N_{\text{pax}}} \cdot \frac{C_{\text{f,gal}}}{\rho_{\text{fuel}}} \tag{3.21}$$

$$C_{\text{oil}} = \frac{m_{\text{oil}}}{r_{\text{bl}} \cdot N_{\text{pax}}} \cdot \frac{C_{\text{oil,gal}}}{\rho_{\text{oil}}} = \frac{0.7 \cdot N_{\text{eng}} \cdot t_{\text{bl}}}{r_{\text{bl}} \cdot N_{\text{pax}}} \cdot \frac{C_{\text{oil,gal}}}{\rho_{\text{oil}}} \tag{3.22}$$

Captain, first officer, and flight attendant salaries are also adapted to 2020 levels. It is assumed that each crew member flies 1000 hours annually and that at least 1 cabin crew member is present for each 50 passengers. The cost of a single crew member, expressed in (USD/seat · nmi), is defined as follows [35]:

$$C_{\text{crew member}} = \frac{1}{N_{\text{pax}} \cdot v_{\text{bl}}} \cdot \left[\left(1 + k_j\right) \cdot \frac{\text{sal}_{\text{crew member}}}{\text{ah}_{\text{crew member}}} + \text{t}_{\text{ef}} \right] \tag{3.23}$$

The parameters in the above equation are explained and quantified in Table 3.5. The annual hull insurance rate (in USD/USD/airplane/year) is taken to be 0.02.

Table 3.5: Parameters related to the cost estimation of the flight crew

Parameter [Unit]	**Symbol**	**Value**
Factor for employer costs [-]	k_j	0.26 [35]
Annual captain salary [USD/year]	$\text{sal}_{\text{captain}}$	277000 [1]
Annual first officer salary [USD/year]	$\text{sal}_{\text{first officer}}$	188000 [1]
Annual cabin crew member salary [USD/year]	$\text{sal}_{\text{cabin crew}}$	43160 [2]
Annual flight hours [hr/year]	ah	1000 [1]
Travel expense factor [USD/hr]	t_{ef}	9 [35]

Secondly, the cost of maintenance ($C_{\text{maintenance}}$) is accounted for through the methods introduced in Section 5.2.2 of Reference [35]. This category includes the labor rates of airframe and engine engineers (2020 averaged salaries), as well as the cost of airframe and engine spares. The latter two aspects require an appreciation of the aircraft and turbofan engine unit purchase prices. New relations are derived to estimate these prices, based on the aircraft OEM and the single-engine static take-off thrust, from recent price figures [123, 124]:

$$P_{\text{AC,2020}}\,[\text{2020 USD}] = 0.0052 \cdot \text{OEM}^{0.927} \cdot 10^6 \tag{3.24}$$

$$P_{\text{eng,2020}}\,[\text{2020 USD}] = 0.1604 \cdot T_{\text{TO,eng}}^{0.878} \cdot 10^6 \tag{3.25}$$

The values of OEM and $T_{\text{TO,eng}}$ in these relations are expressed in kg and kN, respectively. Other cost contributions, such as depreciation and fees related to financing and operations are excluded from the analysis. The reason for this exclusion is that these categories are thought to carry more uncertainty and that they may be dependent on business decisions. For example, the financing cost may depend on the decision whether to buy or lease the aircraft. Additionally, indirect operating costs, such as passenger services, station operation, promotion, and administration, are neglected in the current analysis since these contributions vary per airline.

In Module 7 of Figure 3.2, firstly the direct operating costs of one aircraft are calculated. However, since the climate impact is determined for an operating fleet, for a prolonged period, it is of interest to express the costs in a similar manner. Knowing the operating cost of one aircraft per year ($C_{\text{ops,AC}}$), the total fleet operating costs $C_{\text{ops,fleet}}$ can be computed as follows:

$$\begin{aligned} C_{\text{ops,fleet}} &= C_{\text{ops,AC}} \cdot \text{RPK}_{\text{AC,ann}} \cdot N_{\text{yr}} \cdot N_{\text{AC}} \\ &= (C_{\text{fuel}} + C_{\text{oil}} + C_{\text{crew}} + C_{\text{insurance}} + C_{\text{maintenance}}) \cdot \text{RPK}_{\text{AC,ann}} \cdot N_{\text{yr}} \cdot N_{\text{AC}} \end{aligned} \tag{3.26}$$

where $\text{RPK}_{\text{AC,ann}}$ is the amount of revenue passenger kilometers flown by one aircraft in one year, N_{yr} is the operational life of an aircraft, and N_{AC} is the total number of aircraft in the fleet. Values for the latter parameters may vary between objectives due to a difference in block time and thus productivity. Section 3.3.1 discusses this aspect in further detail and introduces the hypothetical fleet scenario.

---

[1] URL `https://epicflightacademy.com/airline-pilot-salary/` accessed on 24 November 2020

[2] URL `https://www.indeed.com/cmp/American-Airlines/salaries/Flight-Attendant` accessed on 24 November 2020

3.2. Verification of Analysis and Design Methods

This section verifies whether the methods described above work correctly and whether the overall methodology results in a realistic case study. Special attention is paid to the physics-based propulsion discipline in Section 3.2.1 since an accurate estimation of the engine parameters is required to predict the emissions in the climate impact evaluation module. In Section 3.2.2, two aircraft are designed for the same top-level requirements as the Airbus A320-200 and Boeing 777-200 to confirm that the implemented approach allows producing a realistic conceptual aircraft design.

3.2.1. Turbofan Performance Verification

The verification of the propulsion discipline consists of two steps: firstly, the design and off-design analyses produced by the implemented methods are compared to a model of the GE90 in the GSP gas turbine simulation program[3] [125]. Secondly, a performance map for varying Mach numbers and altitudes is constructed and compared to GE90 performance data provided by Nicolai and Carichner [126]. The inputs employed to model the GE90 engine are provided in Appendix A.1.

Table 3.6 presents the results of the first verification step. The subscripts indicate the engine stations according to the ARP 755A station numbering standard. While both the implemented method and the GSP model employ the same inputs, the GSP model also includes component maps that provide component efficiency updates according to the operating condition. It can be concluded that the errors between the two models are relatively small and that simplified methods provide sufficient accuracy. A study of the errors in the design point analysis indicates that these can be attributed to minor differences in the variable specific heat models.

Secondly, an engine deck of the GE90 is created and compared to data provided in Appendix J of Nicolai and Carichner [126]. The results are presented in Figures 3.8a and 3.8b for the net thrust and fuel flow. The values are normalized with respect to the sea-level-static (SLS) values since absolute differences may occur because it is unclear for which exact GE90 type the data is provided. From these figures, it can be observed that the thrust and fuel flow values correspond rather well for varying altitude and Mach number, considering the simplifying assumptions discussed above.

3.2.2. Aircraft Synthesis Verification

This section discusses the validity of the aircraft design methods and synthesis loop introduced in Section 3.1. The comparison between existing aircraft data and the simulated models is based on three aspects: mass estimation, geometry creation, and performance evaluation. These aspects are considered for the Airbus A320-200 and the Boeing 777-200, representing the narrow-body and wide-body categories. Appendix A.2 provides the input values for these two aircraft.

First, Table 3.7 presents the mass estimation obtained with the framework and also compares four key geometric dimensions for both aircraft. These results are obtained after six iterations in the inner convergence loop of the methodology in Figure 3.2. The relative differences for these parameters lie between -1.6% and +2.5%, which is considered

---

[3] URL `https://www.gspteam.com/` accessed on 11 January 2024

Table 3.6: Verification of the performance analysis with the implemented methods versus GSP (conditions according to Table A.1, gray numbers represent input values)

(a) On-design Performance

Parameter [Unit]	**Framework**	**GSP**	**Difference [%]**
T_{T3} [K]	772	771	+0.09
p_{T3} [Pa]	1.42	1.42	+0.04
T_{T4} [10^3 K]	1.43	1.43	0
p_{T4} [Pa]	1.35	1.35	+0.04
$\dot{m}_0$ [10^3 kg/s]	0.557	0.558	-0.17
$\dot{m}_{\text{fuel}}$ [kg/s]	1.16	1.14	+1.37
TSFC [kg/(N s)]	1.49×10^{-5}	1.46×10^{-5}	+1.75
N1 [%]	100	100	0
N2 [%]	100	100	0

(b) Off-Design Performance

Parameter [Unit]	**Framework**	**GSP**	**Difference [%]**
T_{T3} [K]	896	897	-0.13
p_{T3} [Pa]	3.46	3.47	-0.37
T_{T4} [10^3 K]	1.65	1.66	-0.69
p_{T4} [Pa]	3.29	3.30	-0.38
$\dot{m}_0$ [10^3 kg/s]	1.30	1.29	+0.45
$\dot{m}_{\text{fuel}}$ [kg/s]	3.10	3.10	-0.05
TSFC [kg/(N s)]	8.22×10^{-6}	8.22×10^{-6}	-0.05
N1 [%]	106	103	+3.12
N2 [%]	107	106	+0.86

acceptable given the conceptual design level and the simplifying assumptions made in the analysis methods.

Second, Figure 3.9 shows the resulting geometry predictions and the overlap with the actual top view of the aircraft. Although the computational models agree relatively well with the actual planform, two aspects can potentially be further improved. First, the wing taper ratio is overestimated for both cases. This is because the statistical relation, which relates the taper ratio to the wing sweep, produces an averaged value for various aircraft. For example, it underestimates the taper for a Boeing 737-700. Therefore, it is decided not to correct this relation for the aircraft presented here. Also, the main wing of the Airbus A320-200 is placed slightly more aft than expected. Again, this can be attributed to averaged statistical values. In this case, the location of the aircraft center of gravity (c.g.) at OEM with respect to the mean aerodynamic chord ($\xi_{\text{c.g., OEM}} = 0.25\,\text{MAC}$), and the relative location of the horizontal tail to the fuselage length ($x_{\text{ht}}/l_{\text{fus}} = 0.91$). The geometry creation is discussed more elaborately in Appendix B.

Finally, the payload-range diagrams of the aircraft are compared in Figure 3.10 with data from the aircraft characteristics documents to verify whether the aircraft perfor-

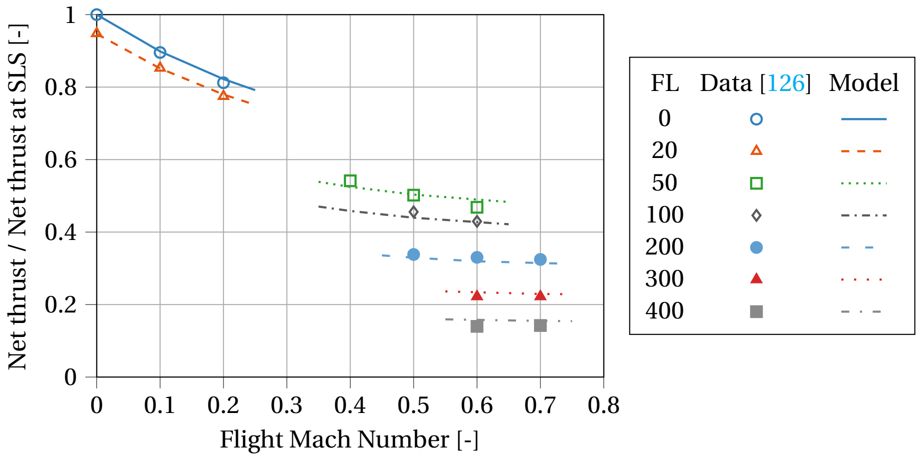

(a) Maximum net thrust

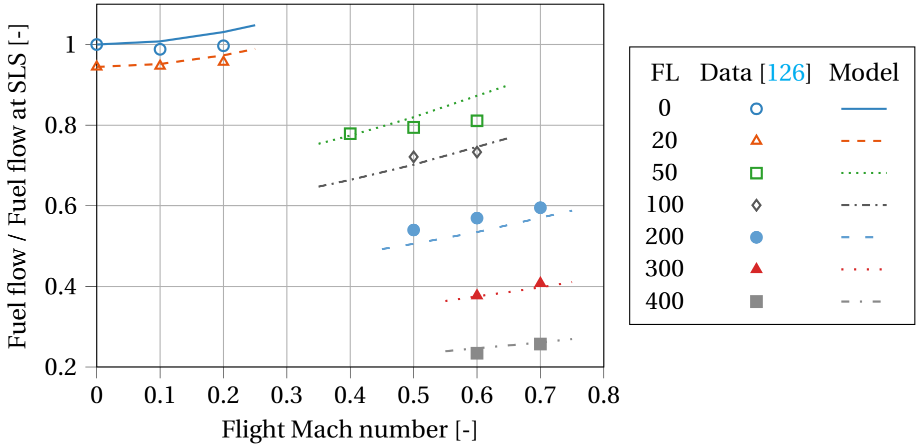

(b) Fuel mass flow at maximum net thrust

Figure 3.8: Validation of engine performance throughout the flight envelope, compared to GE90 engine data [126, Appendix J] (FL = Flight level)

mance is evaluated adequately. The payload-range diagrams show that good agreement is achieved with relatively simple methods. For the Airbus A320, the slope of the line between the harmonic mission and full fuel tanks is marginally underestimated, which is possibly caused by an underestimation of the engine efficiency or lift-to-drag ratio in the cruise segment. This approximation of this slope is better for the Boeing 777, although the range at maximum fuel capacity is somewhat overestimated.

Table 3.7: Validation of aircraft design modules with existing aircraft data [127] (the fuel mass is evaluated at the harmonic range with maximum structural payload)

(a) Airbus A320-200

Parameter [Unit]	**Framework**	**Reference**	**Diff. [%]**
MTOM [metric tons]	72.3	73.5	-1.6
OEM [metric tons]	40.7	41.3	-1.5
Fuel Mass [metric tons]	13.3	13.5	-1.2
Wing area S [m^2]	126	122	+2.5
Wing span b [m]	34.5	34.1	+1.3
Fuselage outer diameter d_{fus} [m]	3.96	3.95	+0.2
Fuselage length l_{fus} [m]	38.2	37.6	+1.8

(b) Boeing 777-200

Parameter [Unit]	**Framework**	**Reference**	**Diff. [%]**
MTOM [metric tons]	242	243	-0.5
OEM [metric tons]	134	136	-1.4
Fuel Mass [metric tons]	52.3	52.2	+0.3
Wing area S [m^2]	437	428	+2.1
Wing span b [m]	61.6	60.9	+1.2
Fuselage outer diameter d_{fus} [m]	6.14	6.20	-1.0
Fuselage length l_{fus} [m]	62.6	62.8	-0.3

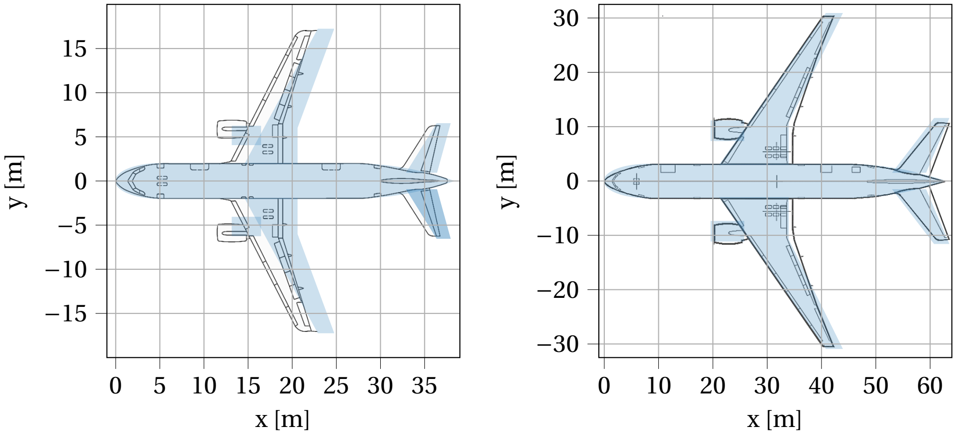

(a) Airbus A320-200

(b) Boeing 777-200

Figure 3.9: Comparison between the top view created by the MDO method (light blue) and the actual geometry (dark lines) [128, 129]

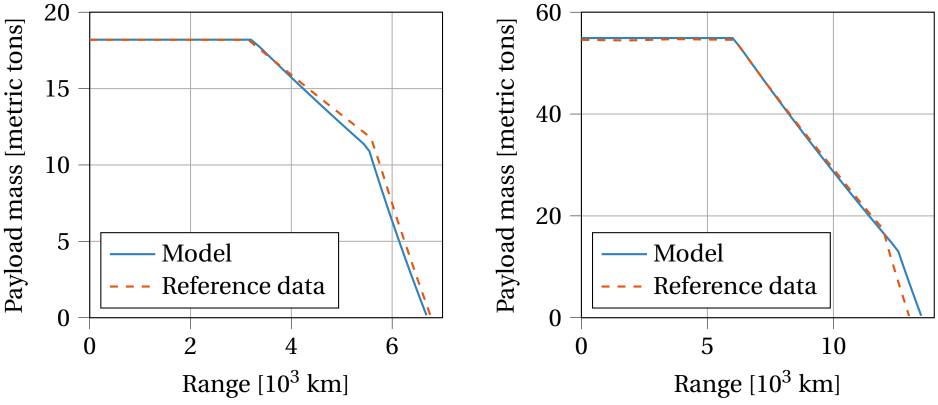

(a) Airbus A320-200 (M_{cr}=0.78, h_{cr}=11.3 km)

(b) Boeing 777-200 (M_{cr}=0.84, h_{cr}=11.9 km)

Figure 3.10: Comparison between payload-range diagrams obtained with the MDO method (blue lines) and the reference diagrams (dashed orange lines) [128, 129]

3.3. RESULTS AND DISCUSSION

Employing the verified methods from Section 3.1, a commercial aircraft design is optimized for a given set of top-level requirements. This section presents the results of a series of optimizations and discusses the rationale behind the design results. Three objectives are considered in the optimizations: the climate impact (ATR_{100}), the fleet-wide fuel mass ($m_{\mathrm{fuel,fleet}}$), and cash operating cost ($C_{\mathrm{ops,fleet}}$).

Table 3.8 presents the top-level requirements that are used throughout all optimization studies. These requirements correspond to a narrow-body, medium-range aircraft, comparable to the Airbus A320 or Boeing 737. The specified structural payload represents a high-density cabin layout of 180 passengers in economy class seats, resulting in a maximum structural payload of approximately 18 metric tonnes.

Table 3.8: Top-level aircraft requirements employed for the aircraft optimization

Requirement [Unit]	**Value**
Maximum structural payload [metric tons]	18.2
Harmonic range [km (nmi)]	3200 (1730)
Approach speed [m/s (kts)]	70.0 (136)
Take-off length (ISA conditions) [m (ft)]	2100 (6890)

Since previous studies [20, 88] revealed that climate-optimized aircraft tend to fly slower, with an increased block time as a result, it is of interest to study whether such an aircraft can maintain the same productivity level. To gain further insight into this matter, the hypothetical fleet scenario includes a productivity constraint, as introduced in Section 3.3.1. Subsequently, Section 3.3.2 present the optimization results. The optimization strategy is elaborated upon separately in Appendix C.1.

3.3.1. FUTURE FLEET SCENARIO DEFINITION

Since the climate impact is calculated from an emission scenario over 100 years, the outcome is dependent on the number of flights taking place in this period, and thus the number of active aircraft. Assuming all aircraft in the hypothetical fleet execute only one fixed mission, the number of flights in a given year (year i) is computed from the number of aircraft available in that year, the block time t_{bl} of that mission, and the annual utilization $\mathrm{U}_{\mathrm{ann}}$ of the aircraft type:

$$N_{\text{flights, year i}} = N_{\text{AC, year i}} \cdot \frac{\mathrm{U}_{\mathrm{ann}}}{t_{\mathrm{bl}}} \tag{3.27}$$

The annual utilization is assumed to be constant and equal to 3900 hours per year for the narrow-body aircraft category studied here. This value follows from statistical analysis of fifteen US-based airlines from 1995 to 2019 [130]. The chosen mission largely determines the block time. In this research, the three objectives are evaluated for a fixed mission with $N_{\mathrm{pax}} = 130$ passengers (i.e. 13 metric tons of payload) and a stage length r_{bl} of 1852 km or 1000 nmi. Research by Husemann, Schäfer, and Stumpf [131] indicates that narrow-body aircraft often operate near this payload-range combination.

Additionally, the block time varies with the cruise speed and is thus different for the three objectives, as shown in the subsequent section. Since the varying block time affects the productivity of an aircraft (i.e. number of passenger-kilometers flown in a given time frame), the required productivity in the year 2050 is constant, but the number of aircraft can vary for each objective. This productivity level is equal for all three objectives under consideration. The imposed level is estimated from passenger transport statistics in the United States for fifteen airlines [130], considering an annual growth of 3% in this region [9]. Hence, this aircraft fleet has to reach a productivity level of approximately 3.95×10^{12} revenue passenger kilometers ($\mathrm{RPK}_{\mathrm{fleet,2050}}$) each year in the period from 2050 to 2055.

By imposing this constraint, also the total number of flights carried out each year is equal for the three objectives. In this case, the maximum number of aircraft to be produced, and the number of aircraft active in the period from 2050 to 2055, is provided by the following relation:

$$\begin{aligned} N_{\text{AC, 2050}} &= \frac{\mathrm{RPK}_{\text{fleet, 2050}}}{N_{\mathrm{pax}} \cdot r_{\mathrm{bl}}} \cdot \frac{t_{\mathrm{bl}}}{\mathrm{U}_{\mathrm{ann}}} \\ &= \frac{3.95 \cdot 10^{12}}{130 \cdot 1852} \cdot \frac{t_{\mathrm{bl}}}{3700} \end{aligned} \tag{3.28}$$

The production of the new, hypothetical aircraft starts in 2020 and continues for 30 years. Each aircraft has a lifetime of 35 years, assuming no hull losses occur. The aircraft concept is thus in operation for a period of 65 years. Figure 3.11 clarifies the scenario construction by presenting the total fleet size and the number of flights for each year in the period of 100 years considered for the climate impact evaluation. The hypothetical scenario does not account for potentially new technology levels being implemented on the aircraft design, such as a new engine option.

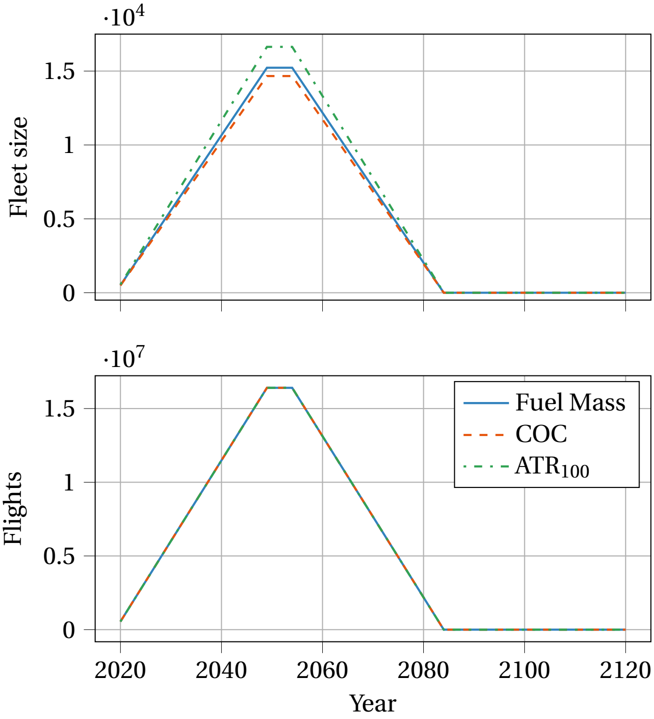

Figure 3.11: Future amount of aircraft in operation and number of flights for the three considered design objectives, in the hypothetical scenario. The number of flights, and thus passengers transported, is the same for the three aircraft, whereas the number of required aircraft, to achieve that same number of flights, is different.

3.3.2. SINGLE-OBJECTIVE OPTIMIZATION RESULTS

Table 3.9 presents the results of the optimizations for the three objectives introduced at the start of this section. On the left-hand side of the table, the absolute values of the parameters are provided for each optimized objective. The right-hand side shows the relative changes with respect to the minimum achievable value. For example, when an aircraft is optimized for ATR_{100}, the operating costs lie 8.2% above the minimum cost achievable, and the fuel burn is 6.6% higher than the minimum fuel mass found.

Table 3.9: Optimized objective values (denoted by *) and relative differences

Parameter [Unit]	**ATR$_{100}$**	**COC**	**Fuel Mass**
ATR [mK]	11.8^* (-)	27.0 (+130%)	26.8 (+128%)
$C_{\text{ops,fleet}}$ [10^{13} USD]	10.4 (+8.2%)	9.62^* (-)	9.87 (+2.6%)
$m_{\text{fuel,fleet}}$ [10^{11} kg]	1.27 (+6.6%)	1.26 (+6.1%)	1.19^* (-)

The results indicate that none of the three objectives leads to the exact same solution. Although the fuel- and cost-optimized aircraft are rather similar, they appear to be conflicting with the global warming objective. Indeed, it seems that the climate-optimized solution does not correspond to the minimum fuel burn solution, due to the relative importance of non-CO_2 effects, and that the operating cost is increased. Tables 3.10 and 3.11 show the selected design variables and other performance indicators, respectively, to shed light on the design choices made for each design objective. The resulting top views of the optimized aircraft are displayed in Figure 3.12.

In the case of the fuel mass objective, it is clear that the optimizer moves to a design point with a high aspect ratio for reduced lift-induced drag. Furthermore, the overall pressure ratio (OPR) of 56.7 approaches the highest value allowed within the specified bounds. The bypass ratio of 9.0 is relatively high, but not maximized. This may be due to a trade-off with installation effects, and because the allowable turbine entry temperature in take-off conditions is limited. These design changes result in an optimal fuel consumption of approximately 5200 kg per flight.

Table 3.10: Optimized design variables for the three design objectives considered

Variable [Unit]	**ATR$_{100}$**	**COC**	**Fuel Mass**
W/S [kN/m^2]	6.08	5.55	6.03
A [-]	12.0	9.05	11.6
$C_{L_{\text{max}}}$ [-]	2.80	2.60	2.69
BPR [-]	10.5	7.12	9.00
Π_{fan} [-]	1.40	1.80	1.59
Π_{lpc} [-]	1.37	1.42	1.80
Π_{hpc} [-]	19.5	20.0	19.8
TET [10^3 K]	1.45	1.55	1.52
h_{cr} [km]	7.56	10.2	10.1
M_{cr} [-]	0.600	0.751	0.708

The design of the aircraft with minimized operating costs (approximately 0.129 $\text{USD}_{2020}/(\text{seat} \cdot \text{nmi})$) appears to be driven by the block time, which is the shortest of the optimized aircraft as can be seen in Table 3.11. This parameter, and its related block speed, play an important role in the labor costs of the crew and maintenance technicians since these costs are related to the flight hours. Although fuel costs play an important role in cost minimization, they are not dominant. Nevertheless, the relative contribu-

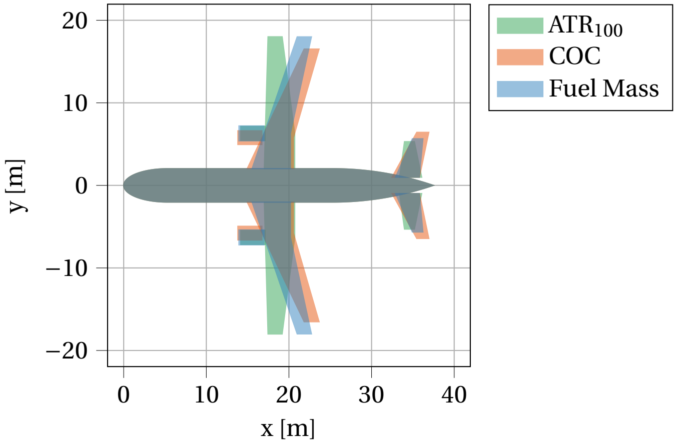

Figure 3.12: Top view of aircraft optimized for three different objectives

tion depends on the fuel price, which is assumed to be 1.78 USD/US gallon in this chapter. Higher fuel prices for given labor rates can make the design more sensitive to fuel burn. Ideally, the aircraft would fly at an even higher Mach number to reduce labor costs further. Nonetheless, this is hindered by the constraint on the maximum lift coefficient, which decreases with increased sweep and thus cruise speed.

Additionally, since this $C_{L,\max}$ constraint appears to be active for all objectives, the variable can be removed from the design vector in future optimization studies with the current framework. $C_{L,\max}$ can rather be calculated directly from the quarter-chord sweep angle, which in turn follows from the selected cruise Mach number.

The climate-optimized aircraft, however, exhibits a different design. The ATR metric also takes the short-lived climate agents into account, of which NO_x and contrails are prevalent and have an altitude dependency. Table 3.10 indicates that the optimal cruise altitude is considerably lower than for the fuel- and cost-optimized aircraft, i.e. 7.56 kilometers vs. 10.1 km. This can be explained as follows: in the case of NO_x, this reduces the radiative forcing due to the creation of short-lived ozone [60]. For contrails, flying lower reduces the probability of contrail formation due to the higher ambient temperatures, as shown in Figure 3.7. These two effects are reinforced by the choice of engine design variables: the lower design OPR (37.4 compared to 56.7 for the fuel-mass objective) reduces the emission index of NO_x and decreases the overall engine efficiency (29.5% compared to 32.7% for the fuel-mass objective). The latter aspect reduces the slope of the mixing line in the Schmidt-Appleman criterion, lowering the probability of persistent contrail formation further. It can be argued that this also reduces the climate impact due to contrail cirrus, although this is not considered in the optimizations.

Schumann [17] observed that contrail formation probability increases with higher propulsive efficiency, which is related to higher bypass ratios. However, the current results show that the ATR$_{100}$-optimal aircraft has a higher bypass ratio (10.5) than the other two aircraft (7.1 and 9.0). This finding does not mean that contrail formation frequency is not affected by the bypass ratio in the current model setup. However, the results show that the cruise altitude performs a more important role than the bypass ratio in the contrail formation and the resulting impact. The bypass result is increased to offset the penalty in fuel consumption and CO_2 emissions due to different operating conditions and lower OPR.

Furthermore, it is observed that the ATR_{100}-optimal aircraft operates at a significantly lower Mach number of 0.60, at the lower bound of this variable. It is expected that two reasons lead to this result: first, the cruise speed has to be adapted to the lower altitude to achieve the optimal lift-to-drag ratio in cruise. Secondly, the lower Mach number does not require a (large) sweep angle and allows for larger thickness-to-chord ratios, both reducing the structural mass of the wing and offsetting the mass increase due to the high aspect ratio. To better suit the operation at such low Mach numbers, it would be of interest to study exchanging the turbofan cycle for a propeller-based propulsion system. This is studied in Chapter 4.

Although the engine efficiency of the climate-optimized aircraft is reduced, the data in Table 3.11 indicates that the thrust-specific fuel consumption (TSFC) is slightly lower compared to the fuel- and cost-optimized aircraft. This appears to be contradictory, however, it is correct that the efficiency of the climate-optimized aircraft is lower, not only due to the decrease in overall pressure ratio but also because of the lower cruise speed. The latter design choice simultaneously lowers ram pressure and ram drag, which causes a beneficial reduction in TSFC and a decrease in the propulsive efficiency of the turbofan engine. These opposing trends of TSFC and propulsive efficiency with respect to flight speed are also documented by Torenbeek [34, Ch. 4].

The temperature response over the next 100 years is presented in Figure 3.13 for the three objectives. The difference in the climate impact of the three aircraft becomes apparent in this figure since the ATR_{100} objective is related to the area under these curves. The line corresponding to the fuel mass objective shows a relatively high maximum in 2075 because the short-term climate effects are prevailing, while the impact of long-lived CO_2 emissions, which relate linearly to fuel consumption, is reduced. For the climate-optimized case, the short-term effects are minimized, but the maximum occurs later due to the delayed effect of CO_2 emissions.

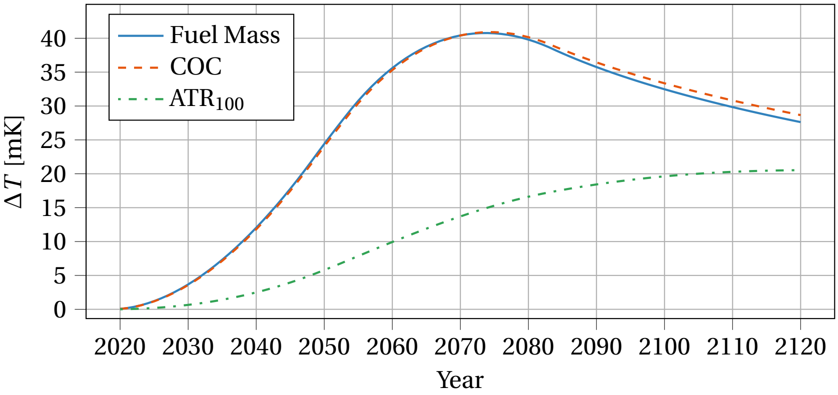

Figure 3.13: Surface temperature change for the three optimized aircraft

Upon further examination of Figure 3.13, the surface temperature change in the year 2120 approaches approximately 20-25 mK for all cases. Hence, one may argue that the final effect is the same. Nevertheless, the climate-optimized airplane does not reach the same level of temperature change around 2075. This is captured by the ATR_{100} metric and shows that this metric can give insight into global warming by capturing the short- and long-term effects of several species.

A final remark on the fixed productivity approach is that approximately 13% more aircraft have to be produced in the case of the climate-optimized aircraft, at a higher production rate, to reach the same productivity level in the period from 2050 to 2055. This is indicated in Figure 3.11. The need for more aircraft is a consequence of the higher block time, which reduces the productivity of a single aircraft. To maintain the same level of fleet productivity, more aircraft of this type have to be operated. Nor the climate impact, nor the costs of this larger production capacity are computed in this research. However, one could argue qualitatively that this increased production raises both the climate footprint and the complete lifecycle cost of the climate-optimized aircraft.

Table 3.11: Performance indicators of optimized aircraft

Parameter	**ATR_{100}**	**COC**	**Fuel Mass**
MTOM [metric tons]	66.9	68.2	68.5
OEM [metric tons]	36.0	37.4	38.5
S [m^2]	108	121	111
$\Lambda_{0.25}$ [deg]	0.0	22.0	16.3
λ [-]	0.460	0.277	0.325
$(L/D)_{\text{cr}}$ [-]	18.8	18.2	19.3
$(T/W)_{\text{TO}}$ [-]	0.317	0.315	0.329
T_{TO} [kN]	207	211	221
TSFC_{cr} [kg/(N s)]	1.47×10^{-5}	1.61×10^{-5}	1.51×10^{-5}
t_{bl} [hrs]	3.95	3.49	3.62
$N_{\text{AC, max}}$ [-]	16.6×10^2	14.7×10^2	15.2×10^2

During the operational lifetime of this aircraft, from 2020 to 2085, the technology levels will likely evolve and affect the propulsion, aerodynamic, and structural disciplines. This study does not quantify the impact of such developments on the optimized aircraft. Nevertheless, a qualitative outlook is provided here. Since a single aircraft type is considered with a market introduction in 2020, the airframe will remain almost constant throughout the considered lifespan, albeit with minor aerodynamic and structural improvements. These improvements can enhance the cruise efficiency, leading to lower fuel burn and reduced absolute emissions. Although the aircraft mass alters contrail properties [74], the effect is mainly dependent on the aircraft category and is difficult to quantify in the conceptual phase. An engine upgrade during the aircraft's lifetime is feasible, which can drastically influence the overall fuel burn and emissions through improved component efficiencies and combustor design. Producing less NO_x emissions at higher overall pressure ratios would be beneficial, and could increase the optimal cruise altitude and Mach number.

3.3.3. MULTI-OBJECTIVE OPTIMIZATION RESULTS

This section describes the results of multi-objective optimization to study the trade-off between climate impact and operating costs. The Pareto front defining this trade-off is presented in Figure 3.14. This image shows that for a marginal cash-operating cost increase of 1 to 2%, a significant reduction in ATR_{100} is possible. This large reduction potential comes mostly from the reduction in cruise altitude and Mach number. The variation in design variables along the Pareto front is discussed further in Section 6.3.2 for different fuel types. Although uncertainties remain, it seems that to significantly lower the climate impact while limiting the cost increase, a design solution near a 50% ATR_{100} reduction and 2% cost increase is preferred over the climate-optimal solution. Beyond this point, the costs rise more rapidly for a marginal decrease in climate impact.

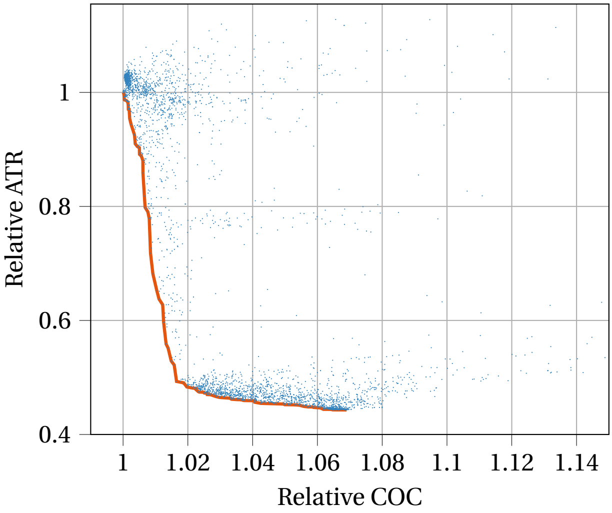

Figure 3.14: Pareto front (orange line) between cost and climate objectives (the data is normalized with respect to the cost-optimal aircraft, blue dots are feasible designs) for the kerosene, medium-range aircraft

3.3.4. COMPARISON WITH LITERATURE

To put these results in perspective and highlight key findings, we compare the optimized designs with previous research by Dallara and Kroo [88] and Koch [20]. In essence, the main design trends for climate-optimal aircraft are similar: lower cruise altitude at reduced Mach number, combined with a higher aspect ratio and bypass ratio, compared to cost-optimal aircraft. Dallara and Kroo report a reduction in ATR_{100} of 35% to 74% depending on the discount rate (0 or 3%, respectively). In this study the climate reduction is estimated to be approximately 57%, assuming a discount rate of zero.

We expect that the main reason for this discrepancy in climate impact reduction is the difference in the contrail effects. The cost-optimal solution in this research has a relative contrail contribution of approximately 48%, while in the case of Dallara and Kroo this contribution is only 17%. Hence, the achievable relative reduction becomes larger when the contrails vanish due to the lower cruise flight. The cost increase for the climate-optimal aircraft appears to be similar for both studies, as can be concluded from the Pareto fronts. This cost rise is approximately 6 to 10%. Small discrepancies may be the result of a different definition of the costs and distinct price assumptions. Especially the ratio between fuel costs and time-related costs, such as salaries, performs an important role in this analysis.

Although the two studies are comparable, the current research also offers insight into the optimal engine parameters. For example, the trend in OPR shows that climate-optimal aircraft do not feature a maximum OPR, presumably to lower the emission index of nitrogen oxides. The engine efficiency of the climate-optimal is lower than that of the fuel-optimal aircraft. This engine efficiency also performs a role in the contrail formation. The lower engine overall efficiency reduces the mixing line slope in Figure 3.7 (on Page 43), reducing the probability of contrail formation. In the current modeling approach, this marginally raises the altitude at which persistent contrails are formed.

Furthermore, due to span constraint imposed in the current optimization definition, the aspect ratio cannot achieve values of nineteen or twenty, as is the case for the optimization by Dallara and Kroo. This limits the L/D of the climate-optimal aircraft, prohibiting a reduction in fuel burn. Nevertheless, considering current airport constraints and technology levels, this span constraint possibly makes the design more realistic.

The aim of this study is also to monitor the influence of a lower cruise Mach number and increased flight time on the operations and/or fleet size of climate-optimal aircraft. To maintain the same level of productivity (i.e. RPKs transported in a time interval), more climate-optimal have to be operated. Such insights were not yet considered in previous studies. The effect of increased flight time on fleet allocation is studied further in Chapter 7.

3.4. CONCLUSIONS

This chapter aims to investigate the change in design variables when designing a medium-range aircraft for different objectives. To this end, a multidisciplinary and multi-objective optimization framework is arranged to study the influence of wing, turbofan, and mission design variables on global warming impact, measured by the average temperature response, and cash operating costs, expressed in USD. For a fixed fleet productivity level, it is estimated that the ATR_{100} can be reduced by approximately 57% when moving from the cost objective to the climate objective, at the expense of a 6.9% increase in operating costs. Although these values are based on a simplified analysis and are subject to uncertainties, it indicates that these objectives are indeed conflicting. The reduction in ATR_{100} can be achieved by lowering the cruise altitude to 7.6 km, flying at Mach 0.60, and by decreasing the engine overall pressure ratio compared to the fuel-optimized case, from 57 to approximately 37. These changes are driven by non-CO_2 effects, i.e. the emission of nitrogen oxides and the formation of contrails.

Flying slower causes the block time of the climate-optimized aircraft to be higher than for the aircraft designed for fuel burn or cost, which reduces its productivity compared to these alternatives. For a hypothetical fleet with constrained productivity, it is concluded that approximately 13% more climate-optimized aircraft are needed than cost-optimized aircraft, to achieve the same level of productivity on a fleet level.

The research in this chapter showed that the design objectives of interest, being the cash operating cost, fuel burn, and climate impact are conflicting. A significant reduction in climate impact is possible, but this design solution leads to a cost increase and a loss in productivity. The multi-objective optimization considered the cost and climate objectives simultaneously, and highlighted the option to significantly reduce ATR_{100} by 50% at a 2% COC increase by focusing on contrail avoidance. This finding is examined further in Sections 6.3.2 and 6.3.4.

Based on the optimizations in this chapter, the methods and optimization setup are updated in the following chapters. The design variable $C_{L,\max}$ is omitted and the parameter is automatically set to its maximum value as a function of the quarter-chord sweep angle. Starting in Chapter 5, a wave drag component is added to the drag polar to reflect the wave drag created at higher subsonic and transonic speeds, leading to an increase in fuel burn in this regime. Furthermore, the mass estimates for operating items and fixed airframe and services equipment are held constant in the optimization, and will no longer be considered a fraction of the MTOM. Additionally, from Chapter 5 onward, a more recent engine technology level is assumed with a higher achievable OPR and higher component efficiencies.

4

TURBOPROP, MEDIUM-RANGE AIRCRAFT DESIGN OPTIMIZATION

This chapter studies the climate impact of propeller aircraft which are optimized for either minimum direct operating costs, minimum fuel mass, or minimum average temperature response (ATR_{100}*). The latter parameter provides a measure of the global warming impact of the aircraft design, considering both *CO_2* and non-*CO_2* effects. The turboprop-powered aircraft are studied in particular because these engines offer higher propulsive efficiency than turbofan aircraft at low altitudes and low Mach numbers. The propeller aircraft are designed for medium-range top-level requirements, employing a multidisciplinary design optimization framework. This framework uses a combination of statistical, empirical, and physics-based methods, which are verified using existing engine and aircraft data. For this medium-range design case, a climate impact reduction of 16% can be realized when shifting from the cost design objective to the climate objective. The optimal solutions for the fuel mass and climate objectives are nearly identical as *CO_2* and other fuel-proportional climate effects are the main contributors. The effects of *NO_x* and contrails are lower than for the turbofan aircraft due to the lower cruise altitude of the propeller aircraft. Compared to turbofan data, propeller-powered aircraft can achieve a further 33% reduction in climate impact, comparing both climate-optimal designs. This reduction is lessened to 23% when the propeller aircraft is constrained to achieve the same mission block time as the turbofan aircraft. Note that these reductions in *ATR_{100}* require a propeller efficiency of 88%. Overall, the results show that the utilization of propeller-powered aircraft in the medium-range category can further reduce the climate impact compared to climate-optimal turbofan aircraft designs.*

The optimizations in this chapter were performed by R. Thijssen as a part of an MSc Thesis research project [132], which contains more details than this chapter as well as extra case studies. Furthermore, the results were presented at the ICAS conference in 2022 [132].

From the studies by Schwartz Dallara [82] and the research in Chapter 3, which focused on turbofan aircraft, it is clear that the climate-optimal, turbofan-powered aircraft has a lower cruise Mach number (≈0.6) and cruise altitude (≈ 6 to 7 km). The combination of the altitude and Mach number reduces the effect of NO_x on the climate and prevents the formation of aviation-induced cloudiness, specifically persistent contrails. However, this cruise altitude and Mach number result in a less-efficient cruise flight of turbofan aircraft, which barely reduces or even slightly increases the contribution due to CO_2. In these cruise conditions, propeller aircraft are known to have a higher propulsive efficiency [34], as conceptually shown in Figure 4.1.

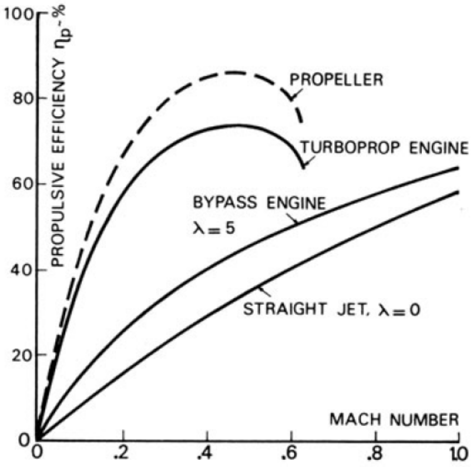

Figure 4.1: Propulsive efficiency of engine concepts versus cruise Mach number [34]

Propeller aircraft have been studied thoroughly as part of the AGILE 3.0 project[1]. Different innovative configurations are tested and their performance and climate impact are evaluated. For example, the study of Stingo et al. [133] compares a wing-mounted propeller aircraft with a tail-mounted propeller aircraft. Della Vecchia et al. [134] measure the climate impact of a propeller aircraft using the global warming potential (GWP). However, GWP is not the best metric without sufficient comparison [135].

Besides the traditional turboprop architecture, the contra-rotating open rotor (CROR) has been researched since its main introduction in the advanced turboprop project by Hager and Vrabel [136]. The CROR has the potential to increase propulsive efficiency and Guynn et al. [137] has estimated that the fuel consumption can be reduced by up to 18% on short-range missions compared to a geared turbofan with a similar technology level. Nevertheless, Guynn et al. [137] also points out this engine configuration can be heavy and poses integration issues. Additionally, the complexity and reduced reliability of such engines are drawbacks of the CROR configuration [138, 139]. Therefore, the turboprop layout is often preferred in literature.

Although research has shown that climate-optimal turbofan aircraft fly at cruise conditions where turboprops typically feature higher propulsive efficiency, it appears that climate-optimal propeller aircraft have not been studied in detail. Therefore, it is of interest to evaluate the climate impact of a medium-range, propeller-powered aircraft. This leads to the second research question introduced in Section 1.4: what are the differences in operating cost, mission fuel, and climate impact between optimized propeller-powered aircraft and a turbofan-powered aircraft optimized for the same objectives, TLARs, and mission?

---

[1] URL `https://www.agile-project.eu/`

This research question yields insight into the performance of propeller-powered aircraft and their design. As turbofan data is available, a direct comparison of the values is made. The study in this chapter can determine if a propeller aircraft design is a realistic option to reduce the climate impact on medium-range routes.

This chapter is structured as follows. First, Section 4.1 discusses the optimization problem including the applied constraints. Subsequently, Section 4.1.2 describes the design methods. Then Section 4.2 focuses on the verification and validation of the methods and Section 4.3 discusses the results and compares the turboprop aircraft to the turbofan alternatives from Chapter 3.

4.1. PROBLEM FORMULATION AND METHODS

To find and study the optimal propeller-powered aircraft, the MDAO framework from Figure 3.2 is adapted to design aircraft powered by turboprop engines. This section describes the new optimization problem and focuses on what has changed in the design methods compared to the setup for turbofan aircraft.

4.1.1. OPTIMIZATION PROBLEM FORMULATION

A medium-range, turboprop aircraft powered by kerosene is optimized for three different objective functions, namely the mission fuel mass (FM or m_{fuel}), the direct operating costs (DOC), and the average temperature response (ATR_{100}). The aircraft designed in this study has a high-wing, T-tail configuration powered by two turboprop engines mounted to the wing. This configuration best represents the current propeller aircraft in operation.

The optimization problem is formulated as follows, where the three objectives are considered separately (i.e. not a multi-objective optimization):

$$\begin{aligned}
\underset{\mathbf{x}}{\text{minimize}} \quad & F(\mathbf{x}) = \text{ATR}_{100}(\mathbf{x}) \ \text{ or } \ \text{DOC}(\mathbf{x}) \ \text{ or } \ \text{E}_{\text{fuel}}(\mathbf{x}) \\
\text{subject to} \quad & W/S_{\text{TO}} \leq \frac{1}{2}\rho_0 \left(\frac{v_{\text{app}}}{1.23}\right)^2 C_{L_{\max}}, \\
& b \leq b_{\max} = 36\,\text{m}, \\
& \text{TET}_{\text{TO}} \leq \text{TET}_{\text{TO, max}} = 2000\,\text{K}, \\
& C_{L_{\text{cr}}} \leq \frac{C_{L_{\text{buffet}}}}{1.3}, \\
& d_{\text{prop-fus}} \geq 0.035\,\text{m}, \\
& d_{\text{prop-ground}} \geq 0.18\,\text{m}, \\
& x_i^L \leq x_i \leq x_i^U \qquad\qquad \text{for } i = 1, 2, \ldots, 6
\end{aligned} \tag{4.1}$$

To design the aircraft, a short design vector is selected while allowing a sufficiently large design space. Two airframe design variables, two engine design variables, and two mission design variables are selected. Table 4.1 presents these six variables together with their respective bounds. The bounds are chosen such that they allow for technological advancements made in the future. An example of this is the compressor pressure ratio limit of 25, which is relatively high for a turboprop engine. Nevertheless, the TP400-D6 Turboprop engine, which is used on the Airbus A400M Atlas, has a pressure ratio of 25 [2]. For this reason, it has been chosen as the upper bound. Additionally, the bounds are chosen such that the aircraft design is restricted by constraints rather than the imposed bounds.

Table 4.1: Design variables and their respective bounds for the optimization of turboprop aircraft

Variable	**Description [Unit]**	**Lower Bound (x^L)**	**Upper Bound (x^U)**
A	Aspect ratio [-]	7	17
W/S	Wing loading [kN/m^2]	2.0	7.0
Π_c	Compressor pressure ratio [-]	5	25
TET	Turbine entry temperature [K]	1100	1650
h_{cr}	Initial cruise altitude [km]	3.0	10.0
M_{cr}	Cruise Mach number [-]	0.25	0.80

The constraints limit the aerodynamic, geometric, and performance characteristics of the aircraft. The inequality constraints are not to be exceeded and ensure the aircraft design adheres to the regulations or restrictions. The constraints regarding the airframe structure are the maximum span, the propeller ground clearance, and the propeller fuselage clearance. The maximum span is limited by the airport category. Narrow-body aircraft are often designed for a category C airport [3]. The maximum span for this category is set to 36 m, similar to the constraints in Section 3.1.1. The propeller ground clearance and propeller fuselage clearance are obtained from regulations. These clearances are set to 18 cm and 35 mm, respectively [140].

The other constraints are the limitation on the turbine entry temperature (TET) at take-off, the wing loading, and the cruise lift coefficient. The TET at take-off is restricted by the engine properties, because the high temperature can damage the high-pressure turbine, limiting the TET during take-off to 2000 K [105]. The wing loading is restricted by the approach velocity of the aircraft, which depends on the aircraft approach category[4]. Similarly to Chapter 3, the approach velocity is set to 70 m/s. This velocity is higher than for certain existing turboprop aircraft (the reference landing speed of the ATR 72-600 is 113 KIAS or approximately 58 m/s [141]). However, the intention of the optimization in this chapter is to match the performance requirements of the turbofan counterparts designed in Chapter 3. The maximum cruise lift coefficient is based on the buffet onset of the aircraft ($C_{L,\text{buffet}}$), potentially causing unwanted vibrations. The maximum cruise lift coefficient is purely dependent on the Mach number, as it is expected that little sweep is achieved. Equation (4.2) is used to calculate the buffet lift coefficient as obtained from polynomial analysis based on data from Vos and Farokhi [142].

---

[2] URL `http://www.europrop-int.com/the-tp400-d6/` accessed on 23 November 2021

[3] URL `https://skybrary.aero/articles/icao-aerodrome-reference-code` accessed on 13 October 2021

[4] URL `https://www.skybrary.aero/index.php/Approach_Speed_Categorisation` accessed on 2 November 2021

$$C_{L,\text{buffet}} = -0.3624M^2 - 1.8905M + 2.0536 \tag{4.2}$$

Figure 4.2 presents the multidisciplinary setup of the optimization problem. Three distinct parts of the XDSM diagram can be distinguished: first, the main optimizer in steps 0-10 provides updates of the design vector. Secondly, the aircraft design convergence loop (steps 1 to 6) ensures each aircraft design is consistent in terms of mass and geometry. Finally, the extra modules, indicated in steps 7 to 9, evaluate the direct operating costs, the climate impact, and the constraints discussed above.

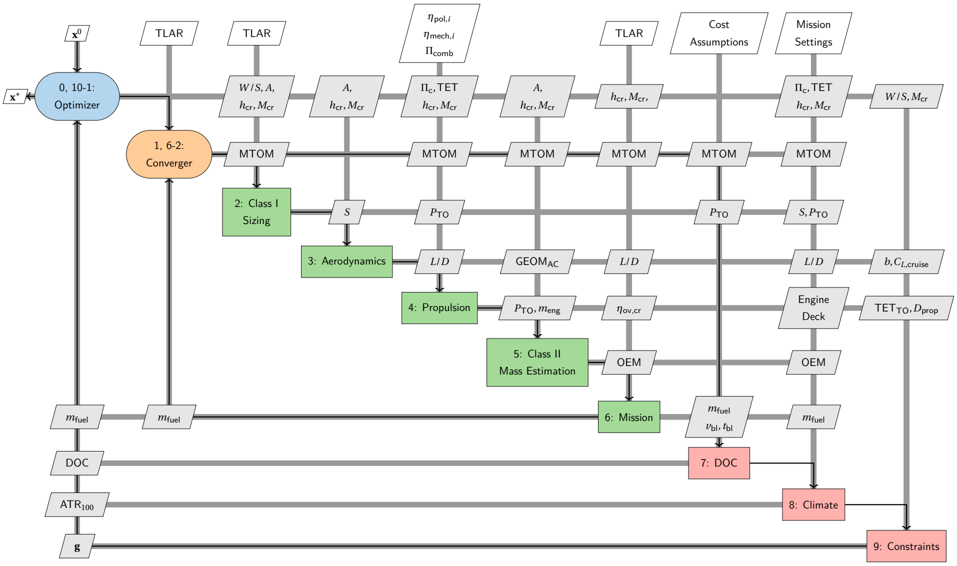
$\mathbf{x}^0$
TLAR
TLAR
$\eta_{\text{pol},i}$ $\eta_{\text{mech},i}$ Π_{comb}
TLAR
Cost Assumptions
Mission Settings
$\mathbf{x}^*$
0, 10-1: Optimizer
$W/S, A, h_{cr}, M_{cr}$
A, h_{cr}, M_{cr}
Π_c, TET h_{cr}, M_{cr}
A, h_{cr}, M_{cr}
h_{cr}, M_{cr}
Π_c, TET h_{cr}, M_{cr}
$W/S, M_{cr}$
1, 6-2: Converger
MTOM
MTOM
MTOM
MTOM
MTOM
MTOM
MTOM
2: Class I Sizing
S
P_{TO}
P_{TO}
S, P_{TO}
3: Aerodynamics
L/D
GEOM$_{\text{AC}}$
L/D
L/D
$b, C_{L,\text{cruise}}$
4: Propulsion
$P_{\text{TO}}, m_{\text{eng}}$
$\eta_{\text{ov,cr}}$
Engine Deck
TET$_{\text{TO}}, D_{\text{prop}}$
5: Class II Mass Estimation
OEM
OEM
m_{fuel}
m_{fuel}
6: Mission
m_{fuel} $v_{\text{bl}}, t_{\text{bl}}$
m_{fuel}
DOC
7: DOC
ATR$_{100}$
8: Climate
$\mathbf{g}$
9: Constraints

Figure 4.2: XDSM diagram of the MDO framework, adapted from the XDSM in Figure 3.2

The installation of the propellers in treated in a conceptual manner in the current optimization setup. The design vector does not include any propeller-related design variables controlling the blade planform or number of blades, and the MDO framework does not contain a discipline which accounts for the aerodynamic installation effects of propellers [143]. Such effects can possibly affect the spanwise wing loading and the lift-to-drag ratio. A more detailed analysis of the propeller and its installation lies outside the scope of the current study since it increases complexity and requires higher fidelity modeling. Nevertheless, it is recommended to add such analysis in future work to have an improved estimate of the propeller efficiency, among other parameters, as a function of the cruise Mach number.

4.1.2. Design and Analysis Methods

The inner convergence loop of the MDO framework designs the aircraft and consists of well-established conceptual design methods. The structure of the design loop is based on the one used in Chapter 3, and has been adapted such that a propeller engine and different wing and tail configurations can be used. The focus of this section lies on the newly implemented methods which facilitate the design of propeller aircraft.

Class I Sizing

The design process starts with the statistical estimation of the maximum take-off mass which is the sum of the operative empty mass, fuel mass, and the required payload mass. The OEM is written in terms of the MTOM, while the fuel mass is obtained from the fuel fraction method which uses the Breguet range and endurance equations [144]. The statistical relation used for the OEM in the first iteration is given in Equation (4.3).

$$\text{OEM} = 0.563 \cdot \text{MTOM} + 1.24 \cdot 10^3 \tag{4.3}$$

Using the estimated MTOM, the wing area S and take-off power P_{TO} are calculated from the wing loading W/S and weight-to-power ratio W/P [144]. While the wing loading is a design variable, the weight-to-power ratio is calculated according to the performance constraints in Equation (4.4). These constraints are derived from the take-off distance and the cruise condition. Note that the aerodynamic values of the aircraft in the first iteration are obtained from statistics.

$$\begin{aligned}\left(\frac{W}{P}\right)_{\text{TO}} = \min\Bigg\{ & \frac{\text{TOP}}{C_{L_{\text{TO}}} \cdot (W/S)_{\text{TO}}}, \\ & \eta_p \cdot \left(\frac{P_{\text{cr}}}{P_{\text{TO}}}\right) \cdot \left(\frac{\rho_{\text{cr}}}{\rho_0}\right)^{\frac{3}{4}} \left[\frac{C_{D_{0,\text{cr}}} \rho_{\text{cr}} v_{\text{cr}}^3}{2 \cdot 0.8 \cdot (W/S)_{\text{TO}}} + \frac{2 \cdot 0.8 \cdot (W/S)_{\text{TO}}}{\pi A e_{\text{cr}} \rho_{\text{cr}} v_{\text{cr}}}\right]\Bigg\}\end{aligned} \tag{4.4}$$

In the above equation, TOP is the take-off parameter which is a function of the set take-off distance [144], and η_p is the propeller efficiency. The factor $P_{\text{cr}}/P_{\text{TO}}$ models the power setting in cruise versus take-off and is assumed to be 0.9 (i.e. 90%). The wing loading in cruise is assumed to be 80% of that in take-off. This assumption may underestimate the wing loading in cruise, depending on the fuel mass fraction of the aircraft under consideration. If the cruise performance in Equation (4.4) is sizing, this can lead to an overestimation of $(W/P)_{\text{TO}}$ and thus an underestimation of the required engine power. At aircraft level, this assumption of 80% can result in an underestimation of the mass, fuel consumption, operating cost, and climate impact.

Geometry & Aerodynamics

With the wing area and take-off power known, a conceptual geometry of the aircraft is constructed. The geometry creation follows the design rules specified in Appendix B, except for the positioning and sizing of the empennage and the design of the engine geometry. The horizontal tail is now positioned on top of the vertical tail, and therefore, the horizontal tail's longitudinal location shifts with the tip section of the vertical tail. Additionally, the volume coefficient for the vertical tail is set to 0.08 for narrow-body aircraft (instead of 0.085) to account for the increased effectiveness. The turboprop nacelle is modeled as a rectangular prism whose dimensions are computed according to the statistical relations discussed in Appendix B.4.

In the aerodynamics module, a conceptual, quadratic drag polar is created based on this geometry. The format of the drag polar, consisting of friction, profile, perturbation, and lift-induced drag, and the way it is computed, is the same as in Section 3.1.2.

PROPULSION

The largest difference with respect to the turbofan MDAO framework lies in the propulsion discipline. For the turboprop-powered aircraft, a three-spool engine, similar to the Pratt & Whitney Canada PW127 engine [145], is modeled as a two-spool engine. We assume that the high-pressure turbine drives the compressor stages, while a low-pressure turbine drives the propeller. This leads to one compressor, a high-pressure turbine (HPT), and a low-pressure turbine (LPT). The latter is the free power turbine that drives the gearbox and thus indirectly the propeller. This simplification leads to the two design variables for the engine, namely Π_c and TET. The methods of Mattingly, Heiser, and Pratt [105, Appendix K] are employed for the thermodynamic on- and off-design analyses of the engine. The efficiencies are also obtained from this reference. Additionally, no power off-take, bleed air, or cooling flows are considered in the current analysis.

The propeller engine analysis makes use of the work interaction coefficient C, which has a propeller and core component. Equation (4.5) shows the definition of the work interaction coefficient, where P is the power, η_{prop} represents the efficiency of the propeller ($F_{\text{prop}} \cdot v_0 / P_{\text{prop}}$), v is the aircraft velocity, F is the thrust, $\dot{m}_0$ is the air mass flow and $h_{s,0}$ is the free-stream, static, specific enthalpy.

$$C_{\text{total}} = C_{\text{prop}} + C_{\text{core}} = \frac{P_{\text{prop}} \cdot \eta_{\text{prop}}}{\dot{m}_0 \cdot h_0} + \frac{F_{\text{core}} \cdot v_0}{\dot{m}_0 \cdot h_0} = \frac{F_{\text{prop}} \cdot v_0}{\dot{m}_0 \cdot h_0} + \frac{F_{\text{core}} \cdot v_0}{\dot{m}_0 \cdot h_0} \tag{4.5}$$

The work interaction coefficient is used to calculate the engine properties such as the thrust-specific fuel consumption (TSFC) and the thermal and propulsive efficiencies. Note that P_{prop} in this chapter refers to the power that is transferred to the propeller, also known as brake horsepower, and not the power transferred by the propeller to the air. During both the on-design point (parametric) analysis and the off-design point (performance) analysis, the variable specific heat model by Walsh and Fletcher is used [112].

The off-design analysis approach from literature requires to iterate upon the inlet mass flow $\dot{m}_0$ and the exit Mach number M_9. The latter iterations are unstable in certain cases, in the code implementation, due to choking of the nozzle. To resolve this issue and make the approach robust in the optimizations, a numerical stabilization scheme is added to the M_9 iterations. This scheme ensures convergence but increases computational time. The stabilizer uses the newly calculated exit Mach number ($M_{9,i-1}$) and the exit Mach number from an earlier iteration ($M_{9,i-2}$) to calculate the new value. The implemented numerical stabilizer is shown in Equation (4.6) where the linear proportional gains (k_1, k_2) control the convergence.

$$M_{9,i} = k_1 \cdot M_{9,i-1} + k_2 \cdot M_{9,i-2} \text{ for iteration } i \text{ where } k_1 = 0.1 \text{ and } k_2 = 0.9 \tag{4.6}$$

Furthermore, it is observed that the equations calculating the work coefficient in literature did not yield a correct output. Therefore, the relations in the book for the work interaction coefficients are corrected by deriving the formulas from the power balance and the definitions in Equation (4.5). This results in the following equations for the calculation of the work interaction coefficients (Equations (4.7) and (4.8)), the thermal, propulsive, and overall efficiency (Equations (4.9) and (4.10)), and the TSFC (Equation (4.12)):

$$C_{\text{prop}} = (1+f)\cdot\eta_{\text{gearbox}}\cdot\eta_{\text{prop}}\cdot\eta_{\text{mech,LPT}}\cdot\tau_{\lambda}\cdot\tau_{\text{HPT}}\cdot(1-\tau_{\text{LPT}}) \tag{4.7}$$

$$C_{\text{core}} = \frac{v_0}{h_{s,0}}\cdot\left[(1+f)\cdot v_9 - v_0 + (1+f)\cdot\frac{T_{s,9}R_9}{v_9}\cdot\left(1-\frac{p_{s,0}}{p_{s,9}}\right)\right] \tag{4.8}$$

$$\eta_{\text{thermal}} = \frac{1}{f\cdot\text{LHV}}\cdot\left(\frac{C_{\text{prop}}\cdot h_{s,0}}{\eta_{\text{prop}}} + \frac{1}{2}\cdot\left[(1+f)\,v_9^2 - v_0^2\right]\right) \tag{4.9}$$

$$\eta_{\text{propulsive}} = \frac{C_{\text{total}}\cdot h_{s,0}}{\frac{C_{\text{prop}}\cdot h_{s,0}}{\eta_{\text{prop}}} + \frac{1}{2}\left[(1+f)\cdot v_9^2 - v_0^2\right]} \tag{4.10}$$

$$\eta_{\text{ov}} = \eta_{\text{thermal}}\cdot\eta_{\text{propulsive}} \tag{4.11}$$

$$\text{TSFC} = \frac{f\cdot v_0}{C_{\text{total}}\cdot h_{s,0}} \tag{4.12}$$

In the above equations, f is the ratio between the fuel mass flow added in the combustor ($\dot{m}_f$) and the air mass flow entering the engine core ($\dot{m}_0$), ignoring any bleed air offtake. The parameter η represents the efficiency of the various components through which the power is transferred from the turbine to the propeller and airflow. The enthalpy ratio over a component is denoted by τ. τ_{λ} is the ratio between the total specific enthalpy behind the combustor ($h_{t,4}$) and the static inflow enthalpy ($h_{s,0}$). The parameters T, p, and R are the temperature, pressure, and gas constant, where the subscripts s and t indicate static or total conditions. The subscripts 0 and 9 correspond to the free-stream conditions and the exhaust exit station, respectively. The gearbox is assumed to be part of the core engine and does not belong to the propulsor, i.e. the propeller.

The results from the parametric and performance analyses help to determine the size and the mass of the engine. The geometry of both the engine nacelle and the engine is determined using relations obtained from the lecture slides by Vos, Melkert, and Zandbergen [146], as specified in Appendix B.4. The same is true for the mass of the engine, where Equation (4.13) is used [147].

$$m_{\text{engine}} = 10\cdot P_{\text{TO}}^{0.266} \tag{4.13}$$

The propeller diameter is found with a similar relation [148]. Note that the propeller size and the rotations per minute (RPM) effects on the propeller efficiency are not taken into account. The propeller efficiency is assumed to be solely dependent on the free-stream Mach number [105, 149]. This propeller efficiency is assumed to be 88% in cruise, which is higher than currently achievable values, however, technological advancements are taken into account [147, 144]. In off-design conditions, the propeller efficiency η_{prop} is modeled as a function of the flight Mach number [105, Appendix K]:

$$\eta_{\text{prop}}(M_\infty) = \begin{cases} 10\cdot M_\infty\cdot\eta_{\text{prop,max}} \text{ if } M_\infty \leq 0.1 \\ \eta_{\text{prop,max}} \text{ if } 0.1 < M_\infty \leq 0.7 \\ \left(1-\frac{M_\infty-0.7}{3}\right)\cdot\eta_{\text{prop,max}} \text{ if } 0.7 < M_\infty \leq 0.85 \end{cases} \tag{4.14}$$

CLASS II MASS ESTIMATION

The Class-II mass estimation updates the OEM of the aircraft using methods that are dependent on the aircraft configuration and size. The aircraft is divided into separate structural groups and each contribution to the aircraft empty mass is estimated separately. Here the weight differences between the design for different objectives due to the different wing, tail, and engine configurations become apparent. Similar to the turbofan-powered aircraft, the methods presented in Torenbeek [34] are used.

The difference with the turbofan configuration is that the aircraft has a high-wing and T-tail instead of a low-wing and conventional tail configuration. The high-wing position increases the mass of the wing-fuselage connection by two-thirds [34]. The main landing gear is stowed in the fuselage, and thus a belly fairing is needed, which adds 7% to the fuselage structural mass. Lastly, the vertical tail needs to be strengthened to accommodate the horizontal tail that is placed on top of the vertical tail. This is accounted for by applying a correction to the specific mass of the vertical tailplane, as elaborated in Section 8.4.1.c of Reference [34].

DIRECT OPERATING COSTS

The cost estimation module estimates the direct operating costs (DOC) of the aircraft. The DOC is calculated based on the methods discussed in Roskam [35]. The DOC is divided into five categories, which are flight costs, maintenance costs, depreciation costs, operational fees, and financing costs. Regarding the flight costs, the main contributors are the fuel and oil costs, and the crew costs. For the latter contribution, the same approach is taken as in Section 3.1.2. Similar to the assumptions for the turbofan aircraft, the fuel price is assumed to be $2.71 per US gallon[5].

The maintenance costs, which are dependent on the utilization of the aircraft, consist of the labor for the airframe and engine and the spare material costs. This requires an estimation of the aircraft price, which is done based on the relation from Section 3.1.2 for the medium-range design case. As the engine has a propeller, its price needs to be added to the price of the engine. Equations (4.15) and (4.16) show the price estimation for both the engine and propeller, respectively.

$$P_{\text{engine},2021} = 3.32 \cdot 2.16 \cdot 10^{6} \cdot (0.533 \cdot \text{sf} + 0.467) \tag{4.15}$$

$$P_{\text{prop},2021} = 3.32 \cdot 10^{0.7746 + 1.1432 \cdot \log_{10}(P_{\text{TO}})} \tag{4.16}$$

Note that the inclusion of the 3.32 factor is the total inflation rate between 1980 and 2021[6]. Also, the scaling factor (sf) is used to incorporate different engine sizes and depends on the shaft horse power (in bhp) divided by 20424 [35, Appendix B2].

For the depreciation costs, the calculations are based on a linear depreciation for the airframe, systems, and engines over 20 years of the usage of the aircraft. Spare parts are also taken into account. Lastly, the finance costs and the fee costs are assumed as a percentage of the total DOC. The finance costs are assumed 7% of the total DOC, while the fee costs are dependent on the MTOM of the designed aircraft [35]. Although these cost contributions are not included in the results in Section 3.3, they are added to the turbofan results to compare the two aircraft types in Section 4.3.2.

---

[5] Obtained from: `https://www.indexmundi.com/commodities/?commodity=jet-fuel&months=60`

[6] URL `https://www.officialdata.org/us/inflation/1980?amount=1` accessed on 19 November 2021

CLIMATE IMPACT EVALUATION

The climate impact evaluation of the turboprop aircraft is performed in the same manner as for the turbofan aircraft. This approach is discussed in Section 3.1.2. In summary, the average temperature response over a period of 100 years is computed using a linearized temperature response model [24] which accounts for the effects due to CO_2, NO_x, soot, and SO_4 emissions, as well as the formation of persistent contrails. An altitude dependency is included in the model for radiative forcing due to NO_x emissions and contrail formation. This forcing factor requires a numeric mission analysis, as briefly described in Section 3.1.2.

4.2. VERIFICATION OF ANALYSIS AND DESIGN METHODS

This section verifies whether the methods to design turboprop-powered aircraft are functioning correctly. The verification of the propulsion module and the aircraft design convergence are discussed in Sections 4.2.1 and 4.2.2, respectively.

4.2.1. TURBOPROP PERFORMANCE MODULE

The propulsion module has to be verified for both the parametric and performance analyses, which are the on-design and off-design point calculations. The paper by Dinç [150] is used to verify the parametric analysis. Additionally, the GasTurb 14 program [7] is used to confirm the correct working of the performance analysis.

The parametric analysis in the paper of Dinç [150] considers various mission conditions for the on-design point. The percentage differences between the paper and the implemented model lie between -2% and 5% for all ten different mission settings. Figure 4.3 shows the differences between the results obtained with the model and the data presented in the paper by Dinç [150]. This difference is seen as acceptable in this conceptual study. The largest errors are attributed to the fact that not all values for the input parameters are known. Therefore, some input parameters had to be estimated.

The second parametric analysis verification is performed with the GasTurb 14 program, of which the input parameters are found Table 4.2. The result of the on-design verification is observed in the second column of Table 4.3. The data shows good agreement, as the maximum absolute difference percentage is less than 1%, which is accurate enough for the conceptual design phase considered in this study.

The performance analysis is quite crucial since it is used much more often during the numerical mission analysis in the climate impact evaluation. The engine parameters in the second and third columns of Table 4.2 are used to determine the off-design point performance of the engine. The results are shown for both analyses in Table 4.3. For the two different off-design points, the overall percentage difference for the first mission is between -2.9% and 3.2%. For the second mission, the differences lie between -2.4% and +2.2%. This is quite accurate given the conceptual design stage which assumes constant component efficiencies.

---

[7] URL `https://www.gasturb.com/` accessed on 15 September 2023

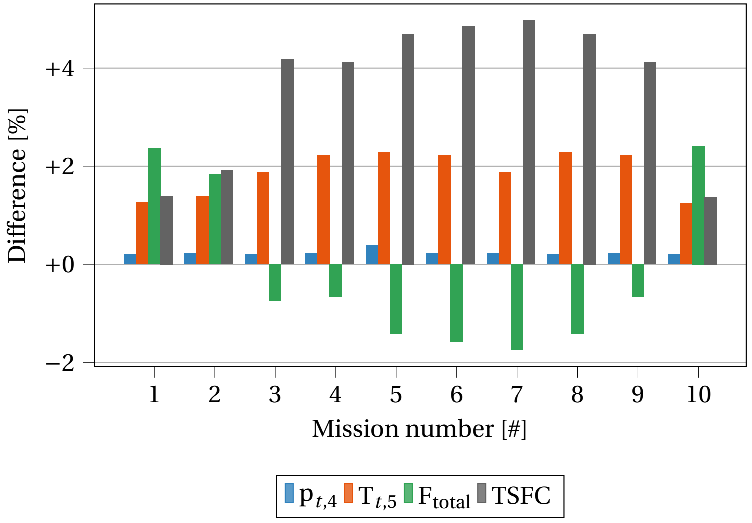

Figure 4.3: Parametric analysis verification of four engine parameters with data provided in the paper by Dinç [150]

Table 4.2: Input parameters for the Gasturb parametric and the two performance analysis verification

Input Parameter	On-Design	Off-Design 1	Off-Design 2
Π_c [-]	15	NA	NA
M [-]	0.6	0.1	0.3
TET [K]	1450	1450	1500
h [km]	6.0	0.0	3.0
$p_{s,\text{amb}}$ [kPa]	47.1	101.3	70.1
$T_{s,\text{amb}}$ [K]	249	288	269

4.2.2. AIRCRAFT SYNTHESIS VERIFICATION

The verification of the multidisciplinary aircraft design loop is completed by comparing the aircraft geometric aspects and weights of reference aircraft to those predicted by the model. The reference aircraft are the ATR 72-600 and the De Havilland Canada Dash 8-400. The top-level aircraft requirements of both aircraft are summarized in Table A.5. For the Dash 8 aircraft, it is important to note that an extra five meters were added to the length of the fuselage cabin to incorporate the extra length in the cabin, which does not seem to be present in other turboprop aircraft [151].

Table 4.4 shows the overview of the values for the ATR 72[8] and the Dash 8 [151]. The table shows the three main mass groups, the wing area, and fuselage diameter and length for both aircraft. The presented values differ by a maximum of 4.3% for the OEM of the

---

[8] URL `https://customer.janes.com/JAWADevelopmentProduction/Display/JAWA0440-JAWA` accessed on 21 September 2021

Table 4.3: Turboprop engine performance verification for GasTurb on-design and two off-design points

(a) On-design Performance

Parameter [Unit]	**Framework**	**GasTurb**	**Difference [%]**
T_{T5} [10^3K]	0.81	0.81	+0.14
p_{T5} [kPa]	265	265	+0.15
$\dot{m}_0$ [10^3 kg/s]	NA	NA	NA
TSFC [kg/(N s)]	1.27×10^{-5}	1.26×10^{-5}	+0.78
F_{total} [kN]	5.9	5.9	-0.77

(b) Off-Design Performance 1

Parameter [Unit]	**Framework**	**GasTurb**	**Difference [%]**
T_{T5} [K]	0.87	0.86	+0.93
p_{T5} [Pa]	110	110	+0.94
$\dot{m}_0$ [10^3 kg/s]	4.52	4.51	+0.13
TSFC [kg/(N s)]	4.14×10^{-5}	4.01×10^{-5}	+3.2
F_{total} [kN]	26.0	27.3	+4.8

(c) Off-Design Performance 2

Parameter [Unit]	**Framework**	**GasTurb**	**Difference [%]**
T_{T5} [K]	0.87	0.86	+0.77
p_{T5} [Pa]	78.9	78.6	+0.43
$\dot{m}_0$ [10^3 kg/s]	3.79	3.79	-0.17
TSFC [kg/(N s)]	7.12×10^{-5}	6.90×10^{-5}	+2.8
F_{total} [kN]	13.6	13.9	-2.5

ATR 72, which is deemed within the limits for validation. The values of the Dash 8 are more accurate with a maximum absolute percentage difference of 1.6%.

The mission performance of the aircraft is also of interest. The payload-range diagram is used for the verification of the performance. The diagrams are shown in Figure 4.4a and Figure 4.4b for the ATR 72 and Dash 8 [151], respectively. Overall, good similarity is achieved, especially for the ATR up until the point where maximum fuel mass is reached. After this point, the slope is underestimated. For the Dash 8 aircraft, the increase in range according to a payload mass reduction is underestimated. The maximum range, however, is quite accurately determined.

4.3. RESULTS AND DISCUSSION

This section discusses the results of the optimization performed for the three distinct objective functions. In addition, these propeller-powered aircraft to their turbofan counterparts. The aircraft design case is the same as in Chapter 3. The top-level aircraft re-

Table 4.4: Validation of ATR 72-600 and Dash 8-400 designs with MDO framework

(a) ATR 72-600

Parameter [Unit]	**Framework**	**Reference**	**Diff. [%]**
MTOM [metric tons]	23.6	23.0	+2.6%
OEM [metric tons]	13.9	13.3	+4.3%
Fuel Mass [metric tons]	2.2	2.19	+1.5%
Wing area S [m^2]	62.7	61.0	+3.5%
Fuselage outer diameter d_{fus} [m]	28.0	27.2	+3.1%
Fuselage length l_{fus} [m]	2.82	2.9	-2.4%

(b) DHC-8 400

Parameter [Unit]	**Framework**	**Reference**	**Diff. [%]**
MTOM [metric tons]	27.5	27.6	-0.3%
OEM [metric tons]	17.1	17.1	+0.2%
Fuel Mass [metric tons]	2.6	2.61	-1.3%
Wing area S [m^2]	62.1	63.1	-1.5%
Fuselage length l_{fus} [m]	33.4	32.8	+1.6%
Fuselage outer diameter d_{fus} [m]	2.74	2.69	+1.5%

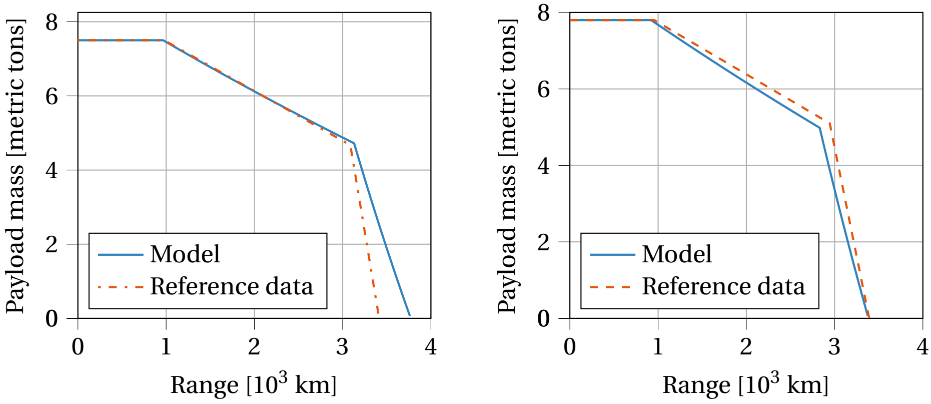

(a) ATR 72-600 (M_{cr}=0.44, h_{cr}=5.18 km)

(b) Dash 8-400 (M_{cr}=0.53, h_{cr}=7.62 km)

Figure 4.4: Comparison between payload-range diagrams obtained with the MDO framework (blue lines) and the reference diagrams (dashed orange lines)

quirements specify a medium-range, narrow-body aircraft. The fuel burn, emissions, and cost are evaluated for a mission with 130 passengers (100 kg per passenger) and a block range of 1852 km or 1000 nmi. A hypothetical, multi-year scenario is considered to compute the objectives. In this scenario, the production of this aircraft type starts in 2020 and continues until 2050. The year 2020 is also the first year in the 100-year time-frame considered in the average temperature response. Each individual aircraft has a lifetime of 35 years, resulting in a complete fleet retirement by 2085. In this scenario, a constant productivity (RPK/year) is assumed, independent of the objective, allowing the fleet size to vary between objectives.

4.3.1. OPTIMIZATION RESULTS

Employing the above case setup, the propeller aircraft are optimized separately for their operating cost (DOC), fuel mass (FM), and global warming impact (ATR_{100}). Table 4.5 shows the optimization results for these three objectives. The columns correspond to an aircraft optimized for the objective specified in the header. The rows present the numeric value of the KPI in the leftmost column. Interestingly, the results for the fuel- and climate-optimal aircraft are nearly identical, even when non-CO_2 effects are considered. This result is different from the turbofan aircraft design solutions, where the two objectives appear to be conflicting. When shifting from the DOC objective to the fuel mass or climate objective, a reduction in ATR_{100} of 15.9% can be obtained. In addition, the mission fuel mass is reduced by 15.5%. However, this change in design comes at a penalty of 21% in direct operating costs.

Table 4.5: Optimized objective functions for medium-range, turboprop aircraft

Parameter [Unit]	$\mathbf{ATR_{100}}$	**DOC**	**Fuel Mass**
ATR [mK]	7.4^* (-)	8.8 (+18%)	7.4 (0.0%)
DOC [USD/seat-nmi]	0.23 (+21%)	0.19^* (-)	0.23 (+21%)
m_{fuel} [kg]	4.9×10^3 (0.0%)	5.8×10^3 (+18%)	$4.9 \times 10^{3*}$ (-)

The difference in objective function values is a direct consequence of the chosen design variable values. An overview of the design variables for each optimal design is shown in Table 4.6. In the overview the overlap between the fuel- and climate-optimal aircraft is evident. The main differences with the DOC-optimal solution are the cruise altitude and cruise Mach number. The higher Mach number results in lower block time, reducing the crew costs. As a consequence, the cruise altitude is increased to reduce the drag during the cruise phase and maintain a suitable lift-to-drag ratio. The wing loading and aspect ratio are limited for all objectives, by the approach speed and span constraints, respectively. An even higher aspect ratio is desired, but cannot be selected due to the span constraint of 36 m. The compressor pressure ratio achieves the upper bound. Furthermore, the engine design point is taken at cruise and therefore the higher TET for the DOC objective is due to the relatively lower throttle setting with the constraining TET at take-off. This enables a higher TET in the cruise segment.

The aircraft characteristics of the three optimal solutions are gathered in Table 4.7. The differences between the fuel- and climate-optimal aircraft are minor, e.g. in the MTOM, OEM, and wing area. It is expected that these differences are due to the numerical setup of the aircraft design convergence and optimization. Due to the increase in cruise Mach number, the block time of the DOC-optimal aircraft is significantly lower than for the other two aircraft, which also reduces the maximum number of aircraft required in the fleet, $N_{ac,max}$. Figure 4.5 Compares the top-view geometries of the three dif-

Table 4.6: Optimal design variables values for the medium-range, turboprop aircraft

Design Variable	**ATR_{100}**	**DOC**	**Fuel Mass**
A [-]	13.9	12.0	13.9
W/S [kN/m^2]	5.84	5.84	5.84
Π_c [-]	$\overline{25}$	$\overline{25}$	$\overline{25}$
TET [K]	1415	1564	1412
h_{cr} [km]	5.0	7.5	4.8
M_{cr} [-]	0.40	0.61	0.39

ferent aircraft. The largest differences between the DOC-optimal aircraft and either the fuel- or climate-optimal solutions are the span, the propeller diameter, and the nacelle size. However, as all aircraft fly relatively low Mach number, no wing sweep is required. This causes the wing planform to be nearly identical for all objectives.

Table 4.7: Performance indicators of optimized medium-range, turboprop aircraft

Parameter	**ATR_{100}**	**DOC**	**Fuel Mass**
MTOM [metric ton]	55.3	58.1	55.2
OEM [metric ton]	28.5	30.1	28.6
S [m^2]	93	97	92
W/P [N/W]	0.053	0.043	0.053
$TSFC_{cruise}$ [kg/(N s)]	0.76×10^{-5}	1.1×10^{-5}	0.77×10^{-5}
t_{block} [hrs]	5.3	3.9	5.2
$N_{ac,max}$ [10^3]	22.1	16.4	22.0
$EI_{NO_x,cruise}$ [kg/kg]	0.011	0.0098	0.011

Figure 4.6 presents the temperature response ΔT of each optimized aircraft design over the 100 years under consideration. The fuel- and climate-optimal aircraft have a nearly identical temperature response. Blue and green dots have been added to clarify this overlap. From the shape of the temperature response and the analysis of the contribution of each climate agent to the ATR_{100}, it is clear that the main contribution for low-flying propeller aircraft follows from fuel proportional emissions and long-lived species, which indicates CO_2 effects are dominant. CO_2 emissions are characterized by a constant emission index and are altitude independent [152, 153]. Also, water vapor emissions contribute to the climate impact. Although the radiative effect of H_2O varies with altitude, this is not modeled in the current analysis. Nevertheless, due to low cruise altitude, the effects due to H_2O are expected to be short-term and small compared to the contribution of CO_2. Since both CO_2 and H_2O emissions scale linearly with fuel consumption, the higher temperature response of the DOC-optimal aircraft is noticeable in Figure 4.6.

The climate impact of NO_x is more complex. The difference in EI_{NO_x} for the objectives is caused by different atmospheric conditions, namely temperature and pressure which vary with cruise altitude. While the total emitted NO_x is similar for the three op-

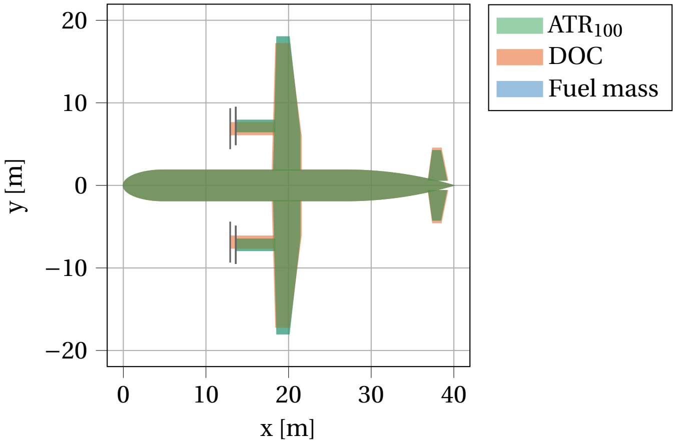

Figure 4.5: Optimal aircraft geometry comparison for the medium-range design case, assuming constant productivity

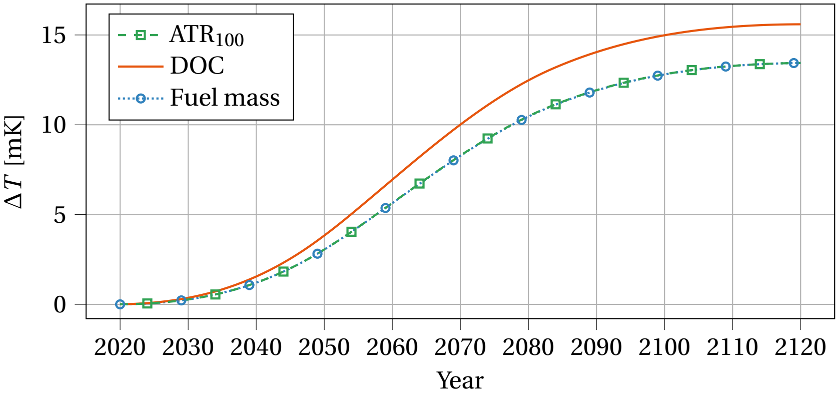

Figure 4.6: Sea-level temperature change for the medium-range, turboprop aircraft

timized aircraft, the effects of the DOC-optimal aircraft are more significant due to the altitude forcing factor [24]. This is true for the cooling and warming effects of NO_x.

The last climate effect is the formation of contrails. Due to the relatively low cruise altitude of all three turboprop-powered aircraft, the conditions for contrail formation (see Section 3.1.2) are not met for the aircraft considered here. Hence, the contribution of contrails is zero for the three aircraft considered here. Under certain conditions, non-persistent contrails may form, but it is assumed these have no direct influence on the climate. Combining both the knowledge that the NO_x effects are minimal and that persistent contrails do not form in the current case study, this leads to the conclusion that the climate impact is caused by fuel-proportional CO_2 emissions. Hence, in the current optimization structure, minimum fuel mass leads directly to the minimum climate impact as well for turboprop aircraft.

Shifting between the objectives does not only have an impact on the objective values but also on the necessary fleet size as the block time changes with the selective objective function (Table 4.7). The constant productivity setup results in more aircraft for the fuel mass and ATR objectives. The fleet size and constant productivity over the time horizon of 100 years are illustrated in Figure 4.7a. This results in a maximum fleet size of approximately 22.0 aircraft for both the fuel and climate objectives and 16.4 thousand aircraft for the DOC objective. This is a difference of 5.6 thousand aircraft or an increase of 34% between the DOC and the other objectives. To put this into perspective, the production rate of the A320 is approximately 540 aircraft per year[9]. Note that the increase in produced aircraft also increases the climate impact. However, the assessment of this impact is outside the scope of this analysis.

4.3.2. COMPARISON WITH TURBOFAN AIRCRAFT

To place the results of the optimization into perspective and study which propulsion type is preferred to reduce the global warming impact of aviation, the propeller aircraft are directly compared to their turbofan-powered counterparts. The TLAR, reference mission, and constant productivity scenario are the same as for the propeller aircraft. Table 4.8 shows the direct comparison of the objective functions between the two types of aircraft. From the table, it is clear that generally speaking the turboprop has a lower ATR_{100}, as a reduction of 33% is realized between either climate-optimized aircraft. This is reduced to 20% when comparing the climate-optimal turbofan aircraft to the DOC-optimal turboprop aircraft.

Table 4.8: Objective function values comparison between the optimal turboprop and turbofan aircraft

	Turboprop			**Turbofan**		
Value	**ATR_{100}**	**DOC**	**FM**	**ATR_{100}**	**DOC**	**FM**
m_{fuel} [kg]	$4.9{\cdot}10^3$	$5.8{\cdot}10^3$	$4.9{\cdot}10^3$	$7.7{\cdot}10^3$	$7.7{\cdot}10^3$	$7.2{\cdot}10^3$
DOC [$/seat-nmi]	0.23	0.19	0.23	0.23	0.20	0.22
ATR_{100} [mK]	7.4	8.8	7.4	11	26	26
t_{block} [hrs]	5.3	3.9	5.2	3.9	3.4	3.6
$\text{EI}_{\text{NO}_x,\text{ cr}}$ [kg/kg]	0.011	0.0098	0.011	0.017	0.011	0.025

The cost benefit of the DOC turboprop objective however is not expected. The current cost-benefit contradicts the current utilization of turbofan aircraft on medium-range routes. For that reason, the current cost prediction for the turboprop is likely underestimated, by the current assumptions. However, since the range of the reference mission is relatively short (1852 km), the difference in block time and time-related cost between the two aircraft types is limited. In addition, the propeller efficiency of 88% reduces the fuel costs more than current technology allows. For longer ranges, it is expected that the advantage of the faster cruise flight of turbofan aircraft becomes more apparent. Nevertheless, the cost estimation must thus be looked at critically.

---

[9] URL `https://www.airbus.com/en/newsroom/press-releases/2021-01-airbus-updates-production-rates-in-response-to-market-environment` accessed on 16 January 2022

The difference in block time per mission, as seen in Table 4.8, has a direct consequence on the fleet size of the objectives between the two aircraft types. This is better illustrated in Figure 4.7. This figure shows the difference in fleet size between the objectives for both the turboprop (Figure 4.7a) and the turbofan aircraft (Figure 4.7b). For example, the fuel- or climate-optimal turboprop fleets need approximately 5500 more aircraft than the climate-optimized turbofan objective. Intuitively, this causes an extra climate impact, but that is out of the scope of this study. As this fleet size discrepancy results in a skewed comparison between the two aircraft types, an extra constraint is added in the next section. A block time constraint can limit the maximum block time to four hours and make the climate impact comparison fairer with the current flight times.

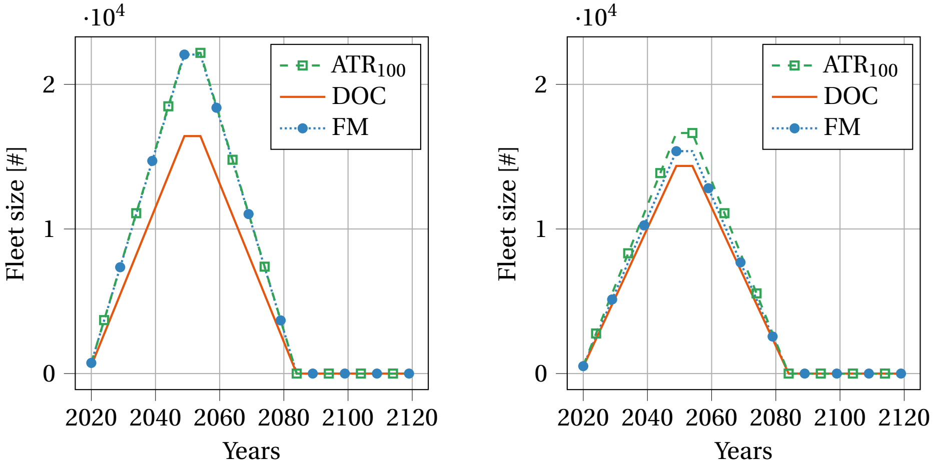

(a) Turboprop aircraft

(b) Turbofan aircraft

Figure 4.7: Fleet size comparison between the turboprop and turbofan aircraft, assuming constant productivity, for the 100-year reference scenario

4.3.3. BLOCK TIME CONSTRAINT

The addition of the block time constraint partly eliminates the large difference in fleet size eminent between the different objectives. Note that the cost-optimal turboprop aircraft remains the same, as the block time per flight is already below four hours. The fuel- and climate-optimal turboprop aircraft change as a result of this constraint.

The new comparison with the turbofan objectives is shown in Table 4.9. Due to the extra block time constraint, there is a clear increase in the fuel mass and ATR_{100} for both the fuel- and climate-optimal turboprop aircraft. For example, the fuel mass for the two objectives is increased from $4.9 \cdot 10^3$ kg to $5.7 \cdot 10^3$ kg, which is still significantly lower than for the fuel-optimal turbofan aircraft. Additionally, the costs per flight are lowered, while the ATR_{100} is increased. Generally speaking, the difference between all turboprop objectives becomes smaller, and more overlap can be observed between the objective values.

The climate impact benefits observed for the turboprop ATR_{100} and fuel mass objec-

Table 4.9: Objective function values comparison between the turboprop aircraft with the block time constraint applied and turbofan aircraft

	Turboprop			**Turbofan**		
Value	**ATR_{100}**	**DOC**	**FM**	**ATR_{100}**	**DOC**	**FM**
m_{fuel} [kg]	$5.7{\cdot}10^3$	$5.8{\cdot}10^3$	$5.7{\cdot}10^3$	$7.7{\cdot}10^3$	$7.7{\cdot}10^3$	$7.2{\cdot}10^3$
DOC [$/seat-nmi]	0.20	0.19	0.19	0.23	0.20	0.22
ATR_{100} [mK]	8.5	8.8	8.6	11	26	26
t_{block} [hrs]	4.0	3.9	4.0	3.9	3.4	3.6
$EI_{NO_x,\,cr}$ [kg/kg]	0.0099	0.0098	0.0099	0.017	0.011	0.025

tives are quite optimistic for current technology levels. One reason is the assumed propeller efficiency of 88% is quite high. A sensitivity analysis is performed in Section 4.4 to study the impact of the assumed propeller efficiency on the results.

When compared to the turbofan objectives, the benefit of utilizing turboprop aircraft is significantly smaller. The benefit in ATR_{100} is reduced to 22%, with a 15% reduction in costs, but, as mentioned, the latter must be looked at critically. The difference in maximum fleet size between the two aircraft types is also reduced and is small between the turboprop aircraft and the climate-optimal turbofan aircraft.

The primary changes to the design variables for the fuel- and climate-optimal design solutions are the cruise altitude and the cruise Mach number. The overview of the design variables is shown in Table 4.10. For the fuel turboprop objective, the higher cruise Mach number changes the cruise altitude as well. The lower air density is better for the higher velocity. The ATR_{100}-optimal turboprop aircraft has a lower cruise altitude to decrease the effect of NO_x. The overall difference between them is however minimal.

Table 4.10: Optimal design variables for the turboprop aircraft with the block time constraint applied

Design Variable	**ATR_{100}**	**DOC**	**FM**
W/S [kN/m^2]	5.84	5.84	5.84
A [-]	13.1	12.1	13.3
TET [K]	1501	1564	1520
Π_c [-]	$\overline{25}$	$\overline{25}$	$\overline{25}$
h_{cr} [km]	7.2	7.5	8.2
M_{cr} [-]	0.58	0.61	0.60

The temperature change over the time horizon of 100 years is compared in Figure 4.8. The long-term CO_2 effects have increased due to the increase in fuel consumption. Regarding NO_x, the increase in cruise altitude results in a higher forcing factor for all NO_x effects and thus a higher contribution to ATR_{100} per kilogram of fuel. Even though the cruise altitude has increased, persistent contrails do not form at the selected altitude and thus still do not contribute to the temperature increase for the turboprop aircraft.

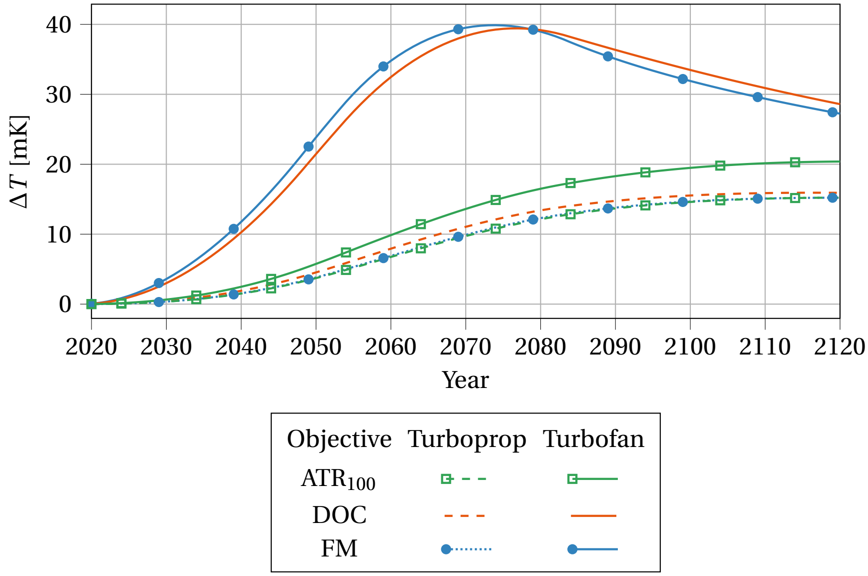

Figure 4.8: Sea-level temperature change comparison between the turboprop aircraft with the block time constraint applied, and the turbofan aircraft

4.4. SENSITIVITY ANALYSIS

The performance of the turboprop aircraft in the previous section showed an optimistic benefit from utilizing the turboprop aircraft on the medium-range route. To put these results into perspective, a sensitivity analysis is performed in this section. This analysis is completed for the standard turboprop aircraft optimization and the optimization with the block time constraint. The maximum propeller efficiency is varied between 70% and 90%. This gives a distinct range and clarifies the impact the propeller efficiency has on the objective values and the design variables.

The impact of the propeller efficiency on the design variables and objective values is shown in Table 4.11. The impact of the propeller efficiency is clear: as the propeller becomes more efficient, the aircraft performs better in all objectives. The mission fuel mass, the direct operating cost, and the climate impact all decrease with increasing propeller efficiency. It is interesting to see that to have a comparable climate impact to that of the ATR$_{100}$ turbofan aircraft, a propeller efficiency of approximately 75% is required. This gives a threshold that needs to be met to have a lower climate impact than turbofan-powered aircraft.

Considering the design variables shown in Table 4.11, the differences appear to be limited. The climate-optimal cruise conditions are independent of the propeller efficiency and thus are constant. The aspect ratio and the TET however both increase with an increase in propeller efficiency. The latter is caused by the easier conversion from propeller power to thrust and thus a lower throttle setting is needed during the take-off segment. This allows for a higher TET during the cruise segment. The increase in aspect ratio with increasing propeller efficiency is due to the reduction of wing area as a result

Table 4.11: The objective functions and design variables for the climate-optimal turboprop aircraft for various propeller efficiencies

Paremeter	$\eta_{\mathbf{prop}}$ = **70%**	**75%**	**80%**	**85%**	**88%**	**90%**
ATR_{100} [mK]	12	11	9.4	8.0	7.4	7.0
DOC [$/seat-nmi]	0.28	0.26	0.25	0.24	0.23	0.22
m_{fuel} [kg]	$9.6 \cdot 10^3$	$7.5 \cdot 10^3$	$6.4 \cdot 10^3$	$5.4 \cdot 10^3$	$4.9 \cdot 10^3$	$4.7 \cdot 10^3$
W/S [kN/m^2]	5.8	5.8	5.8	5.8	5.8	5.8
A [-]	11.2	12.1	12.9	13.6	13.9	14.1
TET [K]	1402	1407	1412	1414	1415	1416
Π_c [-]	25	25	25	25	25	25
h_{cruise} [km]	5.0	5.0	5.0	5.0	5.0	5.0
M_{cruise} [-]	0.40	0.40	0.40	0.40	0.40	0.40

of lower fuel and total aircraft mass, in combination with the active span constraint.

With the block time constraint applied to the optimization, as shown in Table 4.12, the same trends are observed as seen in Table 4.11. Interestingly, the propeller efficiency threshold to perform better than the turbofan alternative has shifted from 75% to 80%.

Table 4.12: The objective functions and design variables for the climate-optimal turboprop aircraft with the block time constraint applied, for various propeller efficiencies

Paremeter	$\eta_{\mathbf{prop}}$ = **70%**	**75%**	**80%**	**85%**	**88%**	**90%**
ATR_{100} [mK]	14	12	11	9.3	8.5	8.1
DOC [$/seat-nmi]	0.25	0.23	0.21	0.20	0.20	0.19
m_{fuel} [kg]	$11 \cdot 10^3$	$8.7 \cdot 10^3$	$7.3 \cdot 10^3$	$6.2 \cdot 10^3$	$5.7 \cdot 10^3$	$5.3 \cdot 10^3$
W/S [kN/m^2]	5.8	5.8	5.8	5.8	5.8	5.8
A [-]	10.8	11.7	12.4	12.9	13.2	13.5
TET [K]	1510	1528	1540	1550	1555	1560
Π_c [-]	25	25	25	25	25	25
h_{cruise} [km]	7.4	7.4	7.4	7.4	7.4	7.4
M_{cruise} [-]	0.59	0.59	0.59	0.59	0.59	0.59

4.5. CONCLUSIONS

The objective of this chapter is to study the potential for turboprop engines on medium-range aircraft to further reduce the climate impact while monitoring the effect on operating cost and fuel consumption. The conceptual, multidisciplinary aircraft design framework is extended to analyze turboprop engines and to perform the initial sizing according to the weight-to-power ratio instead of the thrust-to-weight ratio. The turboprop thermodynamic models is verified with data from literature and a gas turbine performance tool, showing a maximum error of approximately 4% in TSFC. The overall aircraft design routine is validated with data from the ATR 72-600 and Dash-8 400 aircraft, showing good agreement in terms of masses, performance, and geometry.

As hypothesized, turboprop-powered aircraft can indeed yield a further reduction in ATR_{100} when compared to the turbofan aircraft. In comparison with the cost-optimal turbofan aircraft from Chapter 3, the climate-optimal turboprop offers a reduction of approximately 71%, which is a 14% further improvement than the climate-optimal turbofan aircraft. This reduction is possible if no constraint is imposed on the block time. When the block time is constrained to that of the climate-optimal turbofan aircraft, this reduction of 71% with respect to the cost-optimal turbofan aircraft shrinks to 67%. The decrease in climate impact of turboprop aircraft is attributed to a reduction in long-term CO_2 effects. The associated fuel consumption reduction also leads to a decrease in operating cost.

While in Section 3.3 it was concluded that the fuel and climate objectives are conflicting for turbofan aircraft, the fuel- and climate-optimal turboprop aircraft are rather similar. This is because the climate impact of turboprop aircraft is dominated by the long-term CO_2 effect which relates directly to fuel consumption. The contribution of non-CO_2 effects is lower due to the lower cruise altitude of all turboprop aircraft.

These results rely on an assumed propeller efficiency of 88%, which is higher than what currently available propeller technology offers. Therefore, this parameter is varied between 70% and 90% to study the influence on the results. This sensitivity analysis shows a clear improvement in all objectives (fuel mass, cost, and climate impact) with improved propeller efficiency. A propeller efficiency of at least 75% to 80% is needed to have a turboprop aircraft which has a lower climate impact than a turbofan counterpart.

Two recommendations for future research can be derived from the study in this chapter. First, the optimizations show that the compression ratio always reaches the upper bound of 25. This bound is set according to currently available turboprop technology. Nevertheless, since higher overall pressure ratios can be achieved in turbofan engines, the application of these compressors in turboprop engines should be further explored to maximize the potential of turboprop engines on climate-optimized aircraft.

Second, without the block time constraint, the climate- and fuel-optimal turboprop aircraft feature a mission block time of more than five hours on an 1852 km route. Since this block time is considerably higher than that of the cost-optimal turbofan aircraft (approximately 3.4 hours), other modes of transport should be added to the comparison. Depending on the region and the available infrastructure, the door-to-door time of a climate-optimal turboprop aircraft may be similar to that of a train, for example.

5

HYDROGEN, MEDIUM-RANGE AIRCRAFT DESIGN OPTIMIZATION

This chapter focuses on the design optimization of liquid hydrogen aircraft and their performance in terms of climate impact, cash operating cost, and energy consumption. The multidisciplinary design framework for kerosene-powered aircraft is extended to design liquid hydrogen-powered aircraft at a conceptual level. A hydrogen tank is integrated into the aft section of the fuselage, increasing the operating empty mass and wetted area. Furthermore, the gas model of the engine is adapted to account for the hydrogen combustion products. It is concluded that for medium-range, narrow-body aircraft using hydrogen technology, the climate impact can be minimized by flying at an altitude of 6.0 km at which contrails are eliminated and the impact due to NO_x *emissions is expected to be small. However, this leads to a deteriorated cruise performance in terms of energy and operating cost due to the lower lift-to-drag ratio (-11%) and lower engine overall efficiency (-10%) compared to the energy-optimal solutions. Compared to cost-optimal kerosene aircraft, the average temperature response can be reduced by 73% to 99% by employing liquid hydrogen, depending on the design objective. However, this reduction in climate impact leads to an increase in cash operating cost of 28% to 39% when considering 2030 hydrogen price estimates. Nevertheless, an analysis of future kerosene and hydrogen prices shows that this cost difference can be significantly decreased beyond 2030.*

Parts of this chapter have been published in CEAS Aeronautical Journal, 2024, Proesmans and Vos [154].

CHAPTER 3 investigated the potential to reduce the global warming impact of kerosene aircraft through optimization of airframe, engine, and mission variables. It was shown that the objectives of operating cost, fuel mass, and climate impact are conflicting and that flying lower and slower is key to reducing the burden of non-CO_2 effects. Nevertheless, the climate impact reduction of kerosene aircraft, even at low altitudes, is limited by the emissions of CO_2 causing long-term warming.

Hydrogen fuel can provide a more sustainable alternative if it is produced from sustainable energy sources. It eliminates the emissions of carbon dioxide, as well as sulfate and soot particles [155]. Acknowledging the remaining uncertainty, several research projects examined the potential climate impact reduction of hydrogen aircraft. Svensson, Hasselrot, and Moldanova [156] estimated that the Global Warming Potential (GWP) of medium-range aircraft can be reduced by approximately 15% and that in particular flying lower has a notable impact since it prevents contrail formation. In research by Ponater et al. [119], three transition scenarios towards cryoplane technology are assessed. Here, it was concluded that, depending on the scenario, a decrease in surface temperature change of 5 to 15% is possible compared to the kerosene reference scenario.

Both studies considered the increase in water vapor (H_2O) emissions, potential reduction in NO_x discharge, and change in contrail properties. The main contrail properties of interest in these studies were the optical depth and lifetime. The alteration of these contrail properties is caused by the lack of soot particles in the exhaust plume, as examined by Ström and Gierens [157]. From these insights, Marquart et al. [158] further analyzed the radiative effect of contrails and formed the conclusion that the decreased optical thickness can counteract the increased formation frequency due to increased water vapor emissions, although the net effect is still uncertain. More recently, Burkhardt, Bock, and Bier [73] further studied the relation between contrail radiative forcing and initial ice particle number.

Despite this opportunity for significant climate impact reduction, the integration of liquid hydrogen into the existing tube-and-wing concept and its operations does not come without hurdles. First of all, there is the need to store the liquid hydrogen in cryogenic tanks, which require a (near) cylindrical shape to efficiently deal with the pressure differential and the application of insulation material [159]. Furthermore, liquid hydrogen has a low volumetric energy density (approximately 8496 $\mathrm{MJ/m^3}$ compared to 34 511 $\mathrm{MJ/m^3}$ for kerosene [155]), and thus requires a noteworthy volume. These two aspects, shape and volume, practically eliminate the option of storing liquid hydrogen in the relatively thin, high-subsonic wings of commercial aircraft.

The impact of hydrogen propulsion and tank integration on aircraft characteristics and performance has been studied in several research projects. Hydrogen (sub-)system design and analysis are covered in the studies by Brewer [160]. Furthermore, extensive system analyses of hydrogen aircraft were performed in the CRYOPLANE project [161]. It was concluded that the overall energy consumption and the operating empty mass of hydrogen aircraft are higher than the kerosene alternatives, while the net effect on the aircraft's maximum take-off mass is dependent on the category. The ratio OEM/MTOM increases since the higher specific density of hydrogen allows a reduction in fuel mass. Similar trends are observed in the studies by Verstraete [162]. Multiple tank integration options are available and discussed in References [155, 159, 162, 163].

Although much of the cited work investigates the impact of hydrogen on climate impact, research into the conceptual design space exploration and optimization of hydrogen aircraft, with a holistic evaluation of the climate impact, performance, and cost, appears to be missing. It is essential to re-evaluate the trade-off between these different design objectives and find the associated design trends for this new energy carrier. Therefore, this chapter examines the design of hydrogen aircraft for three objectives and compares these concepts with their kerosene alternatives. This chapter targets research question 3 introduced in Section 1.4. Considering a hydrogen-powered, turbofan aircraft with the same top-level requirements and mission as the medium-range, kerosene aircraft:

1. Which set of airframe, engine and mission design variables minimizes the global warming impact and cash operating costs?
2. What is the difference in climate impact, cash operating costs and other flight performance-related parameters when compared to the kerosene alternative?

These questions provide insight the design space of hydrogen aircraft to further reduce the climate impact and the trade-off with energy and operating costs. Since the climate impact of hydrogen emissions and the cryogenic tank technology carry uncertainties, this chapter also studies the influence of uncertain input parameters on the objective values. Additionally, the competitiveness of hydrogen aircraft, in comparison with kerosene counterparts, is assessed as a function of the hydrogen fuel price.

This chapter adheres to the following structure: Section 5.1 outlines the optimization problem and discusses the MDAO framework. The validation of the hydrogen gas model is provided in Section 5.2. Section 5.3 presents the results of the optimization study and compares the two fuel alternatives. Since the conceptual approach includes several assumptions and uncertainties, an assessment thereof is made in Section 5.4. Finally, Section 5.5 presents the conclusions and provides suggestions for further research.

5.1. PROBLEM FORMULATION AND METHODS

Optimized hydrogen aircraft are found by employing multidisciplinary design optimization. For kerosene aircraft, such a framework is introduced in Section 3.1. In this chapter, the MDO routine is extended to design and analyze liquid hydrogen aircraft in a conceptual design stage. In this section, first, the optimization problem and MDO architecture are formulated. Subsequently, the individual disciplines are elaborated in Section 5.1.2, with a focus on the modifications for the hydrogen-powered aircraft.

5.1.1. OPTIMIZATION PROBLEM FORMULATION

The three single objectives are the climate impact measured by the average temperature response (ATR_{100}), the cash operating cost (COC), and the energy consumption (E_{fuel}). Due to the large difference in calorific value between kerosene and liquid hydrogen, the energy consumption rather than the fuel mass is selected as the optimization objective. Nevertheless, setting the energy or fuel burn as an optimization objective does yield the same design since the two objectives are linearly related by the respective calorific value. This yields the following optimization problem definition:

$$\begin{aligned}
\underset{\mathbf{x}}{\text{minimize}} \quad & F(\mathbf{x}) = \mathrm{ATR}_{100}(\mathbf{x}) \;\text{ or }\; \mathrm{COC}(\mathbf{x}) \;\text{ or }\; \mathrm{E}_{\mathrm{fuel}}(\mathbf{x}) \\
\text{subject to} \quad & W/S \leq \frac{1}{2}\rho_0 \left(\frac{v_{\mathrm{app}}}{1.23}\right)^2 C_{L_{\max}} f_{\mathrm{W}}, \\
& b \leq b_{\max}, \\
& \mathrm{TET}_{\mathrm{TO}} \leq \mathrm{TET}_{\mathrm{TO,\,max}}, \\
& \mathrm{OPR} \leq \mathrm{OPR}_{\max}, \\
& \Pi_{\mathrm{fan,\,TO}} \leq \Pi^U_{\mathrm{fan}}, \\
& \Pi_{\mathrm{LPC,\,TO}} \leq \Pi^U_{\mathrm{LPC}}, \\
& \Pi_{\mathrm{HPC,\,TO}} \leq \Pi^U_{\mathrm{HPC}}, \\
& C_{L_{\mathrm{cr}}} \leq \frac{C_{L_{\mathrm{buffet}}}}{1.3} = \frac{0.86 \cdot \cos\Lambda_{0.25}}{1.3}, \\
& x_i^L \leq x_i \leq x_i^U \qquad\qquad \text{for } i = 1, 2, \ldots, 9
\end{aligned} \tag{5.1}$$

This problem aims to find the design vector **x**, defined by the nine variables in Table 5.1, which minimizes one of these objectives or forms a Pareto-optimal point in the multi-objective case. The nine variables are divided into three categories. First, two variables are related to the airframe, being the aspect ratio (A) and wing loading at take-off (W/S). Note that, compared to the optimization definition in Section 3.1.1, $C_{L_{\max}}$ is removed from the design vector. Second, five design variables define the turbofan engine design cycle at top-of-climb, namely the bypass ratio (BPR), pressure ratios of the fan, low-pressure compressor (LPC), and high-pressure compressor (HPC), and the turbine entry temperature (TET). Finally, the initial cruise altitude (h_{cr}) and the cruise Mach number (M_{cr}) influence the mission profile. Table 5.1 also provides the upper and lower bounds employed in the current and following chapters. These are selected based on current technological and operational limitations, while also considering the assumptions made in the conceptual methods.

Table 5.1: Design variables and their respective bounds

Variable	**Description [Unit]**	**Lower Bound ($\mathbf{x}^L$)**	**Upper Bound ($\mathbf{x}^U$)**
W/S	Wing loading [kN/m^2]	3.00	6.50
A	Aspect ratio [-]	7.00	12.0
BPR	Bypass ratio [-]	6.00	11.0
Π_{fan}	Fan pressure ratio [-]	1.30	1.80
Π_{lpc}	LPC pressure ratio [-]	1.20	1.80
Π_{hpc}	HPC pressure ratio [-]	15.0	25.0
TET	Turbine entry temperature [K]	1350	1700
h_{cr}	Initial cruise altitude [km]	6.00	12.0
M_{cr}	Cruise Mach number [-]	0.50	0.90

The design space is confined by eight inequality constraints, denoted by vector **g** in Figure 5.1. The first constraint in Equation (5.1) ensures that the selected wing loading is low enough to meet the minimum approach speed v_{app}, which is set to 70.0 m/s [128]. The value of the maximum lift coefficient ($C_{L_{\max}}$) is derived from the wing quarter-chord sweep, as discussed in the aerodynamics section below. A correction is included to consider that the maximum approach mass is lower than the MTOM. To formulate the constraint for the wing loading at take-off, it is assumed that the maximum approach or landing mass is 12% ($f_{\text{W}} = 1/0.88$) and 4% ($f_{\text{W}} = 1/0.96$) lower than the take-off mass for the kerosene and hydrogen aircraft, respectively. For kerosene aircraft, this fraction is determined from Airbus A320 mass data [128]. For hydrogen aircraft, f_{W} is set such that a similar amount of energy is on board of the aircraft at landing as for the kerosene counterpart. The second constraint limits the wing span b to 36 m, which is the upper limit for aircraft belonging to the ICAO 4C category. Thirdly, the maximum turbine entry temperature at take-off (ISA+15), $\text{TET}_{\text{TO, max}}$, is restricted to 2000 K according to Mattingly, Heiser, and Pratt [105]. The fourth constraint limits the overall pressure ratio (OPR) at top-of-climb to 60. Additionally, the pressure ratios of the fan, LPC, and HPC in take-off are also constrained by the upper boundaries set in Table 5.1. The final constraint prevents the aircraft lift coefficient in cruise from reaching the buffet onset condition. The regulations stipulate that the maximum lift coefficient achieved at any point in flight should be 30% lower than the one at which buffet occurs. The relation is derived from the buffet onset boundaries collected by Obert [107].

The extended design structure matrix in Figure 5.1 presents how the disciplines are connected, which data is shared between them, and the computational order of execution. At the core of the framework is the convergence loop which produces consistent aircraft designs in terms of mass for a design vector provided by the optimization module and a fixed set of TLARs. For each aircraft design, the climate impact, operating costs, and constraints are evaluated (steps 6 to 8) to update the design vector. The airframe and propulsion modules consist of subroutines. For the airframe including a cryogenic hydrogen tank, this subroutine is presented in Figure 5.2. The working principle of the propulsion framework is the same as in Figure 3.4. Although the XDSM in Figure 5.1 is similar for both aircraft types, the individual disciplines differ.

The optimizations are performed with the help of modeFRONTIER software. The single-objective optimizations are performed using a combination of design of experiments and the Nelder-Mead algorithm (termination accuracy of 1×10^{-5} and maximum 2000 function evaluations with automatic restart), while the multi-objective results are obtained using the pilOPT approach. Appendix C.2 provides further details about the optimization algorithm, and convergence and constraint criteria.

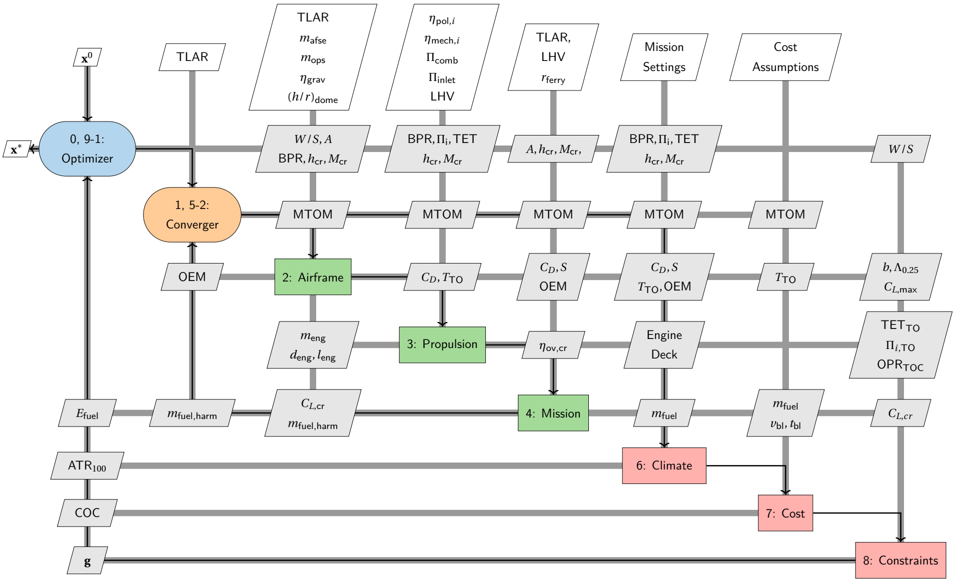
$\mathbf{x}^0$
TLAR
TLAR
m_{afse}
m_{ops}
η_{grav}
$(h/r)_{\text{dome}}$
$\eta_{\text{pol},i}$
$\eta_{\text{mech},i}$
Π_{comb}
Π_{inlet}
LHV
TLAR,
LHV
r_{ferry}
Mission
Settings
Cost
Assumptions
$\mathbf{x}^*$
0, 9-1:
Optimizer
$W/S, A$
BPR, $h_{\text{cr}}, M_{\text{cr}}$
BPR, Π_{i}, TET
$h_{\text{cr}}, M_{\text{cr}}$
$A, h_{\text{cr}}, M_{\text{cr}},$
BPR, Π_{i}, TET
$h_{\text{cr}}, M_{\text{cr}}$
W/S
1, 5-2:
Converger
MTOM
MTOM
MTOM
MTOM
MTOM
OEM
2: Airframe
C_D, T_{TO}
C_D, S
OEM
C_D, S
T_{TO}, OEM
T_{TO}
$b, \Lambda_{0.25}$
$C_{L,\max}$
m_{eng}
$d_{\text{eng}}, l_{\text{eng}}$
3: Propulsion
$\eta_{\text{ov,cr}}$
Engine
Deck
TET_{TO}
$\Pi_{i,\text{TO}}$
OPR_{TOC}
E_{fuel}
$m_{\text{fuel,harm}}$
$C_{L,\text{cr}}$
$m_{\text{fuel,harm}}$
4: Mission
m_{fuel}
m_{fuel}
$v_{\text{bl}}, t_{\text{bl}}$
$C_{L,cr}$
ATR_{100}
6: Climate
COC
7: Cost
$\mathbf{g}$
8: Constraints

Figure 5.1: Extended design structure matrix showing the multidisciplinary design workflow adapted from Section 3.1.1 (Figure 3.2) to design hydrogen aircraft

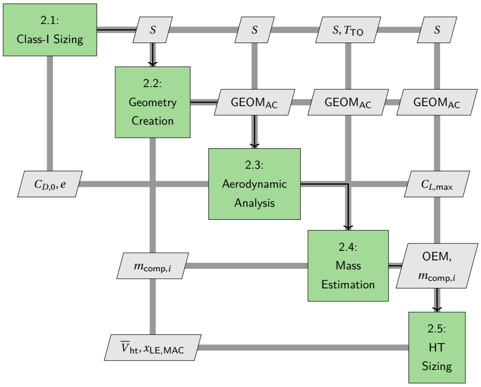
2.1:
Class-I Sizing
S
S
S, T_{TO}
S
2.2:
Geometry
Creation
GEOM_{AC}
GEOM_{AC}
GEOM_{AC}
$C_{D,0}, e$
2.3:
Aerodynamic
Analysis
$C_{L,\max}$
$m_{\text{comp},i}$
2.4:
Mass
Estimation
OEM,
$m_{\text{comp},i}$
$\overline{V}_{\text{ht}}, x_{\text{LE,MAC}}$
2.5:
HT
Sizing

Figure 5.2: Airframe design and analysis workflow (step 2 in Figure 5.1)

5.1.2. DESIGN AND ANALYSIS METHODS

The following sections discuss the design and analysis steps taken in the individual disciplines. Since the modules of the existing aircraft design framework (see Section 3.1) are extended, the sections focus on the changes made for the integration of liquid hydrogen.

CLASS-I SIZING

The Class-I sizing module aims to compute the wing surface area (S) and the sea-level take-off thrust (T_{TO}), which influence geometry creation, mass estimation, and propulsion-system design. The surface area can be computed from the wing loading and the MTOM estimate in the current design iteration. T_{TO} follows from the sea-level, thrust-to-weight ratio, which is selected such that it is the minimum value satisfying all six imposed performance constraints. This is mathematically expressed by the following equation, which is directly dependent on the design variables W/S, A, and M_{cr}, and indirectly on h_{cr}:

$$
\begin{aligned}
\left(\frac{T}{W}\right)_{TO} = \max\Bigg\{ & \frac{W/S}{\mathrm{TOP}}\cdot\frac{1}{C_{L_{\mathrm{TO}}}}, \\
& \frac{T_{\mathrm{TO}}}{T_{\mathrm{cr}}}\left(\frac{\rho_0}{\rho_{\mathrm{cr}}}\right)^{\frac{3}{4}}\left[\frac{C_{D_{0,\mathrm{cr}}}\frac{1}{2}\gamma p_{\mathrm{cr}}M_{\mathrm{cr}}^2}{(W/S)_{\mathrm{cr}}}+\frac{(W/S)_{\mathrm{cr}}}{\pi A e_{\mathrm{cr}}\frac{1}{2}p_{\mathrm{cr}}\gamma M_{\mathrm{cr}}^2}\right], \\
& \left[\frac{c}{v}\right]_{\mathrm{TO,N_{eng}}}+2\sqrt{\frac{C_{D_{0,\mathrm{TO}}}}{\pi A e_{\mathrm{TO}}}},\ \left[\frac{c}{v}\right]_{\mathrm{app,N_{eng}}}+2\sqrt{\frac{C_{D_{0,\mathrm{app}}}}{\pi A e_{\mathrm{app}}}}, \\
& \frac{N_{\mathrm{eng}}}{N_{\mathrm{eng}}-1}\left(\left[\frac{c}{v}\right]_{\mathrm{TO,N_{eng}-1}}+2\sqrt{\frac{C_{D_{0,\mathrm{TO}}}}{\pi A e_{\mathrm{TO}}}}\right), \\
& \frac{N_{\mathrm{eng}}}{N_{\mathrm{eng}}-1}\left(\left[\frac{c}{v}\right]_{\mathrm{app,N_{eng}-1}}+2\sqrt{\frac{C_{D_{0,\mathrm{app}}}}{\pi A e_{\mathrm{app}}}}\right)\Bigg\}
\end{aligned}
\tag{5.2}
$$

The first component within the curly brackets ensures that the required take-off length can be achieved, while the second component verifies that enough thrust is available in cruise conditions. These two constraints are set up according to previously discussed methods [109], where the density ρ and pressure p are altitude-dependent and calculated through the International Standard Atmosphere (ISA) model. The take-off length for the medium-range case study is presented in Table 3.8 along with other top-level requirements. The wing loading at the start of cruise is considered to be lower due to fuel consumed during take-off and climb. The next four components guarantee that the thrust level is sufficient to produce the required climb gradient (c/v) in several all-engines-operating conditions and one-engine-inoperative situations. The subscripts "TO", "cr", and "app" refer to the configuration the aircraft is in: take-off, cruise, or approach, respectively. The zero-lift drag coefficients (C_{D_0}) and Oswald factors (e) are adapted to the applicable configuration. Table 5.2 provides the minimum climb gradients to be achieved in these four situations and references to the respective regulations.

Table 5.2: Climb gradients (c/v) to be met according to regulations

	Take-off	**Approach or Landing**
All engines operating (N_{eng})	0.012 (CS25.111)	0.032 (CS25.119)
One engine inoperative ($N_{\mathrm{eng}}-1$)	0.024 (CS25.121)	0.021 (CS25.121)

These performance requirements are only considered in the Class-I sizing module and are not constraints in overall multidisciplinary optimization. This approach ensures that every design solution coming from the synthesis loop automatically meets these requirements. In addition, this eliminates T_{TO} as a design variable in the overall optimization. However, depending on the selected wing loading and aspect ratio, different requirements may become active. Such a disruptive change can cause problems when a gradient-based optimization algorithm is used. To overcome this issue, a multi-strategy approach is used when solving the optimization problem. Appendix C.2 discusses this approach in more detail.

GEOMETRY CREATION

The aircraft outer geometry is required to determine the drag polar in module 2.3 in Figure 5.2 and to predict the structural mass in module 2.4. The creation is fully automated to facilitate the MDO. This automation is achieved through statistical relationships and assumptions based on existing medium-range, narrow-body aircraft concepts such as the Airbus A320 and Boeing 737 [128, 164]. Appendix B elaborates on the geometry creation methods for each aircraft component. This section summarizes the approach and highlights the differences for hydrogen aircraft.

The wing is sized according to the surface area, retrieved from the Class-I sizing, the aspect ratio, the cruise Mach number, and the lift coefficient. The span is determined directly from S and A, while the remainder of the planform is defined by the quarter chord sweep angle and the taper ratio, which are determined from the cruise Mach number and data of high-subsonic and transonic aircraft [34, 127]. The cruise lift coefficient provides an estimate of the airfoil thickness-to-chord ratio, which in turn is employed in the aerodynamic analysis and mass estimation.

Different from the wing geometry, the fuselage geometry is dependent on the fuel type. For the kerosene-powered aircraft, the fuselage consists of three sections: the cockpit, cabin, and tail. First, the inner and outer diameters are computed based on the number of seats abreast in the cabin and the LD3-45 unit load device in the cargo bay below. For the current study, a six-abreast, single-aisle configuration is selected, leading to inner and outer diameters of approximately 3.91 and 4.06 m, respectively. A maximum capacity of 180 passengers thus results in a cabin consisting of 30 rows and being approximately 27 m long. This maximum capacity is arranged in a single-class configuration, which is taken to be the sizing configuration for the cabin. Two- or three-class configurations can be fitted, albeit at a lower passenger number. This cabin layout is similar to the ones of the Airbus A320 [128] and Boeing 737-900 [164]. The cockpit is assumed to be 4 m long and the tail section is approximately 1.6 times the outer diameter.

For the hydrogen aircraft, a cylindrical, cryogenic tank is integrated into the aircraft. Although various integration solutions exist [155, 163], in this study, the tank is positioned aft of the cabin in the fuselage in a non-integral manner, as conceptually shown in Figure 5.3. This is a rather straightforward solution for the aircraft category under investigation since it results in a relatively short tank and does not interrupt the conventional connection between the cockpit and the cabin.

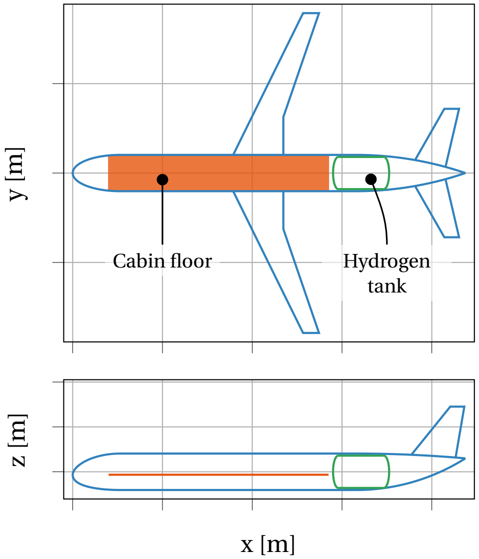

Figure 5.3: Conceptual top and side views of hydrogen tank integration into the fuselage of a medium-range aircraft

The maximum fuel mass ($m_{\text{fuel,max}}$), together with the density of liquid hydrogen (ρ_{LH2} =71 kg/m^3), provides an estimate for the maximum tank volume (V_{tank}). Assuming the tank diameter ($d_{\text{tank}} = 2r_{\text{tank}}$) is equal to the inner diameter of the fuselage and the end caps of the tank are ellipsoids, the tank length can be determined as follows:

$$\begin{aligned} l_{\text{tank}} &= \frac{1}{\pi r_{\text{tank}}^2}\left[V_{\text{tank}} - \frac{4\pi}{3}\cdot r_{\text{tank}}^2 \cdot h_{\text{dome}}\right] + 2h_{\text{dome}} \\ \text{where } h_{\text{dome}} &= r_{\text{tank}} \cdot \left(\frac{h}{r}\right)_{\text{dome}} \quad \text{and } V_{\text{tank}} = \frac{m_{\text{fuel,max}}}{\rho_{\text{LH2}}}\left(1 + f_{V,\text{extra}}\right) \end{aligned} \tag{5.3}$$

Figure 5.4 displays a conceptual longitudinal section of the tank model with the dimensions from the relation above. The ratio between the dome height and the tank radius $(h/r)_{\text{dome}}$ is selected as the control variable since it facilitates scaling the domes automatically with the radius, and because its value lies in the interval between zero and one. Although this ratio only influences the total tank length, it does not influence the mass of the tank itself in the current model. Lower values of $(h/r)_{\text{dome}}$ can reduce the fuselage mass, but any penalty on stress levels due to the internal pressure is not accounted for. In the optimizations, the ratio is set to 0.3. The sensitivities of the objectives to this assumption are discussed in Section 5.4.1.

The tank outer diameter is assumed to be equal to the inner diameter of the fuselage, which is equal to the diameter of the cabin. This leaves approximately 15 cm around the tank for insulation material and structural components. In this approximation, the volume of the tank is determined from the maximum amount of liquid hydrogen it has to hold, plus extra allowances to account for contraction and expansion (+0.9%), ullage (+2%), internal equipment (+0.6%), and trapped fuel (+0.3%) [160, 163]. These allowances are captured by the factor $f_{V,\text{extra}}$ in Equation (5.3). However, no volume allowance is allocated for boil-off resulting from heat leakage into the tank. The effect of this assumption on the optimization objectives and key performance indicators is quantified in Section 5.4.1.

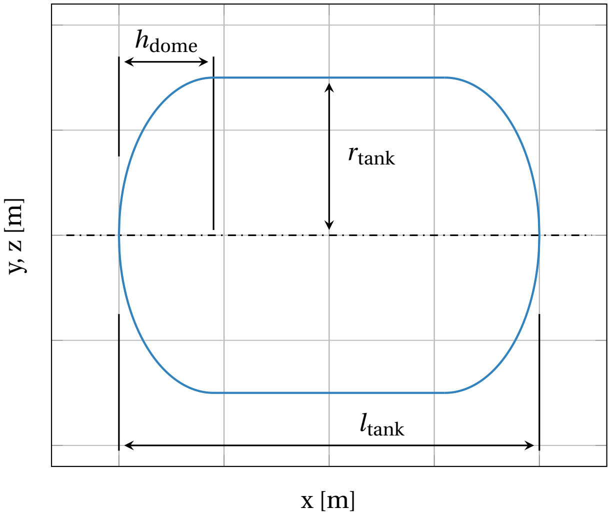

Figure 5.4: Longitudinal section of the liquid hydrogen tank concept

From this chapter onward, the longitudinal location of the main wing and the size of the horizontal tail surface are determined by considering the aircraft mass balance and the longitudinal stability and trim conditions [34]. The design routine computes the in-flight center-of-gravity excursion over the mean aerodynamic chord (MAC) as a function of the longitudinal wing position. Simultaneously, the stability constraints in cruise conditions and the trim conditions in approach (full flaps deployed) are assessed. These constraints provide an estimate of the horizontal tail size area with respect to the reference wing area (S_{ht}/S), for a given c.g. excursion. An internal optimization finds the wing position which minimizes the horizontal tail area, adhering to the imposed stability and trim constraints.

The mass balance and c.g. excursion are determined by first calculating the c.g. position corresponding to the OEM. This step considers the relative, structural mass fractions of fuselage group components (fuselage, empennage, and in the case of the hydrogen aircraft, the tank) and the wing group elements (wing and engines) and their relative positions. While the relative mass fractions for the kerosene concept can be taken from literature, this data is not available for hydrogen aircraft.

Therefore, these mass fractions are updated throughout the iterations, as can be seen in Figure 5.2 where the mass estimation module feeds the component masses $m_{\text{comp},i}$ back to the geometry module. Subsequently, the passengers and fuel are loaded, taking into account several loading scenarios: passenger loading from the front and back, full and empty fuel tank, and the ferry mission with full fuel tank and no passengers. This process finds the largest, critical, in-flight c.g. excursion, which sizes the horizontal tail.

Compared to the kerosene aircraft, the liquid hydrogen counterpart with a tank in the aft fuselage section features a longer tail arm but also a larger in-flight c.g. excursion, assuming the cabin capacity and fuselage diameter are equal for both concepts. Additionally, the stability constraint is updated according to the increase in fuselage length. The net effect is that for the same top-level requirements, the liquid hydrogen aircraft will have a larger horizontal tail size. This increases the OEM and increases the zero-lift drag, negatively influencing energy consumption.

The vertical tail size is determined through a fixed volume coefficient ($\overline{V}_{\mathrm{vt}}$=0.085), based on statistical data [109]. A physics-based sizing approach to the vertical tail is considered outside the scope of the current study since such analysis would require more knowledge about the design. Nevertheless, the effect of the longer fuselage, among other effects, on the vertical tail area should be evaluated, taking into account lateral and directional stability constraints in various conditions, including one-engine-inoperative and cross-wind situations.

The aspect ratios and taper ratios of the horizontal and vertical tails are taken from literature and are assumed to be equal for the kerosene and hydrogen aircraft. These values are summarized in Table B.3. The quarter-chord sweep angle of the horizontal and vertical stabilizers is 3 and 10 degrees, respectively, more than the main wing quarter-chord sweep angle.

AERODYNAMIC ANALYSIS

The aerodynamics module provides an estimation of the aircraft drag polar based on the external shape and size of the aircraft. The propulsion, mission, and Class-I sizing modules require this drag polar to size the propulsion system, evaluate the fuel burn, and evaluate the performance constraints in Equation (3.2). Compared to Section 3.1.2, an updated quadratic drag polar is assumed according to the following formula:

$$C_D = C_{D_0} + \frac{C_L^2}{1.05\pi Ae} + C_{D_w} \tag{5.4}$$

where C_{D_0} is the zero-lift drag coefficient, A is the aspect ratio, e is the Oswald factor, and C_{D_w} is the wave drag coefficient. This component is newly added to the aerodynamics module in this chapter. The zero-lift drag is computed as the sum of the minimum profile drag of all components (wing, fuselage, nacelles, and empennage) and the drag contributions due to excrescences or protuberances, similar to approach from Section 3.1.2. Since the geometry is a direct input for the calculation of C_{D_0}, this parameters is sensitive to the elongation of the fuselage due to the integration of hydrogen tanks.

The Oswald factor is computed according to Equation (3.4). The 5% increase in the product $A \cdot e$ is included to model the influence of wing tip devices that do not contribute to the wing span. This contribution is derived from the Airbus A320 winglet span.

Equation (3.3) provides an estimate of the drag coefficient in clean configuration (i.e., with all flaps and landing gear retracted). To correct this estimation in landing and take-off settings, constant terms are added to C_{D_0} and e [87, 109]. Based on data provided by Roskam [109], the zero-lift drag is increased by 0.015 and 0.085 in take-off and landing configuration, respectively. The contributions of the flaps to e are assumed to be equal to 0.05 and 0.10 during take-off and landing [109], respectively.

The last term in the drag polar equation accounts for the wave drag. This term accounts for transonic flow around the aircraft, leading to an increase in drag when shocks are formed. In this approach, we only consider the wave drag of the wing [165]. The wave drag component is computed using the following equation according to the methods introduced by References [166, 165]:

$$C_{D_w} = \begin{cases} 0 \text{ if } M_{\text{cr}} \leq M_{\text{dd}} - \left(\frac{0.1}{80}\right)^{1/3} \\ 20 \cdot \left[M_{\text{cr}} - M_{\text{dd}} + \left(\frac{0.1}{80}\right)^{1/3}\right]^4 \text{ if } M_{\text{cr}} > M_{\text{dd}} - \left(\frac{0.1}{80}\right)^{1/3} \end{cases} \tag{5.5}$$

where M_{dd} is the drag divergence Mach number at which the drag rise is 0.1 (i.e., $\partial C_D/\partial M = 0.1$). This Mach number is determined as follows:

$$M_{\text{dd}} = \frac{k_a}{\cos(\Lambda_{0.25})} - \frac{t/c}{\cos^2(\Lambda_{0.25})} - \frac{C_{l,\text{crit}}}{10\cos^3(\Lambda_{0.25})} \tag{5.6}$$

where we assume a value of 0.935 for the airfoil technology factor k_a. The parameter $C_{l,\text{crit}}$ is the local critical lift coefficient, which is presumed to be equal to the wing lift coefficient divided by 0.9. t/c is the averaged thickness-to-chord ratio. This parameter and the quarter-chord sweep angle are determined from statistical relations (see Appendix B) to minimize the wave drag at high subsonic conditions. When the design cruise Mach number increases and t/c reaches the lower limit of 0.10, the wave drag starts to increase more rapidly with the design Mach number.

The maximum lift coefficient of an aircraft, defined in the configuration with all high-lift devices fully deployed, is conceptually a function of the wing sweep angle and the type of flap system. While in Chapter 3, $C_{L_{\max}}$ was considered a design variable, and a constraint was implemented to limit its value, from this chapter onward $C_{L_{\max}}$ is automatically set equal to this constrained value. Since the cruise Mach number drives the wing sweep, this design variable also limits the maximum achievable lift coefficient. In the conceptual framework, this reasoning is included through the following equality [107]:

$$C_{L_{\max}} = 2.8 \cdot \cos\Lambda_{0.25} \tag{5.7}$$

MASS ESTIMATION

The convergence loop at the core of the optimization framework ensures that the aircraft evaluated in the climate and cost modules is consistent in terms of mass and geometry. Key parameters in this convergence are the maximum take-off mass and the operating empty mass. The OEM has to be computed based on the aircraft configuration and expected loads. Especially in the case of hydrogen aircraft, the influence of the fuel tank integration on the OEM has to be taken into account.

Similar to the approach taken in the previous, the Class-II methods introduced by Torenbeek [34] provide the necessary update of the OEM, albeit with adaptations for the hydrogen alternative. Although this reference does not provide any specialized methodology to size the hydrogen tank, the assumptions underlying the semi-empirical are not invalidated since they can be used for aircraft with a (kerosene) tank in the fuselage and no fuel in the wings. The main changes to the methodology occur in the estimation of fuselage mass, wing mass, tank mass, the mass of operational items, and the airframe equipment mass.

The first alteration is the elongation of the fuselage due to the integration of the hydrogen tank aft of the cabin, as presented in Figure 5.3. The structural fuselage mass estimation depends largely on the skin area, which automatically increases with the length of the fuselage. The mass also scales with the cabin floor area. While in the conventional aircraft, this floor runs up to the tail section, in the case of the hydrogen aircraft this floor stops in front of the fuel tank. Hence, the floor area is approximately equal for both aircraft types since the passenger requirements remain unaltered.

The analysis of the wing mass remains similar, with the main difference being the mass for which the wing is designed. The method from Reference [34] requires the maximum aircraft mass with zero fuel in the wings. For kerosene aircraft, this can be set equal to the maximum zero-fuel mass (MZFM), while for the hydrogen concept, the MTOM is expected to deliver more accurate results since there is no fuel in the wings and thus no load alleviation.

In this conceptual study, it is assumed that the mass of the landing gear is a function of the MTOM [34, Chapter 8]. This function is independent of the fuel type or aircraft category. However, in the case of the hydrogen aircraft which have a longer fuselage, this relation possibly underestimates the mass of the undercarriage. The landing gear on the hydrogen aircraft may have to be longer and/or be positioned more aft to avoid tailstrike. Also, the increased maximum landing mass of the hydrogen aircraft may result in a heavier landing gear. Overall, the current approach may therefore underestimate the OEM, and as a result the MTOM and energy consumption, of the hydrogen aircraft, leading to an underestimation of the operating cost and climate impact.

In the previous chapters, the mass of the operational items (m_{ops}) and airframe services and equipment (m_{afse}) were set to a fixed percentage of the MTOM. Nevertheless, these masses should not differ between the kerosene and hydrogen alternatives since the cabin layout and passenger services are unaltered. Therefore, it is decided to keep these masses constant for both aircraft types throughout the optimizations, as can be seen in the input block above the airframe step in Figure 5.1. The mass of the operational items and fixed equipment are set to approximately 4770 kg and 8800 kg, respectively.

For the kerosene aircraft, the tank mass is included in the wing mass estimation. However, for the hydrogen aircraft, an additional component has to be added to account for the heavier, cryogenic tanks. A conceptual approach is taken where the tank mass scales with the maximum fuel mass it can hold, using the definition of the gravimetric index or efficiency [167]:

$$\eta_{\text{grav}} = \frac{m_{\text{fuel}}}{m_{\text{fuel}} + m_{\text{tank}}} \Rightarrow m_{\text{tank}} = m_{\text{fuel}} \cdot \left(\frac{1}{\eta_{\text{grav}}} - 1 \right) \tag{5.8}$$

Note that in Reference [163], η_{grav} is defined differently, namely as the ratio between the tank mass and the fuel mass. Although this results in different values for η_{grav}, the tank and fuel mass ratios are similar among research projects [163]. The value of the gravimetric index varies depending on the tank design, but for a medium-range, narrow-body aircraft the value of 0.773 (0.294 in Reference [163]) is selected based on previous designs in literature [163, 167] and kept constant throughout the optimizations. This allows the computation of the tank mass once the maximum fuel mass is known. The latter parameter is calculated in the mission analysis step from the desired ferry range.

The influence of potential tank design options, such as venting pressure, tank shape, position, or insulation materials, is not examined in this research. However, Section 5.4.1 discusses the sensitivity of the objective functions to the selected gravimetric index.

PROPULSION

Based on the five engine design variables defined in Table 5.1, the thrust-to-weight ratio in take-off, and the drag polar, a preliminary turbofan is thermodynamically designed and sized. Both the kerosene- and hydrogen-powered aircraft utilize a two-spool turbofan engine with separate exhausts. This thermodynamic model is required to estimate the fuel burn and emissions throughout the flight in steps 4 and 6 of the XDSM in Figure 5.1, while the engine size and mass are employed to update the drag polar and OEM in step 2.

Based on the cruise conditions, the thermodynamic cycle is determined by the parametric analysis module of Figure 3.4. Subsequently, an off-design analysis is performed to find the required fuel flow for a given thrust at key points in the mission. Both the on-design and off-design point analyses are executed employing the strategies laid out by Mattingly, Heiser, and Pratt [105], and the variable specific heat model introduced by Walsh and Fletcher [112].

In the case of hydrogen combustion, two changes are implemented in the thermodynamic model of the turbofan engine. First of all, when replacing kerosene with hydrogen, the lower heating value (LHV) increases from 43.6 MJ/kg to approximately 120 MJ/kg. Secondly, since the composition of the combustion gases changes, characterized by the lack of carbon dioxide and increased water vapor content, the variable gas model is adapted. In particular, the values for the specific heat at constant pressure (c_p), the specific enthalpy (h), and the temperature-dependent fraction of entropy (ϕ) as functions of temperature are modified. The new relations, applicable through the turbines and the exhaust, are derived as follows:

$$\begin{aligned} c_p(T) &= f_{\mathrm{H_2O}} \cdot c_{p,\mathrm{H_2O}}(T) + f_{\mathrm{N_2}} \cdot c_{p,\mathrm{N_2}}(T) + f_{\mathrm{air}} \cdot c_{p,\mathrm{air}}(T) \\ h(T) &= f_{\mathrm{H_2O}} \cdot h_{\mathrm{H_2O}}(T) + f_{\mathrm{N_2}} \cdot h_{\mathrm{N_2}}(T) + f_{\mathrm{air}} \cdot h_{\mathrm{air}}(T) \\ \phi(T) &= f_{\mathrm{H_2O}} \cdot \phi_{\mathrm{H_2O}}(T) + f_{\mathrm{N_2}} \cdot \phi_{\mathrm{N_2}}(T) + f_{\mathrm{air}} \cdot \phi_{\mathrm{air}}(T) \\ R &= f_{\mathrm{H_2O}} \cdot R_{\mathrm{H_2O}} + f_{\mathrm{N_2}} \cdot R_{\mathrm{N_2}} + f_{\mathrm{air}} \cdot R_{\mathrm{air}} \end{aligned} \tag{5.9}$$

where the f_i factors represent the fractions between the mass flow of compound i and the total core mass flow aft of the combustion chamber. These fractions follow from the simplified chemical equilibrium of hydrogen combustion and the fuel-to-air ratio, far $= \dot{m}_{H_2}/\dot{m}_{\mathrm{air,in}}$, where $\dot{m}_{\mathrm{air,in}}$ is the air mass flow at the inlet of the combustor. Assuming the air at the inlet of the combustor consists purely of oxygen and nitrogen, the following simplified chemical reaction occurs:

$$2\,\mathrm{H_2} + (\mathrm{O_2} + (79/21)\,\mathrm{N_2}) \longrightarrow 2\,\mathrm{H_2O} + (79/21)\,\mathrm{N_2} \tag{5.10}$$

From this reaction, the approximate stoichiometric fuel-to-air ratio can be computed:

$$\left.\frac{\dot{m}_f}{\dot{m}_{\mathrm{air}}}\right|_{\mathrm{st}} = \frac{2 \cdot \mathrm{M_{H_2}}}{\mathrm{M_{O_2}} + \frac{79}{21}\mathrm{M_{N_2}}} \approx 0.029 \tag{5.11}$$

where M_{H_2}, M_{O_2}, and M_{N_2} are the molar masses of hydrogen, oxygen, and nitrogen, respectively. The fractions f_i in Equation (5.9) can be determined by considering a mass balance over the combustor:

$$\dot{m}_{\text{in}} = \dot{m}_{\text{out}} \Rightarrow \dot{m}_{\text{air,in}} + \dot{m}_{H_2} = \dot{m}_{H_2O} + \dot{m}_{N_2} + \dot{m}_{\text{air,out}} \tag{5.12}$$

leading to

$$\begin{aligned} f_{H_2O} &= \frac{\dot{m}_{H_2O}}{\dot{m}_{\text{out}}} = \frac{M_{H_2O}}{M_{H_2}} \cdot \frac{\dot{m}_{H_2}}{(1+\text{far}) \cdot \dot{m}_{\text{air,in}}} \\ &= \frac{M_{H_2O}}{M_{H_2}} \cdot \frac{\text{far} \cdot \dot{m}_{\text{air,in}}}{(1+\text{far}) \cdot \dot{m}_{\text{air,in}}} \approx 8.94 \cdot \frac{\text{far}}{(1+\text{far})} \\ f_{N_2} &= \frac{\dot{m}_{N_2}}{\dot{m}_{\text{out}}} = \left(\frac{79}{21}\right) \frac{M_{N_2}}{2M_{H_2}} \cdot \frac{\dot{m}_{H_2}}{(1+\text{far}) \cdot \dot{m}_{\text{air,in}}} \\ &= \left(\frac{79}{21}\right) \frac{M_{N_2}}{2M_{H_2}} \cdot \frac{\text{far} \cdot \dot{m}_{\text{air,in}}}{(1+\text{far}) \cdot \dot{m}_{\text{air,in}}} \approx 26.13 \cdot \frac{\text{far}}{(1+\text{far})} \end{aligned} \tag{5.13}$$

$$\begin{aligned} f_{\text{air}} &= \frac{\dot{m}_{\text{air,out}}}{\dot{m}_{\text{out}}} = \frac{\dot{m}_{\text{air,in}} - \dot{m}_{H_2} \cdot \left(\left.\frac{\dot{m}_f}{\dot{m}_{\text{air}}}\right|_{\text{st}} \right)^{-1}}{(1+\text{far}) \cdot \dot{m}_{\text{air,in}}} \\ &= \frac{\dot{m}_{\text{air,in}} - \text{far} \cdot \dot{m}_{\text{air,in}} \cdot \left(\left.\frac{\dot{m}_f}{\dot{m}_{\text{air}}}\right|_{\text{st}} \right)^{-1}}{(1+\text{far}) \cdot \dot{m}_{\text{air,in}}} \approx \frac{1 - 34.48 \cdot \text{far}}{1+\text{far}} \end{aligned} \tag{5.14}$$

The value of far in the above equations is not the same as the stoichiometric fuel-to-air ratio as not all core airflow entering the combustor takes part in the combustion process. Together with the gas model relations of water, nitrogen, and air provided by Walsh and Fletcher [112, Chapter 3], these fractions define the gas model aft of the combustor according to Equation (5.9). Section 5.2 discuss the verification of this gas model.

Additional assumptions are made to simplify the thermodynamic modeling, including constant component efficiencies, no cooling flows, and no power offtake. The validity of these assumptions is tested and discussed in Section 3.2.1. Furthermore, in the case of liquid hydrogen, the fuel may have to be heated prior to combustion, which may be done through a heat exchanger or by cooling the turbines. However, this latter aspect is considered out of scope in the current conceptual study.

The relation for the mass of the engines is assumed to be the same for both the kerosene and hydrogen engines but does take into account the mass variation due to bypass ratio, overall pressure ratio, and ingested mass flow (see Section 3.1) [113]. Although the hydrogen turbofan may feature a heat exchanger to gasify the liquid hydrogen, the combustion chamber is possibly shorter due to the reduced residence time [168, 169]. The impact of these changes on the engine mass is not accounted for.

MISSION ANALYSIS

The aim of the mission analysis in the framework of Figure 5.1 is primarily to provide an update of the required fuel mass at the harmonic design point (i.e. the maximum achievable range at maximum structural payload), such that the MTOM can be updated in the convergence loop. Second, it also calculates the maximum fuel mass to fulfill the ferry range (r_{ferry}) requirement. Although kerosene aircraft often have enough storage volume in the wings, the volume required to store the maximum amount of hydrogen fuel is critical in sizing the tank, and subsequently the fuselage and wing.

The assumed mission profile is displayed schematically in Figure 3.6 and features, besides the nominal climb and cruise phases (2 and 3 in Figure 3.6), also diversion and loiter phases (phases 5 to 8 in Figure 3.6). A conservative diversion range of 250 nmi is selected. A total loiter time of 35 minutes at 457 m (1500 ft) is taken, corresponding to 30 minutes of final reserve fuel and 5 minutes of contingency fuel. This fuel policy is set up according to the Easy Access Rules for Air Operations provided by the European Union Aviation Safety Agency (EASA), in particular in Section AMC1 CAT.OP.MPA.150(b).

The mission fuel mass is estimated through the lost-range method introduced by Torenbeek [115]. This method calculates the ratio between the fuel and total take-off masses as a function of cruise range, propulsion efficiency, and lift-to-drag ratio, and applies corrections to account for take-off, climb, and maneuvering phases. The method can be adapted for hydrogen by implementing the respective LHV in the calculation of R_H, the range-equivalent calorific value. Since the statistical estimates for the diversion and loiter phases, as indicated in Figure 3.6, do not uphold for hydrogen aircraft, the estimates are replaced by the respective Breguet equations. Furthermore, the hydrogen fuel mass required for maneuvers in the lost-range method is scaled by the lower heating value as follows:

$$\left(\frac{m_f}{m_{\text{TO}}}\right)_{\text{maneuver, LH2}} = \frac{0.0025}{\eta_{\text{ov}}} \cdot \frac{\text{LHV}_{\text{LH2}}}{\text{LHV}_{\text{ker}}} \tag{5.15}$$

As discussed in Section 3.1.2, the lost-range method does not suffice for the climate impact evaluation since the climate impact of NO_x emissions and contrail formation are dependent on engine off-design performance and altitude. Therefore, a separate mission analysis is performed during the climate impact evaluation which employs simplified flight mechanics and numerical integration. This mission analysis is computationally more expensive and is therefore not used in the aircraft synthesis to save time.

A comparison of the fuel mass estimates obtained from the two methods shows that the lost-range method marginally overpredicts the mission fuel mass. The lost-range method results in a 1 to 4% larger mission fuel mass, without the reserve mission phases, for both the kerosene and hydrogen aircraft. If the detailed mission analysis is considered to be a more accurate representation of reality, this overprediction in the aircraft design loop leads to a heavier aircraft due to the snowball effect. This in turn increases the climate effects which scale with fuel burn. Nevertheless, since the excess fuel mass is limited to 4%, the overestimation of MTOM is smaller. Therefore, it is expected that the overall penalty, introduced by the use of two different methods, is limited.

GLOBAL WARMING IMPACT EVALUATION

Once the evaluation of the previous disciplines has yielded a consistent aircraft design, a climate impact and cost assessment of the concept can be made. Based on these assessments, the optimizer defines a new design vector to march towards the optimal design. Similar to the studies in Chapters 3 and 4, this chapter considers the climate effects of several climate agents, including carbon dioxide, nitrogen oxides, contrails, water, and aerosols, into one comprehensive metric, namely the average temperature response over a period of H years, as defined in Equation (3.11). This metric is again computed for the hypothetical, future operations scenario that is further elaborated in Section 3.3.1. $\Delta T(t)$ is computed through a linear temperature response model which, for kerosene aircraft, is described in Section 3.1 and based on the model provided by Schwartz Dallara, Kroo, and Waitz [24]. The following paragraphs discuss the changes that are applied to this model to assess the climate impact for hydrogen aircraft. The most prominent changes follow from the elimination of carbon dioxide, soot, and sulfur oxide emissions. The former two eliminations are caused by the lack of carbon atoms in the fuel, while the latter emissions are eradicated because hydrogen can be produced free of sulfur [156]. In addition, the NO_x emissions and contrail properties are expected to be different for hydrogen combustion.

The potential effects of hydrogen leakage, at ground level or at altitude, on atmospheric concentrations of hydrogen, methane, and ozone, and the resulting warming [170] are not considered in the present study.

Nitrogen Oxides Nitrogen oxide emissions are still produced in the combustion of hydrogen due to the presence of nitrogen in the air and the relatively high temperatures in the combustion chamber. Nevertheless, hydrogen features wider flammability limits and higher flame speeds than kerosene, allowing a decrease in flame temperature and a reduction in residence time, both curtailing the formation of NO_x [14]. It is estimated that these aspects can reduce the NO_x emissions by 50 to 80% [156, 171] through, for example, lean direct injection or micro-mixing technologies [159, 172, 173]. To evaluate the hydrogen-variant aircraft in this study, the emissions per unit of energy are assumed to reduce by 65%, while the interval boundaries are studied in Section 5.4.2.

Although the NO_x emissions are reduced, radiative forcing effects remain. The current model captures three consequences due to NO_x: firstly, short-lived ozone (O_{3S}) is created, leading to a warming effect. Second, in the long term, methane (CH_4) and long-lived ozone (O_{3L}) are depleted, causing a cooling effect. The influence of NO_x emissions on the mean surface temperature change ΔT is assessed using the same model for both kerosene and hydrogen aircraft. Although also a reduction in stratospheric water vapor is expected due to NO_x emissions [3], this is not considered in the current study.

Water The water vapor emissions in the case of hydrogen are significantly higher than the emissions due to kerosene combustion. The emission index of water vapor can be derived from the chemical reaction in Equation (5.10) and amounts to 8.93 kg per kg of hydrogen. This is approximately seven times as high as for kerosene ($EI_{H_2O} = 1.26$kg/kg). Computing the water vapor per unit of energy yields 7.44×10^{-2} kg/MJ and 2.93×10^{-2} kg/MJ for hydrogen and kerosene, respectively, a difference of approximately 61%.

The radiative forcing per unit of emitted water mass is assumed to be equal for both aircraft types, namely 7.43×10^{-15} W/(m^2 kg). Hence, the relative contribution of water vapor to the total climate impact is expected to increase when shifting from kerosene to hydrogen [119]. In the model, water emissions are treated as a short-lived gas in the atmosphere, although the lifetime varies with emission altitude [156].

Contrails The increased water vapor content also performs an important role in the formation of contrails behind hydrogen aircraft. A higher water vapor emission index tends to increase the probability of contrail formation [158, 119]. Nevertheless, due to the lack of aerosol emissions, such as soot, the contrail properties are expected to change. These two effects are treated separately in the current model implementation.

Contrails are formed because the exhaust gases from the turbofan engines are hot and humid compared to the atmospheric conditions in which aircraft typically operate, i.e. at altitudes in the upper troposphere or lower stratosphere, with cold and dry air. Under certain atmospheric conditions, ice crystals can form around aerosols which act as nuclei. These conditions are that the ambient temperature is lower than the threshold of 235 K (-38 °C) and that the Schmidt-Appleman criterion is satisfied [17], as discussed in Section 3.1.2 on Page 42 (supported by Figure 3.7). This criterion verifies whether the exhaust gases during the mixing process with ambient air reach saturation with respect to liquid water. As discussed in Section 3.1.2, this mixing process for a turbofan engine can be modeled as a linear relationship between the water vapor partial pressure $p^{\mathrm{H_2O}}$ and the temperature T of the mixing gas:

$$\begin{aligned} p^{\mathrm{H_2O}} &= p_{\mathrm{amb}}^{\mathrm{H_2O}} + G \cdot (T - T_{\mathrm{amb}}) \\ &= p_{\mathrm{amb}}^{\mathrm{H_2O}} + p_{\mathrm{amb}} \cdot c_p \cdot \frac{\mathrm{M_{air}}}{\mathrm{M_{H_2O}}} \cdot \frac{\mathrm{EI_{H_2O}}}{\left(1-\eta_{\mathrm{ov}}\right)\mathrm{LHV}} \cdot (T - T_{\mathrm{amb}}) \end{aligned} \tag{5.16}$$

where the slope G is dependent on the emission index of water, the engine overall efficiency, and the lower heating value of the fuel. A higher slope results in a larger contrail formation probability because saturation with respect to liquid water is more likely to occur. In the case of hydrogen fuel, the slope increases due to more water vapor emissions, and it decreases because of the higher calorific value. Furthermore, the exhaust gas composition influences the efficiency, although the effect on G is lower in magnitude.

Due to a lack of soot emissions in the case of hydrogen combustion, also the contrail properties change. A smaller amount of ice crystals develops initially, although they are larger in size [156, 158, 73]. These aspects in turn reduce the optical depth of the contrails and decrease their lifetime, which lowers the resulting radiative forcing. Based on literature [73], a 70% reduction in radiative forcing due to contrails is assumed in this study compared to kerosene aircraft, corresponding to a reduction of 90% in initial ice particle number. For the regular, kerosene-based climate model, a radiative forcing of 1.82×10^{-12} W/(m^2 km) is assumed for contrails [3].

CASH OPERATING COST

Discipline 7 in Figure 5.1 assesses the financial operating costs of the aircraft design. Although the operating costs of a hydrogen aircraft are still uncertain, it is important to put the potential climate impact saving into perspective. In the current study, the financial objective function consists of the cash operating cost which includes costs related to flight and maintenance and which are computed according to the cost models introduced by Roskam [35]. Other categories, such as depreciation, fees, and financing costs, are excluded from this analysis to further limit uncertainty. All costs are expressed in US dollars (USD). In the following paragraphs, the flight and maintenance costs are elaborated.

Flight Costs The costs related to executing missions are divided into three categories: fuel and oil, crew, and insurance. The fuel costs are derived directly from the fuel consumption during the selected mission. For the kerosene aircraft, the fuel price is assumed to be 2.71 USD/US gallon . The cost of sustainable liquid hydrogen is taken to be 4.4 USD/kg (2030 price level) [174], which translates into 1.18 USD/US gallon, corresponding to a decrease of 56% in cost per unit of volume. However, when considering the price per unit of energy, hydrogen is 54% more expensive.

It is recognized that especially this category bears a lot of uncertainty since fuel prices can be volatile. Some aspects that will perform an important role are the local availability of hydrogen and the means of transport to the airport, while the kerosene price may also vary due to future tax schemes, among other influences. Therefore, the sensitivity of the results to these assumptions is evaluated in Section 5.4.3. The cost of oil is set to 60 USD/US gallon with a density of 7.4 lb/US gallon (887 kg/m^3). The total oil mass is linearly related to the number of engines and the block time (t_{bl}) [35].

The crew costs are equal for both aircraft types and scale linearly with the block time and therefore inversely with the block speed (v_{bl}). Lower cruise speeds result in longer flight times for a given trip, increasing the cost of cockpit and cabin crews. The following annual salaries from Table 3.5 are assumed. All crew members are expected to fly 1000 hours annually.

An annual insurance cost of 0.56% of the market price is assumed, where the latter is calculated according to Equation (3.25). Since the market price of future hydrogen aircraft is unknown at the time of writing, it is considered to be equal to the price of a kerosene aircraft. Although this may lead to an underestimation of the insurance costs, this category often performs a minor role in the overall cost picture compared to, for example, fuel and crew costs.

Maintenance In the calculation of the maintenance expenses, no distinction is made between the two aircraft types. The costs are split up into the expenses associated with the airframe and the expenses required to maintain the engines, both requiring labor hours and materials. For either category, the labor costs of a technician (r_{lab}) are estimated to be 33 USD per hour [1]. The total maintenance hours are related to the airframe mass and engine take-off thrust for the airframe and engines respectively, according to the relations provided by Roskam. The cost of spare materials is also calculated according to the methods prescribed by Roskam, assuming 5000 flight hours between engine repairs and a spare part price factor of 1.0 compared to the original material. Furthermore, a cost for the maintenance burden is included [35], which accounts for any overhead costs related to maintenance activities.

The maintenance cost of the hydrogen aircraft may be different due to the inspection and repair of the cryogenic hydrogen tank, the fuel system, and the updated turbofan engines. In the research by [175], a 25% increase in maintenance cost is considered.

---

[1] URL `https://www.indeed.com/career/aircraft-mechanic/salaries` accessed on 30/08/2022

Research by Hoelzen et al. [176] estimates an increase in maintenance cost of 11% for short-range and 17% for medium-range aircraft respectively, not considering the differences in the engine which may require different maintenance procedures or materials.

Wehrspohn et al. [177] provides an overview of the maintenance tasks needed for the tank. In addition to increased cost, this analysis also shows that the burden on the environment due to maintenance materials and facilities may increase for hydrogen aircraft [177]. Taking the above percentages into account, the hydrogen, Pareto-optimal design solutions would show a further 3 to 5% increase in operating cost. However, research also suggests that the hydrogen turbomachinery may feature a longer lifetime, having a positive effect on the maintenance cost [178]. This longer lifetime is possible since hydrogen is a cleaner fuel [179] and since hydrogen potentially features a lower combustor pattern factor [180].

In conclusion, the net impact of hydrogen technology on maintenance costs is uncertain, and further development of design-sensitive cost estimation models is needed. The choice of maintenance cost model can also influence the cost-optimal design choices. This is caused by different sensitivities with respect to engine mass, bypass ratio, and overall pressure ratio, among other variables. This causes the relative importance of the different cost contributions to vary between models. The impact of the choice of maintenance cost estimation model is therefore further discussed in Section 5.4.3.

5.2. VERIFICATION AND VALIDATION

The verification of the overall design and analysis framework has been discussed in Section 3.2. The current section aims to validate whether the simplified model introduced in Section 5.1.2 accurately estimates the gas properties of hydrogen combustion products. Therefore, the model is compared to data provided by Verstraete [181] and Sethi [182]. Figures 5.5a to 5.5c show the comparison for three key parameters from Equation (5.9). It appears that the model agrees well with the data up to temperatures of around 2000 K. Beyond this temperature, chemical dissociation takes place, which is not captured by the current model. Nevertheless, since turbine temperatures are limited to 2000 K, this does not pose an issue fot the current study. Additionally, the enthalpy and entropy data in Figures 5.5b and 5.5c, respectively, consider a non-zero water-to-air ratio which explains a minor underestimation (2-5%) of the model in the graphs.

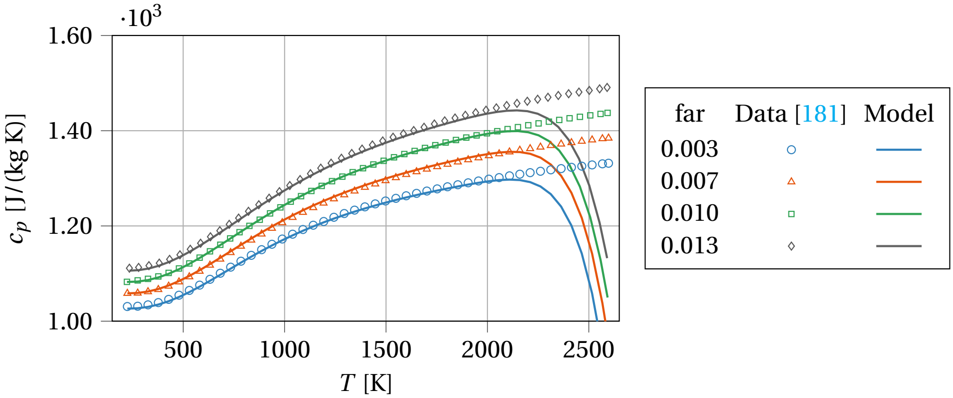

(a) Specific heat capacity

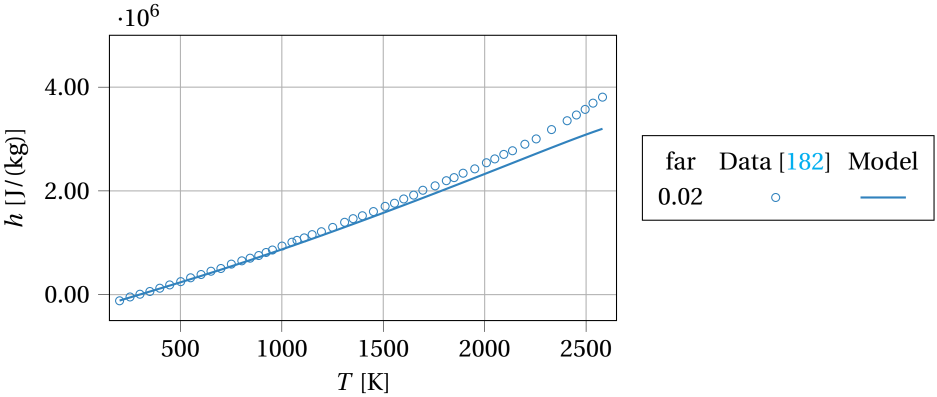

(b) Specific enthalpy

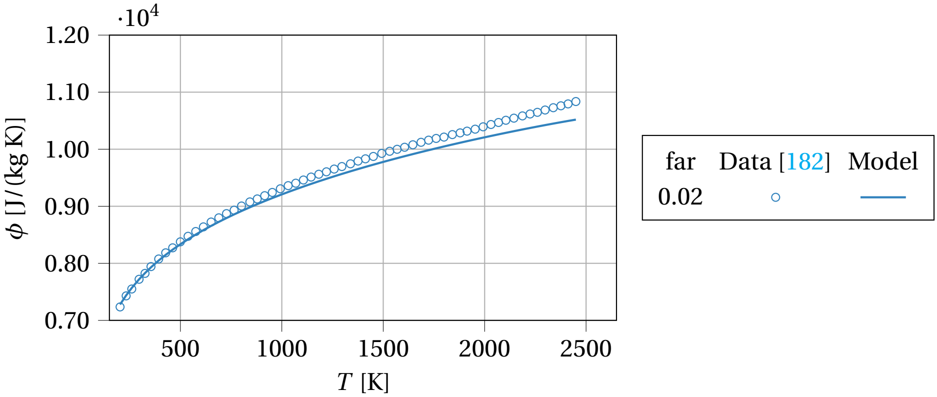

(c) Temperature dependent entropy

Figure 5.5: Validation of gas model parameters as functions of temperature for hydrogen combustion products (far = fuel-to-air ratio)

5.3. RESULTS AND DISCUSSION

With the methods introduced above, design optimizations for different objectives are initiated. The three objectives of interest in this study are the climate impact, measured by ATR_{100}, the cash operating cost, and the energy consumption, which relates directly to fuel consumption. This section presents the optimized designs in Section 5.3.1 and compares the performance of the kerosene and hydrogen concepts in Section 5.3.2.

5.3.1. OPTIMIZED AIRCRAFT SOLUTIONS

This section presents the optimized aircraft solutions and discusses the rationale behind the design decisions. Table 5.3 introduces the design vectors that lead to the minimization of the respective objectives for the kerosene and hydrogen aircraft. For clarity, the optimal solutions designs are treated first per fuel type, after which a comparison is provided in Section 5.3.2.

Table 5.3: Optimized design variables for the three design objectives

	Kerosene			**Liquid Hydrogen**		
Variable [Unit]	**ATR_{100}**	**COC**	**Energy**	**ATR_{100}**	**COC**	**Energy**
W/S [kN/m^2]	5.53	5.30	5.95	5.42	5.15	5.50
A [-]	11.2	7.72	11.5	10.3	10.3	11.3
BPR [-]	10.9	8.43	10.0	10.0	8.83	9.77
Π_{fan} [-]	1.39	1.69	1.55	1.53	1.75	1.70
Π_{lpc} [-]	1.48	1.58	1.56	1.56	1.67	1.50
Π_{hpc} [-]	20.4	22.3	24.1	21.7	20.5	22.3
TET [10^3 K]	1.38	1.52	1.43	1.46	1.47	1.47
h_{cr} [km]	6.01	9.74	10.4	6.02	10.9	10.8
M_{cr} [-]	0.508	0.802	0.726	0.575	0.760	0.720

KEROSENE

The optimization of kerosene aircraft for cost, fuel burn, and climate objectives was the focus of Chapter 3, and therefore the design solutions are not discussed elaborately in the current section. However, since certain elements of the MDO method have been improved, the updated results are presented here. The objective function values and relative differences are summarized in Table 5.4. On the diagonal of the table, the minimum values are shown for each objective function. Off-diagonal entries show the relative change in each performance metric listed in the left column when the aircraft is optimized for the performance metric in the header row, marked with an asterisk.

Since the cost-optimal, kerosene aircraft defines the reference case for the comparison with liquid hydrogen aircraft in Section 5.3.2, its characteristics are briefly summarized here. Table 5.3 presents the optimal design vector for the cost-optimal aircraft. It can be observed that the cruise Mach number ($M_{\text{cr}} = 0.802$) is higher than for the other objectives, reducing the mission block time and, as a consequence, the crew and maintenance costs. The engine features an OPR of approximately 59.9, which is close to the

Table 5.4: Optimized objective values and the relative change with respect to minima obtained for the kerosene aircraft

Parameter [Unit]	ATR_{100}	COC	Energy
ATR [mK]	8.3* (-)	23.2 (+180%)	21.6 (+161%)
COC [10^{12} USD]	9.7 (+17%)	8.3* (-)	8.6 (+3%)
Energy [10^{12} MJ]	4.54 (+8%)	4.69 (+11%)	4.22* (-)

maximum allowed value of 60 and higher than for climate-optimal solution (42.0). The bypass ratio of 8.43, which is lower than for the energy- and climate-optimal aircraft, provides a balance between fuel consumption and engine mass, which drives the related maintenance costs.

Although the cost-optimal kerosene aircraft design is similar to currently available medium-range aircraft, its bypass ratio and aspect ratio are slightly lower than current trends. The bypass and aspect ratios of a modern Airbus A320 are approximately eleven [2] and nine [3], respectively. This underestimation of the optimal bypass and aspect ratios, compared to real aircraft, is partially caused by the selected model for maintenance cost, as discussed in Section 5.4.3.

The kerosene, cost-optimal aircraft has the largest climate impact of all cases considered in this chapter. The main contributors to the climate impact of this aircraft are persistent contrail formation, carbon dioxide emissions, and nitrogen oxide emissions at altitude. Compared to the energy-optimal, kerosene aircraft, the CO_2 emissions are higher due to the higher fuel consumption. When the climate objective is selected for the kerosene aircraft optimization, the aircraft flies lower and slower and features a lower engine OPR. These changes reduce the ATR_{100} by approximately 64%.

The lower cruise altitude prevents the formation of persistent contrails and reduces the radiative forcing due to ozone creation as a consequence of NO_x emissions. Additionally, the lower engine OPR reduces the emissions index of NO_x. However, these changes also lead to a reduction in turbofan efficiency and non-optimal fuel consumption. This makes the CO_2 emissions the largest contributor to the climate impact of the climate-optimal, kerosene aircraft. Therefore, it is expected that liquid hydrogen can further reduce the ATR_{100}.

LIQUID HYDROGEN

In Table 5.5, the optimization results for the three different objectives are shown. This shows that the absolute minimal ATR value for a fleet of medium-range, liquid-hydrogen aircraft is estimated to be approximately 0.3 mK. However, if the objective changes to minimum energy consumption or cash operating cost, the average temperature response is an order of magnitude higher. The trade-off between the cost- and climate-optimal designs is presented graphically in Figure 5.6 together with the design changes. The variations along the Pareto front are elaborated and compared to aircraft powered by other fuels in Chapter 6 (e.g., Section 6.3.2 and Figure 6.10).

---

[2] URL `https://www.cfmaeroengines.com/wp-content/uploads/2017/09/Brochure_LEAPfiches_2017.pdf` accessed on 1 February 2024

[3] URL `https://aviationweek.com/special-topics/sustainability/airbus-x-plane-will-test-inflight-folding-wingtips` accessed on 1 February 2024

Table 5.5: Optimized objective values and the relative change with respect to minima obtained for the hydrogen aircraft

Parameter [Unit]	**ATR_{100}**	**COC**	**Energy**
ATR [mK]	0.2^* (-)	6.3 (+2.49 × 10^3%)	6.2 (+2.45 × 10^3%)
COC [10^{12} USD]	11.5 (+9%)	10.6^* (-)	10.6 (+0%)
Energy [10^{12} MJ]	4.83 (+9%)	4.53 (+3%)	4.41^* (-)

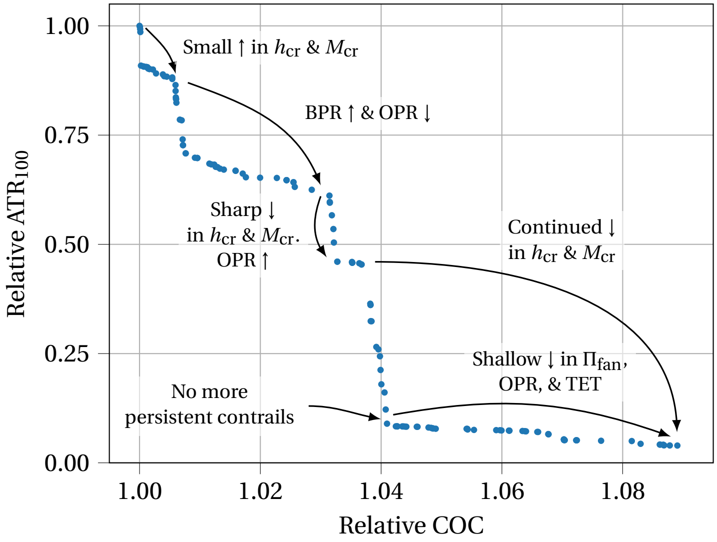

Figure 5.6: Pareto front of cost- and climate-optimal hydrogen solutions, relative to the cost-optimal, hydrogen design (increase and decrease are indicated by ↑ and ↓)

The climate-optimal, hydrogen aircraft features a low cruise altitude (h_{cr}=6.0 km) and Mach number (M_{cr}=0.58). First, this low-altitude operation eliminates contrail formation since the temperature threshold is not met according to the ISA model. Contrails have the largest contribution to the climate impact of hydrogen aircraft, and their elimination thus largely reduces the average temperature response. Second, the impact of $\mathrm{NO_x}$ emissions is also minimized at this altitude, even leading to potentially negative radiative forcing in the long term.

These two effects can be observed in Figure 5.7 where the variation in radiative forcing and ΔT over the considered period are shown for the three climate agents. It can be deduced that the elimination of the persistent contrails in the ATR-optimal case significantly reduces the temperature response. While the long-term effects of $\mathrm{NO_x}$, namely methane and ozone depletion, cause the radiative forcing to become negative for all three objectives, it only causes a negative temperature response for the climate-optimal design due to its low-altitude operation. These two effects lead to a difference of an order magnitude in ATR between the climate-optimal solution and the other two designs. The influence of water vapor as a greenhouse gas is comparable for all three hydrogen aircraft, although the contribution to ATR_{100} is larger than for kerosene aircraft. The residence time of water vapor in the atmosphere increases with altitude, which is not considered in the current climate model. Therefore, it is expected that the climate impact of H_2O will be higher for the aircraft operating at higher altitudes, such as the energy- and cost-optimal designs, compared to the one operating at 6.0 km of altitude.

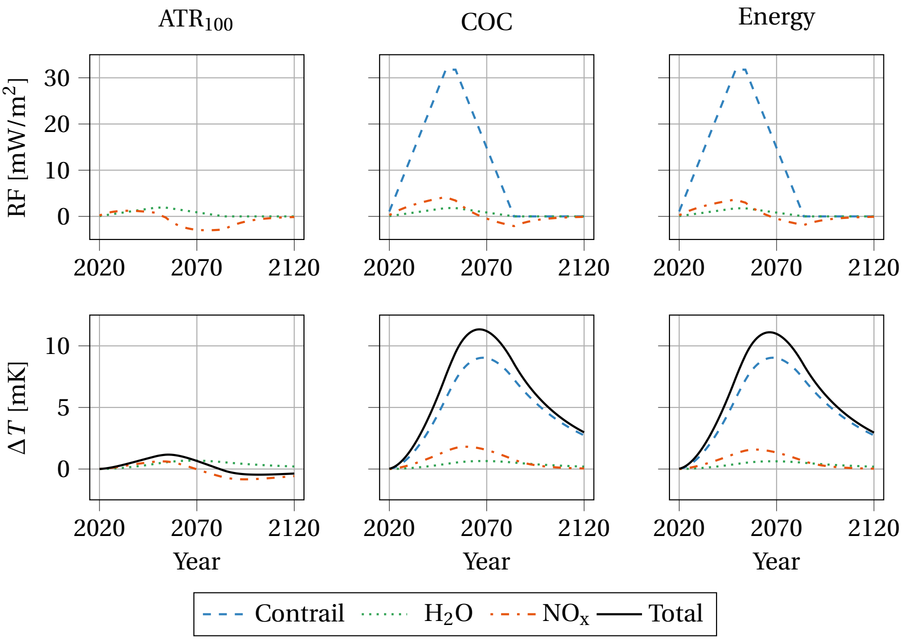

Figure 5.7: Contribution of individual climate agents to radiative forcing (RF) and surface temperature change (ΔT) for the optimized hydrogen aircraft. The title above each column indicates the optimization objective that has been used to design the aircraft.

The climate-optimal aircraft features an unswept wing with an aspect ratio of 10.3 and the maximum achievable $C_{L_{\max}}$ of 2.80, which is facilitated by the Mach number of 0.58. The wing loading is not set to the maximum value limited by the approach speed, but rather close to the W/S value which minimizes the T_{TO}/W ratio. This occurs at the intersection of the OEI climb and take-off constraints in the T_{TO}/W-W/S matching diagram. A bypass ratio of 10.0 is selected by the optimizer together with an OPR of 51.8. This combination minimizes the combined impact of NO_x and water vapor emissions. In the selection of the engine variables, two aspects have to be considered: first, the fuel consumption has to be reduced to lower the total emissions, in particular those of water vapor. Second, a high OPR will lead to an increased emission index of NO_x. These two considerations have to be balanced. Also, since the NO_x emissions at this altitude lead to a cooling effect, the optimizer does not try to minimize fuel burn but makes use of slightly higher absolute NO_x emissions to increase this radiative cooling effect. Nevertheless, a realistic alternative would be to focus on fuel burn reduction while operating at this altitude.

The cost-optimal hydrogen aircraft features the highest cruise Mach number (0.76) and cruise altitude (10.9 km) of the three hydrogen aircraft. The higher cruise velocity, compared to the climate-optimized solution, is crucial to lowering the time-related operating cost. The altitude is increased simultaneously to achieve a near-optimal lift-to-drag ratio to minimize energy consumption. The wing features a quarter-chord sweep angle of 23 degrees as a consequence of the selected cruise Mach number. This limits the achievable $C_{L,\mathrm{max}}$ to 2.58 in landing configuration and, as a result, the wing loading. The wing loading is not set to the maximum value allowed for the approach, allowing for a lower T/W at take-off. The aspect ratio of 10.9 does not reach the upper limit of 12, although the span limit is almost reached. The optimizer selects a bypass ratio of 10.9 in combination with an OPR of 60, which is the upper limit.

The energy-optimal aircraft features similar design characteristics as the cost-optimal aircraft since the operating cost of the hydrogen aircraft is largely driven by the fuel cost. The energy-optimal aircraft cruises at an altitude and Mach number in between the climate- and cost-optimal solutions. A Mach number of 0.72 is selected, requiring less sweep than the cost-optimal aircraft and allowing a higher maximum lift coefficient. This allows for a higher wing loading, compared to the cost-optimal case, and therefore a higher aspect ratio. The wing loading is set to the maximum value allowed to facilitate an approach speed of 70 m/s. With an aspect ratio of 11.3, the wing planform reaches the span limit of 36 m. Also, the buffet constraint is active. Without considering the engine maintenance costs, the optimizer is free to further increase the engine bypass ratio with an OPR value of 57.

Figure 5.8 presents the overlapping top views of the three different hydrogen aircraft. While the geometry of the cost- and energy-optimal concepts are rather similar, a distinction with the climate-optimal aircraft can be observed. Firstly, the quarter-chord wing sweep is zero due to the lower cruise Mach number. Secondly, the fuselage of the climate-optimal aircraft is slightly longer. The climate-optimal aircraft features an engine with lower overall efficiency, due to its operating conditions, resulting in a lower range parameter ($p = \eta_{\mathrm{ov}} \cdot L/D$). This leads to deteriorating fuel consumption and an increase in the fuel mass required to achieve the ferry range. Since the fuel tank is sized for this maximum fuel capacity, the fuselage is longer, in turn leading to more friction drag and worsening the range parameter further. It is expected that in this case, relaxing the ferry requirement would lead to improved flight performance and climate impact, while still being able to serve a large part of the payload-range envelope of the Airbus A320-200, for example.

Figure 5.9 presents the payload-range diagrams for the optimized hydrogen aircraft and compares them to the diagram of the Airbus A320-200. It can be observed that all three hydrogen aircraft have a wider payload-range capability than the Airbus A320-200, caused by the harmonic and ferry range requirements and the higher calorific value of hydrogen. The latter allows achieving a larger range increase with a lower exchange of payload for fuel mass, compared to kerosene. The payload-range envelop of the climate-optimal, hydrogen aircraft also reveals its marginally worse cruise performance com-

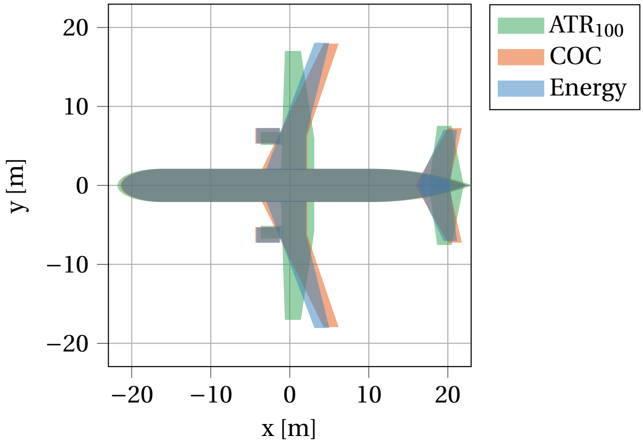

Figure 5.8: Top view of the optimized hydrogen aircraft, where x=0 lies on the quarter-chord point of the MAC

pared to the two other designs, because of the lower range parameter.

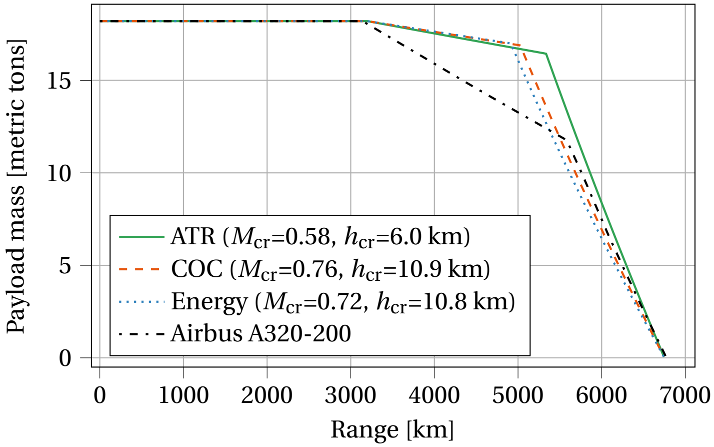

Figure 5.9: Payload-range diagram of the hydrogen aircraft optimized for three different objectives, in this study, and the diagram of the Airbus A320-200 [128]

5.3.2. COMPARISON BETWEEN KEROSENE AND HYDROGEN AIRCRAFT

The current section aims to investigate how the liquid hydrogen alternative compares to the kerosene solution in terms of cost, climate impact, and other performance indicators. These performance indicators are presented in Table 5.6.

By examining the data provided in Tables 5.4 and 5.5, it can be concluded that with respect to the cost-optimal, kerosene aircraft, the cost-optimal hydrogen aircraft can achieve a 73% decrease in average temperature response for the period under consideration, at a 28% cash operating cost increase (assuming a liquid hydrogen price of 4.40 USD/kg). An even larger climate impact reduction can be achieved by optimizing the hydrogen aircraft for minimum climate impact, yielding a 99% reduction in ATR_{100} with an approximate 39% increase in cost. The trade-off between climate impact and cash operating cost for each aircraft type, and between them, is graphically represented by the Pareto fronts in Figure 5.10, where also the influence of varying fuel prices is shown.

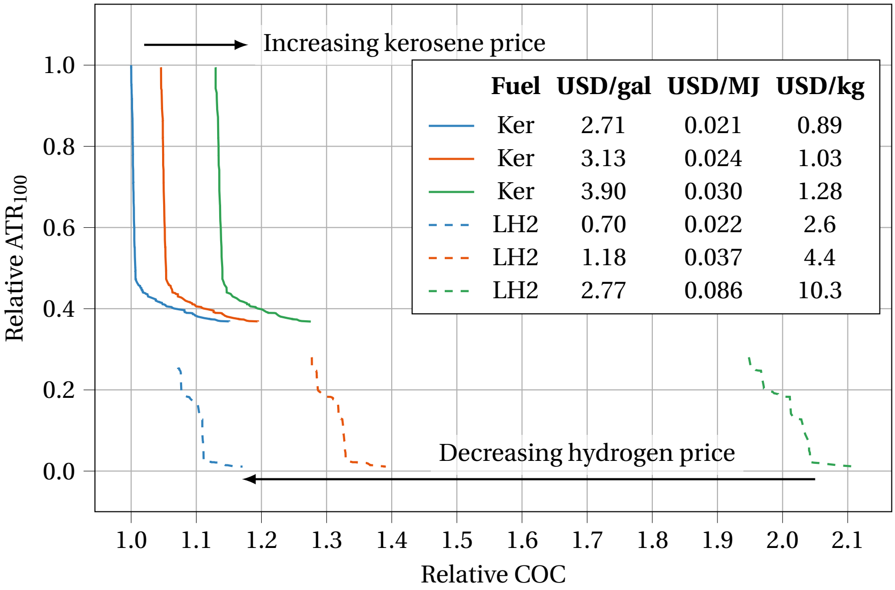

Figure 5.10: Comparison of kerosene and hydrogen Pareto fronts for varying fuel prices, with respect to the kerosene, cost-optimal design

The reason for this immense climate saving potential stems from the eradication of CO_2 emissions and reduction in NO_x emissions, as well as the different contrail properties. The cost increase follows mainly from the liquid hydrogen price. On the other hand, the ATR-optimized hydrogen aircraft does consume 5% more energy than the energy-optimized hydrogen aircraft and 17% more energy than the energy-optimized kerosene aircraft. Since the climate-optimal, hydrogen aircraft suffers from this energy penalty, it also has the largest tank of all three objectives and therefore the longest fuselage.

Table 5.6 presents the performance indicators and geometric parameters for all optimized aircraft. It can be observed that the hydrogen aircraft feature, on average, a 5% lower maximum take-off mass and a 9% increase in operating empty mass compared to the kerosene counterparts. This is primarily caused by the addition of the large fuel tank and the resulting stretch of the fuselage (l_{fus} in Table 5.6). The wing areas are rather similar for all solutions. While the hydrogen aircraft have a lower MTOM, the wing loading is also lower because of the higher maximum landing mass. Therefore, the net difference in wing area is quite small compared to the kerosene aircraft.

From a flight performance perspective, the climate- and energy-optimal hydrogen aircraft are characterized by a lower lift-to-drag ratio in cruise than their kerosene coun-

Table 5.6: Performance indicators for kerosene and hydrogen optimized aircraft

	Kerosene			**Liquid Hydrogen**		
Parameter [Unit]	**ATR$_{100}$**	**COC**	**Energy**	**ATR$_{100}$**	**COC**	**Energy**
MTOM [metric tons]	65.1	68.4	68.2	62.1	65.5	64.5
OEM [metric tons]	36.2	39.5	40.3	40.1	43.8	42.8
S [m^2]	115	127	112	112	125	115
b [m]	36.0	31.3	36.0	33.9	35.8	36.0
$\Lambda_{0.25}$ [deg]	0.0	27.0	18.9	0.0	23.0	18.0
λ [-]	0.460	0.235	0.303	0.460	0.269	0.310
l_{fus} [m]	37.5	37.5	37.5	44.7	43.7	43.5
S_{ht} [m^2]	31	31	26	45	41	39
$(L/D)_{\mathrm{cr}}$ [-]	19.0	16.7	19.2	16.4	17.9	18.4
$(T/W)_{\mathrm{TO}}$ [-]	0.288	0.315	0.330	0.283	0.295	0.303
T_{TO} [kN]	184	211	221	172	190	192
TSFC$_{\mathrm{cr}}$ [10^{-5}kg/(N s)]	1.15	1.41	1.28	0.44	0.48	0.46
$\eta_{\mathrm{ov,cr}}$ [%]	32.6	39.9	39.3	34.8	39.3	38.6
SEC$_{\mathrm{cr}}$ [10^{-4}MJ/(N s)]	4.93	6.05	5.50	5.22	5.71	5.52
Energy [MJ/(pax km)]	0.82	0.85	0.77	0.90	0.83	0.80
t_{bl}	4h23m	3h19m	3h34m	4h1m	3h29m	3h36m
$N_{\mathrm{AC,\,max}}$ [10^3]	18.5	14.0	15.0	16.9	14.7	15.2

terparts. This is largely caused by increased friction drag due to the longer fuselage and larger horizontal tail area. For the energy-optimal aircraft, the wetted area of the fuselage with a hydrogen tank is approximately 18% higher than the wetted area of the fuselage of the kerosene aircraft. On the other hand, the cost-optimal, kerosene aircraft features a lower lift-to-drag than its hydrogen alternative (16.7 versus 17.9). The reason for this is that reducing the fuel cost is more important for the hydrogen aircraft than for the kerosene aircraft, for which the time-bound cost is relatively more important. Therefore, the design of the cost-optimal hydrogen aircraft resembles its energy-optimized variant more closely than the kerosene aircraft, resulting in a higher aerodynamic efficiency.

The engine performance of the hydrogen aircraft sees a 62% to 66% lower thrust-specific fuel consumption due to the higher calorific value of hydrogen. The energy consumption of the energy-optimal, hydrogen aircraft is 4% higher than for the kerosene alternatives. For the cost-optimal aircraft, this trend is again different due to the different relative importance of fuel efficiency.

Finally, Table 5.6 also provides an estimate of the block time t_{bl} of the selected mission, as well as the total number of aircraft $N_{\mathrm{ac,max}}$ to be produced. These numbers vary between the objectives, with slower flying designs resulting in higher block times and more aircraft to meet the required productivity level.

5.4. SENSITIVITIES AND UNCERTAINTIES

The hypothetical future aircraft designs and scenario discussed in this chapter rely on assumptions that have an influence on the objective functions and possibly also the obtained design vector. This section aims to quantify the effect of assumptions related to hydrogen technology, climate modeling, and cost estimation, on the three objective functions considered in the previous section.

5.4.1. HYDROGEN TECHNOLOGY UNCERTAINTY

The first uncertainty is introduced in the conceptual design process of liquid hydrogen aircraft. Although several research projects have looked more closely into the integration of liquid hydrogen tanks and their mass estimation [159, 163, 167, 183], only several aircraft employing hydrogen as fuel have been realized [155]. In the current study, assumptions are made with respect to the mass of the tank, which is determined using the gravimetric index, the extra volume allowance, and the geometry of the tank domes.

Figure 5.11a shows the sensitivity of the three objectives with respect to the gravimetric index for the cost-optimized, hydrogen aircraft. The standard value is taken to be 0.773, which is varied between -14% (0.661) and +3% (0.797), associated with varying design choices [163] and technology scenarios. This value is dependent on the design choices of the tank, such as venting strategy and insulation material choice. From the figure, it can be seen that the gravimetric index has a limited influence on the objective functions, staying within the interval of 3% to -1%, for the cost-optimal aircraft. Although the influence on the operating empty mass is marginally larger (up to 4%), this does not appear to propagate significantly through the other design and analysis disciplines. The sensitivity of ATR_{100} with respect to η_{grav} is the smallest of all objectives. Since there are no CO_2 emissions in this case, the influence of fuel consumption on ATR_{100} is smaller for hydrogen aircraft than for kerosene aircraft.

The sensitivity with respect to the ratio between the dome height and tank radius is presented in Figure 5.11b. The evaluated values are selected based on engineering judgment. This sensitivity is smaller than the one with respect to the gravimetric index. Although $(h/r)_{\mathrm{dome}}$ affects the tank length and hence the fuselage length, the effect seems to be almost negligible (<1%), even on the operating empty mass. Possibly the effect would be higher if the change in dome pressure load due to varying dome radius was considered in the conceptual model.

As mentioned in Section 5.1.2, the employed methods do not account for gaseous hydrogen inside the tank due to boil-off when computing the internal volume of the tank. This additional volume will result in a longer tank, which elongates the fuselage, increasing the mass and drag of the aircraft. Therefore, a sensitivity study is carried out with the parameter $f_{V,\mathrm{extra}}$ to quantify the impact of this volume underestimation on the objectives. Figure 5.11c shows the variation in the objectives as a function of additional fuel tank volume allowance. This analysis shows that when 20% extra volume is considered, the change in objectives appears to be limited to 1.5%. However, this sensitivity only considers the effect due to the elongation of the tank and fuselage, while an increased volume allowance would also affect the tank gravimetric index. Hence, the actual effect is expected to be marginally larger than de sensitivity presented in Figure 5.11c.

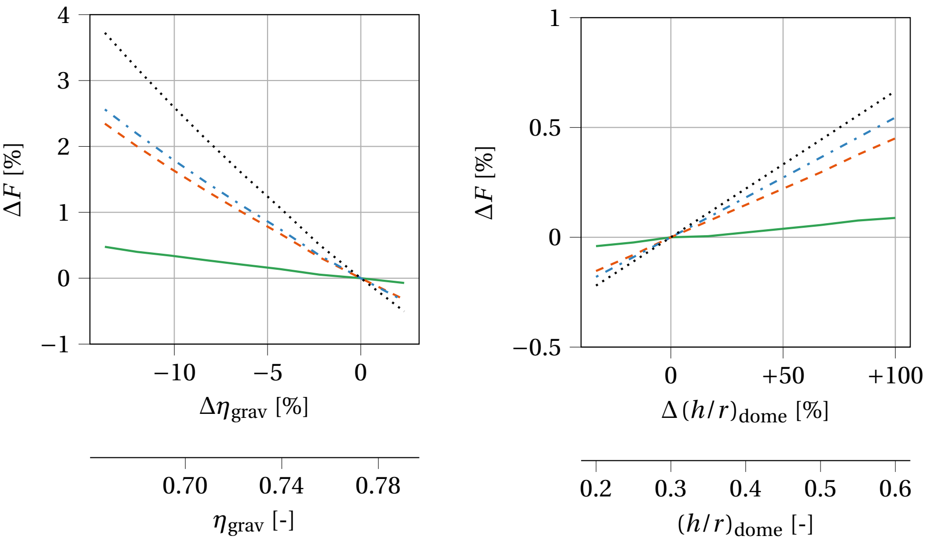

(a) Sensitivity to η_{grav}

(b) Sensitivity to $(h/r)_{\text{dome}}$

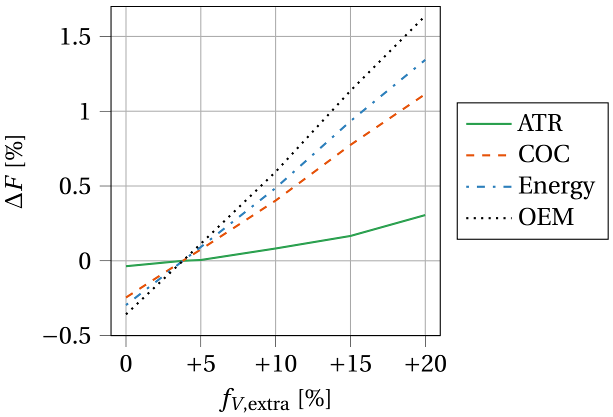

(c) Sensitivity to $f_{V,\text{extra}}$

Figure 5.11: Sensitivity of objective functions and operating empty mass with respect to hydrogen tank parameters for the cost-optimal aircraft

5.4.2. CLIMATE MODEL UNCERTAINTY

The current section aims at quantifying the uncertainty due to climate model assumptions made in Section 5.1.2. The focus lies on the differences between the climate models for the kerosene and hydrogen aircraft, which are the reduction in NO_x emissions and the reduction in contrail radiative forcing. Although the water vapor emissions change, the effect is not considered here since the emission index follows from the chemical balance. Furthermore, it is recognized that more uncertainties apply in the linearized temperature response model. Nevertheless, it is recommended to study and discuss the latter elaborately in separate research.

Figure 5.12 presents the relative difference in temperature response between the kerosene and hydrogen, cost-optimal aircraft for the period under consideration. The estimated line corresponds to the model as employed for the optimizations, assuming a 65% reduction NO_x emissions and a 70% reduction in contrail radiative forcing. The blue band indicates the uncertainty range, considering an interval between 50 and 80% reduction in NO_x emissions [171] and the 90% confidence interval provided by Burkhardt, Bock, and Bier [73]. It can be observed that the uncertainty reduces in time because the uncertainties apply mainly to short-lived effects. Additionally, the overall temperature reduction increases with time because the long-term CO_2 impact is eliminated for the hydrogen aircraft. In summary, the studied uncertainties lead to a variation in ATR reduction between 70 to 75% for the cost-optimal aircraft.

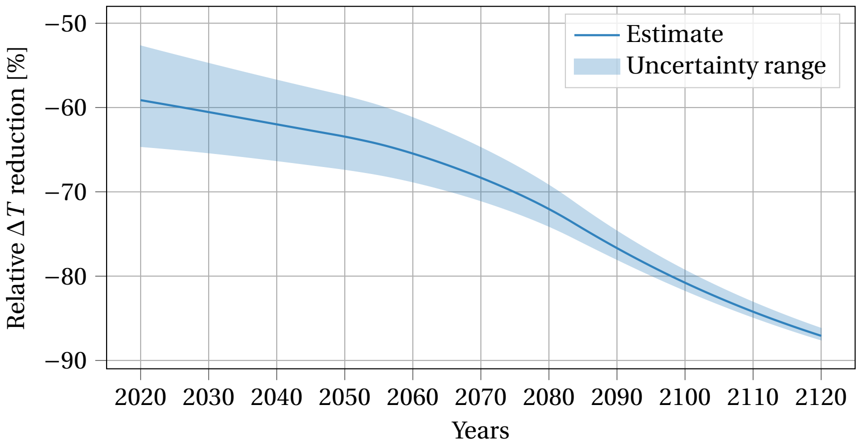

Figure 5.12: Relative surface temperature difference between kerosene and hydrogen, cost-optimal aircraft, including the uncertainty range due to the contrail and NO_x assumptions made in Section 5.1.2

5.4.3. COST MODEL UNCERTAINTY

This section focuses on the uncertainties present in the estimation of the operating costs. Two aspects are considered: the cost model itself and the assumed fuel prices, in particular for liquid hydrogen. The cost model selection can influence the relative importance of fuel- and time-related costs. Examples of the latter group are crew and maintenance costs. This relative importance will favor design choices that minimize fuel impact, reduce flight time, and/or reduce maintenance costs. In the selected cost model, the maintenance costs are in particular sensitive to the engine mass, which is greatly influenced by the chosen bypass ratio. For this reason, the cost-optimal bypass ratio of the kerosene aircraft is lower than current technology standards. Implementation of the AEA model [184, 185], leads to a cost-optimal result with a higher bypass ratio and increased wing aspect ratio, as shown in Table 5.7. However, the optimal OPR is reduced since the AEA maintenance cost estimation is more sensitive to the overall pressure ratio. Nevertheless, the observed trends when moving from the cost-optimal to the climate-optimal solution remain similar. The only difference is that the cost-optimal solution may be closer to either energy-minimizing or time-bound cost-minimizing design points.

Table 5.7: Optimized design variables for the cost-optimal, kerosene-powered aircraft, considering two different maintenance cost estimation methods

Variable [Unit]	**Roskam**	**AEA**
A [-]	7.72	10.0
W/S [kN/m^2]	5.30	5.25
BPR [-]	8.43	10.2
Π_{fan} [-]	1.69	1.68
Π_{lpc} [-]	1.58	1.49
Π_{hpc} [-]	22.3	19.9
TET [10^3 K]	1.52	1.51
h_{cr} [km]	9.74	10.7
M_{cr} [-]	0.802	0.777

Since future operational costs are uncertain for both aircraft types, here the sensitivity of the results with respect to the fuel costs is evaluated. For the hydrogen aircraft, a fuel price of 4.4 USD/kg has been assumed [174] in Section 5.3. During the optimizations, a kerosene price of 2.71 USD/gal is assumed. However, recently the price has been closer to 3.13[4] or has even reached 3.90 USD/gal in May 2022[5]. For kerosene, the cost is varied between 2.71 USD/gal and 3.90 USD/gal. Current price estimates of liquid hydrogen are closer to 10.3 USD/kg. The Pareto front in this case shows a cash operating cost difference of 95 to 111% between kerosene and hydrogen aircraft. Nevertheless, beyond 2030, the price of hydrogen is expected to decrease further, potentially up to 2.6 USD/kg [171]. Considering these projections, the cost of liquid hydrogen is varied between 2.6 and 10.3 USD/kg in this uncertainty analysis.

Figure 5.10 (on page 110) presents the effect of varying fuel prices and the trade-off between cost- and climate-optimal designs. The figure shows that the higher kerosene fuel cost and lower hydrogen fuel cost bring the Pareto fronts closer together. Since it is expected that kerosene prices will continue to rise in the future [171], possibly also because of kerosene taxes, it is clear that the hydrogen and kerosene solution will slowly converge in terms of operating costs.

5.5. CONCLUSIONS

The objective of this chapter is to further explore the potential of liquid hydrogen to power future commercial aviation by performing multidisciplinary design optimizations of hydrogen aircraft and comparing the solutions to kerosene designs. First, a medium-range, hydrogen aircraft is optimized for three objectives, being the energy consumption, cash operating cost, and the average temperature response over a period of 100 years. It is found that the energy- and cost-optimal aircraft are similar due to the large contribution of fuel cost. These aircraft have engines with high bypass and pressure ratios and operate at approximately 10.8 to 10.9 km of altitude and a Mach number of 0.72 to 0.76. The climate-optimal aircraft significantly reduces ATR_{100} by nearly 97%, by flying at an altitude of 6.0 km and Mach number of 0.58, eliminating persistent contrail formation and limiting the radiative effects of short-term ozone creation due to $\mathrm{NO_x}$.

---

[4] URL `https://www.iata.org/en/publications/economics/fuel-monitor/` accessed on 28/09/2022

[5] URL `https://www.indexmundi.com/commodities/?commodity=jet-fuel&months=120` accessed on 29/08/2021

Secondly, it can be observed that the hydrogen cost- and climate-optimal aircraft lead to reductions of 73% to 99% in average temperature response, respectively, compared to the cost-optimal kerosene aircraft. This is caused by the lack of $\mathrm{CO_2}$ emissions, reduced $\mathrm{NO_x}$ emissions, and different contrail properties. Nevertheless, the costs are increased by 28 to 39% because of high hydrogen fuel prices (4.40 USD/kg) and increased energy consumption. The latter is caused by an increase in OEM and a reduction in cruise lift-to-drag ratio, resulting from increased fuselage length due to the integration of the liquid hydrogen tank.

The conceptual design and evaluation requires making key assumptions regarding the hydrogen tank technology level and the projected climate impact due to hydrogen combustion. Considering the cryogenic tank considerations, the design objectives are mostly sensitive to the assumed gravimetric index. The uncertainty in contrail properties and $\mathrm{NO_x}$ emissions of hydrogen aeroengines especially leads to uncertainty in the short-term temperature response reduction, compared to the reference kerosene aircraft.

6

COMPARISON OF FUTURE AVIATION FUELS FOR THREE AIRCRAFT CATEGORIES

Sustainable aviation fuel (SAF) and liquid hydrogen (LH_2) are currently being studied to replace kerosene in commercial aviation to reduce global warming. In this chapter, the question is how do the airplane design variables change when minimizing the global warming impact of aircraft powered by SAF or LH_2? Secondly, how do these aircraft compare in terms of climate impact and operating costs? And, finally, how does this trade-off differ for regional, medium-, and long-range categories? A multidisciplinary design optimization process varies airframe, turbofan engine, and mission design variables. A linearized temperature response model evaluates the average temperature response (ATR) considering CO_2 and non-CO_2 effects. It is concluded that LH_2 can achieve the largest reduction in ATR in all categories. The maximum reduction of 99% compared to the cost-optimal kerosene aircraft comes at an increase of 27, 39, or 64% in operating cost for regional, medium-, and long-range missions. The SAF aircraft can reduce the ATR by 86, 83, and 68% for regional, medium-, and long-range aircraft, leading to an 15, 21, and 27% increase in operating cost. The analysis shows that the SAF-powered aircraft are preferred over the cost-optimal hydrogen aircraft for the regional and medium-range categories. Hydrogen does provide a Pareto-optimal solution for long-range aircraft.

Parts of this chapter have been published and presented at AIAA AVIATION 2022 Forum, Chicago, IL & Virtual, 2022, doi: 10.2514/6.2022-3288, and are currently being reviewed for publication in the AIAA Journal of Aircraft.

THE previous chapter explored the design space of medium-range, hydrogen powered aircraft find the cost-, climate-, and energy-optimal solutions. Compared to the kerosene-powered aircraft, hydrogen can offer significant climate impact savings, especially when designed for this objective. However, due to the integration of the cryogenic tank, the hydrogen aircraft suffer from energy consumption penalties [161, 162]. In combination with the estimated liquid hydrogen prices, the potential climate impact reduction comes at the expense of the operating cost. Therefore, this chapter focuses on another alternative fuel pathway: drop-in sustainable aviation fuels (SAF). These fuel types can offer savings in terms of CO_2 but also affect the aircraft design, costs and non-CO_2 climate effects, such as the formation of contrails and NO_x emissions. Additionally, this chapter extends the design space exploration to the regional and long-range categories.

Sustainable aviation fuels contain hydrocarbon molecules and have properties similar to those of regular kerosene. These fuels can be produced through several pathways such as from a variety feedstocks or a combination of captured CO_2 and hydrogen (H_2) [186, 187]. Since each of these sources, indirectly or directly, take up CO_2 from the atmosphere, the life cycle greenhouse gases (GHG) can be reduced by using SAF compared to fossil Jet-A fuel [186, 187, 188]. However, the exact reduction depends on the feedstock source of the fuel. Furthermore, the reduction of soot emissions of SAF decreases the ice particle number in the exhaust gas and alters the contrail properties [189, 73, 190]. Additionally, the airframe and engines do not require major changes to accommodate these fuels. Nevertheless, estimates have shown that these fuels will be more expensive than fossil-based kerosene [187] as well as electrically-produced liquid hydrogen [171].

Researchers have assessed SAF and hydrogen separately [186, 167]. These studies imposed different aircraft requirements and used methods of varying fidelity. As a result, a consistent comparison between the applications of such novel fuels across different aircraft categories is missing. This chapter compares kerosene, SAF, and liquid hydrogen for fixed sets of aircraft requirements with equal fidelity. The following three aircraft categories are considered: regional, medium-range, and long-range aircraft. This analysis yields insights into what fuel provides the best solution for each category when the climate impact has to be minimized. For each category, the climate impact reduction potential of hydrogen- and SAF-powered aircraft is quantified and compared to a cost-optimal, kerosene-fueled design. Moreover, the influences on operating cost and energy consumption are monitored.

This chapter aims to answer research questions 4 and 5 of Section 1.4. Question 4 focuses on drop-in SAF-powered, turbofan aircraft with the same top-level requirements and mission as in the previous chapters. The following two questions are to be answered:

1. Which set of airframe, engine and mission variables minimizes the global warming impact and cash operating cost?

2. What is the difference in climate impact, cash operating cost, and other flight performance-related parameters when compared to the kerosene and liquid hydrogen aircraft?

Question 5 studies how the trade-off between climate impact and operating cost vary between aircraft categories, considering kerosene, liquid hydrogen, and drop-in SAF.

This chapter is structured as follows. First, the updated optimization problem is formulated and the changes in the design and analysis methods are described in Section 6.1. These methods build upon the MDO framework introduced in the previous chapters. Subsequently, the design methods for regional aircraft are verified in Section 6.2. Section 6.3 presents the results obtained from the optimization studies and compares the climate impact, costs and energy consumption of the three different fuels (kerosene, SAF, and $\mathrm{LH_2}$) for each aircraft category. Finally, Section 6.4 summarizes the findings. In the optimization, the full life cycle impact of the alternative fuels are not considered. Section 8.3 briefly discusses the life cycle effects in more detail.

6.1. PROBLEM FORMULATION AND METHODS

The different fuels, aircraft categories, and design objectives are studied with the same conceptual multidisciplinary design optimization setup. The multidisciplinary methods from the previous chapters are extended to analyze SAF-powered aircraft and regional aircraft. This section briefly re-iterates the definition of the optimization problem and elaborates on the updates in the design and analysis disciplines.

6.1.1. OPTIMIZATION PROBLEM DEFINITION

The MDO setup in this chapter considers two main design objectives: minimizing the climate impact (ATR_{100}) and minimizing the cash operating cost (COC) of the aircraft. By performing these optimization studies in a multi-objective manner, the trade-off between these two objectives can be studied within each aircraft category. Additionally, the optimal aircraft design and/or operational parameters can vary with the selected fuel. The general optimization problem for each combination of fuel and aircraft category can be formulated as follows:

$$\begin{aligned}
\underset{\mathbf{x}}{\text{minimize}} \quad & \mathbf{F}(\mathbf{x}) = \left[\mathrm{ATR}_{100}(\mathbf{x}), \mathrm{COC}(\mathbf{x})\right] \\
\text{subject to} \quad & W/S \leq \frac{1}{2}\rho_0 \left(\frac{v_{\text{app}}}{1.23}\right)^2 C_{L_{\max}} f_{\mathrm{W}}, \\
& b \leq b_{\max}, \\
& \mathrm{TET}_{\mathrm{TO}} \leq \mathrm{TET}_{\mathrm{TO,\,max}}, \\
& \mathrm{OPR}_{\mathrm{cr}} \leq \mathrm{OPR}_{\mathrm{cr,\,max}}, \\
& \Pi_{\text{fan, TO}} \leq \Pi^{U}_{\text{fan}}, \\
& \Pi_{\text{LPC, TO}} \leq \Pi^{U}_{\text{LPC}}, \\
& \Pi_{\text{HPC, TO}} \leq \Pi^{U}_{\text{HPC}}, \\
& C_{L_{\mathrm{cr}}} \leq \frac{C_{L_{\text{buffet}}}}{1.3} = \frac{0.86 \cdot \cos\Lambda_{0.25}}{1.3}, \\
& x_i^L \leq x_i \leq x_i^U \qquad\qquad \text{for } i = 1, 2, \ldots, 9
\end{aligned} \tag{6.1}$$

In the above equation, $\mathbf{x}$ is the design vector consisting of nine design variables related to the airframe, engines, and mission, and $\mathbf{F}$ is the two-dimensional vector containing the objective functions. Table 5.1 summarizes these variables and their bounds. The design variables and the constraints are the same as in Section 5.1.1.

The setup of the multidisciplinary workflow remains the same as in the previous chapter. This workflow is presented in Figure 5.1 and its structure is the same for all fuels and aircraft categories. The differences between the cases lie in the disciplines themselves and the assumed parameters. An optimization algorithm feeds the design vector to the aircraft design iterations. This design convergence ensures that each aircraft is consistent in terms of mass, geometry, and mission performance. A fixed point iteration process, without convergence accelerators, updates the MTOM every iteration based on the OEM estimation from the airframe discipline (Step 2) and the fuel mass from the mission analysis in Step 4. Steps 6 and 7 in Figure 5.1 evaluate the climate impact and costs of a particular aircraft. These analyses provide the objective function values to the optimizer module. The latter then provides an update of the design vector, taking into account the constraint violations determined in step 8.

This multi-objective optimization problem is solved by first performing design of experiments (DOE) with Latin Hypercube Sampling (LHS) and by subsequently applying a multi-strategy, multi-objective optimization algorithm. These two steps are carried out with the help of modeFRONTIER software[1]. The LHS step provides a set of 150 designs to initiate the built-in piLOPT optimization algorithm, which combines local and global search, and different algorithms, including evolutionary methods, to find the Pareto front. The stopping criterion for the piLOPT algorithm is based on number evaluations. The maximum number of design evaluations, including the DOE step, is set to 6000. This number is selected based on convergence studies with respect to the hypervolume indicator [191]. The convergence of the optimizations performed in Section 6.3 is presented in Appendix C.3.

6.1.2. DESIGN AND ANALYSIS METHODS

The design methodology consists of three main design disciplines, indicated by the green blocks in Figure 5.1. Although the design strategy is independent of the fuel type, the steps and assumptions in the disciplines change with the selected fuel and aircraft category. Therefore, this section describes these design steps in more detail. Since the methods for medium-range, kerosene, and hydrogen aircraft have been introduced in Chapters 3 and 5, the focus in this section is the method extension stemming from the analysis of SAF as well as the application to the three different categories.

AIRFRAME

The airframe design step, block 2 in Figure 5.1, consists of four smaller disciplines, namely the Class-I sizing process, the geometry creation, the conceptual aerodynamic analysis, and the Class-II mass estimation, as shown in Figure 5.2. These modules determine the mass, geometry, and aerodynamic characteristics of the wing, fuselage, and empennage. The following paragraphs elaborate further on these four design steps.

Class-I Sizing This step provides an estimate of the wing surface area S and the total take-off thrust, T_{TO}. These two parameters are determined from the wing loading W/S, a design variable, and the minimum thrust-to-weight ratio (T_{TO}/W) which satisfies performance constraints related to the take-off distance, cruise speed and altitude, and climb gradients according to CS25 regulations. The program automatically selects the minimum T_{TO}/W value which satisfies the requirements in Equation (5.2) for the selected wing loading.

---

[1] URL `https://engineering.esteco.com/modefrontier` accessed on 16/02/2022

Geometry Creation A conceptual geometry of the aircraft is generated in each iteration, based on the well-known tube-and-wing configuration. This geometry prediction is used in the aerodynamic and structural disciplines to estimate the operating empty mass and drag polar. During the optimization, mainly the wing and empennage planforms change as a result of the aspect ratio, wing loading, and Mach number. The fuselage geometry is independent of the design vector for the kerosene- and SAF-powered aircraft, while the fuselage length of the hydrogen aircraft varies with the amount of hydrogen on board.

The fuselage is mainly sized around the passenger cabin and cargo compartment, which are modeled after the three reference aircraft the Embraer 175, Airbus A320, and Airbus A350. The assumed cabin length, unit load devices, and resulting fuselage diameters are provided in Table 6.1. A four-meter-long cockpit is added in front of this cabin and a tail extension[2] is added to the rear. The length of this tail extension is computed using the statistical fineness ratios $(l/d)_{\mathrm{tail}}$ in Table 6.1, where d is the outer fuselage diameter of the central fuselage section.

Table 6.1: Geometric and mass assumptions for varying aircraft categories [163, 167]

Parameter [Unit]	**Regional**	**Medium-Range**	**Long-Range**
Cabin length l_{cabin} [m]	21.3	27.0	51.8
Unit load devices	None	LD3-45	2 × LD3
Fuselage inner diameter $d_{\mathrm{fus,\,inner}}$ [m]	2.83	3.91	5.65
Fuselage outer diameter $d_{\mathrm{fus,\,outer}}$ [m]	2.98	4.06	5.99
Horizontal tail aspect ratio A_{HT} [-]	4.5	5.0	4.4
Vertical tail volume coefficient V_{VT} [-]	0.13	0.085	0.051
Vertical tail aspect ratio A_{VT} [-]	1.8	1.7	1.7
Tail section fineness ratio $(l/d)_{\mathrm{tail}}$ [-]	2.1	1.6	1.6
Gravimetric index η_{grav} [-]	0.71	0.77	0.80

For the hydrogen aircraft, a cylindrical tank with ellipsoid endcaps is added behind the cabin in the rear fuselage section. The tank is sized according to the maximum fuel it has to hold, according to the methods introduced in Section 5.1.2. The fuselage tank causes the longitudinal center-of-gravity to shift rearwards and also leads to a larger c.g. excursion, compared to the kerosene and SAF counterparts. These two aspects are reflected in the position of the main wing and the size of the empennage.

The wing planform construction approach, as discussed in Appendix B.2, is the same for all aircraft types considered in this chapter. The framework sizes the horizontal tail by considering the most forward and aft position of the c.g. (i.e., the c.g. excursion) with respect to the mean aerodynamic chord and matching this to the stability and trim constraints. First, the c.g. of the aircraft at OEM is computed using the different components: fuselage, wing, engines, undercarriage, empennage, and tank (for the hydrogen aircraft). In the first aircraft design iteration, the wing longitudinal location is assumed. The engine and undercarriage masses move with the wing location. Later in the aircraft design iterations, the wing location is updated simultaneously with the horizontal tail sizing to yield the smallest horizontal tail surface area. This c.g. position at OEM is used as a starting point to determine the c.g. excursion. The sizing and in-flight c.g. excursion is determined by considering several cases. For kerosene aircraft, the framework constructs the weight and balance diagram by loading all passengers for window, aisle, and in-between seats from the front or the back. Subsequently, the c.g. excursion due to the fuel is added (assuming only wing tanks). The most forward and aft positions are derived from this diagram, adding a 5% margin to these two points. For the hydrogen aircraft, a similar approach is taken by adding passengers and fuel. However, since the fuel tank is positioned in the back of the aircraft, the case where only fuel is loaded without any passengers becomes critical for the most aft c.g. position. This is the largest contributor to the increased c.g. range of the hydrogen aircraft in this study.

---

[2] The tail extension is defined as the distance from the aft-pressure bulkhead to the tip of the fuselage. The tail cone is typically longer than this, housing a part of the cabin.

The vertical tail surface area results from statistical volume coefficients, which are kept constant throughout the optimizations. These volume coefficients together with the tail surface aspect ratios are summarized in Table 6.1. The quarter-chord sweep angle of the horizontal and vertical tails are assumed to be 3 and 10 degrees more than the quarter-chord sweep angle of the main wing, respectively.

Aerodynamic Analysis Based on the geometry and cruise conditions, the aerodynamic analysis provides an update of the drag polar of the aircraft. Similar to the previous chapter, the aerodynamic performance of the aircraft is modeled as a quadratic drag polar consisting of zero-lift drag, lift-induced drag, and wave drag (Equation (5.4)). Corrections are applied to the zero-lift drag coefficient C_{D_0} and Oswald factor e to adapt the drag polar for take-off and landing conditions.

Class-II Mass Estimation The OEM of the aircraft is determined by employing the semi-empirical and statistical methods introduced by Torenbeek [34]. The initial geometry, mass estimate, engine thrust, and load conditions are inputs to these methods. The fuselage mass is largely driven by the outer shell area and the cabin floor mass, among other, smaller components. This makes the fuselage mass sensitive to the integration of hydrogen tanks since this integration elongates the tail extension. For the regional and medium-range aircraft, the tank is assumed to be integrated non-integrally aft of the cabin. The long-range aircraft feature a two-tank layout: one aft of the cabin (60% of the total fuel mass) and one in between the cockpit and the cabin (40% of the total fuel mass). The elongation of the fuselage is reflected in the gross shell weight, while the cabin floor mass is constant for a particular aircraft category.

The structural mass of the wing depends on the geometry (surface area, sweep angle, taper ratio, and span), loading conditions (ultimate load factor and dive speed), $C_{L,\max}$, and the design mass. Torenbeek [34] specifies the design mass as the maximum aircraft all-up mass without fuel in the wing. Therefore, the maximum zero-fuel mass is used in the case of kerosene-powered or SAF-powered aircraft, while the maximum take-off mass is selected for the hydrogen aircraft, as the hydrogen tank is assumed to reside in the fuselage. Furthermore, a correction factor of 0.95 is applied to the calculation of the wing basic structure mass to consider the load alleviation due to two wing-mounted engines [34, Appendix C]. The empennage mass is derived from statistical data, based on the horizontal and vertical tail surface areas and sweep angles.

Within each aircraft category, mass estimates of the operational items and airframe equipment are kept constant throughout the iterations since it is assumed that these contributions do not vary with the selected fuel type, similar to the approach in Section 5.1.2. For the hydrogen aircraft, the tank mass is approximated by assuming a fixed gravitational index η_{grav} which relates the tank mass to the liquid hydrogen mass it can hold (Equation (5.8)). A fixed gravimetric index is assumed for each aircraft category, varying between 0.71 and 0.80, as shown in Table 6.1 [167, 163]. While this gravimetric index is a function of the tank volume and tank design choices, we presume a fixed value per category to simplify the aircraft design iterations and optimization. For medium-range aircraft, the sensitivity with regard to the assumed η_{grav} is discussed in Section 5.4.1. For the long-range category, this sensitivity range of the operating cost is larger, between -4 and +5% for a change in the gravimetric index of -10 or 10%, respectively. The effect on ATR_{100} is limited to -2 and +2% for all categories.

PROPULSION AND FUEL PROPERTIES

The aircraft in this study each feature two turbofan engines with a two-spool, separate-exhaust architecture. A one-dimensional thermodynamic sizing process is applied using the methods from Mattingly, Heiser, and Pratt [105]. These methods allow measuring the impact of engine design choices on fuel consumption and emissions, and in particular, provide the data required to use P3-T3 methods to estimate the NO_x emission index in off-design conditions.

Various types of sustainable aviation fuels exist [187], including hydroprocessed esters and fatty acids (HEFA), alcohol-to-jet, and power-to-liquid SAF. In this study, the latter type is referred to as synthetic kerosene. In the optimizations presented in Section 6.3, a 50-50 mixture of HEFA and kerosene is assumed as the sustainable aviation fuel. In the price sensitivity analysis in Section 6.3.5, also synthetic kerosene and a 100% SAF mixture are studied.

To account for the different fuel types in the thermodynamic on- and off-design analyses, the lower heating values, and the variable specific gas models are adapted. Table 6.2 presents the LHV values and emissions indices used for the different fuels. SAF and hydrogen can be produced free of sulfur [186, 156], and hence the sulfate emissions are assumed to be zero. The sulfate emissions are scaled by the mass percentage of fossil kerosene in the mixture. This assumption is a simplification but the influence is expected to be small because the direct climate impact due to sulfate and soot aerosols is small compared to the other contributions.

The NO_x emission index is computed according to Equation (3.16), as a function of the combustor inlet pressure and temperature. As discussed in Section 6.1.2 we assume a reduction in NO_x emissions for the hydrogen aircraft. This reduction applies to the NO_x emission per unit of energy and not the emissions per unit of kilogram.

Table 6.2: Overview of calorific values and emission indices for fuel types under consideration [24]

	Kerosene	**SAF 50%**	**SAF 100%**	**Hydrogen**
LHV [MJ/kg]	43.0	43.6	44.2	120
EI CO_2 [kg_{CO_2}/kg_{fuel}]	3.16	1.58	0.	0.
EI H_2O [kg_{H_2O}/kg_{fuel}]	1.26	1.32	1.36	8.93
EI Soot [kg_{Soot}/kg_{fuel}]	4.0×10^{-5}	2.0×10^{-5}	0.	0.
EI SO_4 [kg_{SO_4}/kg_{fuel}]	2.0×10^{-4}	1.0×10^{-4}	0.	0.

As can be seen from Table 6.2, the LHV of SAF fuel is slightly higher than that of fossil-based kerosene due to the lower aromatics content, which increases the number of carbon-hydrogen bonds and, as a result, the energy content per unit of mass [192]. Due to the lack or reduction in aromatics, sustainable aviation fuels also have a higher hydrogen mass content. This explains why the water emission index is slightly larger in Table 6.2. The higher water emission index also influences the contrail formation criterion, as discussed in Section 6.1.2.

The thermodynamic model of the engine cycle uses a variable specific heat model such that the isobaric specific heat c_p varies with temperature and fuel-to-air ratio. Since the SAF variants have a higher water content than kerosene, the gas in the turbines is characterized by a higher c_p value. Nevertheless, previous research [193] has shown that the influence of this difference on engine performance is negligible. Therefore, the same gas model from Walsh and Fletcher [112] is used both for kerosene and SAF-based propulsion. For the hydrogen-powered turbofan, the gas model introduced in Section 5.1.2 is employed to reflect the increase in water and lack of carbon molecules in the turbines.

MISSION PERFORMANCE

The mission analysis step in Figure 5.1 provides an update of the required fuel mass in the aircraft design loop, which, together with the updated OEM and specified payload mass, provides an update of the MTOM in the converger (process 1 in Figure 5.1). Additionally, for the hydrogen aircraft, the maximum required fuel is computed in this mission analysis step as a function of the engine and aerodynamic performance. The hydrogen mass is required to estimate the tank size and mass, and as a consequence, to update the size of the fuselage, wing, and empennage.

The fuel mass is updated using the conceptual lost-range method [115] to limit the computational cost in the design convergence process. Section 3.1.2 discusses this method and Section 3.1.2 elaborates on the differences for hydrogen aircraft. Since the calorific value of the SAF mixture is close to that of fossil kerosene, no changes are made to the lost-range method for the SAF-powered aircraft.

CLIMATE IMPACT

The climate impact caused by in-flight emissions and contrail formation is one of the optimization objectives in this study. The aim is to consider both CO_2 and non-CO_2 climate agents and to include both their short- and long-term effects, of the fuels under consideration. Therefore, the climate impact metric of choice is the average temperature response over 100 years (ATR_{100}). The 100-year period under consideration starts in the year that the aircraft model under consideration is introduced into the market. Section 6.1.3 defines the hypothetical fleet scenarios for each aircraft category.

The temperature response ΔT is determined using a linear temperature response model. The working principle of this model and the assumptions for the case of kerosene and hydrogen have been laid out in previous chapters. This section summarizes the particular model assumptions for SAF-powered aircraft. The climate impact model for kerosene and the updates for hydrogen aircraft are discussed in Section 3.1.2 and Section 5.1.2. Since certain climate effects are still not fully understood, uncertainties are present in this climate model. Section 8.5 discusses the uncertainties per fuel type.

The major climate impact reduction from SAF arises from the reduction in CO_2 emissions. Since such fuels are derived from biomass or waste products, the net new carbon introduced into the global carbon cycle is lower than for fossil kerosene [187]. This net effect is discussed in Section 8.3. If we purely consider the impact of in-flight CO_2 emissions, this impact can be assumed to be zero, i.e. carbon-neutral flight [188, 194]. Similar to CO_2, the effects due to soot and sulfur emissions are expected to be zero in the case of 100% SAF or halved when a 50-50 mixture with fossil kerosene is used.

The NO_x emissions and their effects remain unchanged for SAF(-mixtures). This is because the NO_x production depends on the combustion characteristics, such as flame temperature and speed, which are similar for kerosene and SAF. The study by Moore et al. [195] confirms that the NO_x emissions are similar for Jet-A fuel and a 50-50 blend of HEFA and Jet-A.

On the other hand, the use of SAF is expected to lower the radiative impact due to contrails, while the slightly higher water content can lead to the more frequent formation of contrails near-threshold conditions [192]. The reduction in radiative forcing arises from the lower aromatics content in biofuels. These aromatics are precursors for soot [14]. Lower soot emissions lead to a lower amount of condensation nuclei. In turn, this leads to a lower ice crystal number and larger crystal size. This larger crystal size also performs a role during the vortex phase of the contrails, where more ice particles are expected to survive [192, 196]. Nevertheless, the lower ice crystal number and larger size lower the optical thickness of contrails and reduce their lifetime [73]. We assume a 50% reduction in contrail radiative forcing compared to aircraft powered fully by kerosene, approximating an 80% reduction in ice crystal number [73, Figure 1f].

COST

The second optimization objective is the cash operating costs (COC). In the current analysis, the cash operating costs consist of flight costs, namely fuel, oil, and crew, as well as maintenance costs. These components make the COC dependent on cruise efficiency, flight time, and distance flown. Other costs, such as depreciation and fees, are omitted in the current analysis to reduce the uncertainty.

At the time of writing, the fuel price of kerosene is the lowest of the three fuel options considered. The kerosene fuel price is assumed to be 2.71 USD per US gallon. The price of liquid hydrogen is set to 4.40 USD/kg [174], or approximately 1.18 USD per gallon, although this price level is expected to further reduce in the upcoming decades. Considering sustainable aviation fuel, research from the World Economic Forum indicates that

HEFA-SPK will cost approximately 1159 USD per ton, or 3.53 USD per gallon, in 2030 [187]. The price estimate of synthetic kerosene is higher at 1967 USD per ton. In this research, we use the price estimate for HEFA-SPK for the initial optimizations.

The costs associated with the cabin crew, consisting of a captain, first officer, and cabin attendants are modeled according to the methods laid out in Section 3.1.2. The number of flight attendants per flight amounts to at least one cabin crew member per 35 passengers. The assumed salaries for onboard and maintenance personnel represent the average salaries in the United States in 2020 and 2021.

The maintenance cost includes the labor cost for the airframe and engines, the materials for the airframe and engines, and the maintenance burden [35]. The same maintenance cost model for all fuel types. As discussed in Section 5.1.2, the potential increase in maintenance costs for hydrogen aircraft is not considered in this analysis.

6.1.3. TOP LEVEL REQUIREMENTS AND FUTURE FLEET SCENARIOS

Three different aircraft categories are considered in this chapter, being regional, medium-range, and long-range aircraft. Although the names are related to the range requirement, the categories also feature distinct payload specifications. Table 6.3 summarizes the top-level aircraft requirements for each aircraft category. The values are taken from the Aircraft Characteristics and Airport Planning documents of the respective reference aircraft, namely the Embraer 175 [197], the Airbus A320 [128], and the Airbus A350 [198]. The landing mass factors are deduced from the maximum landing mass of the aircraft. For hydrogen aircraft, the landing mass factor is larger because the fuel is lighter.

The climate impact is measured with the average temperature response over 100 years starting in 2020, although this point is chosen arbitrarily. In this period, the aircraft are introduced into the market from 2020 onward, are operated for 35 years, and are retired. The annual aircraft production is constant and ends in the year 2050. This means that the fleet size increases linearly from 2020 to 2050, is constant between 2050 and 2055, and reduces linearly until the complete fleet is retired in 2085.

The fleet size reaches its maximum in 2050 and the number of operational aircraft depends on the productivity level set, similar to the approach taken in the previous chapters. This productivity level is expressed as the revenue passenger kilometers (RPK) per year, for a given aircraft category. These productivity levels in the year 2050 are derived from data in the United States provided by the Bureau of Transport Statistics, the Airline Data Management project [130], and the Regional Airline Association [199]. For each category, a 2% annual growth in RPK is assumed until 2050, yielding the projections provided in Table 6.3. Furthermore, it is imposed that the entire demand is covered by the newly introduced, optimal aircraft. The summary tables in Appendix E indicate the total aircraft produced for each category, depending on the optimization case.

To estimate the emissions and subsequently the climate impact, a reference mission is assumed for each aircraft type. These missions are defined by the number of passengers and stage length in Table 6.3 and represent the average mission flown in the aircraft category. The chosen load factor and block range are derived from transport data in the past decade [130, 199]. These reference missions lie well inside the respective payload-range envelopes and are not constraining design missions.

Table 6.3: Top-level aircraft requirements employed for the aircraft design [128, 197, 198]

Requirement [Unit]	**Regional**	**Medium-Range**	**Long-Range**
Maximum structural payload $m_{\mathrm{pl,max}}$ [metric tons]	10.2	18.2	54.0
Harmonic range r_{harm} [km (nmi)]	2410 (1300)	3200 (1730)	10800 (5830)
Ferry range r_{ferry} [km (nmi)]	4630 (2500)	6750 (3645)	18000 (9720)
Approach speed v_{app} [m/s (kts)]	69.0 (134)	70.0 (136)	72.0 (140)
Take-off length (ISA conditions) [m (ft)]	1700 (5580)	2100 (6890)	2700 (8860)
ICAO Reference Code	3C	4C	4E
Maximum span $b_{\max}$ [m]	36.0	36.0	65.0
Diversion range r_{div} [km (nmi)]	185 (100)	463 (250)	463 (250)
Loiter time t_{hold} [min]	45	35	35
Landing mass factor f_{W} kerosene and SAF [-]	0.91	0.88	0.73
Landing mass factor f_{W} hydrogen [-]	0.97	0.96	0.89
RPK 2050 [pax km / year]	2.98×10^{11}	3.95×10^{12}	1.21×10^{12}
Reference block range r_{bl} [km (nmi)]	894 (483)	1852 (1000)	6060 (3270)
Reference load factor (passengers) [-]	0.80 (67)	0.72 (130)	0.58 (253)

6.2. VALIDATION OF DESIGN METHODS

The majority of the above design methods have been verified in the previous chapters. This verification included the physics-based thermodynamic analysis and design of the engines, both for kerosene- and hydrogen-powered aircraft, and the aircraft design convergence for medium-range and long-range aircraft. No additional verification is required for the SAF-powered engines since these engines are evaluated with the verified kerosene gas model. Only the mass estimation, geometry prediction, and performance calculations have to be evaluated for the regional aircraft.

The Embraer 175 serves as the reference aircraft to verify the assumptions and design methods for regional aircraft. The assumed top-level requirements are equal to the ones provided for regional aircraft in Table 6.3. The geometric parameters for the regional aircraft in Table 6.1 are used to model the Embraer 175. Appendix A.2 summarizes the assumed engine design variables and component efficiencies. Due to the lack of public CF34-8E component efficiencies, these parameters are assumed similar to those of the CFM56 which powers medium-range aircraft such as the Airbus A320. Further details on this engine can be found in Table A.6.

Table 6.4 compares the main mass groups and geometric features of the modeled aircraft with data of the Embraer 175 [197]. These relative differences are deemed acceptable for the current design analysis. Figure 6.1 also indicates that the fuselage geometry and wing planform match well with those of the real aircraft. This similarity indicates that the geometric and performance assumptions allow accurate modeling of the aircraft. The wing position is computed by assuming that the OEM center-of-gravity lies at approximately 35% of the mean aerodynamic chord. Of course, this assumption relies on a conceptual estimation of the masses and relative position of the different structural groups, namely the fuselage, engines, wing, empennage, furnishing, and systems.

Table 6.4: Validation of aircraft design modules for Embraer 175 [197] (the fuel mass is evaluated at the harmonic range with maximum structural payload)

Parameter [Unit]	**Framework**	**Reference**	**Difference [%]**
MTOM [metric tons]	37.1	37.5	-1.0
OEM [metric tons]	21.2	21.5	-1.6
Fuel Mass m_{fuel} [metric tons]	5.78	5.80	-0.3
Wing area S [m^2]	72.2	72.7	-0.7
Wing span b [m]	24.9	26.0	-4.2
Outer fuselage diameter $d_{\text{fus,outer}}$ [m]	2.98	3.01	-1.0
Fuselage length l_{fus} [m]	31.6	31.7	-0.3

Figure 6.2 compares the simulated payload-range diagram to the actual diagram of the Embraer 175 aircraft. Up to the payload-range combination where the maximum usable fuel is reached, the diagram and slope correspond well to the actual performance. Beyond this point, between approximately 3600 km and the ferry range, it appears the range gained due to payload removal is underestimated by the model. Since the slope prior to this section is modeled correctly, it is hypothesized that the cause of this offset is a difference in reserve-fuel calculation or strategy.

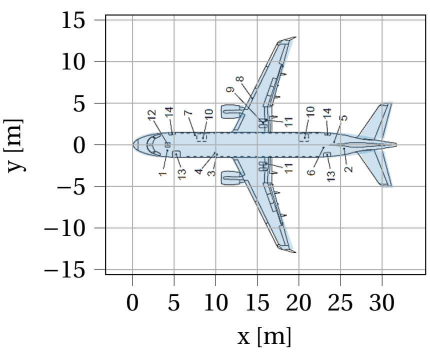

Figure 6.1: Verification of Embraer 175 top view geometry (black lines correspond to actual geometry from Reference [197], the blue shaded shape is the modeled aircraft)

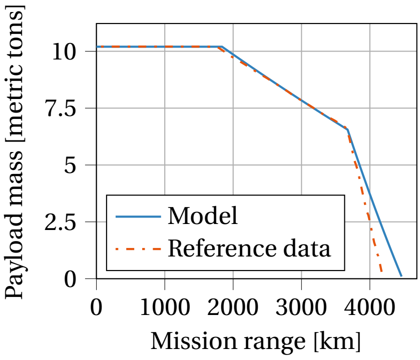

Figure 6.2: Verification of Embraer 175 payload-range diagram [197] (M_{cr}=0.78, h_{cr}=10.7 km)

6.3. RESULTS AND DISCUSSION

The methods from Section 6.1 are employed to perform the multidisciplinary design optimizations for the three fuel types and three aircraft categories. The results for each aircraft type consist of the optimized objective values and design vectors for each fuel type, as well as a comparison of the temperature response. Additionally, the trade-off between the cost and climate design objectives is studied for all fuel types simultaneously by plotting the Pareto fronts, using the kerosene, cost-optimal aircraft as reference cases. For the SAF-powered aircraft considered in Sections 6.3.1 to 6.3.3, a mixture of 50% HEFA and 50% fossil kerosene is assumed, the current (2022) maximum allowed limit. Appendix E provides more insight into the features of each optimized aircraft. Furthermore, a comparison of different SAF mixtures and their influence on the COC is presented in Section 6.3.5.

6.3.1. REGIONAL AIRCRAFT

The optimizations of the regional aircraft show that a significant reduction of up to 71% in ATR_{100} is possible using kerosene. This result and the optimized objective values for each fuel type are presented in Table 6.5. To achieve this climate-impact saving with kerosene, the aircraft is designed to fly at an altitude of 6 km and a Mach number of 0.50, as summarized in Table 6.6. These two design variables reach the lower bounds of the design space. The slower flight and longer block time increase the cash operating costs by approximately 12%. Compared to the other categories, this cost penalty is limited since the regional aircraft have a relatively short cruise phase compared to other mission phases. Therefore, the reduction in block speed has a small effect on time-driven cash operating costs compared to the medium- and long-range categories.

When the SAF mixture is used in regional aircraft, the average temperature response can be reduced by 41% if the aircraft is optimized for costs, and 86% if the climate-

Table 6.5: Relative differences in the objective values for the regional aircraft. The column headers are the objectives for which the aircraft are optimized.

	Kerosene		**Hydrogen**		**SAF - HEFA (50-50)**	
Variable	**ATR_{100}**	**COC**	**ATR_{100}**	**COC**	**ATR_{100}**	**COC**
ATR_{100}	-71%	-	-99%	-67%	-86%	-41%
COC	+12%	-	+27%	+20%	+15%	+3%
E_{fuel}	-10%	-	-5%	-8%	-9%	-1%

optimal solution is taken. Liquid hydrogen can provide the largest ATR_{100} reduction (99%) of all three fuels if the climate objective is prioritized over the costs in the design. The higher fuel price leads to a 27% increase in costs compared to the cost-optimal, kerosene aircraft, as can be seen in Table 6.5.

Table 6.6 presents the design variables corresponding to the optimized objectives in Table 6.5. When switching from the COC objective to ATR_{100}, all aircraft fly lower and slower, have a higher bypass ratio, and feature a lower fan pressure ratio. The lower fan pressure ratio is accompanied by a higher bypass ratio for the climate-optimal alternatives. The OPR reaches the upper limit of 60 for all cost-optimal aircraft, while the OPR is reduced for the climate-optimal aircraft. The climate-optimal kerosene and SAF aircraft feature an OPR in cruise of 44 and 48, which is driven by the NO_x emission index. For hydrogen aircraft, this OPR is only reduced to 54.

The kerosene and SAF aircraft exhibit similar design strategies, despite minor offsets in the optimal design variables. Three reasons are expected to contribute to these differences. First, due to the higher fuel cost of the SAF mixture, the aircraft flies marginally slower and features a higher aspect ratio, moving towards the energy-optimal solution. Second, the SAF fuel features a slightly higher LHV (approximately 1.3%), resulting in a marginally lower fuel mass than its kerosene counterpart. If the SAF aircraft is designed with the same design variables as the cost-optimal, kerosene aircraft, the fuel mass of the harmonic mission is approximately 1% lower than that of its kerosene alternative. This fuel mass reduction also leads to a minor difference in MTOM. This effect is only noticeable because the design approach develops the aircraft specifically for this fuel. In reality, where SAF is likely to be used as a drop-in fuel, the most conservative fuel mass estimate should be used to design the aircraft. Finally, small differences in design variables are expected to be caused by minor convergence errors in the aircraft design and optimization processes due to finite, yet small, termination criteria of 1×10^{-5}.

If the kerosene and SAF aircraft are compared to the hydrogen alternative, several observations can be made. First, the cost-optimal hydrogen aircraft cruises at a lower Mach number and higher altitude. The high cost of hydrogen makes the relative fuel contribution to the operating cost more important, requiring a more energy-optimal solution rather than one that also minimizes the time-driven costs. The need for an energy-optimal solution is also confirmed by the higher aspect ratio of the cost-optimal solution. Although this raises the wing mass, the lower sweep angle limits the mass penalty. Although the Mach number decreases, the cruise altitude is increased because the ideal cruise lift coefficient, to achieve an optimal L/D, is higher for the cost-optimized hydrogen aircraft than for the cost-optimal kerosene and SAF aircraft. Compared to the cost-optimal kerosene aircraft, the cruise lift coefficient is higher since the aspect ratio is increased (10.6 vs. 6.81) and since the hydrogen aircraft has a higher C_{D_0} (0.0212 vs. 0.0185), due to the tank integration increasing the fuselage and empennage size. The higher ideal $C_{L_{\mathrm{cr}}}$ thus forces the aircraft to cruise at a lower dynamic pressure or, equivalently, in less dense air at a higher altitude.

Furthermore, when moving from the cost objective to the climate one, the TET decreases for the kerosene and SAF solutions, while this is not the case for the hydrogen aircraft. In certain cases, the optimizer chooses a lower W/S than the allowed maximum to favor a lower thrust-to-weight ratio T/W in take-off.

Table 6.6: Optimized design variables for the regional aircraft, considering each fuel type and design objective. The bottom and top bars indicate design bounds.

	Kerosene		**Hydrogen**		**SAF**	
Variable [Unit]	**ATR$_{100}$**	**COC**	**ATR$_{100}$**	**COC**	**ATR$_{100}$**	**COC**
W/S [kN/m^2]	5.33	5.13	5.47	5.18	4.95	5.08
A [-]	$\overline{12.0}$	6.81	10.1	10.6	$\overline{12.0}$	7.16
BPR [-]	10.3	7.25	$\overline{11.0}$	8.46	9.45	7.49
Π_{fan} [-]	1.45	1.74	1.55	$\overline{1.80}$	1.49	1.76
Π_{lpc} [-]	1.49	1.59	1.58	1.45	1.53	1.50
Π_{hpc} [-]	20.4	21.7	22.0	22.9	21.0	22.6
TET [10^3 K]	1.42	1.49	1.51	1.48	1.42	1.51
h_{cr} [km]	$\underline{6.00}$	9.63	$\underline{6.00}$	10.8	$\underline{6.00}$	9.87
M_{cr} [-]	$\underline{0.50}$	0.80	0.60	0.75	$\underline{0.50}$	0.79

All climate-optimal aircraft reach the lower bound of the cruise altitude, and the kerosene and SAF aircraft also feature a Mach number close to the lower bound. A post-optimality study reveals that the climate impact can indeed be reduced further by lowering the cruise altitude and Mach number (i.e., positive Lagrangian multipliers). This analysis indicates that the climate-optimal designs should be able to cruise at even lower altitude and/or Mach numbers. However, these options are not considered in the current paper since several design considerations apply. First, when lowering the Mach number below 0.5 or 0.6, a logical design step, from a flight performance perspective, is to switch to propeller-based propulsion which improves propulsive efficiency in these operating conditions. This will lower the fuel burn and CO_2, and consequently the operating cost and climate impact. Second, a minimum design cruise altitude of 6 km is maintained to clear certain mountain ranges on medium-range missions. This bound can be overcome by offering the optimizer the possibility to fly lower, but imposing a higher service ceiling constraint. Finally, by flying at lower cruise altitudes, different weather conditions or frequency of turbulence may be become of importance for airframe and systems design. However, these considerations are outside the scope.

The tables in Appendix E provide more information about the optimized aircraft, including constraint values. Although these tables show that not all constraints are active for the cost- and/or climate-optimal aircraft, it is important to keep all constraints in the optimization definition since the constraints can become active along the Pareto front.

One can compare the different geometries of the regional aircraft concepts in Figure 6.3. For both the cost and climate objectives, it is clear that the kerosene- and SAF-powered aircraft are nearly identical. The hydrogen aircraft, on the other hand, features a longer fuselage to house the cryogenic tank. This integration elongates the fuselages by 2.9 m in the case of cost-optimal aircraft and by 3.7 m for the climate-optimal alternative. A larger tank is required for the climate-optimal solution due to its higher energy consumption. Furthermore, the cost-optimal, hydrogen aircraft flies at a lower Mach number and therefore has a lower wing sweep angle compared to the other fuels.

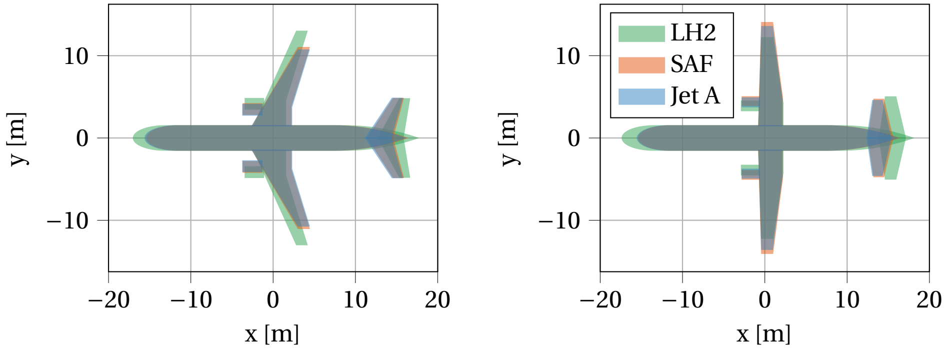

(a) Cost-optimal

(b) Climate-optimal

Figure 6.3: Comparison between top-view geometries of cost- and climate-optimal, regional aircraft employing different fuel types. x=0 lies on the quarter-chord point of the MAC.

The ATR_{100} objective is computed from the mean surface temperature response over the 100 year considered in the hypothetical scenario. While the ATR offers an overall evaluation of the climate impact, the temperature response yields more insight into the timeline of the climate impact due to the fleet operation. Figure 6.4 presents the temperature response for the cost- and climate-optimal design, considering different fuels. Comparing Figure 6.4b to Figure 6.4a, one can deduce that mainly the short-term, hence non-CO_2, effects are reduced by flying lower and slower. In particular, the contrail contribution, which is 58% for the cost-optimal kerosene aircraft, vanishes by applying these changes in the mission profile. The difference between the kerosene and SAF responses is due to the altered contrail properties and CO_2 reduction. The response of SAF is lowered further by switching to hydrogen because CO_2 emissions are eliminated and because the NO_x emissions are reduced. Nevertheless, the contribution due to H_2O is higher for the hydrogen aircraft. The relative contribution of water as a greenhouse gas for the cost-optimal, hydrogen aircraft is approximately 4% whereas it is less than 1% for the kerosene counterpart.

In Figure 6.4b, the hydrogen, climate-optimal aircraft shows a low to slightly negative temperature response between 2080 and 2120. This is a result of the long-term NO_x effect in the absence of contrails or long-term CO_2 contributions. When emitting NO_x emissions at a relatively low cruise altitude, e.g. 6 km, the radiative forcing due to short-term ozone creation (warming effect) is smaller than the cooling effect due to long-term

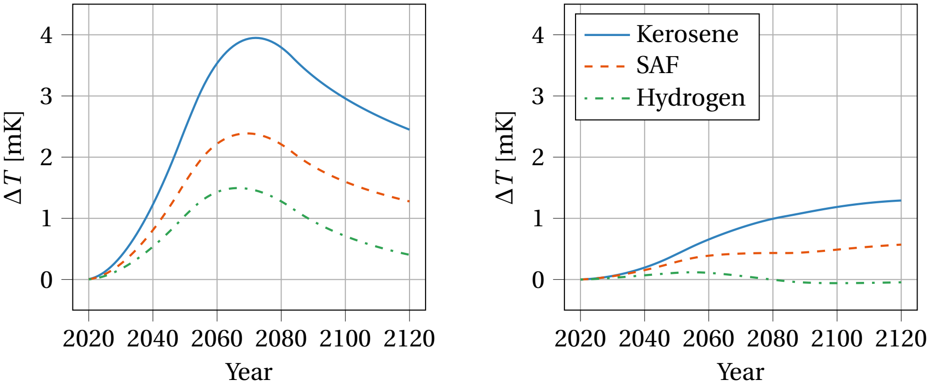

(a) Cost-optimal

(b) Climate-optimal

Figure 6.4: Comparison between mean surface temperature responses of cost- and climate-optimal, regional aircraft employing different fuel types

methane and ozone depletion. The net effect of NO_x emission at these altitudes is thus a cooling radiative forcing. This effect is presented in the research by Köhler et al. [60], on which the current model is based. In the case of single-objective optimization of hydrogen aircraft, the optimization algorithm makes use of this potentially negative temperature response to minimize ATR_{100}. Nevertheless, from an aircraft design perspective, it might be beneficial to prioritize energy consumption minimization at this altitude rather than emitting extra NO_x to minimize the climate impact.

In Figure 6.5, the trade-off between cash operating costs and climate impact reduction is studied for the different fuels in the regional aircraft category. The kerosene-powered aircraft would allow a significant climate impact reduction of 65% before the SAF aircraft becomes Pareto-optimal. A redesigned kerosene aircraft would therefore be preferred to a SAF-powered aircraft since it can provide a similar climate impact reduction at a lower cost increase. SAF can reduce the climate impact further, up to 86% for a 15% increase in costs. The maximum climate impact reduction is achieved with liquid hydrogen. However, only the design solutions close to the climate-optimal hydrogen design appear to be Pareto-optimal. This indicates that, for the regional market, SAF aircraft are preferred to cost-optimized hydrogen aircraft.

6.3.2. MEDIUM-RANGE AIRCRAFT

Table 6.7 presents the objective values for the optimized medium-range aircraft, relative to the kerosene, cost-optimal aircraft. While a reduction of 64% in ATR_{100} can be realized with kerosene aircraft, the potential savings with SAF and hydrogen are larger. As shown in the table, sustainable aviation fuels (here HEFA and kerosene mixture) can offer a reduction between 47 and 83%, for a cash operating cost increase of 4 to 21%. Along with this decrease in ATR_{100}, the in-flight energy consumption (E_{fuel}) of the SAF aircraft is similar to that of the kerosene reference case or even slightly lower.

The hydrogen aircraft offer the largest climate impact reduction potential for the hypothetical fleet, up to 99%. This reduction follows from the elimination of CO_2 emissions

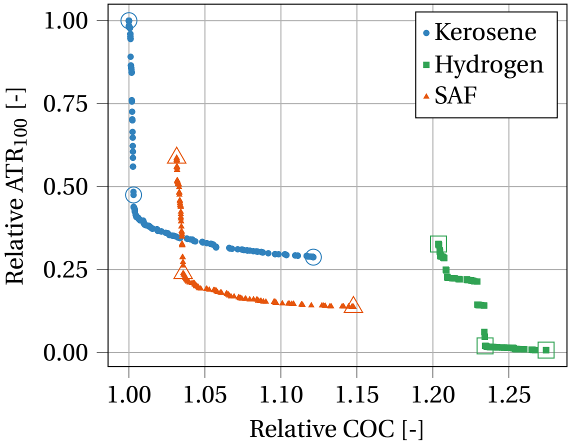

Figure 6.5: Comparison of Pareto-optimal solutions for regional aircraft. All values are presented relative to the cost-optimal, kerosene aircraft. The large, non-filled markers highlight the design solutions discussed in Sections 6.3.1 and 6.3.4.

Table 6.7: Relative differences in the objective values for the medium-range aircraft. The column headers are the objectives for which the aircraft are optimized.

	Kerosene		Hydrogen		SAF - HEFA (50-50)	
Objective	**ATR_{100}**	**COC**	**ATR_{100}**	**COC**	**ATR_{100}**	**COC**
ATR_{100}	-64%	-	-99%	-73%	-83%	-47%
COC	+17%	-	+39%	+28%	+21%	+4%
E_{fuel}	-3%	-	+3%	-3%	-3%	-1%

and contrail formation. The remaining contributions are NO_x effects and H_2O emissions. However, this climate impact reduction is accompanied by a 39% increase in cash operating costs and a 3% increase in in-flight energy consumption. More energy is required due to the increased mass and drag as a result of the tank integration. The larger energy requirement and higher fuel costs lead to the significant increase in COC.

Table 6.8 presents the design variables corresponding to the optimal solutions introduced above in Table 6.7. When moving from the cost to the ATR_{100} objective, the variation in cruise altitude, Mach number, turbine entry temperature, and fan pressure ratio show similar trends for the three fuel types. These four parameters decrease to reduce the climate impact. First, a lower cruise altitude lowers the effects due to NO_x emissions, in particular the formation of ozone, and simultaneously lowers the impact of contrails, up to an altitude where contrails are no longer formed. The altitude variable reaches the lower bound in all climate-optimal cases. Second, M_{cr} reduces alongside h_{cr} to maintain a lift-to-drag ratio in cruise close to the energy-optimal value. Finally, the optimizer chooses to lower Π_{fan} and TET while increasing the BPR. Appendix D discusses in more detail how the optimal TET follows from the other design choices. Lowering the Mach number with altitude allows a reduction of the wing sweep, which increases the maximum achievable $C_{L,\max}$ [107]. This, in turn, allows a higher wing loading W/S for the climate-optimal aircraft. The optimizer makes use of this higher W/S for the kerosene and SAF aircraft. Nevertheless, the wing loading is not necessarily maximized to the value imposed by the approach speed but chosen to also reduce the $(T/W)_{\mathrm{TO}}$ required. Similar to the regional aircraft, the cost-optimal hydrogen aircraft flies slower, at Mach 0.76, at a higher initial cruise altitude than the kerosene- and SAF-powered aircraft.

Table 6.8: Optimized design variables for the medium-range aircraft, considering each fuel type and design objective. The bottom and top bars indicate design bounds.

	Kerosene		**Hydrogen**		**SAF - HEFA**	
Variable [Unit]	**ATR$_{100}$**	**COC**	**ATR$_{100}$**	**COC**	**ATR$_{100}$**	**COC**
W/S [kN/m^2]	5.53	5.30	5.42	5.15	5.54	5.33
A [-]	11.2	7.72	10.3	10.3	11.3	7.97
BPR [-]	10.9	8.43	10.0	8.83	10.1	9.41
Π_{fan} [-]	1.39	1.69	1.53	1.75	1.45	1.68
Π_{lpc} [-]	1.48	1.58	1.56	1.67	1.49	1.62
Π_{hpc} [-]	20.4	22.3	21.7	20.5	20.2	22.0
TET [10^3 K]	1.38	1.52	1.46	1.47	1.40	1.57
h_{cr} [km]	$\underline{6.00}$	9.74	6.02	10.9	$\underline{6.00}$	9.67
M_{cr} [-]	0.51	0.80	0.58	0.76	0.50	0.80

Similar to the observations in Section 5.3, one may deduce from Table 6.8, that the selected bypass ratios are rather low compared to state-of-the-art engines. The sensitivity of the cost module with respect to the engine mass and thus bypass ratio, keeps this variable relatively low, as discussed in Section 5.4.3.

Table E.2 presents the engine mass, nacelle diameter, and cowl length of the medium-range aircraft. These three parameters appear to decrease when moving from the cost objective to the climate objective. The mass of the engine increases with bypass ratio, OPR, and ingested mass flow at take-off [113]. Due to the above design changes, several considerations apply; the bypass ratio increases, the OPR at TOC decreases while at take-off the values are rather similar, and the T/W_{TO} decreases, resulting in a lower thrust at take-off. The net effect is a lower engine mass. The fan and nacelle diameters are smaller since the ingest air is more dense at the design point, requiring a smaller inlet area for a given mass flow. Similarly, the length scales inversely with the ambient density in the assumed sizing relations [87, Appendix C]. As a result, the installation penalties of the turbofan engines (i.e. mass and drag) are reduced. This trend appears to be similar for all of the categories and fuels, except for the regional, hydrogen aircraft. In the latter case, the mass marginally increases by less than 2%.

Figure 6.6 compares the top-view geometries of the kerosene-, SAF-, and hydrogen-powered aircraft, considering the cost and climate objectives separately. The fuselage of the hydrogen aircraft is noticeably longer for both objectives because of the hydrogen tank integration in the fuselage. Furthermore, the horizontal tail is larger due to the greater center-of-gravity excursion. The long fuselage and larger horizontal tail lead to a heavier structure, a larger operating empty mass, and a higher zero-lift drag coefficient. By comparing Figure 6.6a and Figure 6.6b, one can see the wing sweep angle and the consequent change in horizontal tail planform are the most prominent geometric changes. Similar to the regional aircraft, the geometries of the kerosene and SAF aircraft are almost the same.

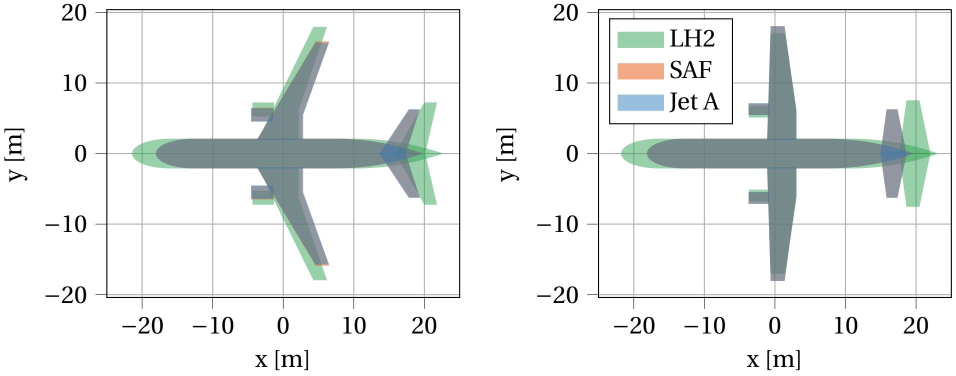

(a) Cost-optimal (b) Climate-optimal

Figure 6.6: Comparison between top-view geometries of cost- and climate-optimal, medium-range aircraft employing different fuel types

Figure 6.7 compares the mean surface temperature response for all optimal medium-range aircraft. From Figure 6.7a it is clear that the SAF and hydrogen solutions reduce the overall temperature response, mainly because of long-term CO_2 emissions. In addition, the short-term peak is lowered due to the altered contrail properties and, in the case of hydrogen aircraft, the reduced NO_x emissions. The lack of a peak near the year 2070 in Figure 6.7b indicates that, by optimizing the aircraft for their climate impact, the short-term effects from NO_x and contrails can be reduced, irrespective of the fuel. A long-term CO_2 contribution remains in the year 2120 for the kerosene and SAF aircraft.

While Table 6.7 shows the results of single-objective optimizations, solutions exist that are Pareto-optimal and lie in between the extremes. Figure 6.8 presents the Pareto fronts for the three fuels under consideration. This figure shows that kerosene aircraft offer low-cost solutions for a climate impact reduction of 59%. After this point, SAF aircraft concepts offer the largest climate impact reduction for a given increase in costs. However, a reduction in ATR_{100} above 83% can only be achieved with hydrogen-powered aircraft. But this fuel also yields the largest cost penalty. These results strongly depend on the fuel prices of SAF and hydrogen in the future.

Figure 6.10 shows how the design variables vary along the Pareto fronts in Figure 6.8. In each column, the leftmost data points correspond to the cost-optimal solution, while the climate-optimal solutions are obtained by moving to the right. For example, the bottom two rows show how the cruise altitude and Mach number decrease when moving toward the climate-optimal solution. However, in between the two extreme solutions, the hydrogen aircraft first flies at a marginally higher cruise altitude, before discontinuously switching to an initial cruise altitude of 8.5 km. This discontinuous move in the design space is associated with a jump to a lower cruise Mach number, allowing a higher

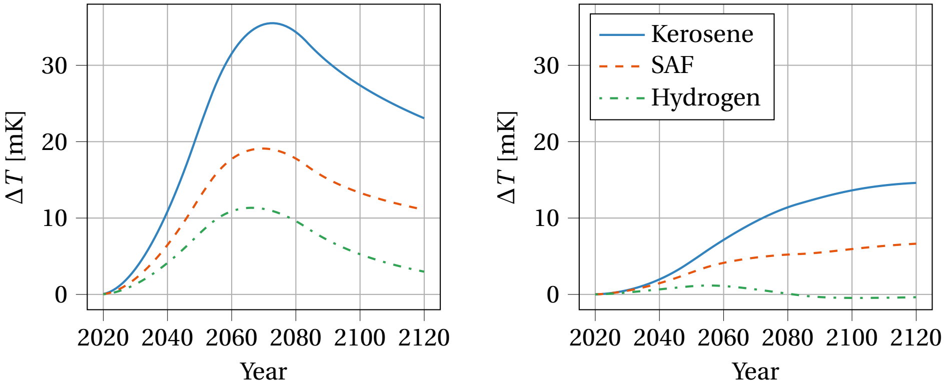

(a) Cost-optimal

(b) Climate-optimal

Figure 6.7: Comparison between mean surface temperature responses of cost- and climate-optimal, medium-range aircraft employing different fuel types

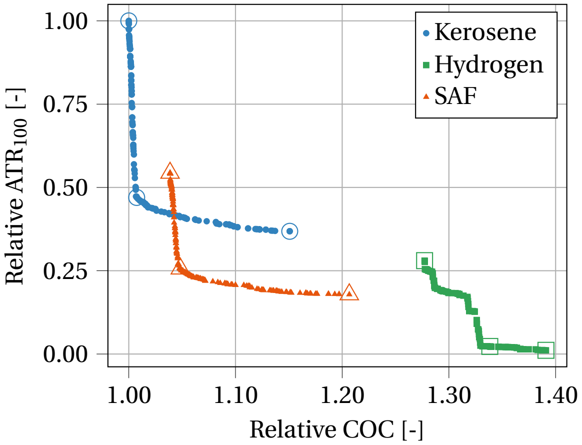

Figure 6.8: Comparison of Pareto-optimal solutions for medium-range aircraft. All values are presented relative to the cost-optimal, kerosene aircraft. The large, non-filled markers highlight the design solutions discussed in Sections 6.3.2 and 6.3.4.

wing loading as well. To offset the increase in ozone radiate forcing sensitivity associated with this small altitude increase [$s(h)$ in Equations (3.18) and (3.20)], the LPC and HPC pressure ratios are lowered to reduce the NO_x emission index. While these changes marginally reduce the climate impact compared to the cost-optimal, hydrogen solution, the changes result in Pareto-optimal solutions. For all fuels, the fan and high-pressure compressor ratios decrease along the Pareto front, while the bypass and aspect ratios increase.

The kerosene- and SAF-powered Pareto fronts feature a characteristic kink, indicated by the gray dashed line, moving from a large climate impact reduction at a limited cost increase to a shallow climate impact reduction at a relatively large cost increase. Before this kink, the cruise altitude decreases by approximately 1 km, the Mach number is reduced, and the combination of a higher BPR and lower Π_{fan}. At a limited cost increase, these changes simultaneously reduce the radiative forcing due to NO_x emissions, reduce the radiative forcing of contrails up to the point they are no longer formed, and increase fuel efficiency. The latter change lowers the CO_2 emissions.

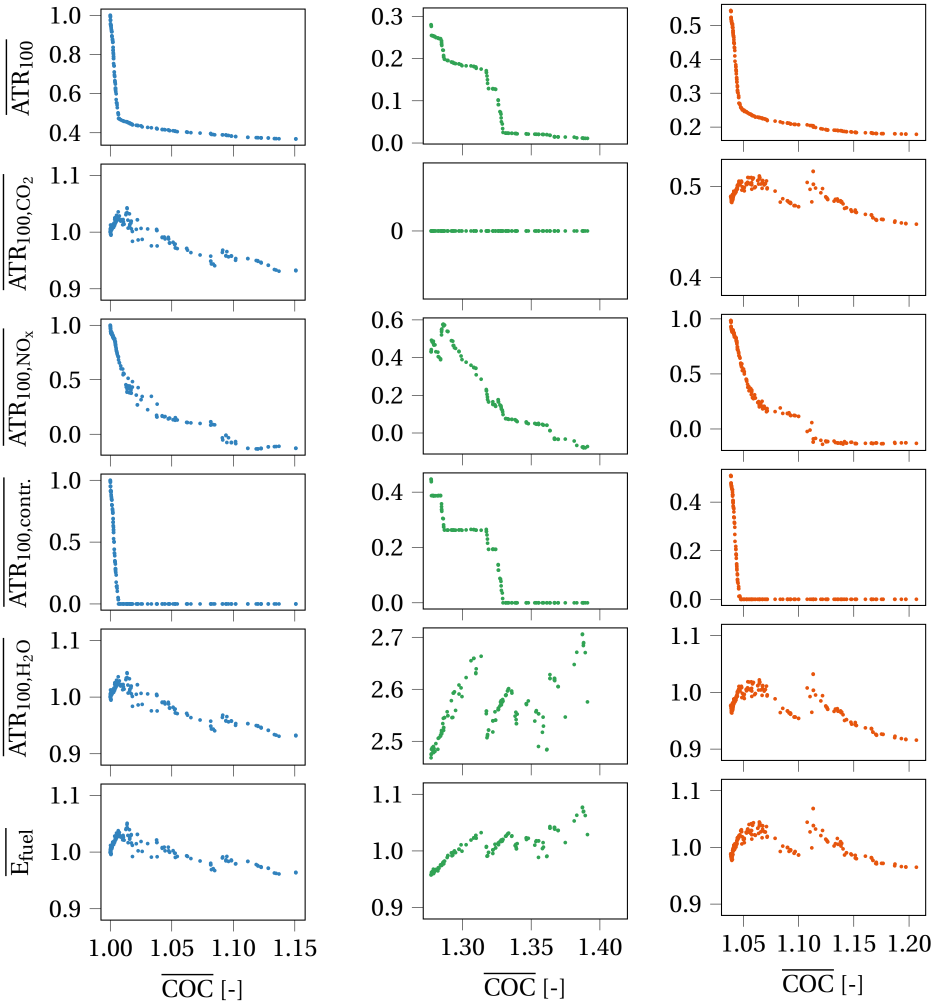

(a) Kerosene (b) Hydrogen (c) SAF

Figure 6.9: Variation in individual ATR_{100} components and energy consumption along Pareto fronts for medium-range aircraft. The parameters are normalized with respect to the kerosene, cost-optimal values.

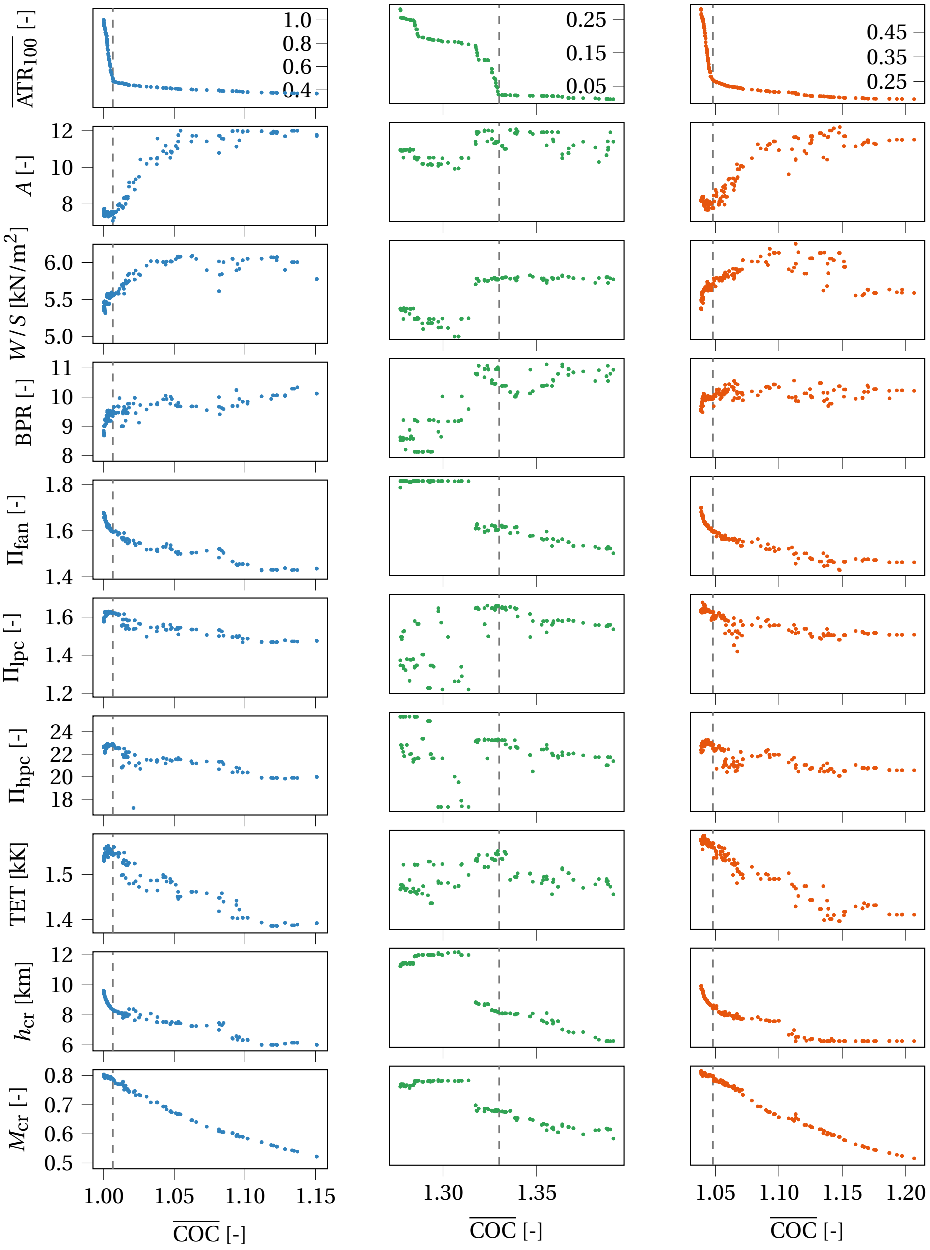

(a) Kerosene

(b) Hydrogen

(c) SAF

Figure 6.10: Variation in design variables along Pareto fronts for medium-range aircraft. The cost ($\overline{\mathrm{COC}}$) and climate impact ($\overline{\mathrm{ATR}_{100}}$) are normalized with the value of the cost-optimal, kerosene aircraft. The gray, dashed lines correspond to the kink points discussed in Section 6.3.4.

6.3.3. LONG-RANGE AIRCRAFT

Table 6.9 shows the objective function values for the long-range aircraft designed for different objectives and different fuel types. The possible ATR_{100} reduction for the kerosene aircraft has shrunk to 36%, whereas it was 71 and 64% for the regional and medium-range aircraft, respectively. This is because the relative contributions of the different climate agents change between categories. In the long-range category, the CO_2 emissions are relatively more important for the cost-optimal aircraft. CO_2 contributes approximately 61% to the total ATR_{100} for the cost-optimal, long-range aircraft, whereas it only contributes 39% in the medium-range category. However, the CO_2 effect cannot be reduced as much as the other contributions within the current design space. For the other aircraft categories, the contribution due to contrails is larger in the cost-optimal case, and hence, when switching to the climate objective, a larger reduction can be achieved. Note that the relative contributions of the climate species are also dependent on the chosen mission in the payload-range envelope. This is particularly important in the current modeling approach where the impact of contrails scales with the distance covered, but not with the fuel consumption or thrust level.

When burning SAF or hydrogen, the climate impact can be significantly improved by up to 68% and 97%, respectively. Comparing the climate-optimal kerosene and SAF solutions, it seems that the SAF concept is interesting because, for a cost increase of 5% instead of 23%, the ATR_{100} can be reduced by 47% instead of 35%. The application of hydrogen fuel yields the largest potential since CO_2 emissions perform an important role for long-range aircraft. Nevertheless, long-range flight and its corresponding energy usage require large tanks, which strongly penalize the energy consumption of long-range aircraft, up to 14% for the climate-optimal aircraft. Although hydrogen is the most attractive option from a climate-point perspective, this fuel causes a 38% to 64% increase in cash operating costs, as indicated in Table 6.9.

Table 6.9: Relative differences in the objective values for the long-range aircraft. The column headers are the objectives for which the aircraft are optimized.

	Kerosene		**Hydrogen**		**SAF - HEFA (50-50)**	
Variable	**ATR_{100}**	**COC**	**ATR_{100}**	**COC**	**ATR_{100}**	**COC**
ATR_{100}	-35%	-	-97%	-77%	-68%	-47%
COC	+23%	-	+64%	+38%	+27%	+5%
E_{fuel}	+7%	-	+14%	+4%	+5%	-2%

To achieve the climate-optimal solutions, the design variables shown in Table 6.10 should be applied. Similar to the two other categories, the trend is to fly lower and consequently slower to reduce the climate impact. However, time-driven costs perform a more important role in the long-range category. This drives the Mach number in the case of the cost-optimal aircraft. When flying slower, Table E.3 in Appendix E shows that the mission block time increases from 8h22m to 10h36m for the kerosene aircraft, a rise of 27%. This explains why the cost penalty for long-range aircraft is larger than for regional or medium-range concepts.

Furthermore, Table 6.10 shows that the optimizer tries to achieve maximum energy efficiency by pushing A, BPR, and Π_{hpc} to the upper bounds of the design space. Along with the high BPR, the fan pressure ratio is lowered which also prevents the violation of the OPR constraint. The climate-optimal kerosene and SAF aircraft, as well as the cost-optimal hydrogen aircraft are close to the span constraint of 65 m.

Table 6.10: Optimized design variables for the long-range aircraft, considering each fuel type and design objective. The bottom and top bars indicate design bounds.

	Kerosene		**Hydrogen**		**SAF - HEFA**	
Variable [Unit]	**ATR$_{100}$**	**COC**	**ATR$_{100}$**	**COC**	**ATR$_{100}$**	**COC**
W/S [kN/m^2]	7.12	6.87	6.60	6.22	7.38	7.13
A [-]	11.3	9.01	$\overline{12.0}$	11.5	$\overline{12.0}$	9.75
BPR [-]	10.7	10.6	10.8	$\overline{11.0}$	10.9	10.6
Π_{fan} [-]	1.42	1.60	1.49	1.68	1.42	1.58
Π_{lpc} [-]	1.51	1.63	1.49	1.64	1.48	1.60
Π_{hpc} [-]	20.4	22.9	21.0	21.5	20.3	22.3
TET [10^3 K]	1.43	1.57	1.43	1.55	1.43	1.54
h_{cr} [km]	6.37	8.70	$\underline{6.00}$	9.69	$\underline{6.00}$	8.70
M_{cr} [-]	0.58	0.79	0.55	0.73	0.57	0.77

Figure 6.11 compares the top-view geometries of the long-range aircraft. The most obvious features are the fuselage length and horizontal tails of the hydrogen aircraft. The length is increased from 65 m to approximately 87 and almost 90 m to facilitate the tank integration, which makes the aircraft longer than the Airbus A340-600[3] and Boeing 777-9[4] aircraft (see Table E.3 for more information). Possibly, this long fuselage prohibits the operation of this aircraft with current airport facilities. The horizontal tail area of the hydrogen aircraft is significantly larger, up to 20%, than its kerosene and SAF counterparts. This is due to the larger potential, in-flight c.g. excursion caused by the two tanks in the fuselage. Although the two-tank layout appears to help in minimizing the tail area [163], compared to one aft tank, unbalanced emptying of the tanks can be critical for longitudinal stability and trim. Additionally, the elongated fuselage front of the wing has a destabilizing effect.

Figure 6.12 compares the global, mean surface temperature responses for the six optimized long-range aircraft. The responses are similar to the results found for the two smaller aircraft categories, with a significantly lower temperature response for the SAF and hydrogen aircraft. Also, by selecting ATR$_{100}$ as the optimization objective, the peak caused by short-term climate effects disappears. The relevance of CO_2 emissions on long-distance routes can be recognized in Figure 6.12a where the peak for kerosene and SAF-powered aircraft occurs later than for the hydrogen concept. This is indicative of a long-term, warming effect, namely the significant contribution of CO_2 emissions.

---

[3] URL https://www.airbus.com/en/who-we-are/company-history/commercial-aircraft-history/previous-generation-aircraft/a340-family/a340-600 accessed on 26 January 2024

[4] URL https://www.boeing.com/Commercial/777x#technical-specs accessed on 26 January 2024

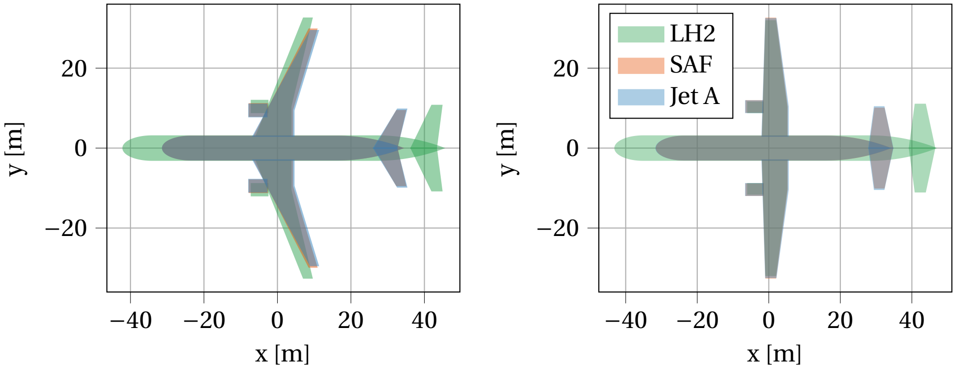

(a) Cost-optimal

(b) Climate-optimal

Figure 6.11: Comparison between top-view geometries of cost- and climate-optimal, long-range aircraft employing different fuel types

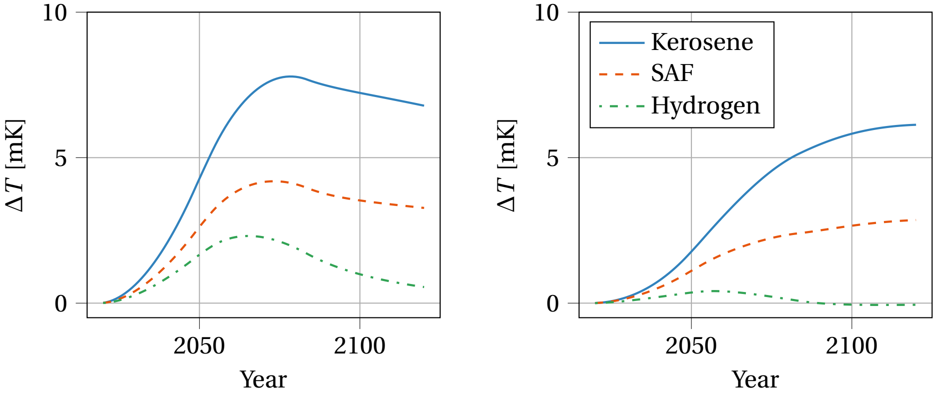

(a) Cost-optimal

(b) Climate-optimal

Figure 6.12: Comparison between temperature responses of cost- and climate-optimal, long-range, aircraft employing different fuel types

Figure 6.13 presents the Pareto-optimal points in the trade-off between cost and climate impact for the long-range aircraft. Similar to the smaller aircraft categories, it is clear that SAF aircraft provide Pareto-optimal solutions for climate impact reduction which is not achievable with kerosene. Also here the hydrogen alternative yields the largest potential ATR_{100} reduction. However, compared to the trade-offs for the other categories in Figures 6.5 and 6.8, the maximum achievable ATR_{100} savings with kerosene and SAF are limited to 36 and 68%, respectively. This makes the hydrogen, cost-optimal aircraft Pareto-optimal. The sudden step in costs observed can be attributed to the current cost model, which assumes that when the block time is longer than 10 hours, an additional cockpit crew is needed.

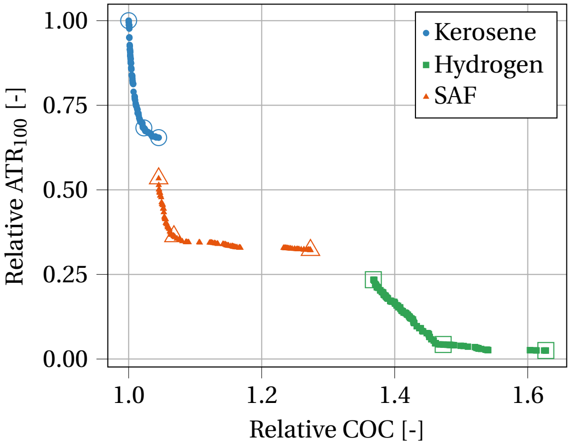

Figure 6.13: Comparison of Pareto-optimal solutions for long-range aircraft. All values are presented relative to the cost-optimal, kerosene aircraft. The large, non-filled markers highlight the design solutions discussed in Sections 6.3.3 and 6.3.4.

6.3.4. MULTI-OBJECTIVE SOLUTIONS

The previous sections presented the single-objective designs and the Pareto fronts which bridge the gaps between these two solutions. However, all the Pareto fronts show a “kink” in between the cost- and climate-optimal aircraft designs. Such a kink follows a steep reduction in ATR$_{100}$ for a limited operating cost increase. Beyond this kink, the climate impact can be further reduced, albeit at a higher cost increase. This makes the aircraft design which lies at this kink attractive both from a climate and cost perspective. These kink points are denoted as multi-objective solutions in the current and subsequent chapters, often abbreviated as “MO”.

For all aircraft categories and fuel types, this kink corresponds to the point where no more persistent contrails are formed, according to the current climate model. This means that the cruise altitude has been reduced, together with other design changes, up to a point where the conditions for contrail formation are no longer met. This is indicated by the gray, dashed lines in Figure 6.10a for the medium-range aircraft. Since contrails have a significant contribution to the total climate impact, eliminating contrail formation has a large climate impact reduction potential. Additionally, lowering the cruise altitude lowers the climate impact due to short-term ozone creation. The design changes which lead to this point, do not result in a high cost penalty. For the hydrogen aircraft, however, the operating cost increase between the cost-optimal point and the kink is larger than for the kerosene and drop-in SAF counterparts.

These aircraft design points are therefore analyzed further and are also considered viable options in the fleet allocation in the next chapter. Tables 6.11 to 6.13 present the design variables and relative objective values at these kinks for each aircraft category. Additional aircraft details are provided in the tables in Appendix E in the columns with the “MO” header.

Table 6.11: Multi-objective design solutions positioned at kinks in Pareto fronts of regional aircraft

Variable [Unit]	**Kerosene**	**Hydrogen**	**SAF**
Relative ATR_{100} [-]	-53%	-98%	-75%
Relative COC [-]	+0.3%	+23%	+3.6%
A [-]	6.66	10.2	7.00
W/S [kN/m^2]	5242	5509	5200
BPR [-]	7.37	9.50	8.19
Π_{fan} [-]	1.67	1.63	1.67
Π_{lpc} [-]	1.61	1.59	1.58
Π_{hpc} [-]	22.3	23.1	22.5
TET [10^3 K]	1.50	1.51	1.54
h_{cr} [km]	8.63	8.04	8.63
M_{cr} [-]	0.79	0.66	0.78

Table 6.12: Multi-objective design solutions positioned at kinks in Pareto fronts of medium-range aircraft

Variable [Unit]	**Kerosene**	**Hydrogen**	**SAF**
Relative ATR_{100} [-]	-53%	-98%	-75%
Relative COC [-]	+0.7%	+33%	+4.8%
A [-]	7.59	11.2	7.58
W/S [kN/m^2]	5580	5720	5657
BPR [-]	9.47	10.8	9.82
Π_{fan} [-]	1.59	1.59	1.58
Π_{lpc} [-]	1.62	1.64	1.61
Π_{hpc} [-]	22.8	23.0	22.5
TET [10^3 K]	1.54	1.54	1.56
h_{cr} [km]	8.32	7.93	8.22
M_{cr} [-]	0.79	0.67	0.79

6.3.5. SENSITIVITY TO SAF TYPES AND MIXTURES

In the results above, a 50% mixture of HEFA and traditional kerosene is assumed as sustainable aviation fuel. Nevertheless, different types of SAF are currently being researched and, once regulations change and challenges regarding the aromatic content are overcome, a higher percentage of SAF may be used. To study the effect of these alternatives on the relative cost difference between kerosene and hydrogen, two other SAF alternatives are considered: first, a mixture of 50% synthetic kerosene (power-to-liquid) and 50% traditional kerosene, and secondly, a mixture of 100% synthetic kerosene.

Figure 6.14 compares these alternatives for medium-range aircraft. It can be observed that the achievable Pareto front of SAF shifts to the right, indicating higher operating costs. While the 50% mixture with synthetic kerosene is still dominating the hydrogen, cost-optimal solution, the 100% synthetic jet fuel concepts are no longer Pareto-

Table 6.13: Multi-objective design solutions positioned at kinks in Pareto fronts of long-range aircraft. The bottom and top bars indicate design bounds.

Variable [Unit]	**Kerosene**	**Hydrogen**	**SAF**
Relative ATR_{100} [-]	-31%	-96%	-63%
Relative COC [-]	+2.3%	+47%	+6.9%
A [-]	10.3	11.7	10.2
W/S [kN/m^2]	7396	6515	7368
BPR [-]	10.6	$\overline{11.0}$	10.9
Π_{fan} [-]	1.49	1.59	1.48
Π_{lpc} [-]	1.52	1.62	1.53
Π_{hpc} [-]	21.0	22.3	21.4
TET [10^3 K]	1.48	1.55	1.49
h_{cr} [km]	7.30	7.45	7.26
M_{cr} [-]	0.75	0.67	0.75

optimal. This indicates that hydrogen can provide a competitive solution if a solution is required with high climate impact reduction potential, especially if the liquid hydrogen price decreases.

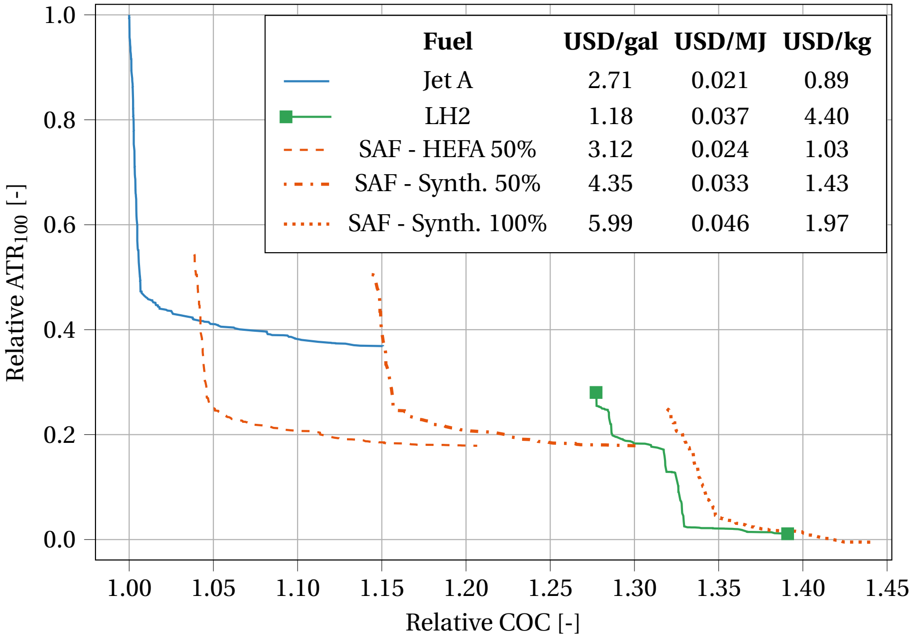

Figure 6.14: Comparison of Pareto-optimal solutions for medium-range aircraft considering the influence of SAF prices. All values are presented relative to the cost-optimal, kerosene aircraft.

6.4. CONCLUSIONS

The objective of this chapter was to compare the climate impact reduction potential of several aviation fuels for three commercial aircraft categories: regional, medium-, and long-range. The fuels under consideration were traditional kerosene, liquid hydrogen, and 50% HEFA sustainable aviation fuel (SAF). The cost-optimal, kerosene-powered aircraft provided the reference case for all multidisciplinary aircraft design optimizations. By considering both the cash operating cost and ATR_{100} as optimization objectives, the trade-off between the cost and climate impact is made for all the three fuel types in the three categories.

In all three market segments, the hydrogen-powered aircraft offer the greatest ATR_{100} reduction potential, up to 99%. This is due to the elimination of CO_2 emissions, the reduction in NO_x effects, and the lack of contrail formation by flying lower (h_{cr}=6.0 km) and slower (M_{cr} between 0.5 and 0.6). For the regional and medium-range categories, the climate-optimal SAF aircraft design (50% HEFA or synthetic kerosene blends) can offer a similar ATR_{100} reduction as the cost-optimal hydrogen aircraft at lower cash operating costs. For the long-range aircraft, where CO_2 contributions perform a dominant role in the climate impact, cost-optimal hydrogen aircraft do provide a Pareto-optimal solution when costs and climate impact are considered. Nevertheless, the cash operating costs of hydrogen aircraft increase by 20 to 39% for regional and medium-range aircraft. For long-range missions, the operating costs rise between 38 and 64% due to the fuel price and the tank integration penalty.

It is estimated that the use of SAF mixtures (50-50 with fossil kerosene) can lower the climate impact between 41 and 86% for regional aircraft, and 47 and 83% for medium-range aircraft. For long-range aircraft, a maximum reduction of 68% can be achieved with this SAF mixture. The application of SAF reduces the climate impact because less carbon is added to the existing global carbon cycle and because the contrail properties are different due to lower soot production. In the case of a HEFA fuel mixture, the cash operating cost penalty is limited to 3-5% for the cost-optimal SAF aircraft, while it can rise up to 27% for climate-optimal compared to the standard kerosene aircraft.

The analyses in this chapter are subject to uncertainties, in particular in the climate model and the assumptions made for the future aviation fuels. These uncertainties and the conequences are discussed in Chapter 8.

7

FLEET ALLOCATION AND NETWORK-LEVEL ANALYSIS

The previous chapters have shown that airplanes designed for minimal climate impact have a reduced cruise speed and fly at a lower altitude. The climate impact can be even further reduced by employing liquid hydrogen or drop-in sustainable aviation fuels. This chapter suggests a multidisciplinary, multi-level approach to evaluate the consequences of such design and fuel choices at the network level. Following the aircraft design step, a dynamic programming routine allocates three different aircraft types to an existing network of city pairs and schedules the flights to maximize the network profit. The study focuses on a hub-and-spoke network operating from Atlanta, with demand for domestic and international destinations. Compared to the reference cost-optimal kerosene fleet, a fleet consisting of climate-optimized kerosene aircraft can reduce the climate impact by 55% at a loss in network profit of approximately 24%. This requires allocating an additional eight aircraft to the original fleet of 38 aircraft. A fleet operating climate-optimal, hydrogen aircraft reduces the climate impact by 99%. However, the high operating cost of long-range, hydrogen aircraft lowers the achievable profit by 35%. In addition, the number of profitable flights in the long-range segments drops by 35%. Fleets powered by drop-in SAF also provide Pareto-optimal solutions which lie in between the profit-maximizing kerosene and the climate-minimizing hydrogen fleets. These insights can be used to make decisions about the allocation of future aviation fuels in a network as well as drive the payload-range requirements of future aircraft.

The studies presented in this chapter were performed in collaboration with F. Morlupo, B.F. Santos, and R. Vos and have been published in Reference [200]

THE previous chapters focused on the design optimization of aircraft to minimize the climate impact. These optimizations showed that using alternative fuels and designing for a climate objective positively influence the climate impact. However, the introduction of slow-flying, climate-optimal, kerosene-powered aircraft requires a different fleet allocation. Additionally, replacing aircraft in the fleet with hydrogen- or SAF-powered alternatives may favor a different allocation and/or require different top-level aircraft requirements. Therefore, a system-of-systems approach is needed to develop sustainable fleets where the aircraft and their operations are assessed simultaneously.

Several studies have implemented multi-level approaches. Jansen and Perez [25, 26, 27] proposed a method to optimize aircraft families and their allocation in different markets, showing that a reduction in fuel burn, operating and acquisition costs can be achieved. This requires solving optimizations at multiple levels, typically a nonlinear aircraft design optimization and a (mixed-integer) linear programming approach for fleet allocation. A similar approach was taken by Moolchandani et al. [28] to assess the environmental impact of new technologies, mainly focusing on CO_2 emissions. Hwang et al. [29] proposed a modular adjoint approach to solve such combined problems, resulting in fleet profit gains. Also, uncertainties in aircraft technologies and forecasts can be taken into account [30]. Govindaraju, Davendralingam, and Crossley [31] employed a multi-level approach to study potential fuel burn savings under operational uncertainty.

Although the problem of coupled aircraft design and fleet allocation has been studied in the literature, the challenge of increased block time of climate-optimal aircraft and the effect on aircraft design and fleet allocation has not yet been examined in detail. In addition, it is important to study how fuel selection plays a role in this and how to allocate novel fuels optimally.

Therefore, this chapter proposes a multidisciplinary, multi-level approach to address these two issues which relate to research questions 6 and 7 in Section 1.4. The first research question is: considering an available network demand, what is the optimal fleet diversity and allocation of climate-minimal, kerosene aircraft in an airline network to maximize the profit? Once this question is answered, the problem is extended to examine how future aviation fuels can further reduce the climate impact of the network. The effects on total network profits and energy consumption are monitored in this problem.

This chapter employs the aircraft designs presented in Section 6.3, and combines the regional, medium-, and long-range aircraft for each fuel type in one fleet. The multidisciplinary aircraft design framework is extended with a dynamic programming fleet allocation model to assign the aircraft and evaluate the network-level performance. Note that the current multi-level problem considers a fixed weekly network demand, without studying changes in demand or fleet composition with time. Additionally, the network and airline markets may change depending on the available aircraft in the future, while we assume the network demand to be the driving factor for new aircraft in this study.

This chapter is structured as follows. In Section 7.1, the approach to allocate aircraft is introduced. Subsequently, a cost-optimal reference case is constructed that only employs kerosene-powered aircraft in Section 7.2. By studying this reference case, the coupling between the two levels and the decision-making process of the dynamic programming routine is verified. In Section 7.3, the two research questions introduced above are addressed. Finally, the method and results are summarized in Section 7.4.

7.1. MULTIDISCIPLINARY, MULTILEVEL SETUP AND METHODS

To address the research question formulated above, the multidisciplinary aircraft design and optimization framework is extended with a second level to perform fleet allocation and flight scheduling. This setup is employed to design aircraft of different sizes, burning different fuels, and allocate these aircraft optimally on a chosen network. First, Section 7.1.1 further clarifies the overall problem of interest and the setup. Subsequently, Section 7.1.2 focuses on the fleet allocation. The methods to evaluate the network cost and climate impact are treated in Sections 7.1.3 and 7.1.4

7.1.1. MULTIDISCIPLINARY, MULTILEVEL PROBLEM DEFINITION AND SETUP

The multidisciplinary design analysis and optimization setup tries to solve two problems: first, the optimization of aircraft for given top-level aircraft requirements and selected objective functions. The aircraft design objective functions considered in this study are the cash operating costs (COC) and the climate impact quantified by the average temperature response over a period of 100 years (ATR_{100}). As discussed in Chapter 6, aircraft design optimization is done for three sets of top-level aircraft requirements corresponding to different market segments (regional, medium-, and long-range). The second goal of the MDAO framework is to consider this set of three aircraft types, designed for the same objective, and to allocate them on a given route network to maximize the profit on that network.

This two-step approach aims to analyze how the aircraft types designed for a single objective function are used together in a fleet and to measure the change in network profit and climate impact. In particular, the fleet composition and schedule change are studied for varying aircraft design objectives. The aircraft design step can also design aircraft with the same top-level requirements and objectives but with different fuels, such as drop-in sustainable aviation fuels or liquid hydrogen. Hence, this setup allows assessing how the aircraft designed for different objectives and fuels drive the fleet composition and schedule.

Figure 7.1 presents the overall strategy and workflow. Block 0 in this diagram manages the aircraft design optimization defined in Equation (5.1). The first level (steps 1 to 6) is the aircraft design loop which ensures that consistent and feasible aircraft are created. The details of the aircraft design process are discussed in Sections 5.1.2 and 6.1.2. The aircraft design routine passes on flight performance information, such as the drag polar and engine deck parameters, for fleet allocation and fleet-level assessment of energy consumption, climate impact, and profit. This aircraft design loop covers three sets of top-level requirements, covering three market segments. This multi-aircraft analysis is highlighted by the stacked disciplines in Figure 7.1, contrary to the network-level analysis that considers all three aircraft simultaneously. The information of the aircraft is passed on to the second level where all three aircraft types are considered for allocation simultaneously. Figure 7.2 shows how the aircraft-level analyses and data from the previous chapter connect to the fleet case studies in the current chapter.

The second level (steps 7 to 11) allocates and schedules the synthesized aircraft on the network to maximize the overall profit, considering the available network demand between origin-destination (OD) pairs, which are for example imposed by an airline. The demand and airports to be included are gathered in the "Network Info" block in

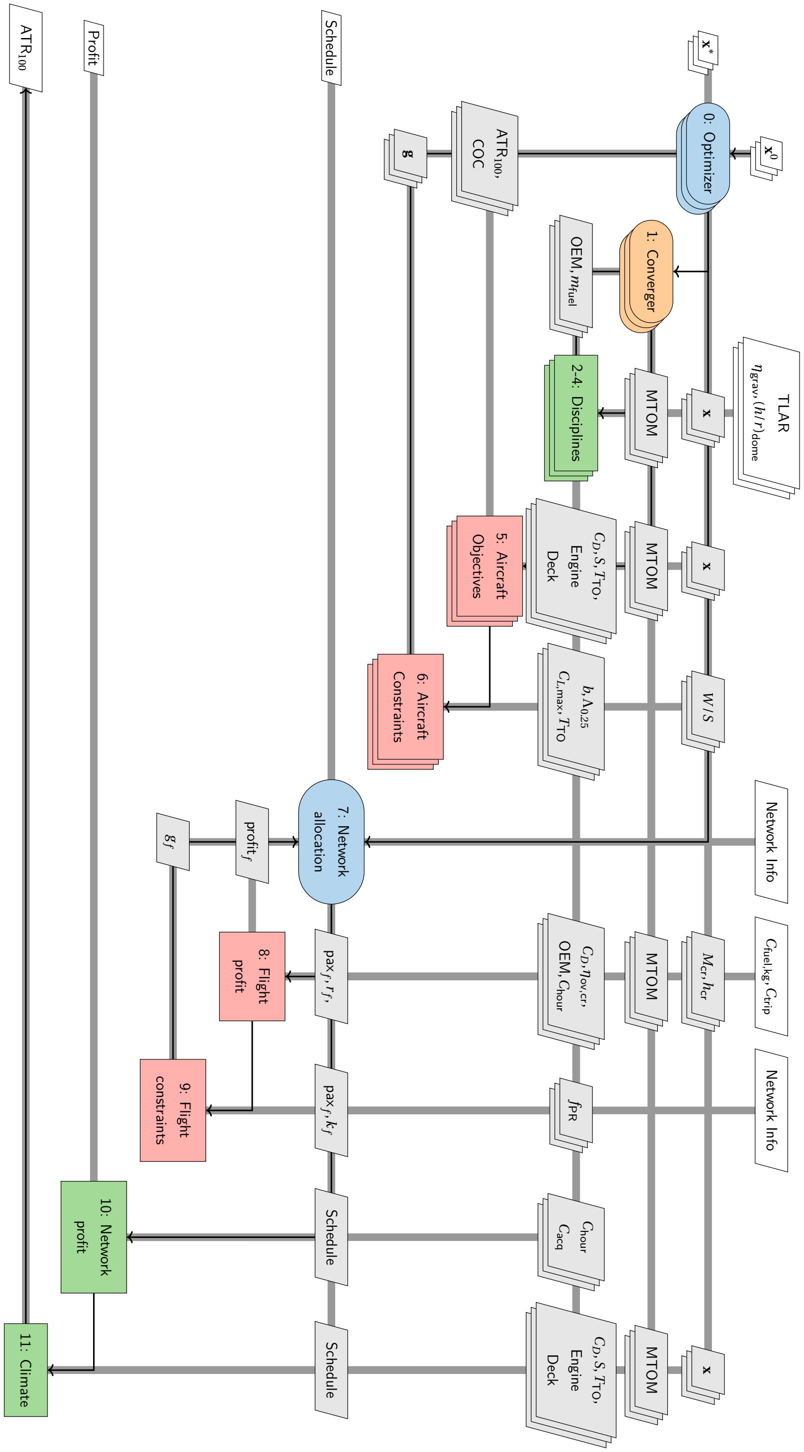
$\mathbf{x}^*$
0: Optimizer
$\mathbf{x}^0$
1: Converger
TLAR
$\eta_{grav}, (h/r)_{dome}$
Network Info
$C_{fuel,kg}, C_{trip}$
Network Info
ATR$_{100}$, COC
$\mathbf{g}$
OEM, m_{fuel}
2-4: Disciplines
$\mathbf{x}$
MTOM
C_D, S, T_{TO}, Engine Deck
5: Aircraft Objectives
6: Aircraft Constraints
$b, \Lambda_{0.25}$ $C_{L_{max}}, T_{TO}$
W/S
7: Network allocation
profit$_f$
g_f
8: Flight profit
9: Flight constraints
pax$_f$, r_f,
pax$_f$, k_f
$C_D, \eta_{ov,cr}$, OEM, C_{hour}
M_{cr}, h_{cr}
f_{PR}
C_{hour} C_{acq}
10: Network profit
11: Climate
Schedule
Profit
ATR$_{100}$

Figure 7.1: Extended design structure matrix (XDSM) representing the multidisciplinary workflow

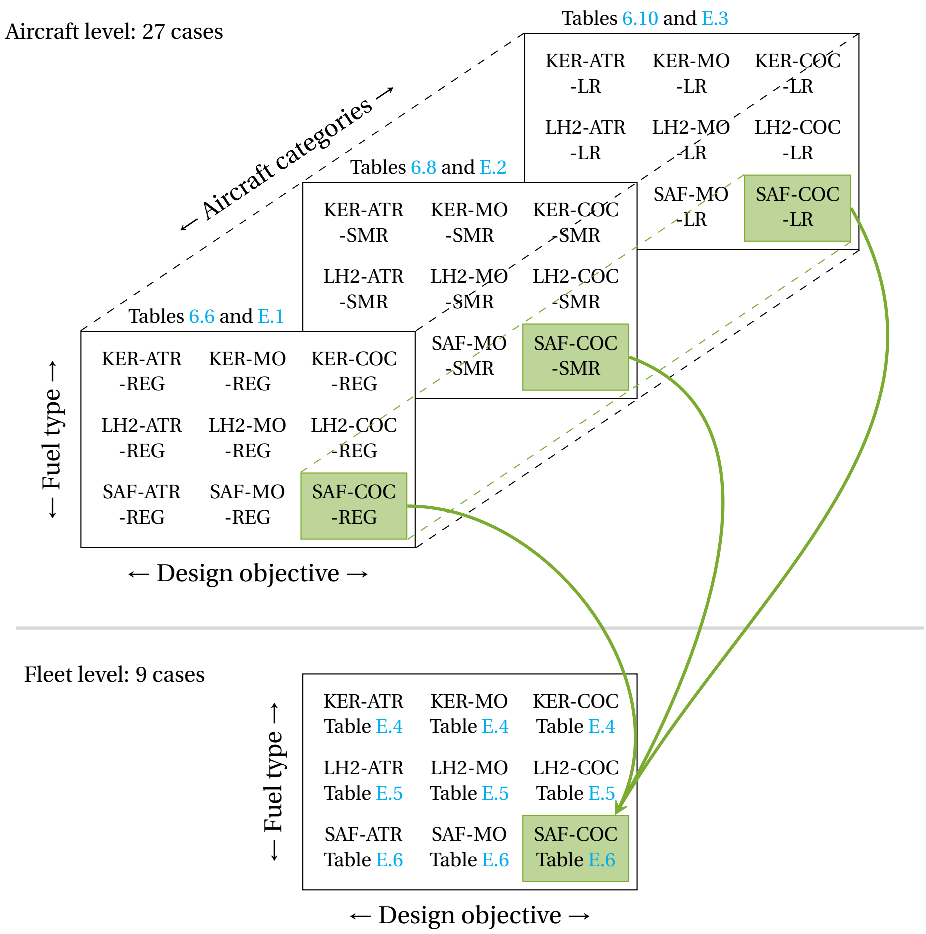
Aircraft level: 27 cases
Tables 6.10 and E.3
KER-ATR -LR
KER-MO -LR
KER-COC -LR
LH2-ATR -LR
LH2-MO -LR
LH2-COC -LR
SAF-MO -LR
SAF-COC -LR
← Aircraft categories →
Tables 6.8 and E.2
KER-ATR -SMR
KER-MO -SMR
KER-COC -SMR
LH2-ATR -SMR
LH2-MO -SMR
LH2-COC -SMR
SAF-MO -SMR
SAF-COC -SMR
Tables 6.6 and E.1
KER-ATR -REG
KER-MO -REG
KER-COC -REG
LH2-ATR -REG
LH2-MO -REG
LH2-COC -REG
SAF-ATR -REG
SAF-MO -REG
SAF-COC -REG
← Fuel type →
← Design objective →
Fleet level: 9 cases
KER-ATR Table E.4
KER-MO Table E.4
KER-COC Table E.4
LH2-ATR Table E.5
LH2-MO Table E.5
LH2-COC Table E.5
SAF-ATR Table E.6
SAF-MO Table E.6
SAF-COC Table E.6
← Fuel type →
← Design objective →

Figure 7.2: Connection between aircraft-level and fleet-level case studies and the associated data. The shaded elements and arrows provide an example of the SAF-powered aircraft and fleet. MO represents the multi-objective aircraft studied in Section 6.3.4.

the top row of the XDSM. This information is fixed for all types of fuel and all design objectives. Section 7.1.2 elaborates upon the steps in the fleet allocation model. The fleet allocation is done according to profit maximization. The flight operating cost and aircraft acquisition cost are inputs to this profit calculation. Section 7.1.3 describes how these two cost contributions are calculated. Once an optimal allocation and schedule are created, the climate impact of this network is evaluated, as discussed in Section 7.1.4.

By running this workflow for different aircraft design objectives and fuels, the resulting schedules can be compared regarding profit and climate impact. Additionally, since the allocation of passengers is an output of the fleet allocation, updates to the initial top-level aircraft requirements, such as maximum structural payload mass and design range, can be proposed, which are tailored to the design objective and/or fuel. However, the automated update of such top-level parameters is considered outside the scope of this paper and is proposed as a recommendation.

7.1.2. FLEET ALLOCATION APPROACH

Steps 7 to 11 of Figure 7.1 allocate the aircraft on a given network to maximize the profit while considering operational constraints. The network profit is defined as the sum of all profits collected over all allocated flights minus the ownership costs of all assigned aircraft. The dynamic programming method was chosen to model the fleet assignment problem. Dynamic programming is an optimization method that breaks down a complex problem into smaller, simpler sub-problems and solves each sub-problem only once, storing the solution to avoid redundant calculations. Dynamic programming has been widely used in aviation to optimize operational problems and find the optimal sequence of decisions [201]. Dynamic programming is selected instead of linear programming to allow non-linear calculations. The method adopted in this study is inspired by the work of Seaone Álvarez [202] and Noorafza et al. [203]. Figure 7.3 shows how the allocation algorithm works.

The approach requires three types of input data, which are labeled with different numbers. Block I1 contains all the network-related information, including potential routes, and airport data (curfew, UTC deviation, and runway length and width). More information on this input data can be found in Section 7.2.1. The data in I2 holds the available aircraft types and their seating capacity, range, and fuel consumption. Block I3 consists of passenger demand data, which is elaborated upon later in this section. This block is subject to a condition that must be verified before initiating the dynamic programming routine: passenger demand must exist (or must be greater than a certain value chosen by the airlines). As indicated in Figure 7.3, this demand data is updated in the iterations whenever a new aircraft is added to the fleet.

Once the passenger demand condition is verified, the dynamic programming routine is initiated. Within this block, a flight scheduling problem is solved for each aircraft type in the fleet, to identifying the aircraft type that yields the highest operational profit. The most profitable aircraft is then virtually assigned to the network, its flight schedule is built, and its overall profit is determined, including the aircraft ownership costs. If the total profit is greater than zero (or greater than a benchmark chosen by the airline), the aircraft is added to the fleet. Otherwise, the procedure is repeated for the next-best aircraft type, and so on until a profitable aircraft type is found.

Two different profit calculations are performed: first, the flight profit is computed, which is the sum of the yield the aircraft makes in a certain period by transporting passengers, minus the operating cost of those flights. This profit measure is used to select the most flight-profitable aircraft type. Second, there is the overall profit which amounts to the flight profit made in the considered period, minus the acquisition or ownership cost of that aircraft type for that period. Although an aircraft may achieve the highest flight profit of all available aircraft types, the net profit may be negative if it is expensive to own. In this case, this aircraft type is removed from the set of available aircraft types, and the next best aircraft type is considered.

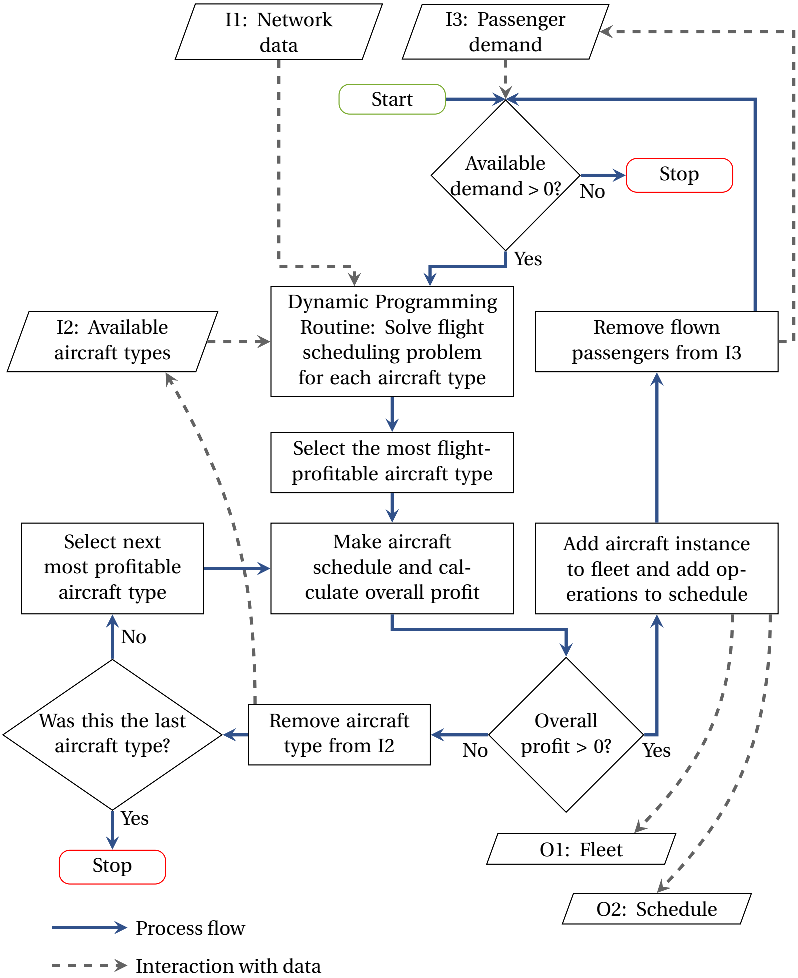
I1: Network data
I3: Passenger demand
Start
Available demand > 0?
No
Stop
Yes
I2: Available aircraft types
Dynamic Programming Routine: Solve flight scheduling problem for each aircraft type
Remove flown passengers from I3
Select the most flight-profitable aircraft type
Select next most profitable aircraft type
Make aircraft schedule and calculate overall profit
Add aircraft instance to fleet and add operations to schedule
No
Was this the last aircraft type?
Remove aircraft type from I2
No
Overall profit > 0?
Yes
Yes
Stop
O1: Fleet
O2: Schedule
Process flow
Interaction with data

Figure 7.3: Dynamic programming approach employed to solve the fleet allocation problem (adapted from [202])

If none of the aircraft types result in a positive overall profit or if no demand is left, the algorithm stops. However, if a profitable aircraft type is identified, the aircraft is added to the fleet, and the passenger demand assigned to its schedule is removed from the input data. The cycle repeats iteratively until one of the two stopping criteria is met. Ultimately, the algorithm output is the best aircraft fleet for the airline (i.e., how many aircraft instances of each aircraft type), which is collected in block O1, and the schedule for each assigned aircraft for the considered period in block O2.

Flight Scheduling Problem The idea behind dynamic programming is the possibility of solving one sub-problem at a time. Each time the dynamic programming routine is accessed, as many sub-problems are solved as there are aircraft types available. Each sub-problem is a flight scheduling problem with only one aircraft and it is solved using the Bellman-Ford algorithm [204, 205]. The Bellman-Ford algorithm is a shortest path algorithm that can be used to find the shortest path between two nodes in a graph.

In this case, the graph is built on a space-time network, where the spatial coordinates are the airports and the temporal coordinates are the time bands (whose width is the resolution of the model). The algorithm works by repeatedly relaxing all edges in the graph until the shortest path distances converge. In this study, it is used to find the best route for each aircraft to maximize the operational profit. The output consists of the best schedule for the aircraft under consideration. The problem is subject to the following three operational constraints:

1. the number of passengers carried and the distance to be flown must fall within the aircraft's range-payload diagram. The payload-range envelope is modeled as a function (f_{PR} in Figure 7.1) which returns the maximum allowed payload mass for a certain aircraft type at a certain range;
2. a flight cannot depart after the airport closure for curfew and cannot land before the airport opening at the end of curfew;
3. a flight cannot depart if the departure airport's runway is shorter than the aircraft's required runway or if the arrival airport's runway is shorter than the aircraft's required runway.

This scheduling approach offers increased flexibility and reduces computational time compared to exact optimization methods, but provides a sub-optimal solution. However, the optimality of the resulting schedule is not the primary focus of this research and does not affect the validity of the results obtained. These results mainly focus on the differences in the allocation of fleets with aircraft fueled by different fuels or designed for different objectives. Also, the proposed schedule is only used for the purpose of strategic airline planning and cannot be used for exact day-to-day planning.

Demand Input Modeling and Passenger Selection This problem formulation considers a period of one week. This time interval is chosen because it offers periodicity and provides a balance between other intervals, such as one day or one month. Selecting one week instead of one day considers frequency changes throughout a week, due to the difference in demand between business and leisure travelers, for example. A one-month period also offers this insight, but requires many more discrete time steps for the scheduling algorithm. This would increase the computational cost. Hence, the one-week period provides a balance between computational effort and an accurate representation of varying demand. However, one week does not capture the seasonal demand variations, such as a highly demanding summer period for leisure travel. Therefore, the impact of such high-demand periods on the analysis has to be studied in future research.

The passenger demand per origin-destination (OD) pair per week is an input to the model. Nevertheless, the demand throughout the week is not constant. The required input is a demand schedule per OD pair where the weekly demand is divided into discrete demand peaks throughout the week. The demand is normally distributed around each peak. For each OD pair, this results in an array of 504 elements of 20-minute intervals. Each interval has either no demand (0) or a positive integer indicating the number of passengers willing to travel a specific route at that time. This approach ensures that it will be more attractive to keep flying at certain high-demand periods, no matter what the design objective of the aircraft is. Hence, it is assumed that in general passenger preferences will still be regarded when defining the flight schedules and that the airline remains competitive. Visual representations of such demand schedules are provided in Figures 7.4 and F.1a.

This demand schedule influences how many passengers can be transported between an origin-destination pair at the departure time under consideration by the algorithm. As discussed above, the input to the allocation problem is a demand schedule where each demand peak is spread out over multiple time slots of 20 minutes. When the algorithm considers a possible flight at a given departure time slot, the maximum passenger number that can be taken on board is the minimum value of either

- the demand available in that 20-minute time slot plus the demand available in the surrounding n_{attr} time slots, or
- the maximum amount of seats the aircraft type under consideration (seat_k), multiplied by a given load factor.

The parameter n_{attr} is the attraction band. In the current study, the attraction band is set to nine, meaning that the algorithm can pick up any available demand from the three hours prior and three hours after the considered departure time. This simulates the willingness of a subset of the passengers to take a slightly earlier or later flight. This passenger selection at a departure time t for route i can be formulated as follows:

$$\text{pax}_{i,t} = \min\left(\text{seat}_k \cdot \text{LF}_k\,, \sum_{x=t-n_{\text{attr}}}^{t+n_{\text{attr}}} \text{demand}_{i,x}\right) \tag{7.1}$$

Model Considerations The approach presented and adopted in this research is based on some model considerations, both methodological and numerical. The most significant considerations are listed below:

- The objective is to maximize profit. Also in the case of climate-optimized aircraft, it is assumed that the operator would still prefer to maximize its profit.
- The model simulates an average week of operations, thus it produces the flight schedules for seven days. In practice, an aircraft does not operate all days of the year. This is not accounted for in the current setup. Depending on the maintenance requirements of the aircraft considered in the analyses, some aircraft may have a lower annual utilization. This would result in fewer flight operations, and thus a lower network profit and less revenue passenger kilometers covered than estimated by the current method.

- The time resolution of the model is 20 minutes. The resolution of the model indicates the width of the time intervals in which time is discretized. This concept is used to represent the airline flight network on which the Bellman-Ford algorithm is applied.

Furthermore, when developing the schedule for a particular aircraft, the algorithm considers a turn-around time (TAT) between two consecutive flights. It is assumed that this turn-around time is particular to a certain aircraft type and independent of the number of passengers onboard. The turn-around time (in hours) is approximated using the relation proposed by Jansen and Perez [26]:

$$\mathrm{TAT}_k = \left(2.0 + \frac{n_{\mathrm{seats},k}}{c_1 \cdot n_{\mathrm{doors},k}} + \frac{n_{\mathrm{seats},k}}{c_2} + \frac{n_{\mathrm{seats},k}}{c_3 \cdot n_{\mathrm{doors},k}} + 3.0\right) / \, 60 \tag{7.2}$$

where $n_{\mathrm{seats},k}$ and $n_{\mathrm{doors},k}$ are the number of seats and opened doors for aircraft type k, respectively. The coefficients c_1, c_2, and c_3 depend on the seat configuration and are determined according to Table 2 in Reference [26]. In practice, the TAT may vary depending on how many passengers are carried on board a specific flight. However, in this study, a constant, conservative turn-around time is assumed with the maximum number of seats occupied and only one open door at the gate for all flights.

7.1.3. OPERATING COST ANALYSIS

In the dynamic programming routine, the operating cost for each potential flight is calculated to assess the achievable flight profit. In this study, only the direct operating cost (DOC) is considered. In the previous chapters, the cash operating cost was considered, which amounts to the DOC minus fees. The indirect operating costs, which are strongly dependent on airline strategic decisions, are neglected. The direct operating costs are dependent on fuel consumption, oil usage, crew costs, maintenance costs, insurance, and landing fees. The cost to execute a flight, C_f, is defined as follows:

$$C_f = C_{\mathrm{fuel}} + C_{\mathrm{oil}} + C_{\mathrm{crew}} + C_{\mathrm{maint}} + C_{\mathrm{ins}} + C_{\mathrm{landing}} \tag{7.3}$$

$$= C_{\mathrm{fuel/kg}} \cdot m_{\mathrm{fuel,bl}} + C_{\mathrm{hour}} \cdot t_{\mathrm{bl}} + C_{\mathrm{landing}} \tag{7.4}$$

The fuel costs are calculated from the fuel mass consumed on that particular flight. This fuel mass is estimated using the analytic relations from Torenbeek's lost-range method [115] where the cruise range is set to the great-circle distance between the origin and destination of the considered flight. The payload mass is dependent on the number of passengers assigned to this flight by the allocation algorithm. The lost-range method also includes fuel spent during take-off and climb as a function of the initial cruise altitude and velocity, and the method adds a fraction to account for maneuvering. Additionally, reserve mission fuel is considered in the mass estimation, but this part is not added to the cost estimation since it is unlikely that this fuel will be used on every flight.

The landing fee C_{landing} is a fixed fee per flight. In the current model, this fee is assumed to be the same for every airport in the network. In the current model, the other cost elements in Equation (7.4) scale with the block time t_{bl} of the flight. The block time is the sum of four terms: 1) the cruise time, 2) the time spent in take-off, climb, descent, and landing, 3) the time covered by ground maneuvers such as taxiing to and from the runway, and 4) the time covered in the air for maneuvering. The cruise time is equal to the great-circle distance between the origin and destination divided by the cruise speed. The flight times before and after cruise are estimated by performing a numeric mission of the aircraft. The following relation, suggested by Roskam [35], estimates the ground maneuvering time t_{gm}:

$$t_{\mathrm{gm}} = 0.51 \cdot 10^{-6} \cdot \mathrm{MTOM} + 0.125 \tag{7.5}$$

where MTOM is the aircraft's maximum take-off mass in kilograms. Ten minutes are added to account for airborne maneuvers. All non-cruise time components are collected in the landing and take-off time parameter (LTOT). This time is also taken into account in the scheduling algorithm. The time spent on ground operations while the aircraft is parked, such as the unloading and loading of passengers, is not added to the block time but is considered in the turn-around time between flights, as discussed above. This time-dependent cost term C_{hour} is based on the methods introduced by Roskam [35] and uses cost estimates from the previous chapters.

As discussed in the fleet allocation algorithm section, once the most profitable aircraft is selected, the net profit has to be computed by subtracting the weekly ownership costs from the profits obtained from the flights throughout the week. This ownership cost is modeled as an annual fee for acquiring the aircraft, either through purchase or leasing. The annual leasing cost is assumed as a fraction of the aircraft purchasing price [26]:

$$C_{\mathrm{acq,week},k} = 0.0835 \cdot \mathrm{APP}_k / 52 = 0.0835 \cdot \left(\mathrm{AFP}_k + n_{\mathrm{eng}} \cdot \mathrm{EPP}_k\right) / \, 52 \tag{7.6}$$

where AFP is the airframe purchase price and EPP is the engine purchase price. These prices are estimated using Equation (3.25). The daily ownership cost for aircraft type k is equal to $C_{\mathrm{acq,week},k}$ divided by seven in the current setup. This approach may underestimate the daily or weekly ownership costs since an aircraft does not operate every day because of maintenance tasks, for example.

7.1.4. CLIMATE IMPACT ASSESSMENT

Once the fleet has been allocated and the schedule is known, the climate impact of the network can be evaluated. The climate impact cannot be calculated during the fleet allocation iterations since the computation requires a multi-year emission scenario as input which is not known when the objective function is evaluated due to the backward-solving procedure of the dynamic programming routine. An alternative approach would be to consider the emission and contrail length during the schedule creation as metrics for climate impact. However, this would not capture differences in the short- versus long-term effects of the different species. In this chapter, similar to the optimizations in the previous chapters, the climate impact is measured by the average temperature response over a period of 100 years, ATR_{100}.

The temperature response is calculated using the linearized temperature response model introduced in the previous chapters. This parameter considers the effects due to carbon dioxide (CO_2) emissions, nitrogen oxides (NO_x) emissions, contrail formation, and emissions of soot and sulfate (SO_4). While the effects of NO_x and contrails on $\Delta T(t)$ are typically short-lived (from hours to decades), the warming effect due to CO_2 emissions can span over centuries. Therefore, a period of 100 years is selected which provides a balance between the short- and long-lived effects [20].

The time horizon considered for the climate impact evaluation starts in 2023 and continues until 2123. The fleet is operated for 35 years, approximately the lifespan of an aircraft, starting in 2023. The network schedule is repeated 52 times per year. This leads to an operational scenario where the annual emissions and contrail formation are constant, but non-zero, for the first 35 years and then abruptly fall to zero from 2058 onward. In reality, it is likely that network demand will increase in the future [206, 207] and that the fleet composition will change due to this growth, new technologies, and potential policies. Demand growth and the impact of new technologies are not captured in the current. However, this approach allows answering the research questions posed in Section 1.4 which focus on the comparison of fleets and aircraft designs, rather than accurately computing the actual climate impact of a future scenario.

To create the 35-year emission scenario, the emissions for all flights in the weekly schedule have to be computed and added. The carbon dioxide emissions follow directly from fuel consumption. However, the NO_x emissions and contrail formation have to be evaluated at discrete steps in the mission since these effects are altitude-dependent. Therefore, a numeric mission analysis is carried out for each unique flight performed in the weekly schedule. A unique flight is defined by the route, the aircraft type, and the number of passengers carried, since this will affect the flight performance. For all flights with a certain aircraft type, the initial cruise altitude from the aircraft design optimization is used. Nevertheless, it is possible that this is not the optimal cruise altitude, not in terms of profit, nor climate impact, for the given payload-range combination since the aircraft mass varies. Therefore, it is recommended to study the potential effects of varying cruise altitude and Mach number inside the allocation algorithm.

The data per flight obtained through this mission analysis are the CO_2 emissions, NO_x emission distribution per flight level, and contrail length distribution per flight level if persistent contrails are formed. For each of these climate species, these values and distributions are multiplied by the frequency of this particular flight and subsequently added to achieve the total value or distributions of the one-week period. Finally, the data is multiplied by 52 to model the contribution of one year. The emission indices, contrail formation criteria, and contrail properties are different for each considered fuel. Table 6.2 presents the data used in this study.

The linearized temperature response model introduced in Sections 3.1.2, 5.1.2, and 6.1.2, first translates the emission scenario into radiative forcing, then normalized radiative forcing, and finally into the temperature response. This model considers the warming effects due to changes in atmospheric concentrations due CO_2, short-term ozone (as a result of NO_x emissions at altitude), as well as the warming effects due to contrails. The effect of contrails is currently studied and may consist of warming and cooling effects [80], depending on the time and location. However, in this study, the net effect of persistent contrails results in global warming. The temperature response calculations also consider the cooling effects due to long-term methane and ozone depletion as a result of NO_x emissions.

7.2. COST-OPTIMAL REFERENCE CASE AND VERIFICATION

This section introduces the reference network on which the different aircraft sets will be allocated. The focus lies on the allocation of cost-optimal, kerosene aircraft, which allows the verification of the dynamic programming approach and provides a reference case for the solutions in Section 7.3. The aircraft design methods have been verified in the previous chapters (Sections 3.2 and 6.2) for the three aircraft categories, but the connection to the network level is new in this chapter. Therefore, the verification step here targets this connection and the fleet allocation model itself. Note that the fleet allocation algorithm requires inputs and assumptions, such as airport landing fees and ownership costs, which are not made publicly available for all airports or operators. Therefore, the verification in this section aims at reproducing the realistic decision-making process of an operator rather than obtaining 100% accurate cost or profit measures.

7.2.1. REFERENCE NETWORK DATA AND COST-OPTIMAL AIRCRAFT

The reference network is based upon the North American network operated by Delta Airlines, as introduced by Jansen and Perez [208]. The hub of this network is Atlanta Airport (ATL). From this hub, passenger demand exists towards nineteen domestic and eleven international airports. The passenger demand introduced in the work by Jansen and Perez is translated into a weekly demand and gathered in Table F.1. The demand for the five additional transatlantic routes is taken from the Bureau of Transport Statistics (BTS) Air Carriers: T-100 International Segment (US Carriers Only) [1] database. The network demand in Table F.1 is assumed to be symmetric, meaning that there is an equal weekly demand from each destination airport to Atlanta.

The weekly passenger demand is transformed into a demand schedule, as introduced in Section 7.1.2. This proposed schedule assumes demand peaks at discrete times throughout the week. The demand at a particular time is subsequently distributed over a three-hour interval, with the peak time at the center of the interval. If an aircraft cannot depart at the time of the peak due to surrounding flights, for example, it can still capture a fraction of the demand because of this distribution. For each demand peak, the model assumes a six-hour window in which passengers are willing to depart.

Figure 7.4 shows examples of the demand schedules for the Atlanta-Boston route and the Atlanta-Amsterdam connection. The demand schedule for domestic routes is set up such that multiple demand peaks are present each day, representing an expected daily frequency of 6 or 7. For transatlantic routes, the demand is modeled after the current flight departure times in the late afternoon or early morning. The heatmap in Figure F.1a shows how the demand for each route in the network is spread throughout the week, per time step of 20 minutes, for the considered network. The dark green regions indicate the highest demand, while the light yellow regions indicate moments of zero demand. The demand schedule is arranged so that each route's highest demand occurs during the day. For each airport, departures have to occur between five o'clock in the morning and eleven in the evening, representing a curfew of six hours each day.

Since the objective of the fleet allocation is to maximize the network's profit, the allocation needs cost and yield estimates as input. Table 7.1 provides an overview of the

---

[1] URL `https://www.transtats.bts.gov/Fields.asp?gnoyr_VQ=GDK` accessed on 19 April 20223

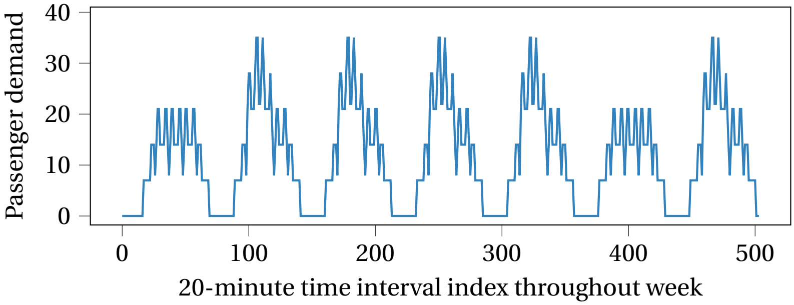

(a) Atlanta - Boston route

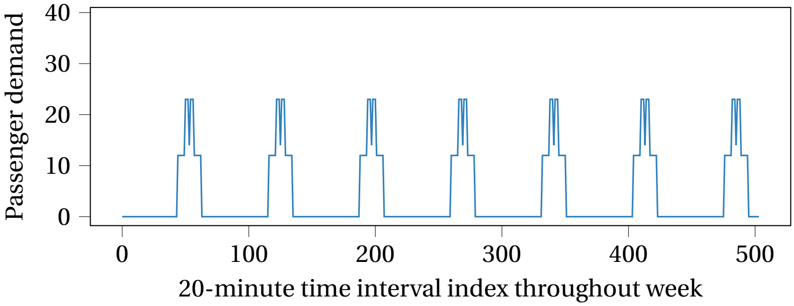

(b) Atlanta - Amsterdam route

Figure 7.4: Examples of demand schedules on routes in the reference network

assumptions for the reference network. The remaining overnight parking cost applies whenever an aircraft has to spend the night at an airport other than the hub, which is Atlanta Airport. Because of airport curfews, sometimes the aircraft cannot return to the hub on the same day and has to be parked at the destination airport. Typically, this period is less than eight hours long. A landing fee is added to the operating costs for each flight. The remaining overnight and landing fees are assumed to be the same for all considered airports, although, in practice, these numbers will be different for each airport or country. The yield per passenger-kilometer in Table 7.1 is an average value based on economy-class ticket prices over the considered routes in 2023 [2].

The baseline set of aircraft consists of three aircraft types which are all optimized to minimize the cash operations costs at the aircraft level. Table 6.3 summarizes the top-level of these three aircraft categories, targeting the regional, medium-, and long-range market segments. In the upcoming sections, these three aircraft types are referred to using the acronyms "REG", "SMR", and "LR". The top-level requirements are based on existing aircraft [128, 197, 198], and these requirements are the same for all considered aircraft design objectives and fuels in this research.

Following the data connection from Figure 7.2, the required inputs for the kerosene-powered fleet are collected in Table E.4. The chosen design variables result from the optimization defined in Equation (6.1) and are based on the design optimizations in Section 6.3. The data of the aircraft designed for the minimal operating cost (the columns

---

[2] URL `https://www.delta.com/flight-search/book-a-flight` accessed on 19 April 2023

Table 7.1: Cost and yield assumptions for the reference network, applicable to all airports or flights

Parameter	**Value**
Remain overnight parking cost (stay cost) [USD/hr]	48
Landing fee [USD/landing]	7.8
Kerosene cost [USD/kg]	0.89
SAF (HEFA 50-50 mixture) cost [USD/kg]	1.03 [187]
Liquid hydrogen cost [USD/kg]	4.4 [174]
CO_2 tax [USD/kg]	0
Revenue per passenger-kilometer [USD/(pax km)]	0.148

below the COC header in Table E.4) is used to define the reference scenario and to complete the verification step in Section 7.2.2. The provided mass and performance metrics are inputs to the fleet allocation model.

7.2.2. VERIFICATION

By performing the allocation routine for the network and the three cost-optimal, kerosene aircraft types, the maximum profit is achieved by allocating 38 aircraft. This fleet consists of nine regional aircraft, 21 medium-range aircraft, and eight long-range aircraft. The total network profit in one week is approximately 26.7 million USD, including operating and ownership costs according to Section 7.1.3. However, this figure does not include any indirect operating costs or taxes related to emissions or noise.

Figure 7.5 shows the convergence of the network profit and transported revenue passenger kilometers versus the aircraft added to the operational fleet. The aircraft added correspond to the iterations carried out by the allocation algorithm (see Figure 7.3). As can be seen in Figure 7.5, first large passenger aircraft are added, which offer large profits on long-range, intercontinental flights. The corresponding routes are shown in Figure 7.6c. However, the long-range aircraft do not cover the most RPKs, as can be seen from the distribution in Table 7.2. Subsequently, small, medium-range aircraft are allocated. These aircraft cover most of the revenue passenger kilometers (65%) by capturing the high demand on domestic routes. Finally, regional aircraft are operated to pick up the remaining profitable demand relatively cheaply and flexibly. However, this aircraft type covers the least amount of RPKs (10%) and contributes only 4% to the overall profit.

Figure 7.6 presents the routes operated by each aircraft type. The long-range aircraft transfer passengers to transatlantic destinations, except for Dublin, and to high-demand routes to the west coast of the USA. The Dublin route is not included in the schedule because the combination of demand, range, and revenue per passenger-km does not increase the network profit. Although long-range aircraft, in theory, can also operate shorter domestic routes profitably, this option is prevented by the minimum distance constraint discussed below. The medium-range aircraft focuses on domestic routes. This aircraft type is preferred since it can operate these routes at a lower cost than the long-range aircraft while being able to carry more passengers than the regional aircraft. Finally, the regional aircraft aim to transport the remaining domestic demand and serve the Central and South American routes with low weekly demand.

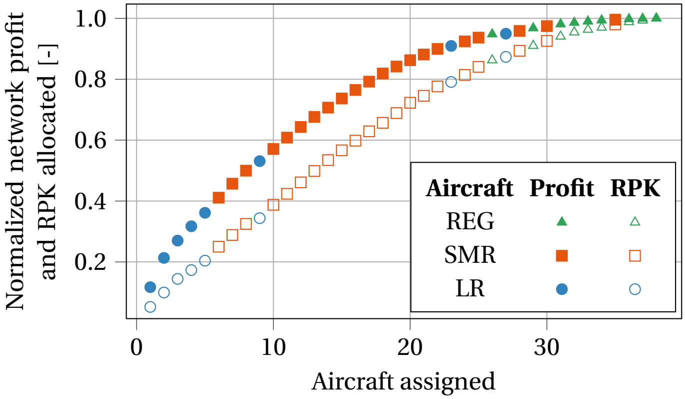

Figure 7.5: Convergence of network profit (objective) and allocated RPKs with aircraft allocation. The profit and RPK values are normalized with the total network values.

Based on this fleet allocation, it is concluded that the current dynamic programming approach converges and can realistically model the profit-seeking decision-making process. For the current case study (three aircraft types, 30 routes, seven days with 20-minute time steps), the allocation process take approximately 30 minutes[3]. Nevertheless, it is recommended to address the following two characteristics of the current dynamic programming implementation in the future.

First, for the considered network, there is a leftover demand from the hub to locations in Europe on the last day of the week and from the same locations in Europe to the hub on the first day of the week. This demand cannot be captured because an aircraft would have to leave at the overseas location on the first day and leave the hub airport on the last day. However, the current approach imposes that any aircraft should depart from the hub on the first day and end operations at the hub on the last day. The algorithm should be updated to reflect this periodic continuity across the boundaries of the considered period. Although these missing flights do affect the total revenue and profit, the focus lies on the differences between allocating different types of fleets for the same network demand. Hence, all fleets studied in this research experience a similar deficit in uncaptured demand, revenue passenger kilometers, and profit.

Second, when studying the allocation of the cost-optimal aircraft, it was observed that the large passenger aircraft were allocated to the transatlantic flights since these routes are the most profitable ones. To fill the weekly schedule of these large passenger aircraft, the algorithm added flights to domestic destinations, which are profitable. Nevertheless, regional or medium-range aircraft may make more profit on these shorter routes since they are less expensive to operate and acquire. However, since the demand on these short routes was already partially covered by the large aircraft, the smaller aircraft did not have the chance to transport these passengers in later iteration steps. This led to a sub-optimal allocation of the aircraft.

---

[3] Windows 10 Enterprise, Intel(R) Xeon(R) W-2223 CPU @ 3.60GHz, 32GB RAM, single-thread execution, Python 3.7

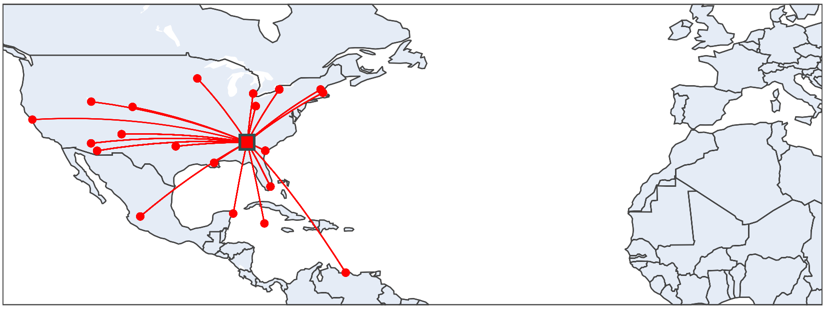

(a) Regional aircraft

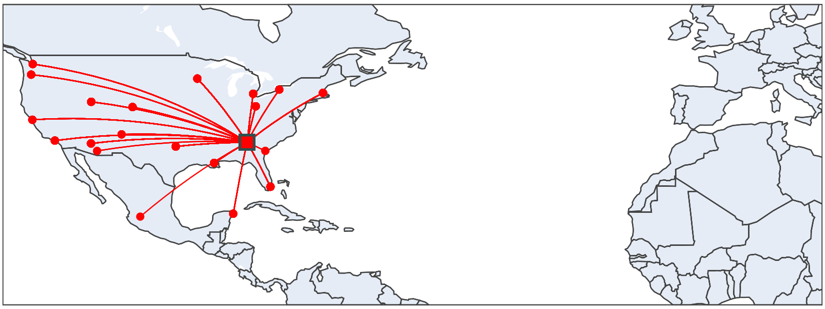

(b) Medium-range aircraft

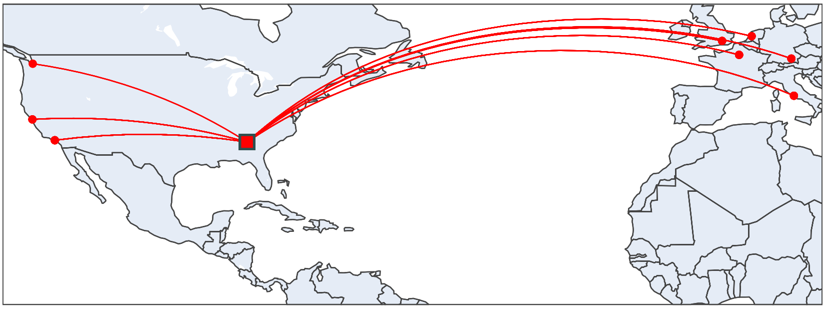

(c) Long-range aircraft

Figure 7.6: Routes operated by the three aircraft types considered in the cost-optimal, kerosene case. The square marker indicates the hub (Atlanta International Airport).

To circumvent this issue, a minimum route distance was imposed on the operations of the large passenger aircraft of 3000 km (1620 nmi). This constraint leads to an increase in overall fleet profit and a reduction in total fuel burn. Although this range is set arbitrarily at the moment, such that only high-demand operations on the West Coast and transatlantic flights can be operated by large passenger aircraft, it is recommended to choose the constraint value strategically in the future based on relative aircraft operating and ownership costs. Alternatively, longer turn-around times and/or higher operating costs on these routes can penalize domestic operations with the LR type.

7.3. RESULTS AND DISCUSSION

Using the reference, cost-optimal case introduced in Section 7.2 as a starting point, the method from Section 7.1 is now employed to examine how the aircraft sets designed for the climate objective and powered by different fuels should be allocated to maximize the profit while monitoring the effect on climate impact. Figure 7.2 summarizes how the aircraft-level data is combined into fleet-level analyses.

First, the aircraft redesign for the climate objective, using fossil-based kerosene, are considered. This is discussed in Section 7.3.1. Subsequently, the impact of introducing liquid hydrogen- or SAF-powered aircraft concepts is studied in Section 7.3.2. The results for the SAF-powered fleets use a 50-50 blend between HEFA and fossil kerosene. Additionally, the aircraft discussed in Section 6.3.4, offering a high climate impact reduction at low cost increase, are combined into fleets according to the fuel type. These fleets, which of multi-objective optimal aircraft, are denoted by “MO” in this section.

Throughout this section, the input network demand, the ticket price, and the associated demand schedule throughout the week, as described in Section 7.2.1, remain equal, irrespective of the considered design objective or fuel.

7.3.1. ALLOCATION OF CLIMATE-OPTIMAL, KEROSENE AIRCRAFT

This section studies how climate-optimal, kerosene-powered aircraft should be allocated on the network to maximize profit. These aircraft-level input parameters for this case are gathered in Table E.4. Compared to the cost-optimal reference case, a crucial change in the aircraft design is the lower cruise altitude to minimize non-CO_2 effects [87]. A reduced cruise Mach number accompanies this lower cruise altitude to maintain a near-optimal lift-to-drag ratio in cruise. However, these changes lead to a lower cruise velocity and a longer mission block time. Therefore, it is hypothesized that these climate-optimal aircraft cannot reach the same productivity level (RPK/unit of time) as the cost-optimal counterparts unless more aircraft of the same capacity are operated.

The changes in fleet composition (i.e., number and types of aircraft) and operations as a result of climate design objective can be found in Tables 7.2 to 7.11. The overall network profit is reduced by 24%, while the climate impact decreases by 55%. The reduction in profit is due to the increased operating costs per flight, the reduced cruise speed and longer block time, and the 28% reduction in revenue passenger kilometers covered overall (see Table 7.3). The latter is expected to be caused by the longer flight time, which limits the consecutive flights per aircraft instance in a given period (day or week). Additionally, some flights that carry few passengers over a short distance become less profitable due to the increased operating cost.

The reduction in climate impact is mostly attributed to the reduction in non-CO_2 effects. The redesigned aircraft feature a lower cruise altitude which targets the contribution due to NO_x emissions and contrail formation. The impact of contrails is eliminated for the climate-optimal kerosene network since the aircraft are flying lower, in conditions where persistent contrails cannot form. The observation that the reduction in non-CO_2 effects is the largest contributor to the overall climate impact reduction, rather than the lower RPKs covered, is supported by two observations: first, the reduction in climate impact is much larger than the reduction in RPKs. Second, the total energy consumption of the climate-optimal, kerosene fleet is only 6% smaller than that of the cost-optimal fleet. This indicates that the CO_2 emissions and the associated warming are only slightly lower for the climate-optimal fleet. Based on this information, it is concluded that the decrease in non-CO_2 is the largest contributor to the 55% reduction in total climate impact.

In the cost-optimal fleet, the medium-range category contributes most to the climate impact, as shown in Table 7.4. This corresponds to the highest share of revenue passenger kilometers. When switching to the climate objective, the long-range category becomes relatively more important. It is expected that the reason for this observation is that the maximum achievable climate impact reduction for long-range aircraft is lower than for medium-range aircraft, as discussed in Section 6.3.3.

To maximize the profit, the climate-optimal fleet requires 46 aircraft, eight more than in the case of the cost-optimal fleet. Seven medium-range and two long-range aircraft are added to the fleet, while one regional aircraft is removed. In terms of relative profit, RPK, and departures, it is observed that the contribution of regional aircraft to these parameters shifts towards the medium-range category when moving from the cost to the climate objective. Nevertheless, despite the increase in number of SMR aircraft and relative RPK coverage, the number of departures by SMR aircraft stays approximately the same (see Table 7.10). Although two long-range aircraft are added to the fleet, the total departures among long-range aircraft decrease from 98 to 96, and one destination is added (Table 7.11). One flight per week is added to Portland for the long-range category. The number of departures by regional aircraft decreases by 74%, and the designations Dallas, Minneapolis, and San Francisco are no longer operated by regional aircraft.

The study in Section 6.3 indicates that 23, 32, or 27% more aircraft would be required when switching from a cost objective to a climate objective, for the regional, medium- and long-range categories, respectively. The current analysis shows that 21% (46 versus 38) more aircraft are allocated, of which none are extra-regional aircraft. This difference exists because of the constant productivity assumption made in the previous chapters, where it was assumed that the same productivity level had to be achieved by the climate-optimal aircraft. However, in this research, no constraint is imposed on the productivity level or flight frequency, instead, the profit drives the fleet selection.

The current analysis shows that the increase in aircraft number is less than previously expected because adding more aircraft would not be profitable. Hence, it would be irrational to acquire 23% more regional or 27% more long-range aircraft if a subset of these cannot be allocated profitably. This aspect makes the current approach more realistic. Additionally, the current approach allows the routes flown and demand captured to vary between objectives and fuels. Nonetheless, the validity of this conclusion is only tested for the reference network considered in this study.

In this analysis, the allocation algorithm can assign as many aircraft of each type as it seems fit to maximize profit, without any further considerations. However, this does not account for the additional climate impact of increased aircraft production. Moreover, this unconstrained approach assumes that additional aircraft are simply available and can be operated, without considering the extra pressure on original equipment manufacturers and maintenance infrastructure. It is recommended to study these aspects in more detail and apply constraints or bounds where necessary.

When comparing the average load factor in Table 7.9, a slight increase in load factor for the regional and long-range aircraft types is present. This indicates that the algorithm tries to have full aircraft, which is now required to ensure that a flight becomes profitable. Nevertheless, the increase in load factor is only marginal since the difference varies between 3 and 5%.

Table 7.2: Comparison of network profit [Million USD]

		Kerosene	SAF	Hydrogen
COC	REG	1.2 (4%)	0.9 (3%)	0.7 (4%)
	SMR	14.7 (55%)	14.5 (56%)	13.9 (68%)
	LR	10.8 (40%)	10.4 (40%)	5.8 (28%)
	Total	26.7	25.8	20.4
MO	REG	1.0 (4%)	1.2 (5%)	0.6 (3%)
	SMR	14.9 (56%)	14.2 (55%)	12.8 (66%)
	LR	10.7 (40%)	10.4 (40%)	5.9 (31%)
	Total	26.6	25.8	19.3
ATR_{100}	REG	0.5 (2%)	0.5 (2%)	0.5 (3%)
	SMR	11.1 (54%)	10.8 (55%)	11.4 (66%)
	LR	8.8 (43%)	8.3 (43%)	5.4 (31%)
	Total	20.4	19.6	17.3

Tables 7.2 to 7.11 also present the outcome of the allocation of the multi-objective (MO) aircraft designs corresponding to the kinks in the Pareto fronts, as discussed in Section 6.3.4. Since these aircraft only deviate marginally from the cost-optimal aircraft, the network profit and RPKs covered are similar for these two fleets. However, the climate impact of the MO fleet is approximately 36% smaller (68 vs. 108 $\cdot 10^{-3}$ mK according to Table 7.4) because of contrail avoidance and a reduction in RF due to NO_x emissions. However, the energy consumption is slightly higher (Table 7.5), indicating that the CO_2 emissions are not lowered. The fleet composition remains unchanged, while the regional aircraft carry out fewer departures but to more destinations. This analysis of the MO fleet offers an appealing solution to achieving climate impact reduction with minimal impact on fleet allocation and network profit.

Table 7.3: Comparison of RPK [10^9 km]

		Kerosene	SAF	Hydrogen
COC	REG	0.49 (10%)	0.40 (8%)	0.38 (9%)
	SMR	3.12 (65%)	3.18 (67%)	3.20 (74%)
	LR	1.19 (25%)	1.19 (25%)	0.77 (18%)
	Total	4.80	4.77	4.35
MO	REG	0.42 (9%)	0.47 (10%)	0.32 (8%)
	SMR	3.17 (66%)	3.09 (65%)	2.96 (73%)
	LR	1.19 (25%)	1.17 (25%)	0.77 (19%)
	Total	4.79	4.73	4.05
ATR_{100}	REG	0.19 (5%)	0.19 (6%)	0.30 (9%)
	SMR	2.32 (67%)	2.23 (66%)	2.56 (73%)
	LR	0.94 (27%)	0.96 (28%)	0.64 (18%)
	Total	3.45	3.38	3.50

Table 7.4: Comparison of climate impact [10^{-3} mK]

		Kerosene	SAF	Hydrogen
COC	REG	14.2 (13%)	7.1 (12%)	3.6 (15%)
	SMR	54.2 (50%)	29.3 (51%)	14.9 (62%)
	LR	39.7 (37%)	20.8 (36%)	5.7 (23%)
	Total	108	57.3	24.2
MO	REG	8.5 (12%)	4.8 (14%)	0.9 (20%)
	SMR	31.0 (45%)	15.4 (44%)	2.4 (53%)
	LR	29.3 (43%)	14.8 (42%)	1.2 (26%)
	Total	68.7	35.0	4.5
ATR_{100}	REG	2.4 (5%)	1.2 (5%)	0.1 (6%)
	SMR	20.7 (43%)	9.7 (41%)	0.4 (43%)
	LR	25.4 (52%)	12.5 (53%)	0.5 (51%)
	Total	48.5	23.4	1.0

7.3.2. Introduction of Future Aviation Fuels

As discussed in the previous section, redesigning the aircraft for a climate-focused objective such as ATR_{100} can significantly reduce the climate impact of the network by 55%. Nevertheless, introducing future aviation fuels, such as drop-in sustainable aviation fuels and liquid hydrogen, can reduce the climate impact even further, especially when combined with ATR_{100} as the design objective. In this section, the allocation of aircraft powered by different fuels is studied. The aircraft performance indicators for the LH2-

Table 7.5: Comparison of in-flight energy consumed [10^8 MJ]

		Kerosene	SAF	Hydrogen
COC	REG	0.28 (9%)	0.25 (8%)	0.22 (8%)
	SMR	1.36 (45%)	1.39 (46%)	1.44 (55%)
	LR	1.41 (46%)	1.39 (46%)	0.99 (37%)
	Total	3.05	3.02	2.65
MO	REG	0.27 (9%)	0.29 (10%)	0.20 (7%)
	SMR	1.39 (45%)	1.37 (45%)	1.46 (52%)
	LR	1.41 (46%)	1.38 (45%)	1.13 (40%)
	Total	3.07	3.04	2.78
ATR_{100}	REG	0.15 (5%)	0.16 (6%)	0.20 (8%)
	SMR	1.29 (45%)	1.26 (45%)	1.41 (53%)
	LR	1.43 (50%)	1.41 (50%)	1.03 (39%)
	Total	2.87	2.83	2.64

Table 7.6: Comparison of pax transported [10^3]

		Kerosene	SAF	Hydrogen
COC	REG	20 (13%)	18 (11%)	18 (13%)
	SMR	106 (68%)	108 (70%)	110 (75%)
	LR	30 (19%)	30 (19%)	18 (13%)
	Total	155	156	147
MO	REG	18 (12%)	20 (13%)	15 (10%)
	SMR	106 (69%)	105 (68%)	110 (75%)
	LR	30 (19%)	29 (19%)	21 (15%)
	Total	153	155	147
ATR_{100}	REG	11 (7%)	11 (7%)	15 (10%)
	SMR	107 (72%)	106 (72%)	106 (74%)
	LR	31 (21%)	31 (21%)	23 (16%)
	Total	149	148	144

and SAF-powered aircraft sets are summarized in Tables E.5 and E.6.

Bringing all design objectives and fuels together results in a total of nine case studies. Figure 7.7a presents the resulting fleet performance of each of these fleets, where the point (1,1) corresponds to the reference cost-optimal, kerosene fleet discussed in Section 7.2. This plot shows that the hydrogen, climate-optimal fleet has the lowest climate impact, but this gain comes with a 35% decrease in the network profit. The large reduction in ATR_{100} is facilitated by the lack of CO_2 emissions and persistent contrails,

Table 7.7: Comparison of distance flown [10^6 km]

		Kerosene	SAF	Hydrogen
COC	REG	0.41 (19%)	0.37 (17%)	0.35 (17%)
	SMR	1.20 (55%)	1.24 (56%)	1.30 (64%)
	LR	0.58 (27%)	0.58 (26%)	0.39 (19%)
	Total	2.18	2.19	2.04
MO	REG	0.39 (18%)	0.43 (20%)	0.31 (16%)
	SMR	1.21 (55%)	1.19 (54%)	1.26 (64%)
	LR	0.58 (27%)	0.57 (26%)	0.40 (20%)
	Total	2.18	2.18	1.97
ATR_{100}	REG	0.24 (13%)	0.26 (14%)	0.30 (16%)
	SMR	1.14 (60%)	1.11 (58%)	1.17 (64%)
	LR	0.53 (28%)	0.54 (28%)	0.35 (19%)
	Total	1.92	1.90	1.82

Table 7.8: Comparison of number aircraft allocated to the fleet

		Kerosene	SAF	Hydrogen
COC	REG	9	9	9
	SMR	21	22	23
	LR	8	8	5
	Total	38	39	37
MO	REG	9	10	8
	SMR	21	21	24
	LR	8	8	6
	Total	38	39	38
ATR_{100}	REG	8	8	8
	SMR	28	28	25
	LR	10	10	7
	Total	46	46	40

as well as a reduction in NO_x emission index and reduced radiative forcing due to the lower cruise altitude.

Between the two extreme solutions, i.e., the kerosene, cost-optimal fleet and the hydrogen, climate-optimal fleet, the SAF-powered counterparts and the multi-objective fleets are Pareto optimal. Aircraft using a 50-50 SAF mixture can reduce the climate impact of the fleet between 47 and 78%. The cost-optimal SAF fleet is the closest option to the reference kerosene case. These aircraft are similar in design, except for the small dif-

Table 7.9: Comparison of average load factor per flight

		Kerosene	SAF	Hydrogen
COC	REG	87%	86%	92%
	SMR	90%	90%	92%
	LR	69%	69%	70%
MO	REG	85%	87%	91%
	SMR	90%	91%	92%
	LR	69%	69%	73%
ATR_{100}	REG	91%	89%	92%
	SMR	90%	91%	94%
	LR	74%	73%	82%

Table 7.10: Comparison of number of departures

		Kerosene	SAF	Hydrogen
COC	REG	270 (26%)	246 (24%)	238 (25%)
	SMR	652 (64%)	670 (66%)	664 (69%)
	LR	98 (10%)	98 (10%)	60 (6%)
	Total	1020	1014	962
MO	REG	250 (25%)	270 (27%)	196 (21%)
	SMR	652 (65%)	646 (64%)	664 (72%)
	LR	98 (10%)	96 (9%)	66 (7%)
	Total	1000	1012	926
ATR_{100}	REG	144 (16%)	146 (16%)	188 (21%)
	SMR	664 (73%)	646 (73%)	628 (71%)
	LR	96 (11%)	98 (11%)	64 (7%)
	Total	904	890	880

ference in the selected cruise Mach number. Therefore, the reduction in network profit and RPKs is mostly driven by the higher fuel cost of drop-in SAF.

In Figure 7.7b, the revenue passenger kilometers covered by each fleet solution are plotted versus the climate impact. Similar to the observation made in comparing the design objectives in Section 7.3.1, the SAF- and LH2-powered aircraft reduce the transported RPKs. This results from the different fuel prices and the resulting cruise velocity. SAF and hydrogen have a higher fuel cost per flight since the cost per unit of energy is higher than for kerosene. This makes all flights less profitable. Additionally, the aircraft in the kerosene, cost-optimal fleet are designed to have the highest cruise velocities and shortest block times. The cost-optimized SAF and LH2 aircraft cruise at lower speeds than the kerosene alternative since the fuel-related operating cost becomes relatively more important than the time-bound cost in the design process. Therefore, the LH2 and

Table 7.11: Comparison of number of destinations

		Kerosene	SAF	Hydrogen
COC	REG	20	19	19
	SMR	20	19	17
	LR	8	8	6
	Total	29	29	28
COC	REG	22	22	20
	SMR	19	19	19
	LR	8	8	7
	Total	30	30	29
ATR_{100}	REG	17	19	20
	SMR	19	19	19
	LR	9	9	7
	Total	29	29	28

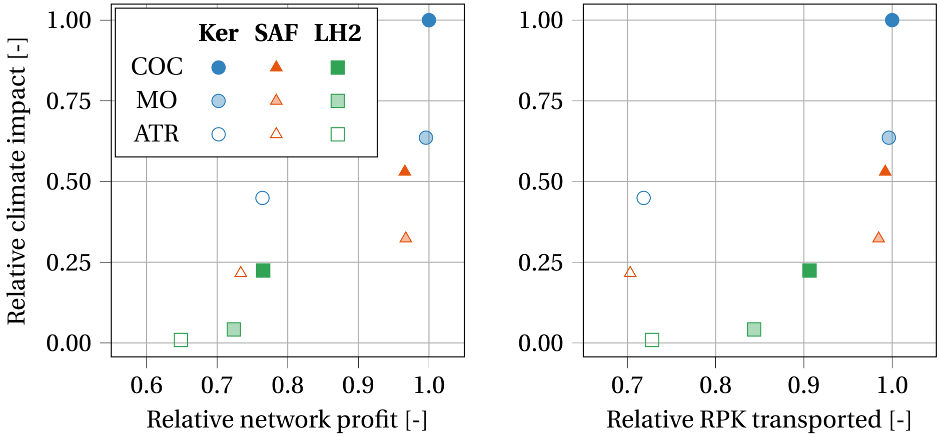

(a) Network profit versus Climate Impact

(b) RPK transported versus Climate Impact

Figure 7.7: Comparison between network key performance indicators for different aircraft design objectives and different fuels. The values are normalized with respect to the performance of the cost-optimal, kerosene fleet discussed in Section 7.2.

SAF cost-optimal aircraft designs are closer to an energy-optimal design.

By inspecting the fleet composition and schedule parameters in Tables 7.6 to 7.11, it is observed that the operations do not differ significantly between the kerosene- and SAF-powered fleets. Also, the relative contributions of each of the three SAF aircraft types are nearly identical to those of the kerosene fleet, for all design objectives. The trends observed in the previous section, such as the increased number of aircraft when the climate objective is selected, also hold for the SAF-powered fleet.

The fleet composition and scheduling choices of the hydrogen aircraft are quite different. The relative contribution of the hydrogen, long-range aircraft to the network profit and RPKs is smaller than for the other two fuels. Only five or seven long-range aircraft are allocated instead of eight or ten, as shown in Table 7.8, and only six or seven destinations are operated instead of eight or nine. Of the set of transatlantic destinations, four are operated, namely Amsterdam, London, Paris, and Rome. The routes to Munich and Dublin are not profitable. Also, the domestic route to San Francisco is not operated profitably by hydrogen, long-range aircraft. This difference in operations can also be observed by comparing the allocation shown in Figure F.2i (on Page 246) to the allocation of the long-range, kerosene counterpart (Figure F.2g on Page 246).

The hydrogen, long-range aircraft, independent of the chosen design objective, is allocated less because of the energy and cost penalties due to the hydrogen tank installation and the higher fuel price. In the current study, a two-tank configuration is selected for the long-range aircraft with tanks in front and aft of the cabin. The tank itself adds mass to the operating empty mass and elongates the fuselage, without altering the fuselage diameter. The elongated fuselage structure is heavier and also results in more friction drag. For the considered transatlantic flights, the energy consumption of the hydrogen aircraft is on average 4% higher than for the kerosene alternative, depending on the passenger number and route. Additionally, the cost-optimal hydrogen aircraft cruises at Mach 0.73, instead of 0.79, to have a lower energy consumption. However, this leads to a penalty in mission block time, making it less profitable and making the scheduling more difficult.

The long-range penalties are caused by the long cylindrical tank inside the fuselage. This tank is sized according to the energy and fuel mass needed to match approximately the payload-range capabilities of the Airbus A350-900. However, in this case study, the allocated routes have a shorter range than the design range of a long-range aircraft, as shown in Figure F.2i. Therefore, one can conclude that the hydrogen tank is oversized for the routes considered in this network. If only the current network is considered, a logical design decision would be to reduce the design range such that the maximum fuel mass decreases, leading to lower tank volume and a shorter cylindrical tank. This, in turn, reduces the mass and drag penalties at the aircraft level. This shorter range option is considered in Section 7.3.3. Potentially, this can also increase the cost-optimal cruise velocity of the aircraft.

The profit figures in Figure 7.7a are broken down into the three aircraft categories in Figure 7.8. Although these figures show that the regional and long-range hydrogen aircraft encounter the largest profit loss, the largest absolute profit loss occurs in the long-range category. Nevertheless, hydrogen provides a competitive solution in the medium-range category (Figure 7.8b). In this category, the cost-optimal hydrogen aircraft suffers a loss of only 4% in profits at a 73% decrease in ATR_{100}, making it a Pareto-optimal solution close to the multi-objective SAF solution. Note however that this marginal reduction in network profits is also because now the medium-range aircraft captures a part of the demand to West Coast destinations (LAX, SFO, and SEA) which is captured by long-range aircraft for the kerosene and SAF fleets. For the long-range market, SAF provides Pareto-optimal solutions. The benefit of the cost-optimal SAF aircraft is that its cost-optimal cruise speed is only 2% lower than the kerosene reference aircraft. This minimizes the time penalty which is, in particular, active on long-range flights.

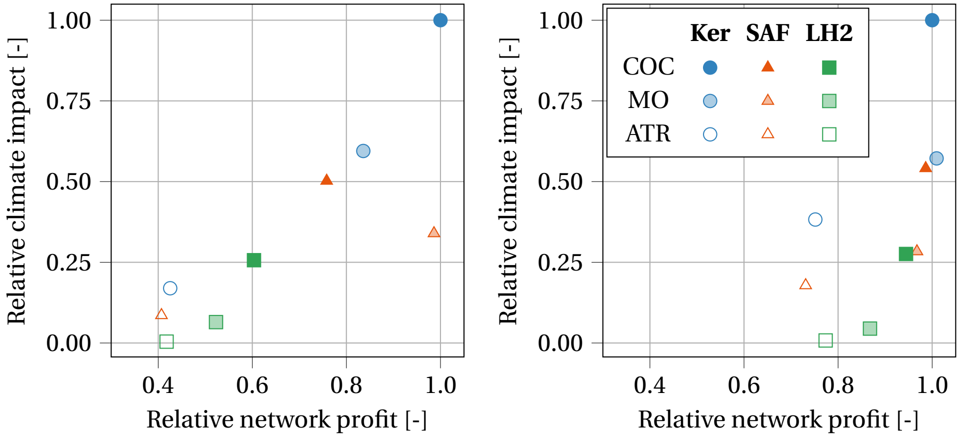

(a) Regional aircraft

(b) Medium-range aircraft

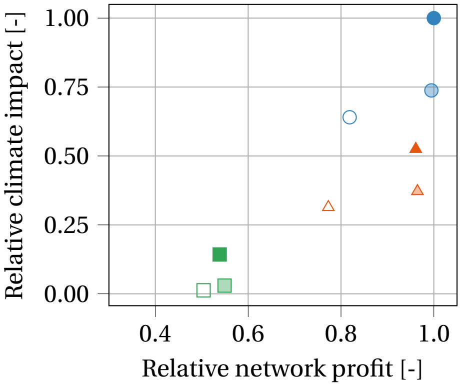

(c) Long-range aircraft

Figure 7.8: Comparison between network key performance indicators for different aircraft categories. The values are normalized with the reference metrics of the kerosene, the cost-optimal value for each category.

While the payload-range capability of the long-range hydrogen aircraft results in a large tank which makes the aircraft less profitable, the climate-optimal hydrogen aircraft appears to have an advantage compared to the kerosene and SAF counterparts. When exchanging payload mass for fuel mass to achieve more range, the hydrogen achieves a larger increase in range for a given reduction in payload mass, compared to the other fuels, due to the high energy density of hydrogen. Therefore, the payload-range diagram features a more gradual slope, as shown in Figure F.3f (Page 247), allowing more payload between 2200 and 3600 km of range. The allocation algorithm makes use of this extra capability and operates flights to Los Angeles, Seattle, and Portland which cannot be captured by the regional kerosene and SAF aircraft.

Table 7.9 indicates that, when moving from kerosene to SAF and LH2, the average load factors increase marginally. This trend does not necessarily mean that SAF or LH2 aircraft always take more passengers on board than the kerosene alternative. The passenger number on a kerosene flight is also maximized wherever possible due to the equality in Equation (7.1). This trend in load factor is caused by the fact that kerosene aircraft have a larger profit margin per flight, and can therefore also make profitable flights with fewer passengers on board. When adding flights in the dynamic programming routine throughout the week, the routine can add profitable flights with kerosene without requiring a high load factor. This is for example useful when only little demand is remaining on a given route and there is enough time in the schedule to carry out the flight to add a marginal profit. This leads to a lower average load factor. On the contrary, the higher fuel costs of SAF and LH2 often require a higher load factor before a flight is added to the schedule.

7.3.3. REDUCING THE DESIGN RANGE OF LARGE PASSENGER AIRCRAFT

The previous section discussed why the long-range hydrogen aircraft are allocated less than their kerosene- or SAF-powered counterparts. This section briefly explores the design option to reduce the design range of these long-range aircraft according to the needs of the chosen network. Therefore, four new wide-body aircraft are designed and added to the respective available fleet options.

First, a wide-body, kerosene aircraft is designed with the same design variables as the cost-optimal, long-range aircraft, but with a harmonic range of 6500 km (3510 nmi) and imposed ferry range of 11 000 km (5940 nmi), instead of the range requirements in Table 6.3. Second, a kerosene aircraft with these new range requirements is created but with climate-optimal design variables. The third and fourth aircraft are based on the long-range cost- and climate-optimal hydrogen aircraft, respectively. However, for these two aircraft, the harmonic range is set to 4000 km (2160 nmi). The ferry range is the same as the new kerosene aircraft, being 11 000 km (5940 nmi). Figure 7.9 compares the payload-range diagrams of these four new aircraft to the one of the reference, kerosene, long-range aircraft. To distinguish these four aircraft from the other cases, the letter combination "RWB" is used, which stands for *redesigned wide-body aircraft*.

The redesigned wide-body aircraft have the same payload requirements but at a reduced range. This means that they are designed to carry less fuel and therefore have a lower maximum take-off mass. This in turn reduces the required wing area and therefore the OEM, creating a snow-ball effect. For the redesigned wide-body aircraft, the MTOM decreases by 16% to 19% compared to the long-range alternatives. In particular, for the hydrogen aircraft, this change is accompanied by a reduction in maximum fuel capacity of 45-47%, resulting in a reduction of 11-12% in fuselage length and a 15-16% lower OEM. However, these changes do not consider potential changes in the hydrogen tank gravimetric index as a result of the change in hydrogen volume.

Subsequently, four fleet allocations are performed. The kerosene and hydrogen, cost- and climate-optimal cases from Section 7.3.2 are assessed once more, but now with the newly designed aircraft added as a fourth option to the available fleet. Hence, when allocating the aircraft, the algorithm can now choose from four aircraft types, instead of the three original categories. Figure 7.10 compares the network-level performance indi-

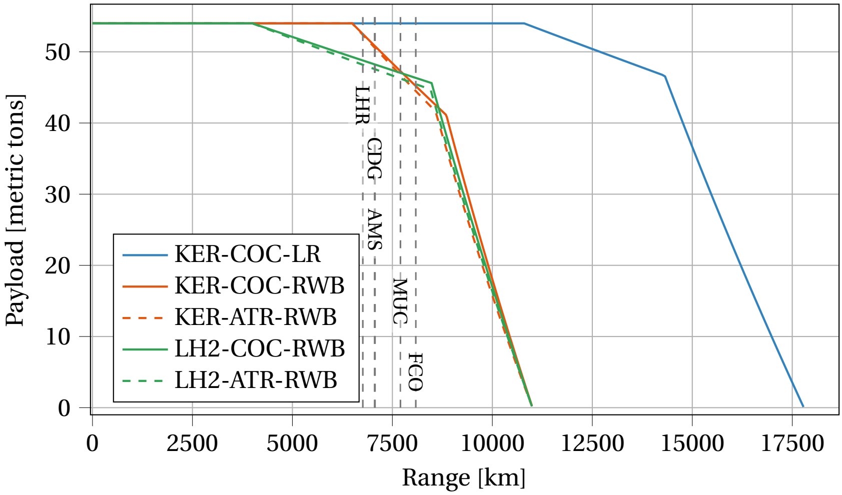

Figure 7.9: Comparison of the payload-range diagrams of the redesigned wide-body aircraft (RWB) and the reference cost-optimal, kerosene, long-range (LR) aircraft. The vertical, gray, dashed lines indicate the great-circle ranges between the Atlanta (ATL) hub airport and the transatlantic destinations, according to Table F.1.

cators of these fleets. For all considered fleets, the reduction in design range of the wide-body aircraft results in a network profit increase of 3% to 5%, with a minimal impact on the climate impact. Figure 7.10b shows that the influence on the RPKs transported than the change in profit.

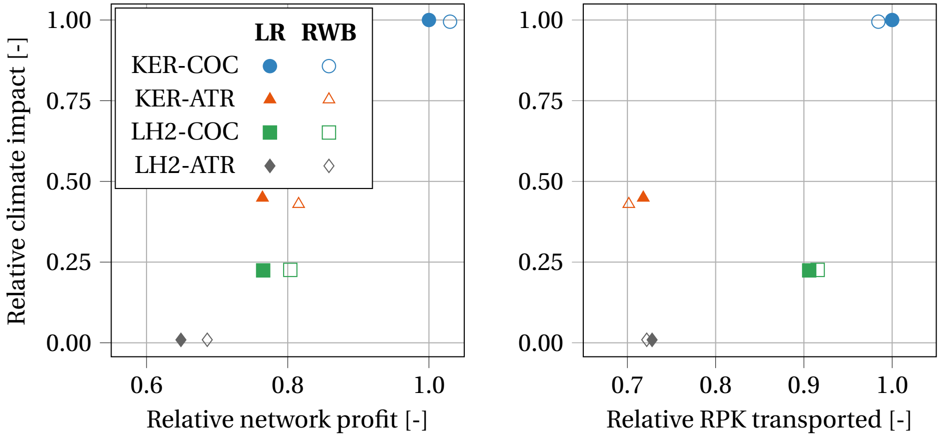

(a) Network profit versus Climate Impact

(b) RPK transported versus Climate Impact

Figure 7.10: Comparison between network key performance indicators for different fleets with and without the redesigned wide-body (RWB) aircraft. The values are normalized with respect to the performance of the cost-optimal, kerosene fleet discussed in Section 7.2.

For all cases, it is observed that the original long-range aircraft are no longer allocated since the new wide-body variants, which are tailored to this network, consume less fuel. This allows the RWB aircraft to operate at a lower cost, which increases the network profit. Since no changes are made to the payload requirements or flight speed, the differences in RPKs are relatively small. The number of aircraft allocated remains equal for the KER-ATR and LH2-COC cases, while one aircraft is added to both the KER-COC and LH2-ATR fleets.

This analysis shows that strategically reconsidering the top-level aircraft requirements can have a positive effect on the profit and RPK transported at the network level. Although the improvements in network profit are marginal and specific to the current reference network, they are achieved by only varying one top-level requirement of one category. Hence, it is recommended to also rethink other requirements, such as payload capability, to develop more climate-friendly aircraft solutions which are also appealing from profit and productivity perspectives. Furthermore, it has to be noted that the cruise altitude was not altered for the four RWB aircraft. Updating this cruise altitude according to the change in mass and lift-to-drag ratio could further improve the fuel consumption. This reasoning also applies to other design variables. For example, due to the lower MTOM and wing area, the RWB could potentially feature a higher aspect ratio before the wing span constraint is reached.

7.4. CONCLUSIONS

This research aimed to examine how climate-optimal aircraft and aircraft powered by different fuels should be allocated on an international network while monitoring the effect on key performance indicators such as total network profit, revenue passenger kilometers, and climate impact, considering both CO_2 and non-CO_2 effects. The multidisciplinary design analysis and optimization framework was extended to achieve this objective with a fleet allocation and flight scheduling level. This allocation approach employs a dynamic programming routine to find the most profitable allocation of a given set of aircraft types on a US-based network with domestic and international demand. The reference fleet is a set of three cost-optimized, kerosene aircraft targeting different market segments.

First, the allocation of climate-optimal, kerosene aircraft was considered. These aircraft are characterized by a lower cruise altitude (6 km) and reduced cruise Mach number (0.50 to 0.58). Compared to cost-optimal reference allocation, a 55% reduction in total network ATR_{100} is achieved, while the total network profit is reduced by 24%. The reduction in climate impact is primarily caused by a reduction in non-CO_2 effects. However, the increased operating cost of the aircraft and increased flight time also reduce revenue passenger kilometers by 28%. The profit is reduced because of the lower amount of revenue passenger kilometers operated and an increase in the direct flight operating cost. In particular, the time-related costs increase due to the reduced cruise velocity. The reduced profit margin on flights and lower productivity lead to a lower amount of RPKs covered. It is estimated that 46 climate-optimal aircraft are required instead of 38 cost-optimal aircraft to maximize the profit.

When aircraft powered by liquid hydrogen or drop-in sustainable aviation fuels are considered, the climate impact can be further reduced. The ATR_{100}-optimal, hydrogen-fueled fleet offers the largest reduction in climate impact up to 99%. However, the network profit is reduced by 35% in this case. The largest loss in absolute profit is caused by the operation of long-range, hydrogen aircraft, which suffer from a large penalty in operating costs and flight time. The long-range, hydrogen aircraft covers between 32 and 35% less RPKs than the kerosene counterparts. Nevertheless, the medium-range, hydrogen aircraft offer more competitive solutions with a climate impact reduction between 73 and 99%, while only reducing the profit of mid-range operations between 5 and 22%. The fleets fueled by drop-in SAF offer Pareto-optimal solutions. Overall, this analysis highlights that the current coupled approach between aircraft design and network operations can yield useful insights regarding the profitability and composition of climate-optimal fleets.

The conclusions drawn in this study are specific to the considered network. Transfer passengers or the demand between destination airports is not considered. A fixed demand schedule and constant attraction bands are assumed. Additionally, the turnaround procedure and maintenance schedule of hydrogen aircraft are taken to be similar to the kerosene and SAF aircraft. Therefore, a first recommendation is to conduct a sensitivity analysis to establish the sensitivity of the results and conclusions to these assumptions. Secondly, the current study analyzes the allocation of optimized aircraft in a network but does not yet feed the information back to the aircraft design loop. Hence, it is suggested to establish this link to determine the optimal payload-range requirements and possibly a design objective function that combines the cost and climate metrics.

8

DISCUSSION ON SUSTAINABILITY ASPECTS AND CLIMATE IMPACT UNCERTAINTIES

So far, this dissertation has focused on reducing the global warming impact of aircraft and the associated trade-off with operating costs. However, more aspects, such as air quality, noise, and economics, are essential to creating a sustainable aviation industry. This chapter discusses these aspects and evaluates the impact of the design changes and the novel fuels from the previous chapters on these three disciplines. This discussion highlights the need to include these disciplines in the MDO framework and suggests future research.

Furthermore, this chapter elaborates on the life-cycle impact of future aviation fuels. While such fuels can significantly reduce the in-flight climate impact, their life-cycle effect is not zero. The selected production pathway of SAF or hydrogen determines these fuels' overall life-cycle impact; consequently, the impact can vary regionally depending on the available pathways.

The final section of this chapter assesses the uncertainty of the linear temperature response model used throughout the thesis. It is found that at the time of writing (2023), the contribution of contrails leads to the largest uncertainty in the ATR_{100} *reduction potential. A robustness-based optimization shows that fuel-optimal aircraft can offer the most robust solutions, although more research is required to confirm this. A sensitivity analysis of the uncertain parameters highlights the need to reduce the uncertainty in contrail radiative forcing to improve the robustness of climate-optimal aircraft. This section also describes the influence of uncertain climate effects of hydrogen and drop-in SAF on the obtained design solutions.*

Parts of this chapter have been published in Deliverable 5.2 of the GLOWOPT project, in the thesis by P. Bos [209], and are currently being reviewed for publication in the Journal of Aircraft

SUSTAINABLE aviation is not only defined by the global warming induced by aviation. Current aircraft operations also lead to pollution and noise, which can impact ecosystems and human health. This chapter qualitatively discusses four crucial aspects of sustainable aviation not considered in the previous chapters. Sections 8.1 and 8.2 focus on the effects on air quality and noise, respectively, including insights gained in the GLOWOPT project [1].

In the GLOWOPT project, novel climate functions for aircraft design (CFAD) were developed and tested in the MDO of a long-range, wide-body, kerosene aircraft [210]. These CFADs estimate ATR_{100} based on the emissions and mission profile of the considered aircraft design. The novelty lies in the surrogate model-based approach, built from AirClim [66] evaluations, which reduces the computational time needed for climate impact evaluation. Additionally, the CFADs inherently include a route network and thus consider variations in radiative forcing with latitude and longitude. Since the design trends derived in this thesis are similar to the ones observed for the climate-optimal GLOWOPT aircraft, conclusions from the GLOWOPT project are used to support the discussions in Sections 8.1 and 8.2.

In comparing different fuels in Chapters 6 and 7, only the global warming due to in-flight emissions is considered. Nevertheless, the production of future aviation fuels, such as drop-in SAF and liquid hydrogen, will also lead to emissions. Section 8.3 considers the potential life-cycle impact of these fuels. The changes in operating costs and schedule changes will potentially influence the economics of air travel. This aspect is treated in Section 8.4.

The discussion of these four aspects is mainly qualitative in this chapter. Nevertheless, it is recommended to evaluate the design solutions in terms of these four disciplines. Alternatively, these four disciplines can be included in an extended MDO formulation of Equation (5.1) and Figure 5.1 (or Figure 7.1) as additional objectives or constraints. This dissertation does not evaluate the total life-cycle impact of the aircraft, which would also account for the production phase, maintenance actions, and disposal. These phases become important when more aircraft are operated due to the longer flight time, as observed in Chapters 3 to 7. The evaluation of the impacts of these non-flight phases is left as a recommendation for further research.

The previous chapters offered only limited insight into the uncertainties present in the climate impact evaluation. This remaining uncertainty, mainly due to non-CO_2 effects, influences the absolute objective values and their relative trade-off in the previous chapters. Consequently, the obtained aircraft designs are sensitive to this uncertainty, so their design robustness has to be evaluated. Section 8.5 focuses on the uncertainty quantification and robust MDO in a quantitative manner.

---

[1] URL `http://www.glowopt.eu/` accessed on 7 December 2023

8.1. AIR QUALITY

Some aircraft emissions not only influence global warming but also deteriorate air quality. Non-ideal combustion products, such as nitrogen oxides (NO_x), sulfur oxides (SO_x), soot, and hydrocarbons, contribute to air pollution [211]. In the case of aviation, fine particulate matter ($PM_{2.5}$) and ozone are the most important contributors. Due to fossil kerosene combustion, $PM_{2.5}$ is directly emitted in the form of soot or unburnt hydrocarbons (i.e., primary $PM_{2.5}$) and $PM_{2.5}$ is created when the exhaust gases mix with the ambient air, also known as secondary $PM_{2.5}$. This secondary pathway contributes most to the overall $PM_{2.5}$. Figure 8.1 provides an overview of the various pathways and reactions for fossil kerosene.

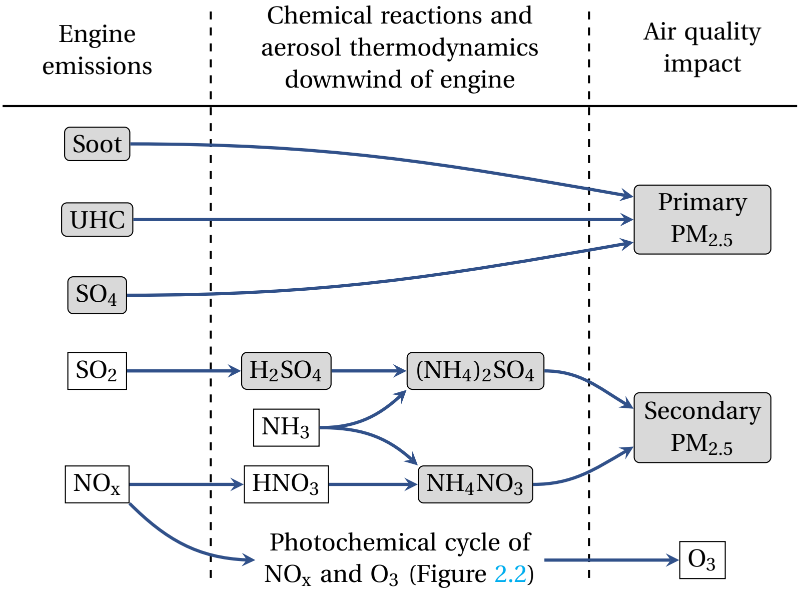
Engine emissions
Chemical reactions and aerosol thermodynamics downwind of engine
Air quality impact
Soot
UHC
SO_4
SO_2
NO_x
H_2SO_4
NH_3
HNO_3
$(NH_4)_2SO_4$
NH_4NO_3
Primary $PM_{2.5}$
Secondary $PM_{2.5}$
Photochemical cycle of NO_x and O_3 (Figure 2.2)
O_3

Figure 8.1: Overview of pathways from engine emissions to compounds which (adapted from Reference [212]), in the case of hydrocarbon fuels with non-zero sulfur content (rectangular boxes indicate gases, whereas rounded gray boxes correspond to aerosols)

Of the various pathways, mainly fine particulate matter and ozone (O_3) reduce the air quality. These compounds can lead to respiratory and circulatory problems, and mortality [213, 214]. Thus, aviation-induced air pollution negatively impacts human health [215]. Recent research by Eastham et al. [216] estimates that approximately 58,000 premature mortalities occur annually due to deteriorated air quality due to aviation emissions. However, this estimate and the relative contributions of $PM_{2.5}$ and ozone vary greatly between studies. Earlier studies by Yim et al. [217] found approximately 16,000 premature deaths per year (90% CI: 8300–24,000). Despite the remaining uncertainty, the direct impact of aviation emissions on society through air pollution is expected to be larger than that of global warming [218, 211].

These health effects and premature mortalities are not only the result of emissions in the landing and take-off cycle (LTO) but are also caused by emissions at altitude during the cruise phase [215, 216]. In particular the formation of ozone at altitude leads to a large number of premature non-LTO deaths. Additionally, emissions in a particular region, e.g., Europe, affect the air quality in other regions, such as Asia and North America [215]. This difference in emission location and location of impact complicates the formulation of policies. The following two sections discuss the influence of the design changes from the previous chapters, first at a local level and subsequently at a global level.

8.1.1. LOCAL AIR QUALITY

The local air quality evaluation aims to assess the impact of emissions at and around airports, which are covered by the landing and take-off cycle. A crucial contributor to air pollution in these phases is NO_x, and the International Civil Aviation Organization (ICAO) provides regulations and goals for maximum NO_x emissions [219]. These regulations impose a maximum NO_x pollutant mass $D_p(NO_x)$ based on four thrust settings which are applied for a given time, divided by the thrust at sea-level static conditions (F_{SLS} or F_∞). The mass pollutant is defined as follows [219]:

$$D_p(\mathrm{NO_x}) = \sum_i \mathrm{EI}_{\mathrm{NO_x},i} \cdot \dot{m}_{f,i} \cdot t_i \text{ for } i = \text{ TO, CO, App, and Idle} \tag{8.1}$$

where $\mathrm{EI}_{\mathrm{NO_x},i}$ is the NO_x emission index (in kg/kg), $\dot{m}_{f,i}$ is the fuel mass flow (in kg/s), and t_i is the interval time considered for LTO phase i. The four LTO phases are gathered in Table 8.1.

Table 8.1: LTO Cycle mission phases for the computation of NO_x pollutant mass [219]

LTO Phase	**Thrust level as percentage of rated SLS thrust F_∞**	**Time in phase [minutes]**
Take-off (TO)	100%	0.7
Climb-out (CO)	85%	2.2
Approach (App)	30%	4.0
Idle or taxi	7%	26

Although this analysis is not performed for the aircraft designed in Chapter 6, a similar study is carried out in the GLOWOPT project. A long-range, wide-body aircraft is optimized for its climate impact using novel climate functions for aircraft design [210]. This climate-optimized aircraft has similar features as the long-range kerosene aircraft presented in Section 6.3.3, but with a lower overall engine pressure ratio at top of climb. Figure 8.2 presents the NO_x pollutant mass, according to Equation (8.1), of this aircraft and compares it to a reference aircraft which is representative of current cost-optimal aircraft. The reduction in design OPR also reduces the OPR in sea-level static conditions (OPR_{SLS} or Π_∞), which in turn lowers the NO_x emission index in take-off. This design change is beneficial for the LTO air quality impact.

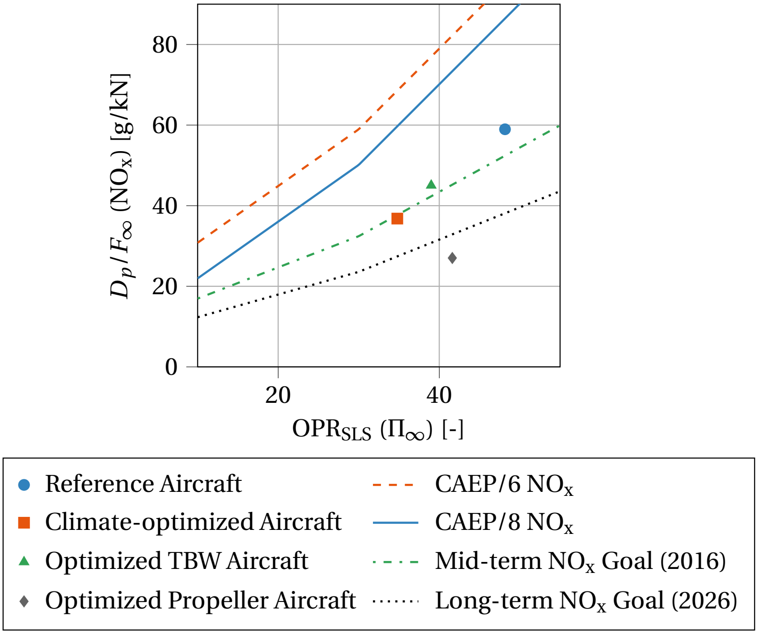

Figure 8.2: NO$_x$ emissions of GLOWOPT reference and optimized aircraft designs with respect to ICAO CAEP regulations and goals [219]. All aircraft are designed for the same requirements as the long-range, wide-body aircraft in Chapter 6 and are powered by fossil kerosene. TBW stands for truss-braced-wing. The optimized aircraft feature a lower OPR (23.8) than the reference aircraft (50.0) at top of climb. (Figure adapted from Reference [220])

Nonetheless, the reduced OPR also increases the fuel mass flow in the LTO cycle. Since the emissions of other particulates, such as soot and sulfur oxides, vary with fuel burn, the air pollution due to these compounds can increase for climate-optimal aircraft. Although the contribution of these particulates to the Air Quality Social cost (CAQSC) is expected to be significantly smaller than for NO$_x$ (3.5% versus 95% [218]), this contribution may change as a consequence of the climate-optimal design changes. More analysis is required to quantify this impact on local air quality.

8.1.2. GLOBAL AIR QUALITY

Non-LTO emissions also lead to PM$_{2.5}$ and ozone formation. The relative contribution between LTO and non-LTO PM$_{2.5}$ formation depends on the season [215], among other factors. When considering global air quality, it is expected that NO$_x$ has the largest contribution [218]. Therefore, this section focuses on the global impact of NO$_x$ emissions.

Similar to the aircraft in Chapters 3 and 6, the GLOWOPT climate-optimal aircraft operates at a lower cruise altitude and has a reduced OPR. These two design variations reduce the global warming impact due to NO$_x$. While flying lower reduces the radiative effect, a lower OPR reduces the emission index of NO$_x$ and, therefore, the full-flight NO$_x$ emissions. For the GLOWOPT aircraft, the lower OPR reduces the NO$_x$ emissions by approximately 42% (0.67 tons instead of 1.2) on a flight transporting 350 passengers over a range of 10,000km. This reduction also has a positive effect on the air quality.

The sensitivities published by Quadros, Snellen, and Dedoussi [215] are employed to quantify the impact of this NO_x reduction on $PM_{2.5}$ and ozone formation. Table 8.2 summarizes these sensitivities for different regions, per teragram of fuel and teragram of NO_x, using the emission indices from Table S-2 in the supplementary material of Reference [215]. The sensitivities per unit of fuel are converted to the sensitivity per unit of NO_x because the GLOWOPT climate-optimal aircraft has a higher fuel consumption but lower NO_x emission than the reference aircraft.

Table 8.2: Population-weighted, regional, yearly averaged PM2.5 and ozone increases per additional mass of fuel burn for different regions [215, Figure 5B]

	Asia	**Europe**	**North America**
Original, full-flight $PM_{2.5}$ concentration sensitivity $[ng \cdot m^{-3}/Tg\ fuel]$	0.69	1.08	0.47
NO_x-based, full-flight $PM_{2.5}$ concentration sensitivity $[ng \cdot m^{-3}/Tg\ NO_x]$	41.8	72.0	34.3
Original, full-flight ozone mixing ratio sensitivity $[ng \cdot m^{-3}/Tg\ fuel]$	4.07	7.25	5.06
NO_x-based, full-flight ozone mixing ratio sensitivity $[ng \cdot m^{-3}/Tg\ NO_x]$	247	483	369

Figures 8.3 and 8.4 compare the $PM_{2.5}$ concentration and ozone mixing ratio changes for the reference GLOWOPT aircraft and the climate-optimal alternative for three regions. These figures show that the reduction in NO_x, which initially targeted the global warming impact, also positively influences the global air quality.

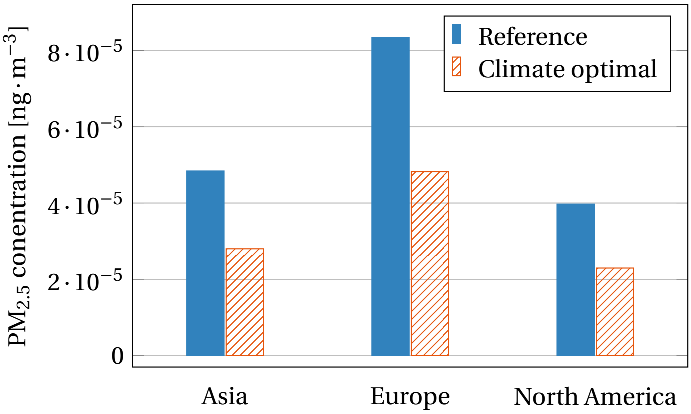

Figure 8.3: Increase in $PM_{2.5}$ concentration due to 10 000 km mission of the GLOWOPT reference and climate-optimal aircraft for different regions. The optimized aircraft feature a lower OPR (23.8) than the reference aircraft (50.0) at top of climb, leading to reduced NO_x emissions and a lower $PM_{2.5}$ concentration increase. (Figure adapted from [220])

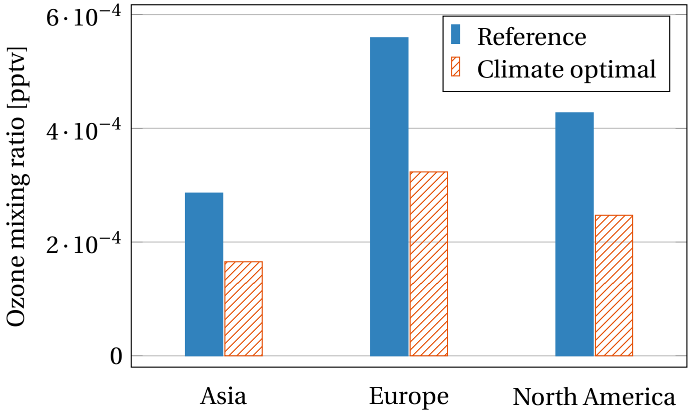

Figure 8.4: Increase in ozone mixing ratio due to 10 000 km mission of the GLOWOPT reference and climate-optimal aircraft for different regions. The optimized aircraft feature a lower OPR (23.8) than the reference aircraft (50.0) at top of climb, leading to reduced NO_x emissions and reduced ozone mixing ratio. (Figure adapted from [220])

Although this conceptual analysis indicates that climate-optimal aircraft potentially also improves global air quality, the following limitations apply:

1. The sensitivities in Reference [215] are computed for a reference fleet of aircraft which cruises at an altitude of approximately 10 to 11 km, whereas the climate-optimal cruise between 6 and 7 km. Hence, the sensitivities have to be reevaluated for this lower cruise altitude.

2. Due to changes in operations and engine performance, the relative contribution between LTO and non-LTO emissions may change.

3. The sensitivities are calculated using a global reference fleet of 2005 and atmospheric conditions of that year. New, climate-optimal aircraft will only be introduced after 2035. Hence, the changing background conditions should be taken into account.

4. The NO_x emission reduction found in the previous chapters is lower than for the GLOWOPT aircraft due to a difference in the estimation of short-term ozone impact. Hence, the reduction in $PM_{2.5}$ concentration and ozone mixing ratio from Figures 8.3 and 8.4 is expected to be smaller.

It is recommended to consider the above elements when further evaluating climate-optimal aircraft. Additionally, it would be helpful to have methods to evaluate this global air quality, possibly as a function of altitude and/or geographic location, to perform multidisciplinary analyses and optimizations of novel aircraft and engine technologies. Such functions can, for example, be added as additional objectives or constraints in an optimization problem.

In conclusion, the reduction of NO_x emissions for climate-optimal aircraft design aligns with the air quality objective. This means that the climate-optimal, kerosene aircraft likely also reduce the negative impact on global air pollution through a decrease in $PM_{2.5}$ and O_3 formation.

8.1.3. AIR QUALITY IMPACT OF ALTERNATIVE FUELS

The pathways in Figure 8.1 will differ when considering the other fuels discussed in this dissertation. Drop-in SAF can be produced free of sulfur, eliminating the resulting pathways to $PM_{2.5}$ formation. The NO_x pathways of SAF remain the same as those for fossil kerosene. Therefore, the observations from Sections 8.1.1 and 8.1.2 regarding the impact of NO_x emission also apply when drop-in SAF fuels are combusted to power aircraft.

In the case of hydrogen combustion, only the pathways originating from NO_x remain since no carbon or sulfur is present in the fuel. Nonetheless, since NO_x is the primary cause for air quality deterioration due to aviation, switching to alternative fuels does not greatly improve this aspect of sustainability if the technology level remains unchanged. As Lewis [221] points out, this air quality aspect should also be considered in the switch to hydrogen power and propulsion solutions. Potentially, updates to the CAEP regulations for hydrogen-powered aircraft should be provided as a function of engine parameters.

8.2. NOISE

With increasing aircraft operations and airport movements, noise pollution around airports becomes an important aspect of sustainable growth in aviation. However, a complete assessment of the noise impact of a new aircraft design is complicated, given the conceptual level considered in this research. Therefore, this section provides qualitative insights into the potential impact of the climate-optimal design changes on noise levels. These insights are based upon the concurrent work completed for Deliverable 5.2 of the GLOWOPT project [220] and discussions with acoustic experts. More quantitative analyses are required to support the discussion on noise of climate-optimized aircraft.

First, when considering turbofan engine noise, design variable changes such as higher bypass ratio and reduced OPR in top-of-climb conditions result in different engine performance. Additionally, the design point of the turbofan engines is at a lower altitude and reduced freestream Mach number. These changes also influence the off-design performance in the LTO cycle. These variations may influence the following two turbofan engine noise sources:

- Changes in the engine off-design performance influence the exhaust velocities of the turbofan engines. For the GLOWOPT, climate-optimized aircraft, it is observed that the exhaust velocities at take-off are higher than for the reference aircraft. Since jet noise acoustic power scales with these exhaust velocities to the power of eight [222], the engine noise during departure is expected to be higher. In the approach phase, the jet exhaust velocities are similar for both aircraft; hence, small differences in noise levels are expected.
- The climate-optimal aircraft feature a larger bypass ratio but a smaller fan diameter due to the more dense air at the design point. These parameters influence the

N1 speed of the low-speed shaft and, as a consequence, affect the frequencies of the fan tones. Therefore, the acoustic lining in the inlet and bypass duct has to be adapted according to these frequency changes.

In the case of propeller-based propulsion, as studied in Chapter 4, the noise levels will differ since no noise shielding is present around the propeller. However, more information about the propeller is required for a fair comparison. Therefore, this comparison is considered outside the scope of the current discussion.

Second, the differences in airframe noise of the cost- and climate-optimal aircraft are expected to be small. This conclusion is drawn by comparing the aircraft configuration, high lift devices, and landing gear designs. The following three reasons are identified, which support the expectation that the differences in airframe noise are small:

1. The cost- and climate aircraft share the same tube-and-wing configuration with turbofan engines mounted on the wing. Although the climate-optimal aircraft features a non-swept wing, the relative positioning of the wing and engines is approximately the same, as shown in Figures 6.3, 6.6 and 6.11.

2. The cost- and climate aircraft are assumed to have the same flap system. Although the difference in maximum lift coefficients and wing sweep likely leads to a difference in flap size and deflection, this effect cannot be quantified with the current conceptual design methods and geometry.

3. The landing gear configuration is the same for the cost- and climate-optimized aircraft. Although the geometry of the landing gear is not created in the current multidisciplinary framework, the longer fuselage and increased maximum landing mass of the hydrogen aircraft may lead to a more bulky landing gear than the kerosene or SAF alternatives.

Finally, the different operating conditions of the climate-optimal aircraft (i.e., lower cruise altitude and cruise Mach number) may also influence the perceived noise levels. Since the aircraft operates at lower speed, a small decrease in airframe noise levels can potentially be achieved for the climate-optimal aircraft [223]. The lower cruise altitude of approximately 6 to 7 km may lead to higher noise levels on the ground, although the perceived noise level is still expected to be small. Nonetheless, the ground area exposed to the noise is larger; therefore, the number of people affected by the noise is higher.

As discussed in Chapter 7, the low cruise velocity of climate-optimal aircraft drives how these aircraft are operated. As a result, the number of LTO cycles and, thus, airport movements change compared to the cost-optimal alternatives. According to Table 7.10, fewer departures take place due to the increased operating cost and scheduling issues of climate-optimal aircraft. This reduction in flight movements around airports can lead to a decrease in noise exposure for local residents. However, this insight is subject to the type of network, airline strategy, and airport operations.

In conclusion, the largest difference in noise levels between turbofan-powered climate- and cost-optimal aircraft is expected to occur due to variations in the engine off-design performance during the departure phase, in particular if the exhaust velocities are high. Therefore, a suggestion is to monitor or constrain these values in future MDO studies.

Due to the low flight Mach number of the climate-optimal aircraft, it is beneficial to consider propeller-based propulsion instead of turbofan engines (see Chapter 4). Nonetheless, from a noise perspective, this may lead to different noise levels. Therefore, the gains in fuel consumption and climate impact must be weighed against noise penalties.

8.3. LIFE CYCLE IMPACT OF FUTURE AVIATION FUELS

In the optimizations presented in the previous chapters, only the in-flight emissions and the associated climate impact are considered. Nevertheless, the climate and economic impact of alternative fuels may reach beyond this in-flight phase of the life cycle. It is vital to consider the global warming of the production phases, the effect on pollutants, and economic consequences potentially affecting other sections. Although the climate effects of the production phases may also drive the aircraft design, it is decided not to include them in the current scope since other projects have focused on the life cycle assessment of SAF [188, 186, 32] and hydrogen [32, 224, 225]. Additionally, specific life-cycle effects depend on the region of production and local availability of the respective fuel, which would further increase the uncertainty in this study. Nevertheless, this section summarizes other aspects that must be considered when considering aircraft powered by SAF and/or liquid hydrogen.

Drop-in sustainable aviation fuels can be produced through several pathways [188, 32, 187]. Although the net life cycle impact (measured in equivalent CO_2 per megajoule) of each feedstock-based pathway is expected to be lower than that of fossil kerosene, the net effect is not expected to be zero. Research by Prussi et al. [188] found that the life-cycle impact of SAF production pathways can be reduced by 18 to 94% (Fischer-Tropsch based on municipal solid waste) compared to petroleum-derived jet fuel, depending on the production pathway and location. For HEFA, the SAF type considered in Sections 6.3.1 to 6.3.3, the life cycle impact can be reduced between 33 and 84%. Research by Jong et al. [186] reports a reduction in well-to-wake emission of 85 to 93% for Fischer-Tropsch and 37 to 69% for HEFA processes (using the energy allocation method). Important in such analyses is also to account for land use changes and the effects on feedstock prices, in the case of main products and the use of fertilizers [226].

The well-to-wake impact of hydrogen and its relative difference with fossil kerosene can vary greatly between production pathways [224, 227, 228]. Producing hydrogen from renewable energy sources such as wind power or hydropower can significantly reduce the equivalent CO_2 emissions [227, 228]. On the other hand, hydrogen produced from natural or methane gas can have a similar impact as fossil kerosene. In the recent study by Kossarev, Scholz, and Hornung [229], the importance of the choice of production method becomes apparent in the life cycle assessment of a long-range aircraft concept. The production type may determine whether or not a hydrogen- or biofuel-powered aircraft has a lower net impact. In reality, if hydrogen is adopted as commercial aviation fuel, the net life-cycle impact is thus dependent on the production type, which may vary regionally or even a mix of production pathways.

In conclusion, while it is assumed that the in-flight CO_2 emission indices of SAF-HEFA and liquid hydrogen are zero, it is important to note that the obtained aircraft solutions are not 100% carbon neutral. The net life cycle impact of SAF and hydrogen is still expected to be larger than zero with the currently available production pathways.

8.4. ECONOMICS

The trade-off studies with operating cost and fleet allocation highlighted the financial impact and operational distortion of the aircraft-level design choices. This section elaborates qualitatively on the economic consequences and what they mean for stakeholders, including passengers, airlines, and original equipment manufacturers (OEMs). A complete, quantitative economic analysis is outside the scope of the current discussion due to its complexity. Nevertheless, this section highlights potential research areas and couplings between aircraft design, fleet allocation, and economics, which can be implemented in the multidisciplinary approach.

In Chapters 3 to 6, the economic trade-off with climate-focused design choices is measured by the direct or cash operating cost (DOC or COC). The increase in COC for climate-optimal aircraft ranges between 12% for kerosene, regional aircraft, and 64% for hydrogen, long-range aircraft, as discussed in Chapter 6. Although these cost increases are significant, it is essential to note that they do not directly translate into an increase of 12% or 64% in ticket prices.

The direct operating costs amount to approximately 45% to 60% of the total airline costs [230], or, as a rule of thumb, 50% can be taken [122]. This number varies with airline strategy, aircraft type, and stage length, among other factors. Additionally, unplanned operations can lead to a higher fraction of direct operating costs. In this case, DOC includes flight operations, maintenance, depreciation, and amortization cost elements. This means that 55% to 40% of the cost is incurred due to indirect operating cost (IOC) contributions. These contributions include costs for passenger services, landing and airport charges, ticketing, sales, promotion, and other administrative tasks [122].

The ticket pricing is based not only on the sum of the direct and indirect operating costs but also on the demand and services offered by the airline [231]. A mix of these aspects is often applied to determine the ticket price. Additionally, the exact fare is dependent on the travel class. Therefore, it is difficult to estimate the exact outcome of the increased COC on the ticket price in this study without the data from a specific airline.

Nevertheless, to gain insight into the ticket price increase, a simplified approach can be taken where the ticket price is primarily based on the cost plus a profit margin, the DOC is assumed to vary linearly with the COC, the IOC is assumed to remain constant, and a limited range of DOC contributions is considered. Combining these assumptions allows the computation of the ratio between the new ticket price and a reference value as a function of the ratio between the new DOC and a respective reference value, according to the assumptions in Appendix G. The relative ticket price increase is plotted in Figure 8.5 employing Equation (G.7). This figure shows that the increase in ticket price is smaller than the increase in DOC.

In Chapter 7, however, the revenue per RPK (\$0.148/RPK) and the demand are assumed to be constant for each route, irrespective of aircraft type, route, or passenger class. As a consequence, it is assumed that the airline incurs a profit loss due to the increase in operating costs. This assumption allows a fixed ticket price for a given route, and thus, theoretically, no changes occur in demand for that given route. Nevertheless, such assumptions are unrealistic. The following paragraphs hypothetically and conceptually explore how customer demand and airline supply change due to the different fuels and climate-optimal design changes.

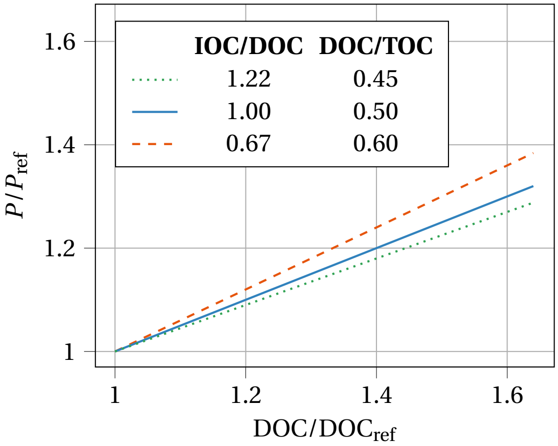

Figure 8.5: Relation between ticket price change versus the change in DOC for varying relative contribution of DOC to the TOC, assuming a cost-based ticket pricing approach (DOC=direct operating cost, IOC=indirect operating cost, TOC=total operating cost=DOC+IOC, P=ticket price)

Figure 8.6 considers the demand and supply curves for a network route (OD pair) considered by an airline. The x-axis shows the quantity of the considered product, which is the number of travelers on that route on a given day. Note that this is not the same as the amount of passengers on a single flight. The y-axis shows the ticket price P. The demand curve shows how many travelers (Q) are willing to pay ticket price P to fly this route with this airline.

On the other hand, the supply curve shows how many travelers the operator is willing to transport for a given ticket price. The equilibrium point E shows where demand and supply match. The ticket price at equilibrium, P_E, comprises the direct operating cost (DOC), indirect operating cost (IOC), and the desired profit of the airline on a single ticket sale, as seen from the airline's perspective. The ticket price corresponds to $\$0.148 \cdot \text{RPK}$ according to the approach in Chapter 7.

However, increasing the DOC by changing the fuel or operating climate-optimal aircraft reduces the profit margin for the airline, sometimes up to the point where no profit can be made and no aircraft is allocated (see Chapter 7). In a realistic scenario, the airline will include the cost increase in the ticket price. This is similar to a production cost increase, which causes the supply curve to shift to the left as shown in Figure 8.7 [232]. Assuming all other cost contributions and the targeted profit remain constant, the equilibrium point moves from E to E' in Figure 8.7, which corresponds to a higher ticket price $P_{E'}$ and a lower quantity $Q_{E'}$. To include this equilibrium change in the allocation method of Chapter 7, the available demand should be updated, and a fixed profit per route should be defined instead of a fixed revenue. The former change requires a demand price elasticity model, highlighting the need for further research.

The approach in Figure 8.7 assumes that the travelers completely pay the extra operating costs. Nevertheless, this simulates an extreme alternative to the case where the airline covers all extra costs at a profit penalty. An airline may accept a marginal profit

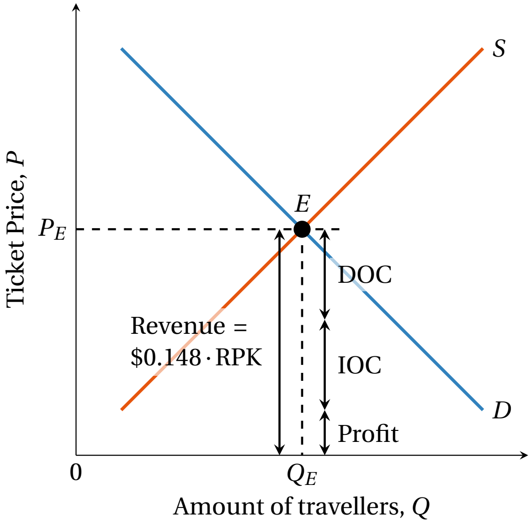

Figure 8.6: Baseline supply and demand for a route between an origin and destination airport, as considered by an airline (not drawn to scale) similar to the fleet allocation model in Chapter 7

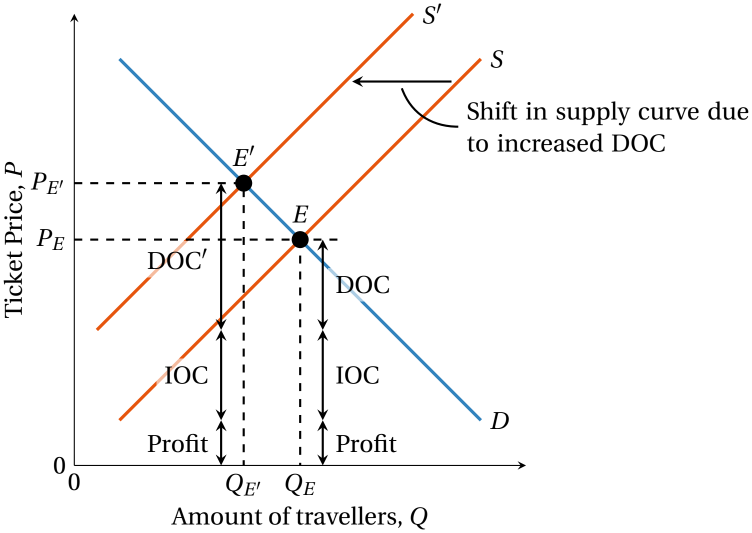

Figure 8.7: Shift in supply curve since the airline wants to keep the same profit for the considered route, but the DOC′ is higher than the initial DOC due to increased fuel prices and/or increased flight time (not drawn to scale)

reduction by partially covering the increased cost and billing a part to the customers. This would result in an equilibrium in between E and E'. Alternatively, a new policy is introduced to, for example, incentivize climate-optimal aircraft or novel fuels.

Besides price elasticity, the demand on this route is subject to time elasticity [233]. Time elasticity causes demand to change due to flight time or frequency modifications. Changes in frequency can influence the total trip time of a business traveler, for example. In general, an increase in flight time or total trip time for a given route reduces the demand for that route [233]. This causes the demand curve to shift to the left, as indicated by line D'' in Figure 8.8. Combined with the shift in supply introduced above, this results in a new equilibrium point E'' which features an even lower quantity transported (i.e., $Q_{E''} < Q_{E'} < Q_E$), but a lower ticket price than the supply-adjusted value (i.e., $P_{E''} < P_{E'}$). Similar to the suggestion above, the demand elasticity with respect to trip has to be known before including this in the allocation method.

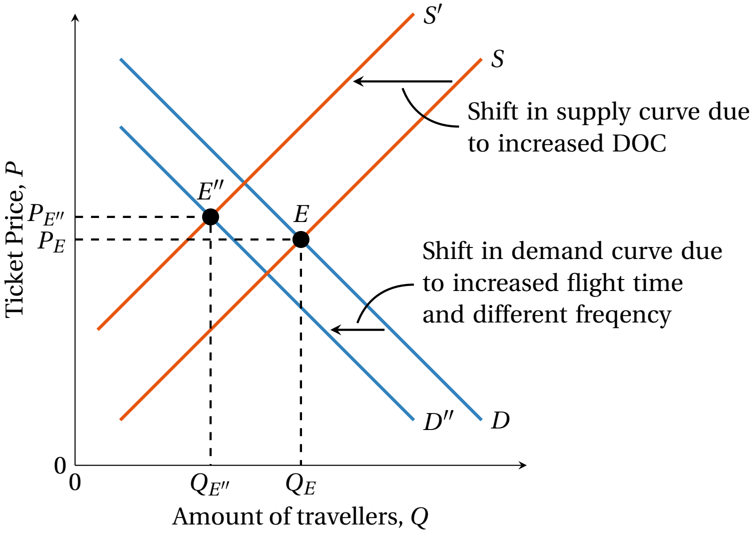

Figure 8.8: Shift in demand as a result of time demand elasticity (not drawn to scale)

The reduction in demand and equilibrium quantity can manifest itself in different ways, depending on the route length, type of traveler, and services of other airlines. The following scenarios may result from increased operating costs and increased flight time:

- travelers choosing for another airline which offers the route at a lower ticket price (mostly leisure travel, high price elasticity [233])
- travelers choosing for another airline which offers the route with a shorter flight time or higher frequency (mostly business travel, high time elasticity[233])
- people deciding not to travel at all due to the higher ticket price and the lack of a reasonable alternative
- travelers choosing for a more direct connection to another airport
- travelers selecting another mode of transport on regional routes, such as trains

This conceptual analysis suggests that when demand is variable, climate-optimal design changes and fuel choice may lead to different range and payload requirements for new aircraft. Section 7.3.3 showed that reconsidering the design range can impact the allocation of long-range, hydrogen aircraft and the overall network profit. When a shift in supply and demand elasticity is considered, the payload requirements of aircraft should also be re-evaluated. This can be achieved through a feedback link in the approach outlined in Figure 7.1 on Page 150.

Figure 8.9 presents a hypothetical MDAO workflow including such a feedback link. Additional design variables targeting the aircraft payload and range requirements are included ($\mathbf{x}_{\mathrm{TLAR}}$) and updated based on the outcome of the fleet allocation, similar to the approaches in References [25, 234]. This workflow also no longer includes separate aircraft objectives but suggests new aircraft design vector based on the network allocation. Although not included in Figure 8.9, a demand discipline could be added in between the network allocation optimization and flight profit blocks. This discipline updates the demand on a given route based on the ticket price to achieve a more realistic representation of the economic aspects discussed above.

Besides different aircraft types and technologies, policies and the customer's perspective can influence the equilibrium point. If potential customers are informed about the reduction of climate impact, for example, through a marketing campaign, the airline with such technologies can be preferred over competitors. This will shift the demand curve to the right, depending on the design objective and fuel selection. Alternatively, taxes on fossil kerosene can shift the supply curve to the left specifically for kerosene-powered aircraft, making the hydrogen- or SAF-powered aircraft relatively more appealing. A tax can be included in the operating cost estimation in the allocation procedure. Including such measures is recommended for future research.

It is important to note that the presented economic analysis is simplified and focuses purely on the microeconomic decisions of an airline in a simplified manner. The following list of considerations apply:

- The plots assume a linear relation between the quantity and price for both demand and supply. Typical models for demand are log-linear and include the time parameter [233, 232]. Also, no distinction is made between the different travel classes, such as economy, business, or first class, nor their subcategories.

- The supply lines are smooth, while in reality, steps may be present due to the discrete number of aircraft available [232].

- The discussion does not fully consider the dichotomy of demand and supply: not all passengers specifically demand that a particular OD-pair is flown but use this OD-pair to reach a different final destination. Hence, by adapting flight times or frequencies, such passengers miss connections or have another preferred route, resulting in lower demand.

- The demand and supply models do not account for seasonal variability in demand, such as connections to popular holiday destinations [230].

- Macroeconomic effects and external constraints on the operations (such as public service obligations) are not considered.

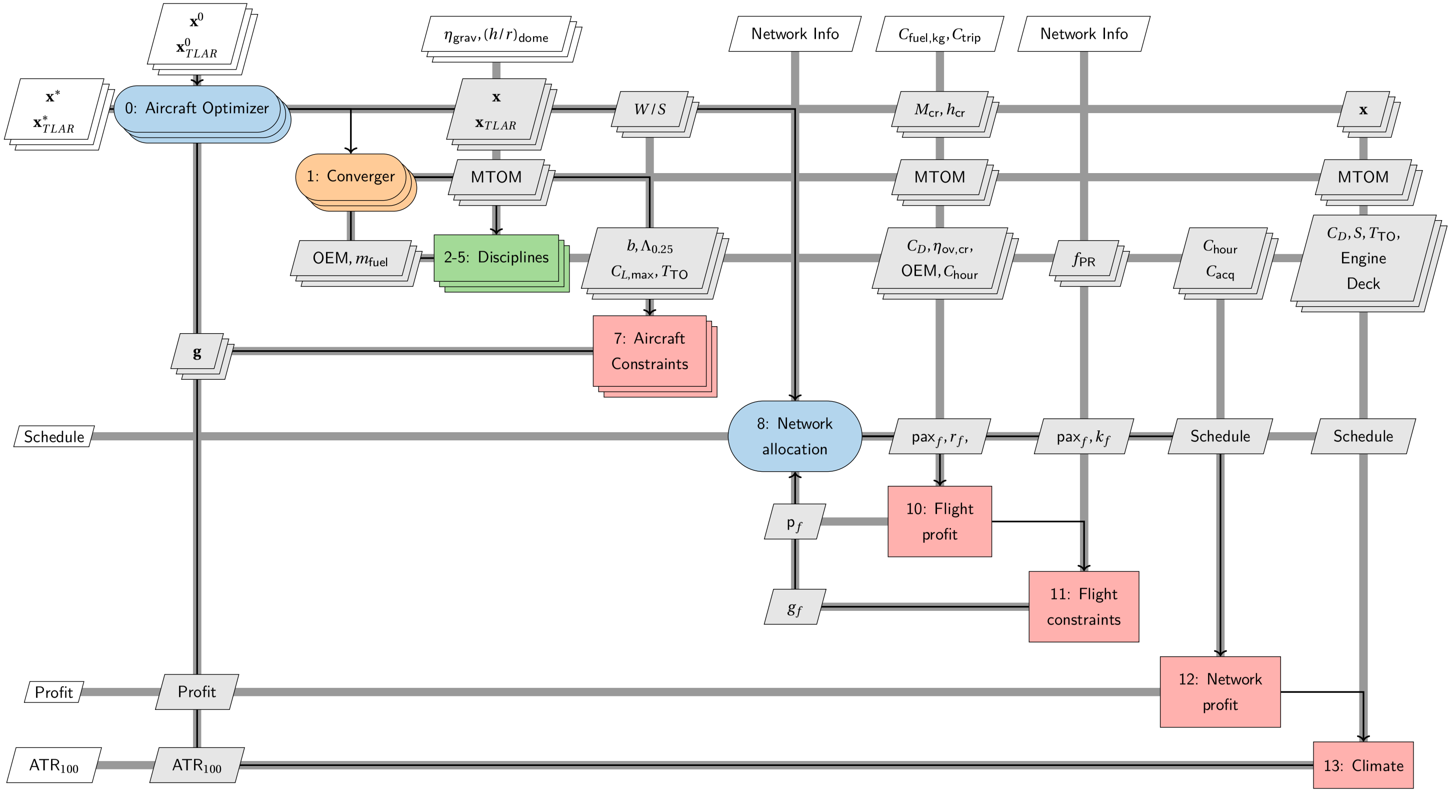
$\mathbf{x}^0$
$\mathbf{x}^0_{TLAR}$
$\mathbf{x}^*$
$\mathbf{x}^*_{TLAR}$
0: Aircraft Optimizer
$\eta_{\text{grav}}, (h/r)_{\text{dome}}$
Network Info
$C_{\text{fuel,kg}}, C_{\text{trip}}$
Network Info
$\mathbf{x}$
$\mathbf{x}_{TLAR}$
W/S
$M_{\text{cr}}, h_{\text{cr}}$
$\mathbf{x}$
1: Converger
MTOM
MTOM
MTOM
OEM, m_{fuel}
2-5: Disciplines
$b, \Lambda_{0.25}$
$C_{L,\max}, T_{\text{TO}}$
$C_D, \eta_{\text{ov,cr}}$,
OEM, C_{hour}
f_{PR}
C_{hour}
C_{acq}
C_D, S, T_{TO},
Engine
Deck
$\mathbf{g}$
7: Aircraft Constraints
Schedule
8: Network allocation
pax_f, r_f,
pax_f, k_f
Schedule
Schedule
p_f
10: Flight profit
g_f
11: Flight constraints
Profit
Profit
12: Network profit
ATR_{100}
ATR_{100}
13: Climate

Figure 8.9: Extended design structure matrix (XDSM) presenting a hypothetical MDAO, multilevel workflow where the aircraft payload and range requirements are design variables (captured in $\mathbf{x}_{\text{TLAR}}$).

8.5. UNCERTAINTY QUANTIFICATION AND ROBUST DESIGN

This section elaborates on the validity of the climate modeling approach and the remaining uncertainties. As shown in Figure 1.3 on Page 4, by evaluating the temperature response instead of emissions, the analyses become more relevant but also more uncertain. In addition, the current approach uses a linearized temperature response model to estimate the average temperature response of the aircraft fleet. This model is expected to have lower fidelity than more advanced climate modeling approaches, such as chemistry-climate or Earth system models. Nevertheless, the linearized model allows a fast evaluation of the temperature response [82], which is required for the optimizations. Due to the choice of metric and the level of fidelity, the remaining uncertainties have to be evaluated.

It is difficult to verify the linearized temperature response model with other frameworks or existing literature due to the setup of the reference scenario, the choice of climate impact metric, and the scenario assumptions. For the medium-range, kerosene aircraft, the reduction in climate impact and design solutions have been compared to results obtained by Dallara and Kroo [88] in Section 3.3.4. This comparison highlighted that the results are similar but that the relative contribution of contrails in the current implementation is higher. Furthermore, the current modeling approach uses a different response function, includes the Schmidt-Appleman criterion for contrail formation, and considers engine design variables. The reduction in ATR_{100} due to lower and slower cruise flight has also been confirmed in research by Dahlmann et al. [19], using the AirClim model, and by Radhakrishnan et al. [210], using climate functions for aircraft design.

This section first dives deeper into the uncertainties of the climate impact modeling approach for kerosene aircraft, based on the studies performed by Bos [209]. This section only focuses on uncertainties in the climate impact model, not those in other disciplines. Subsequently, Section 8.5.2 discusses the remaining uncertainty of future aviation fuels and predicts the potential impact on the obtained aircraft designs in Section 6.3.

8.5.1. UNCERTAINTY ANALYSIS OF CLIMATE IMPACT MODEL

When considering the uncertainty of the climate-optimal solution in Chapter 3, the quantity of interest is the variability in the reduction in ATR_{100} with respect to a reference aircraft. In this discussion, the reference aircraft is the cost-optimal kerosene-powered, medium-range aircraft. The reduction in ATR_{100} is called the ATR reduction potential (ATRRP), which is defined as follows:

$$\mathrm{ATRRP} = \mathrm{ATR}_{100,\text{ cost optimal}} - \mathrm{ATR}_{100,\text{ climate optimal}} \tag{8.2}$$

and its uncertainty is defined as the standard deviation of this parameter, denoted by σ_{ATRRP}. Considering this quantity of interest, it is essential to note that this section focuses on the uncertainty of the reduction in ATR_{100} achieved through optimizing the aircraft for minimal ATR_{100}. Although the uncertainty of ATR_{100} is calculated in the process, it is not the primary indicator in this study.

In fact, the uncertainty in ATR_{100} of the climate-optimal aircraft is expected to be lower than the uncertainty in ATR_{100} of the cost-optimal aircraft. This is because contrails form the largest contribution to the uncertainty of the climate impact, as discussed below. However, no contrails are formed for low-flying, climate-optimized aircraft. Hence, the largest uncertainty is present in the climate impact of cost-optimal aircraft, the first term in the computation of ATRRP in Equation (8.2).

Five steps are taken to address the uncertainty of the ATR_{100} calculation [209]. Figure 8.10 shows the workflow for the uncertainty investigation of the climate-optimal aircraft. Step A, being the deterministic climate impact model, comprises the emissions modeling and the linear temperature response model discussed in Section 3.1.2, starting on Page 39. The subsequent steps are performed in the study by Bos [209], and the reader is referred to this reference for a more elaborate discussion. The following paragraphs summarize the findings of each step.

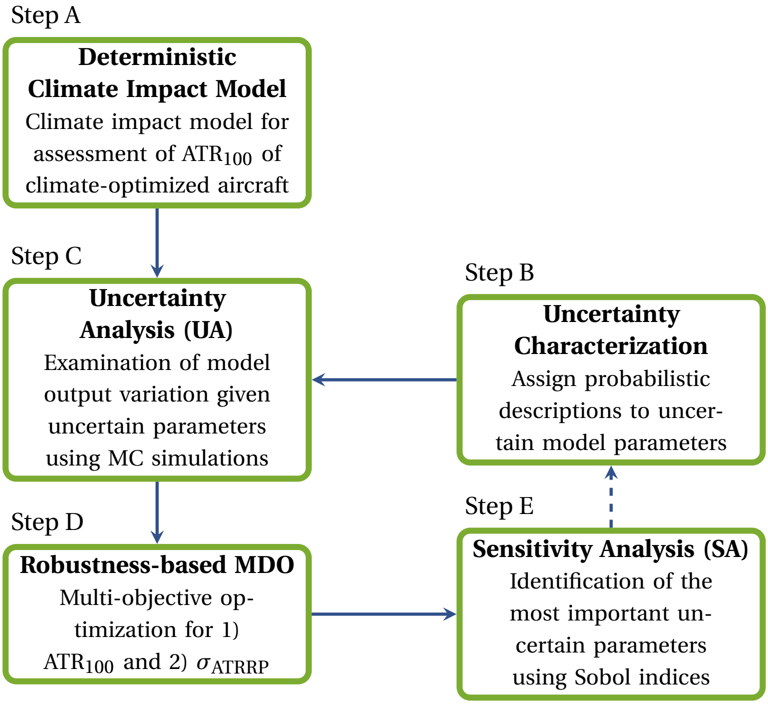
Step A
Deterministic Climate Impact Model
Climate impact model for assessment of ATR100 of climate-optimized aircraft
Step C
Uncertainty Analysis (UA)
Examination of model output variation given uncertain parameters using MC simulations
Step B
Uncertainty Characterization
Assign probabilistic descriptions to uncertain model parameters
Step D
Robustness-based MDO
Multi-objective optimization for 1) ATR100 and 2) σATRRP
Step E
Sensitivity Analysis (SA)
Identification of the most important uncertain parameters using Sobol indices

Figure 8.10: General workflow used for uncertainty investigation of the climate-optimized aircraft design. MC stands for Monte-Carlo, steps A to E indicate the order (adapted from [209], inspired by Mavromatidis, Orehounig, and Carmeliet [235])

Uncertainty Characterization The first step is to identify the model input parameters that carry uncertainty and assign probabilistic distributions to them. Two types of uncertainty are assessed. First, the climate impact assessment is subject to scientific uncertainty due to insufficient scientific knowledge and inexact modeling. Future scenario assumptions introduce the second type of uncertainty.

The scientific uncertainty is addressed by assigning probability distributions to the model's input parameters. Such uncertain input parameters are fixed throughout the deterministic optimizations in the previous chapters. Uncertainties apply to the emission estimates, concentration changes, radiative properties, lifetimes of species, and temperature response modeling. Appendix A of Reference [209] provides an overview of the considered uncertain parameters, their best estimates, and assigned probability distributions [2, 3, 117, 236]. In total, 32 uncertain parameters are considered in the current analysis.

The uncertainties are mainly applied independently, although there are two exceptions. First, since the radiative effects of NO_x are connected (i.e., long-term ozone's impact is coupled to methane depletion), the radiative efficiency probability distributions are modeled as a bivariate distribution, employing a correlation parameter. Second, the uncertainty in altitude-dependent forcing factors $s_i(h)$, applied to contrails and NO_x effects, cannot vary freely between altitudes. The forcing factors at nearby altitudes are likely to be correlated. Therefore, the uncertainties are applied at four discrete altitudes, and a linear variation is assumed between these discrete points.

The primary scenario uncertainty identified in this study applies to the background concentration of CO_2, χ_{CO_2}. This parameter performs a role in calculating the normalized radiative forcing in Equation (3.15). Research predicts with high confidence that this background concentration will increase in the coming decades [237]. A higher background concentration results in a smaller radiative forcing response for a given concentration increase [135]. Four future CO_2 concentration projections are evaluated to determine the impact on the observed ATR_{100} and ATRRP. These projections are captured in Representative Concentration Pathways (RCPs) which specify future projections of the greenhouse gas concentrations in the atmosphere [238]. The four CO_2 concentration scenarios considered in the current uncertainty analysis are RCP2.6 [239], RCP4.5 [240], RCP6.0 [241], and RCP8.5 [242]. Figure 8.11 shows the respective CO_2 concentration scenarios.

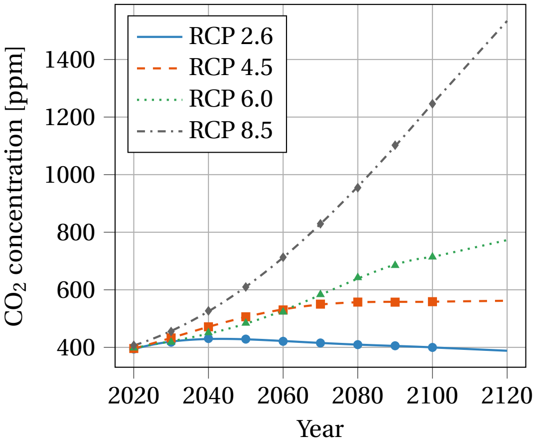

Figure 8.11: Atmospheric CO_2 Representative Concentration Pathways (RCPs) 2.6 [239], 4.5 [240], 6.0 [241], and 8.5 [242] considered in the scenario uncertainty analysis. The pathways are interpolated between the data points and linearly extrapolated up to 2120 for the uncertainty quantification.

Uncertainty Analysis The assigned probability distributions are direct inputs to the uncertainty analysis. A quasi-random Monte Carlo (MC) simulation assesses the uncertainty in ATRRP for the climate-optimal aircraft and all the Pareto solutions. A quasi-random approach, instead of a fully random method, is selected since it offers a faster convergence of the Monte-Carlo estimation error, which is the error between the estimated mean from sampling and the expected mean from the deterministic model. Although the convergence depends on the number of uncertain parameters, or dimensionality, for the quasi-random method, this method provides an acceptable estimate of uncertainty at a smaller sample size than the fully random approach. After convergence studies of the error with sample size, a Monte-Carlo simulation (MCS) with Sobol sequencing is selected for the uncertainty analysis, with 2^{14} samples.

Figure 8.12 shows the correlation between the ATRRP and its standard deviation along the ATR_{100}-DOC Pareto front of kerosene, medium-range aircraft. When moving from the cost- to the climate-optimal solution, the ATRRP and its variability increase. The standard deviation is approximately 6.4 mK for the climate-optimal solution with an ATRRP of 15 mK. This indicates the uncertainty for the climate impact reduction is high. Figure 8.13a indicates the corresponding ATRRP variability (90% confidence interval) on the ATR_{100}-DOC Pareto front. Figures 8.12 and 8.13b show that the variability increases with increasing ATRRP when moving from the cost- to the climate-optimal solution.

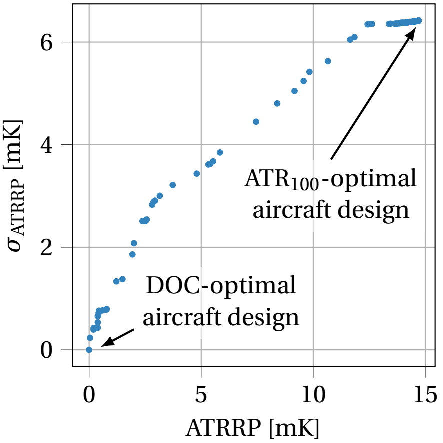

Figure 8.12: Variation in ATR_{100} reduction potential (ATRRP) and its standard deviation (σ_{ATRRP}) along the Pareto front of kerosene, medium-range aircraft in Chapter 3, adapted from Reference [209]

The uncertainty analysis of the climate impact of the individual species shows that the contrail impact features the largest uncertainty, followed by NO_x-induced effects. Nevertheless, the standard deviation of the ATR_{100} of contrail is an order of magnitude larger than that of NO_x.

Robustness-based MDO, RMDO Since the climate-optimal aircraft has a large uncertainty in terms of ATRRP, the question arises whether design vectors exist that do not minimize ATR_{100}, but offer a significant ATRRP at a lower σ_{ATRRP}, ignoring the operating

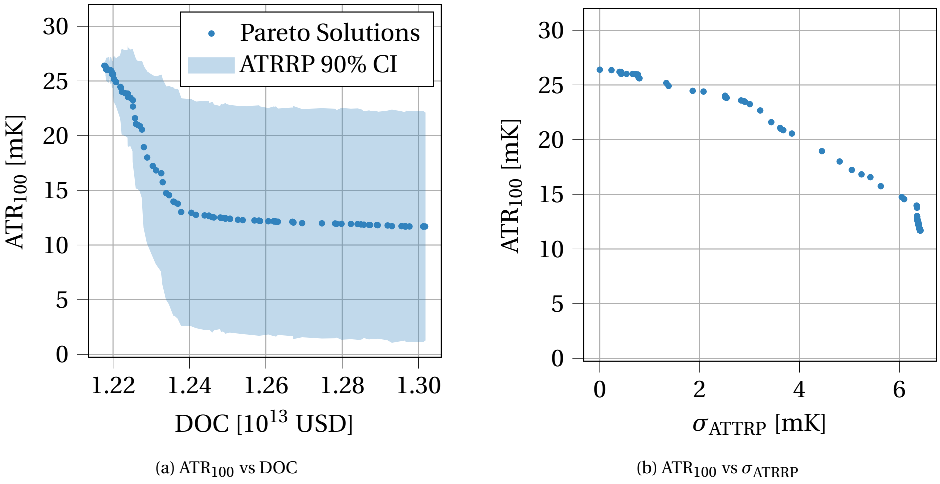

(a) ATR$_{100}$ vs DOC

(b) ATR$_{100}$ vs σ_{ATRRP}

Figure 8.13: Uncertainty analysis of Pareto-optimal aircraft designs (kerosene, medium-range, as presented in Chapter 3), adapted from Reference [209]

cost objective. This requires solving a multi-objective optimization problem [243] considering the following two objectives: the mean of ATRRP and its variability (i.e., σ_{ATRRP}), which is the robustness objective. Note that the former has to be maximized, while the latter needs to be minimized. Therefore, one of the objectives is multiplied by -1.

During this optimization, the uncertainty analysis is carried out at every design evaluation with a Monte-Carlo simulation using 2048 samples. Verification of this sample size shows an MCS estimation error smaller than 0.5%. The multi-objective optimization uses a genetic algorithm (GA), specifically NSGA-II [244]. The reason for employing a GA in this case is threefold:

1. The algorithm operates on a set of candidate solutions rather than one point and, therefore, concurrently explores different regions of the design space.
2. The applicability of GAs includes non-convex and discontinuous design spaces.
3. This algorithm does not require the computation of gradients. Since the robustness objective σ_{ATRRP} is determined through Monte-Carlo simulations, accurate gradients cannot be obtained unless the sample size is sufficiently large. This is too computationally expensive in the optimization steps.

Starting from the ATR$_{100}$-DOC Pareto front in Section 3.3.3 on page Page 58, an optimization with 15 generations and a population size of 50 yields a σ_{ATRRP}-ATRRP Pareto front, which has similar design solutions. This indicates that the cost-optimal aircraft design is the most robust option. Nevertheless, an extended optimization with 40 generations does show a marginal improvement in robustness of 4% to 6%. In this case, the optimizer focuses on CO_2 impact reduction since it has a high relative contribution to ATR$_{100}$ but a small uncertainty. As a result, the Mach number is lowered, and the aspect ratio and bypass ratio are increased. This leads to a more fuel-optimal solution. However, 15 generations has not lead to an entirely converged hypervolume indicator in this case. Therefore, continuing this optimization with more generations is recommended to verify that the fuel-optimal design choices are indeed more robust.

This analysis has shown that the climate-optimal aircraft has a high standard deviation of the ATR_{100} reduction potential σ_{ATRRP}. However, as pointed out above, the standard deviation of ATR_{100} itself is actually smaller due to the lack of contrail formation. Therefore, performing a robustness-MDO using ATR_{100} rather than ATRRP is interesting. Such optimization can show that the climate-optimal aircraft is more robust in terms of climate impact.

Sensitivity Analysis The final step is to perform a sensitivity analysis of the climate-optimal and robust design solutions. This sensitivity analysis quantifies the contribution of uncertain model parameters to the variability in the climate impact reduction potential. The sensitivity analysis includes a global sensitivity analysis (GSA), focusing on the 32 input parameters with an assigned probability distribution, and a local sensitivity analysis (LSA) considering the impact of the background χ_{CO_2} scenarios.

A two-step approach is employed in the GSA to reduce the computational effort. First, the Morris, one-step-at-a-time method qualitatively finds the top ten parameters which have the highest influence on the uncertainty, σ_{ATRRP}. Each parameter in the set of 32 uncertain inputs is varied one by one within the respective uncertainty interval, keeping the other parameters constant. This allows the computation of the mean and standard deviation of the elementary effect of each variable. The measure μ^* estimates the mean distribution of the absolute values of elementary effects rather than the signed, positive or negative, elementary effects [235, 245]. Subsequently, the uncertain parameters are ranked according to μ^*, and the top ten most influential ones proceed to the next step.

The Sobol indices are calculated for these ten parameters in the second stage. Unlike the Morris method, computing the Sobol indices is a “variance-based” technique that also captures the interactions between parameters. The first-order effect of parameter i is denoted by $S_{1,i}$, while the total effect, including interactions, is captured in $S_{T,i}$.

Figure 8.14 shows the top ten most influential parameters, based on the first step, and their respective first order and total Sobol indices for the climate-optimal, kerosene, and medium-range aircraft. The parameters are used in the climate model introduced in Section 3.1.2 starting on page Page 39. The assumed radiative forcing per unit of flown distance contributes most to the uncertainty of this design solution. This is followed by contrail altitude forcing factors and the radiative forcing corresponding to a doubling in CO_2. Since the $S_{1,i}$ and $S_{T,i}$ bars are almost the same height, it is concluded that the contribution of interactions is small.

Note that the results in Figure 8.14 are specific to the climate-optimal solution. Other solutions along the Pareto front, between the climate- and cost-optimal solution, have different Sobol indices. Although the assumed radiative forcing per unit of flown distance remains an influential parameter for all design solutions, the contrail altitude forcing factors $s_{\mathrm{contrails}}(2)$ and $s_{\mathrm{contrails}}(3)$ become more important when the aircraft forms persistent contrails.

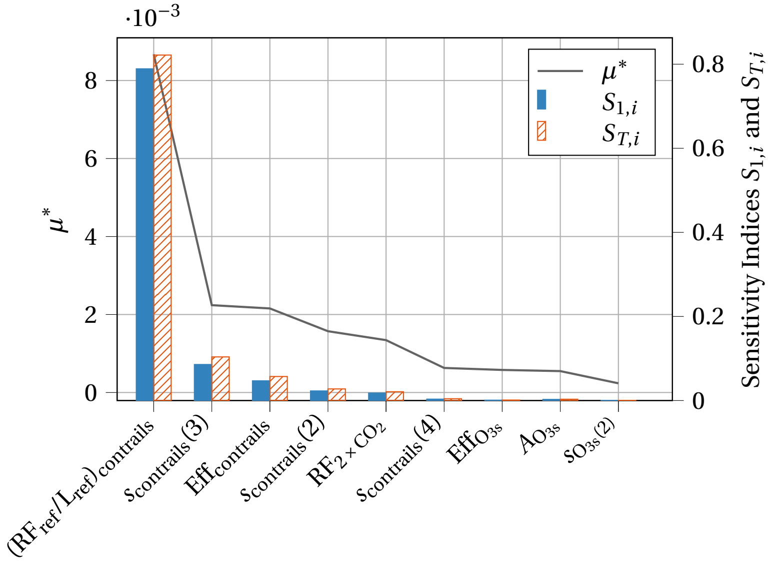

Figure 8.14: Global sensitivity analysis of climate-optimal, kerosene, medium-range aircraft presenting the most influential uncertain parameters with respect to σ_{ATRRP}. The parameters are introduced in Section 3.1.2 starting on page Page 39

The local sensitivity analysis studies indicate how sensitive the ATR_{100}, ATRRP, and σ_{ATRRP} metrics are to different future projections of the CO_2 background concentration χ_{CO_2}, as shown in Figure 8.11. It is observed that, with increasing χ_{CO_2}, the CO_2 contribution to ATR_{100} decreases. Since non-CO_2 effects mostly drive the climate-optimal aircraft design, the ATRRP stays approximately the same for all scenarios. Nevertheless, the normalized ATRRP and σ_{ATRRP} increase. The design space for improved robustness shrinks since non-CO_2 effects become even more important, and the possibility to trade-off CO_2 with non-CO_2 is smaller.

The dashed arrow in Figure 8.10 between the sensitivity analysis and the uncertainty characterization indicates that this workflow is iterative. Since the sensitivity analysis gives insight into which parameters have the largest influence on the variability of the model's outcome, it directly informs designers and scientists which uncertainty should be reduced first to achieve more robust solutions. The current analysis shows that contrails, by far, induce the largest uncertainty and drive the aircraft design. Therefore, it is highly recommended that the formation and radiative impact of contrails and contrail-cirrus be further studied to reduce the related uncertainty. This will lead to more robust aircraft design decisions.

8.5.2. UNCERTAINTY OF FUTURE AVIATION FUELS

For aircraft powered by hydrogen combustion, a 50% to 75% reduction in in-flight equivalent CO_2 emissions (including non-CO_2 effects) compared to kerosene-powered aircraft is expected in Reference [171]. This range, although not measured in ATR_{100}, is in line with the climate impact reduction of 67% to 77% observed in this study for cost-optimal hydrogen aircraft (Tables 6.5, 6.7 and 6.9). Ponater et al. [246] compare several scenarios of hydrogen aircraft introduction. A best-estimate reduction of 10% in temperature impact, including non-CO_2 effects, is observed by the year 2050, but the benefit of hydrogen is expected to be larger (45%) in the long term. This is smaller than the values observed in this study. However, these numbers also strongly depend on the assumed technology level. In particular, the impact due to contrail and contrail-cirrus has a large uncertainty for hydrogen combustion.

For kerosene, the largest uncertainty lies in the radiative forcing and consecutive temperature response due to contrail formation. The scientific level of understanding of this climate species is considered low at the time of writing [3]. Among other aspects, the uncertainty in impact due to contrails exists since they both have a cooling and warming effect, which may depend on the time of day and because the linear persistent contrails may lead to contrail cirrus. In addition, the formation and radiative forcing depend on the latitude and longitude of contrail formation, while the current study only considers the effect of altitude on radiative forcing. In the optimizations in Sections 6.3.1 to 6.3.3, the latter aspect leads to a lower cruise altitude until an altitude is reached where contrails are no longer formed. Varying geospatial conditions (temperature and relative humidity) can lead to different climate-optimal altitudes and, therefore, different climate-optimal cruise Mach numbers.

Furthermore, uncertainty exists with respect to the impact of NO_x emissions [3]. Although the level of understanding is considered higher than for contrails, the radiative forcing per unit of NO_x, for each effect, and the dependency on altitude is susceptible to uncertainties [24]. If the NO_x impact is higher than considered in the current study, the optimizer will try to further decrease absolute NO_x emissions by reducing the engine OPR and/or trying to reduce the radiative forcing by flying at a lower cruise altitude.

Compared to the impact of kerosene aircraft, the difference in contrail impact of SAF(-mixture) combustion leads to the largest source of uncertainty in the climate impact modeling of SAF aircraft. This adds to the already present uncertainty in climate impact due to contrails and contrails cirrus of kerosene. The effect of underestimating or overestimating this impact on the optimal designs is expected to be similar, mostly influencing the chosen cruise altitude and Mach number. Since the effect due to NO_x emissions is assumed to remain unchanged, no additional uncertainty is introduced for the SAF aircraft.

Compared to kerosene aircraft, the uncertainty in the climate impact of hydrogen aircraft lies in the estimation of the NO_x emission index and the formation and impact due to contrails. In the current study, a reduction in EI_{NO_x} is assumed, as discussed in Chapter 5. The formation and radiative characteristics of contrails due to hydrogen combustion are uncertain due to the complete lack of soot particles in the engine exhaust, compared to the kerosene or SAF-based fuels. Nevertheless, it is expected that the climate-optimal aircraft still flies at an altitude that avoids contrail formation.

9

CONCLUSIONS AND RECOMMENDATIONS

THE research in this dissertation aimed at examining the potential climate impact reduction of commercial aircraft by exploring the conceptual design space and considering different fuels. A holistic approach is taken, considering multiple design disciplines and multiple objectives. This chapter summarizes the research questions and the respective answers in highlighted boxes. Additionally, recommendations are presented for further research and design solutions.

9.1. CONCLUSIONS

Current available commercial aircraft contribute to global warming due to fossil kerosene combustion. New technologies, fuels, and operations procedures are needed to keep up with the increasing global demand for air travel while limiting global warming. The research in this dissertation focuses on three elements that complicate the path towards sustainable aviation:

1. The climate impact of combustion-powered aviation is caused by CO_2 and non-CO_2 effects such as contrail formation and indirect NO_x effects. Contrary to CO_2 emissions, the non-CO_2 contributions depend on formation location, have different lifetimes, and do not scale with fuel consumption. Therefore, the aircraft design objective has to account for such effects.

2. Due to non-CO_2 effects, the climate objective does not align with the classic design objectives, such as operating cost or fuel burn. Therefore, when evaluating technologies, a multi-objective approach has to be used to trade off all aspects.

3. A vast design space has to be considered, including mission variables such as cruise altitude and speed. However, these variables also influence the airline operations. Therefore, the impact of design changes should be assessed not only at the aircraft system level but also at the network level. This requires a multi-level approach.

Considering these three elements, the objective of the research in this dissertation is to *study the potential of aircraft design optimization and fleet allocation to minimize the global warming impact of an airline network while observing the change in energy consumption and financial costs for the operator, considering various technologies and fuels.* The related research questions focus on climate-optimal aircraft design trends, the potential of liquid hydrogen and drop-in SAF to reduce further the climate impact, and the influence of these design changes and fuels on airline operations and network-level performance. The key findings are presented in this order in Sections 9.1.1 to 9.1.3.

A multidisciplinary design optimization (MDO) framework is developed to answer the research questions. This framework aims to minimize the climate impact, cash operating cost, and in-flight energy consumption by varying airframe, engine, and mission variables. The framework develops consistent aircraft designs by iteratively evaluating airframe, propulsion, and mission disciplines, featuring statistical, empirical, and physics-based methods. Inequality constraints ensure aircraft adhere to regulations, available technology, and geometric limits. The average temperature response over 100 years (ATR_{100}) measures the climate impact using a linear temperature response model.

9.1.1. CLIMATE-OPTIMAL, KEROSENE AIRCRAFT DESIGN

Research question 1

Which design vectors minimize the global warming impact and cash operating cost of a medium-range, kerosene-powered turbofan aircraft?

The climate impact ATR_{100} can be reduced by approximately 64% compared to its cost-optimal counterpart, at a cash operating cost penalty of 17%. This is achieved by flying at a lower cruise altitude, reduced cruise Mach number, and lower turbofan overall pressure ratio.

The optimization of a medium-range, turbofan aircraft powered by kerosene shows that the climate impact ATR_{100} can be reduced by approximately 57% to 64% compared to its cost-optimal counterpart, at a cash operating cost increase of 7% to 17%, depending on the lower cruise Mach number bound, among other factors. This shows that the objectives are indeed conflicting. This single-objective optimization assumes a multi-year scenario of a fleet of aircraft with a fixed productivity.

The reduction in climate impact is achieved by flying at a lower cruise altitude ($h_{\mathrm{cr}} \approx 6-7\mathrm{km}$) and a lower cruise Mach number ($M_{\mathrm{cr}} \approx 0.5-0.6$). The engine overall pressure ratio (OPR) is reduced by 35% to 29%, together with the turbine inlet temperature. In contrast, the bypass ratio increases up to 11 when moving from the cost to the climate-optimal solution. The decrease in Mach number leads to an unswept wing with a higher aspect ratio (11 to 12) and a higher, yet not maximized, wing loading. The exact changes in design variables are also susceptible to assumed technology levels such as engine component efficiencies.

These design adaptations primarily reduce the non-CO_2 effects of kerosene combustion: as a result of the low cruise altitude, the contrail formation criteria are no longer satisfied, and contrails are eliminated. Furthermore, the impact of NO_x effects is reduced by lowering the cruise altitude and the engine OPR. The lower cruise altitude leads to less short-term ozone creation. The reduced OPR results in a lower combustor inlet temperature and pressure, reducing the NO_x emission index and the total NO_x emissions. Nonetheless, this engine design choice reduces engine's thermal efficiency. As a result, the overall efficiency drops from 40% to 33%. The switch to propeller-based propulsion is considered to offset this loss in efficiency and reduce the CO_2 impact.

Research question 2

What are the differences in operating cost, mission fuel, and climate impact between optimized turboprop aircraft and optimized turbofan aircraft?

Optimization of a turboprop-powered, medium-range, kerosene aircraft indicated that the ATR_{100} could be reduced up to 72% compared to a cost-optimal turbofan aircraft. Employing turboprop engines positively influences fuel consumption and cash operating costs in the case of the climate impact objective.

For all considered cases, the multi-objective optimization identifies a “kink” in the Pareto front between the cost- and climate-optimal solutions. This kink corresponds to a multi-objective (MO) design that offers a significant ATR_{100} reduction (53% for the medium-range category) for a limited cost increase (1%) by eliminating contrail formation and lowering the short-term ozone impact at a small block time increase. Although the energy consumption of this in-between solution is higher than the cost-optimal solution (up to 5%), this design solution is a promising alternative to the costly climate-optimal design. It highlights the relative importance of contrail avoidance.

9.1.2. IMPACT OF LIQUID HYDROGEN AND DROP-IN SAF

Another pathway to lower the climate impact is to employ novel aviation fuels, such as liquid hydrogen or drop-in sustainable aviation fuels. While these fuels primarily target a reduction in net CO_2 emissions, the fuel choice also influences the non-CO_2 effects.

Research question 3

What is the difference in climate impact and cash operating cost of optimized hydrogen aircraft compared to the kerosene baseline? And how do the design vectors change?

Cost-optimized, hydrogen can reduce ATR_{100} by 73% at an operating cost penalty of 28%, compared to the cost-optimal, kerosene reference aircraft. These aircraft fly higher than their kerosene alternative but feature a lower cruise Mach number and higher aspect ratio. By flying at lower cruise altitudes and cruise Mach numbers, the ATR_{100} of hydrogen aircraft can be reduced up to 99%.

A cost-optimized, hydrogen, medium-range aircraft can lower the climate impact by

73% at a cost increase of 28% if a hydrogen fuel price of 4.4 USD/kg is assumed. This aircraft features a wing with a high aspect ratio (10.3 vs. 7.7) but a lower wing loading (5.15 vs. 5.30 kN/m^2) than its kerosene counterpart due to an increase in landing mass. The cost-optimized hydrogen aircraft operates at a higher cruise altitude but at a lower Mach number. The fuel-bound costs are relatively more important for the hydrogen aircraft than for the kerosene or SAF alternatives. Although the 73% reduction in ATR$_{100}$ is significant, the largest climate impact contribution is due to the formation of contrails.

The climate-optimized, hydrogen aircraft reduce the latter impact by flying at a lower altitude, eliminating the persisting contrails and lowering the radiative impact due to NO$_x$ emissions. This leads to a climate impact reduction of 99%, at an increase of 39% in cash operating cost (COC). The climate-optimal altitude is also 6 km, similar to aircraft powered by other fuels, but the cruise Mach number is higher (0.58 instead of 0.5). This hydrogen, however, also suffers from a penalty in in-flight energy consumption due to installation penalties of the tank and non-optimal operating conditions.

These observations are similar for regional and long-range hydrogen aircraft, with climate impact reductions of 67% and 77%, respectively, if the COC design objective is employed. For all climate-optimal, hydrogen aircraft, ATR$_{100}$ is reduced by nearly 99%, offering the largest impact reduction of all options considered in this dissertation.

The comparison between kerosene and hydrogen aircraft is susceptible to uncertainty, both in terms of climate impact and fuel cost. Although the current fuel-price difference between hydrogen and kerosene is large, this contrast is likely to reduce due to the increasing cost of kerosene (plus potential carbon taxes) and new technologies making the liquid hydrogen supply less expensive.

Research question 4

What is the difference in climate impact and cash operating cost of optimized aircraft powered by a 50-50 SAF mixture compared to the kerosene baseline? And how do the design vectors change?

The MDO of medium-range aircraft powered by a SAF-kerosene blend leads to designs that decrease ATR$_{100}$ by 47% to 83%, compared to the kerosene, cost-optimal design. The design vectors for kerosene and SAF aircraft show marginal differences.

SAF-powered aircraft can lower the climate impact by 47% to 83% for medium-range aircraft, compared to the kerosene, cost-optimal design. The exact value depends on the chosen design objective: COC or ATR$_{100}$. The COC is expected to increase by 4% to 21%, respectively. For regional aircraft, SAF can reduce the climate impact by 41% to 81% at a COC penalty of 3% to 20%, respectively. An ATR$_{100}$ reduction between 47% and 68% can be obtained for long-range aircraft, increasing the cost by 5% to 27%.

The cost- and climate-optimal SAF aircraft designs are similar to their kerosene counterparts because the fuel properties are nearly identical. Small changes in the cost-optimal aircraft design occur as a result of the increased fuel price. This forces the optimizer to emphasize fuel-minimizing design choices such as a lower cruise Mach number and higher bypass ratio. Furthermore, due to the marginally higher specific energy of

SAF blends, the fuel mass and MTOM are lower for SAF-powered aircraft. Nevertheless, the differences between SAF and kerosene, cost-optimal aircraft, are minor compared to hydrogen aircraft. Additionally, new aircraft should be designed to use both fossil kerosene and SAF blends, requiring a robust solution for both fuels.

Research question 5

How does the trade-off between climate impact and operating cost vary between aircraft categories?

The observed design trends for regional and long-range turbofan aircraft are similar to those for medium-range aircraft, although the design values are different. In the case of kerosene, the climate-optimal regional aircraft achieve a 71% reduction in ATR_{100} for a 12% cost increase. For the long-range category, the above design changes can reduce ATR_{100} by 35% at a cost increase of 23%.

The climate impact reduction potential shrinks, and the cost penalty increases for aircraft designed for more payload and longer ranges. The lower cruise Mach number leads to a higher cost penalty for long-range missions due to the relatively long cruise phase compared to other flight phases. The ratio between time spent in cruise and total block time is smaller for medium-range or regional missions.

Comparing the fossil kerosene, a 50-50 SAF blend, and liquid hydrogen simultaneously allows the identification of Pareto-optimal design solutions. For the regional and medium-range categories, it is found that kerosene aircraft are cost-optimal and are Pareto-optimal up to an ATR_{100} reduction of approximately 65% (regional) or 59% (medium-range). Beyond this point, it is advised to use SAF-powered aircraft, offering a larger climate impact reduction at a lower cost increase. To reduce ATR_{100} by more than 83%, hydrogen should be used for regional and medium-range aircraft, although such aircraft have to be specifically designed to limit climate impact and not aim at minimizing the operating cost.

In the case of long-range aircraft, all design solutions of the three fuels are Pareto-optimal. This means that, different from the other categories, also the cost-optimal hydrogen aircraft is Pareto-optimal. Nevertheless, the long-range hydrogen aircraft suffer from large energy penalties (up to 15%) because of the longer fuselage (87 to 90 m instead of 65 m) and the horizontal tailplane which has a 20% larger area than its kerosene or SAF counterparts. These geometric changes are required to store the large tanks inside the fuselage and to satisfy the stability and trim constraints. However, these changes lead to mass and drag penalties.

Reflection on uncertainty

Uncertainty analysis of the ATR_{100} reduction of the climate-optimal, kerosene, medium-range aircraft yields a large standard deviation of 6.4 mK for an ATR_{100} reduction of 15 mK. The uncertainty in contrail radiative forcing is the largest contribution to the overall uncertainty.

9.1.3. FLEET ALLOCATION OF ATR$_{100}$-OPTIMAL AIRCRAFT AND FUELS

All climate-optimal aircraft and the cost-optimal hydrogen aircraft in this study feature lower cruise Mach numbers, which result in extended flight times and, consequently, longer mission block times. This block time increase has several consequences:

1. the crew costs increase, which is captured in the cash operating cost figures in the previous two sections,
2. the productivity of an aircraft (i.e., the amount of payload transported in a given time frame) is reduced, and
3. the flight schedule must be adapted since an aircraft will take longer to return to the hub airport.

Hence, the research in this dissertation performs a fleet allocation to evaluate the effect of the above changes on strategic airline planning. For a given reference network based in the United States, the regional, medium-, and long-range aircraft are simultaneously allocated per set of design objectives and fuels. The allocation procedure aims to maximize the overall network's profit, given a weekly demand schedule on 30 routes and aircraft performance constraints.

Research question 6

Considering an available network demand and fixed yield per passenger kilometer, what is the optimal fleet diversity and allocation of climate-minimal kerosene aircraft in an airline network to maximize profit?

For a network with US domestic and international demand, the fleet consisting of climate-optimal aircraft needs 21% more aircraft than the fleet with cost-optimized aircraft. The in-flight climate impact reduces by 55% whereas the network profit decreases by 24%.

Figure 9.1 provides a summary of the results of these network allocation studies. The fleet consisting of kerosene, cost-optimized aircraft serves as the reference case and features the highest network profit, the highest number of revenue passenger kilometers covered, and the largest climate impact. The figure shows that the lowest climate impact occurs in the case of climate-optimal hydrogen aircraft. Nevertheless, this fleet also has the largest network profit loss and RPK loss. The cost-optimal and multi-objective, hydrogen, and SAF solutions offer Pareto-optimal solutions in terms of climate impact and network profit.

Analysis of the kerosene fleets shows that the climate-optimal fleet needs 46 aircraft instead of 38 to achieve the maximum profit. The climate-optimal fleet includes eight more medium-range aircraft and two additional long-range aircraft. This increase is similar in the case of a fleet powered by a 50-50 SAF-kerosene blend. The hydrogen, climate-optimal fleet only holds three more aircraft than its cost-optimal counterpart, 40 vs. 37. Although the fleet size increases, the number of flights drops by approximately 11% when operating climate-optimized aircraft. The hydrogen fleets offer fewer departures and fewer destinations than kerosene or SAF fleets.

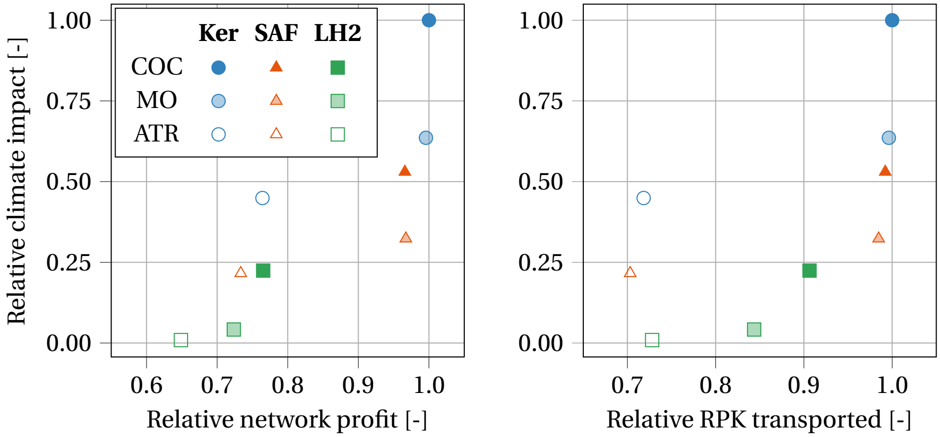

(a) Network profit versus Climate Impact

(b) RPK transported versus Climate Impact

Figure 9.1: Comparison between network key performance indicators for different aircraft design objectives and different fuels. The values are normalized with respect to the performance of the cost-optimal kerosene fleet. (repeated from Page 171)

Research question 7

What is the optimal fleet diversity and allocation of liquid hydrogen or drop-in SAF aircraft in an airline network to maximize the profit?

Compared to the cost-optimal kerosene fleet, fleets powered by 50-50 SAF blends reduce the climate impact between 47% and 78% at network profit penalties of 3% and 27%, following similar allocation trends as the kerosene fleets. The climate-optimal, hydrogen-powered fleet achieves a maximum ATR_{100} reduction. However, this comes at a 35% loss in profit due to the poor performance of the long-range aircraft. Fewer aircraft are operated in the latter case.

In the case of the climate-optimal hydrogen fleet, most of the profit is lost due to the long-range aircraft. Especially on long, transatlantic routes, the low cruise Mach number is detrimental to the operations. In combination with the increased hydrogen fuel price, this long-range aircraft type covers up to 35% less revenue passenger kilometers than other long-range variants. However, the long-range aircraft are designed for a much larger design range than the considered network requires. Designing long-range aircraft with range requirements tailored to the considered network can increase the overall network by up to 4% for fleets powered by hydrogen.

Reflection on research objective

This research shows that, to achieve sustainable aviation, it is essential to consider new technologies, fuels, and operations, **as well as their interactions**.

9.2. RECOMMENDATIONS

This dissertation studies the optimization of aircraft and their fleet allocation in a holistic yet conceptual manner to strike a balance between accuracy, insightfulness, and computational complexity. Nevertheless, several elements of the research approach can be further improved, both inside the disciplines and in the overall setup of the optimization. The high-level approach, however, also provides insights into which concepts possess high potential for climate impact reduction and deserve further analysis. This section provides recommendations for future research, focusing on modeling and reformulating the optimization problem and specific design solutions.

Research into the following disciplines can further improve the accuracy and completeness of this research:

- In the climate impact estimation, the radiative forcing of contrails is assumed to scale with the distance of persistent contrails (i.e., $\mathrm{mW}/(\mathrm{m}^2\,\mathrm{km})$). Although this value depends on fuel choice and flight altitude, this value should also be made sensitive to the size of the aircraft, for example, through the cruise thrust level and aircraft mass.

- As highlighted in Chapter 8, reducing the uncertainty of the contrail radiative forcing can greatly improve the robustness of climate-optimal design solutions. Hence, reducing this uncertainty is a high priority from an aircraft design and flight performance perspective.

- The current approach assumes the same maintenance cost estimation methods for all considered fuels. However, the integration of hydrogen tanks into the airframe and the use of engines featuring hydrogen combustion are likely to increase the maintenance cost, at least in the short term. This should be reflected in the maintenance cost model.

- The integration penalties of the hydrogen tank are modeled in a conceptual manner. The hydrogen aircraft design analysis can benefit from further studies into hydrogen powertrains and maturation of the technology.

- Although the discussion on air quality showed that the climate and air quality objectives may be aligned, it is recommended to include this discipline in the MDAO workflow. Ideally, air quality functions for aircraft design (AQFAD) are developed in a similar way as the climate functions for aircraft design (CFAD) in the GLOWOPT project [210]. Based on the flight profiles and emissions, the AQFAD can determine the changes in regional pollutant concentrations or mixing ratios. An even more relevant metric would be the number of premature deaths.

- The MDO setup does not account for the total life cycle impact of the fuels and aircraft. Therefore, it is suggested to include a life-cycle assessment discipline that considers other phases such as production, transport (in the case of fuels), maintenance, and disposal (in the case of aircraft). Although the exact metric for the overall life cycle impact is still to be selected, this metric can be employed as an objective function or constraint in the optimization.

The optimization workflow can be updated using novel MDO architecture elements and by reformulating the problem definition:

- The fleet allocation and the discussion on economics reveal that new climate-optimal aircraft, potentially powered by different fuels, can benefit from different payload and range requirements. Therefore, it is recommended to include the maximum structural payload and design range as design or coupling variables in the optimization formulation. This allows the optimizer to find the optimal requirements for each fuel and technology combination. However, this will increase the computational complexity of the MDO workflow. Hence, this coupling has to be implemented in a smart, non-brute-force manner.

- The current aircraft design approach creates an aircraft specifically developed for a given number of passengers. However, in reality, the fuselage of an aircraft type can be shrunk or stretched by removing or adding fuselage elements. This is often referred to as a family concept. It is recommended to add such design rationale to the MDO problem formulation. Including the option of creating family derivatives leads to more realistic decision-making, evaluates the penalties of having such derivatives, and enlarges the design space.

- In the current research, fuels, and technology options are studied individually. This approach yields the desired insights but at a high computational cost since many non-dominant design solutions are considered. Dynamic MDAO workflows with built-in switch nodes [247] can improve the multi-objective optimization runtime and result in a Pareto-optimal set with different engine technologies and fuel types.

The research identified the following aircraft concepts, engine features, as well as case studies that should be investigated further:

- The research shows that, when operating at climate-optimal altitudes and flight speeds, propeller-based propulsion can improve the CO_2 emissions, fuel burn, and operating cost compared to turbofan counterparts. However, this analysis was limited to an OPR of 25, the highest OPR currently available for turboprop aircraft. It is argued that the thermal efficiency and design objectives can be improved further by allowing higher values.

- Hydrogen aircraft offer the largest climate impact reduction, but at a significant cost and in-flight energy consumption penalty, depending on the category. The latter two aspects may be improved by considering turboprop technology instead of turbofan engines. At the aircraft level, turboprop technology can offer hydrogen climate-optimal solutions at a lower cost increase. At the fleet level, this technology potentially leads to hydrogen fleets with a higher network profit. However, four instead of two engines may be required for long-range aircraft, which also increases the engine maintenance cost.

- Contrail avoidance systems should be prioritized in the coming years since the analysis shows that eliminating contrails is possible at a marginal cost increase. This can also decrease the uncertainty of the climate impact of aviation.

- The multi-level MDO workflow setup, as currently implemented, can and should be used for different networks with different routes and varying demand schedules to verify the robustness of the conclusions.

- Future research can employ the multi-level MDO workflow to assess the impact of policies on aircraft design and fleet allocation through taxes, incentives, or minimum ranges for flights. However, to study such policies fully, it is recommended to include variable demand in the fleet allocation methodology, as discussed above.

Some of these recommendations may have already been picked up in projects without the author's knowledge. However, the main suggestion is to bring all disciplines and expert knowledge more closely together in a computational and collaborative framework, including technical and social sciences.

A

DATA FOR VERIFICATION AND VALIDATION

This appendix summarizes the data used for verification and validation.

A.1. DATA FOR PROPULSION DISCIPLINE VERIFICATION AND VALIDATION

The conditions and data presented in Tables A.1 and A.2 are adopted to model the General Electric GE90 engine for verification and validation purposes in Section 3.2.1. Table A.3 presents the assumed input parameters for the CFM56 engine in the validation of the Airbus A320-200 aircraft design loop in Section 3.2.2.

Table A.1: Design requirements assumed for the GE90 engine model

Operating Condition	**Net Thrust** [kN]	**Altitude** [km]	**Mach** [-]	$\Delta T_{\mathbf{ISA}}$ [K]
Cruise	77.85	10.67	0.80	0.00
Take-off	376.80	0.00	0.00	15.00

Parts of this chapter have been published in Journal of Aircraft, **59**, 5, 2022, Proesmans and Vos [87].

Table A.2: Parameters assumed in the model of the GE90 engine at design point (cruise) [248, 249, 113]

Component	**Parameter**	**Value**	**Unit**
Inlet	Total pressure loss ΔP_T	0.980	-
Fan	Bypass Ratio BPR	8.50	-
	Total pressure ratio Π_{fan}	1.58	-
	Polytropic efficiency η_{pol}	0.915	-
Low Pressure Compressor	Total pressure ratio Π_{lpc}	1.26	-
	Polytropic efficiency η_{pol}	0.910	-
High Pressure Compressor	Total pressure ratio Π_{hpc}	20.0	-
	Polytropic efficiency η_{pol}	0.900	-
Combustor	Total pressure loss ΔP_T	0.950	-
	Combustion efficiency η_{comb}	0.990	-
	Turbine entry temperature TET	1430	K
High Pressure Turbine	Polytropic efficiency η_{pol}	0.930	-
	Mechanical efficiency η_{mech}	0.990	-
Low Pressure Turbine	Polytropic efficiency η_{pol}	0.930	-
	Mechanical efficiency η_{mech}	0.990	-

A.2. DATA FOR AIRCRAFT SYNTHESIS VERIFICATION

Table A.4 presents the top-level airplane requirements for the Airbus A320-200 and Boeing 777-200 aircraft employed for verification and validation in Section 3.2.2. In Table A.5, the input parameters for the verification and validation of the turboprop aircraft in Section 4.2.2. Table A.6 summarizes the assumptions for the modeling of the CF34-8E engine in the verification of the Embraer E175 in Section 6.2.

Table A.3: Parameters assumed in the model of the CFM56 engine at design point (cruise)

Component	**Parameter**	**Value**	**Unit**
Inlet	Total pressure loss ΔP_T	0.980	-
Fan	Bypass Ratio BPR	6.0	-
	Total pressure ratio Π_{fan}	1.6	-
	Polytropic efficiency η_{pol}	0.89	-
Low Pressure Compressor	Total pressure ratio Π_{lpc}	1.6	-
	Polytropic efficiency η_{pol}	0.86	-
High Pressure Compressor	Total pressure ratio Π_{hpc}	12.7	-
	Polytropic efficiency η_{pol}	0.9	-
Combustor	Total pressure loss ΔP_T	0.94	-
	Combustion efficiency η_{comb}	0.99	-
	Turbine entry temperature TET	1240	K
High Pressure Turbine	Polytropic efficiency η_{pol}	0.86	-
	Mechanical efficiency η_{mech}	0.97	-
Low Pressure Turbine	Polytropic efficiency η_{pol}	0.87	-
	Mechanical efficiency η_{mech}	0.97	-

Table A.4: Top-level airplane requirements employed for the aircraft synthesis verification and validation [127]

Requirement [Unit]	**Airbus A320-200**	**Boeing 777-200**
Maximum structural payload [metric tons]	18.2	54.9
Harmonic range [10^3 km (10^3 nmi)]	3200 (1730)	6000 (3200)
Cruise Mach number [-]	0.78	0.84
Cruise altitude [km (FL)]	11.3 (37)	11.9 (39)
Approach speed [m/s (kts)]	70.0 (136)	70.0 (136)
Take-off length (ISA conditions) [m (ft)]	2200 (7220)	2440 (8010)

Table A.5: Aircraft design convergence verification input parameters

Parameter	**ATR 72-600**	**Dash 8-400**
Harmonic Range [km]	987	955
Maximum Structural Payload [kg]	7500	7800
Cruise mach number [-]	0.44	0.53
Cruise altitude [m]	5180	7620
Take-off length [m]	1278	1268
Aspect Ratio [-]	12	12.8
W/S_{TO} [N/m^2]	3697	4351

Table A.6: CF34-8E engine design parameters assumed for the design point (cruise). The component efficiencies are modeled after the CFM56 turbofan engine [249, 113, 250]

Parameter [Unit]	**Value**	**Parameter [Unit]**	**Value**
Inlet total pressure loss ΔP_T	0.98	Combustor total pressure loss ΔP_T	0.94
Bypass Ratio BPR	5.0	Combustion efficiency η_{comb}	0.99
Fan total pressure ratio Π_{fan}	1.5	Turbine entry temperature TET [K]	1250
Fan polytropic efficiency η_{pol}	0.89	HPT polytropic efficiency η_{pol}	0.86
LPC total pressure ratio Π_{lpc}	1.35	HPT mechanical efficiency η_{mech}	0.97
LPC polytropic efficiency η_{pol}	0.86	LPT polytropic efficiency η_{pol}	0.89
HPC total pressure ratio Π_{hpc}	14	LPT mechanical efficiency η_{mech}	0.97
HPC polytropic efficiency η_{pol}	0.90		

B

GEOMETRY CREATION METHODS

Based on the design variables, a separate module creates a conceptual geometry of the aircraft employing empirical, statistical, and physics-based relations. Data from the geometry model propagates to the aerodynamic and Class-II mass estimation disciplines to compute the zero-lift drag component and structural mass, respectively. This section summarizes the methods used to create the conceptual outer line of the aircraft.

B.1. FUSELAGE

Since the passenger number and mission range are the main drivers for the fuselage, the geometry remains the same throughout the optimization iterations. This is because the inputs for the fuselage, namely the TLARs and design assumptions per aircraft category, are held constant. The fuselage geometry methodology consists of three steps. Firstly, the cabin cross-section is designed. The number of seats abreast is determined from the maximum number of passengers ($N_{\text{pax, max}}$), in an all-economy layout, according to the following relation:

$$N_{\text{seats abreast}} = \max\left(\left\lfloor 0.47 \cdot \sqrt{N_{\text{pax, max}}} \right\rfloor, 6\right) \tag{B.1}$$

One aisle is introduced if the number of seats abreast is 6 or lower, while two aisles are considered for more seats. The required cabin width is then determined from a summation of seat and aisle widths, assuming the parameters in Table B.1 which are derived from existing cabin layouts [128, 164, 198, 129]. Based on the cabin width and the unit load device (ULD) selection, the smallest possible inner cross-section radius is determined. To determine the outer diameter of the cross-section (d_{outer}), constant thicknesses are assumed according to the values in Table B.1.

Secondly, the longitudinal layout of the fuselage is created. The interior of the fuselage consists of three parts: the cockpit, cabin, and tail. The total length of the fuselage is the sum of the lengths of these three sections. The number of rows multiplied by a

---

Parts of this chapter have been published in Journal of Aircraft, **59**, 5, 2022, Proesmans and Vos [87].

Table B.1: Assumed parameters and design choices to determine the fuselage geometry

	Narrow-body **(≤ 6 seats abreast)**	**Wide-body** **(> 6 seats abreast)**
Seat width [m (inch)]	0.457 (18.0)	0.457 (18.0)
Aisle width [m (inch)]	0.457 (18.0)	0.584 (23.0)
Armrest width [m (inch)]	0.05 (1.97)	0.05 (1.97)
Cabin length factor k_{cabin} [-]	0.900	1.17
Cross-section d_{outer} [m (inch)]	d_{inner} + 0.150 (5.91)	d_{inner} + 0.340 (13.4)
Loading device	LD3-45	2 x LD2 or LD3

statistical factor, k_{cabin}, determines the cabin length according to

$$N_{\text{rows}} = \frac{N_{\text{pax, max}}}{N_{\text{seats abreast}}} \tag{B.2}$$

$$l_{\text{cabin}} = k_{\text{cabin}} \cdot N_{\text{rows}} \tag{B.3}$$

The factor k_{cabin} also accounts for the length due to galley areas and exits. The total fuselage length follows by adding the cockpit length (assumed to be 4 m) and the tail length, which is assumed to be 1.6 times the outer cabin diameter.

Finally, the outer geometry of the fuselage is shaped. Similar to the inner layout, three distinct sections are considered: the nosecone, central fuselage, and tailcone. The nose- and tailcones are longer than their respective interior sections, while the center fuselage is shorter than the cabin. For the nosecone, a finess ratio of 1.3 with respect to d_{outer} is assumed, while for the tailcone this ratio is 3. Subsequently, the length of the central part is equal to the total length of the fuselage, minus the lengths of the nose- and tailcone sections.

The central section of the fuselage is assumed to be a cylinder with a diameter equal to d_{outer}. The nosecone cross-sectional area decreases parabolically towards the nose point, which is located slightly below the fuselage center line according to a 4-degree droop angle measured from the front section of the central part. The tailcone starts tangentially to the central fuselage section and grows smoothly towards the tail point which is located above the fuselage central line, taking into account an upsweep of 7 degrees.

B.2. WING PLANFORM

The design vector contains two variables that directly influence the wing geometry, being the aspect ratio and the wing loading. The wing surface area S follows from dividing (MTOM $\cdot\, g$) by the wing loading. This area includes a trapezoidal section covered by the fuselage. The total wing span b then results from the surface area and the aspect ratio. The area S and span b establish the main dimensions but do not fully define the wing planform. The other parameters required to conceptually determine the drag coefficient and structural mass are the quarter-chord sweep angle, taper ratio, and root and tip chord thicknesses.

In this study, it is assumed that the quarter-chord sweep angle ($\Lambda_{0.25}$) is driven by the cruise Mach number according to the following statistical relationship for transport aircraft, based on data from References [34] and [144]:

$$\Lambda_{0.25} = \begin{cases} 0 \text{ if } M_{\mathrm{cr}} < 0.66 \\ \arccos\left(\frac{1.16}{M_{\mathrm{cr}}+0.5}\right) \text{ if } M_{\mathrm{cr}} \geq 0.66 \end{cases} \tag{B.4}$$

The taper ratio of the wing has to be adjusted according to the sweep angle to unload the tip section at higher sweep angles. Conceptually, the taper ratio can be related to the quarter-chord sweep angle as follows:

$$\lambda = -0.0083 \cdot \Lambda_{0.25} + 0.4597 \tag{B.5}$$

Furthermore, the trailing edge sweep angle is zero up to 30% of the semi-span to facilitate easier integration of the landing gear and high-lift devices, which are placed perpendicular to the freestream flow direction. This assumption, combined with the above parameters, fully defines the top-view planform of the wing.

Although the exact 3D outer mold line of the wing is not created, the aerodynamic and structural modules require an approximation of the root- and tip-chord thicknesses. The following relations provide such estimates [21]:

$$\begin{aligned} t/c_{\mathrm{tip}} =& \max\Bigg(0.10, \\ & \min\left[\frac{\cos^3\left(\Lambda_{0.5}\right) \cdot \left[0.935 - \left(M_{\mathrm{cr}} + 0.03\right) \cdot \cos\left(\Lambda_{0.5}\right)\right] - 0.115 \cdot C_{L,\mathrm{cr}}^{1.5}}{\cos^2\left(\Lambda_{0.5}\right)}, 0.18\right]\Bigg) \end{aligned} \tag{B.6}$$

$$t/c_{\mathrm{root}} = t/c_{\mathrm{tip}} + 0.03 \tag{B.7}$$

The twist and dihedral angles are not considered in the current approach, since the implemented methods are not sensitive to these parameters. The longitudinal position of the wing is determined simultaneously with the empennage size. Therefore, this aspect is discussed in the subsequent section.

B.3. EMPENNAGE PLANFORM AND WING PLACEMENT

The geometry module employs tail volume coefficients to determine the areas of the horizontal and vertical tail surfaces. The volume coefficients are derived from statistical data and are assumed to be independent of the design choices made by the optimizer. The volume coefficients are selected based on state-of-the-art technology and regulations. The respective surface areas, S_{ht} and S_{vt}, follow from the definitions of the volume coefficients for the horizontal ($\overline{V}_{\mathrm{ht}}$) and vertical ($\overline{V}_{\mathrm{vt}}$) tail.

$$\overline{V}_{\mathrm{ht}} = \frac{\left(x_{\mathrm{ht}} - x_{\mathrm{c.g., aft}}\right) S_{\mathrm{ht}}}{S \cdot \mathrm{MAC}} \Rightarrow S_{\mathrm{ht}} = \overline{V}_{\mathrm{ht}} \cdot \frac{S \cdot \mathrm{MAC}}{x_{\mathrm{ht}} - x_{\mathrm{c.g., aft}}} \tag{B.8}$$

$$\overline{V}_{\mathrm{vt}} = \frac{\left(x_{\mathrm{vt}} - x_{\mathrm{c.g., aft}}\right) S_{\mathrm{vt}}}{S \cdot b} \Rightarrow S_{\mathrm{vt}} = \overline{V}_{\mathrm{vt}} \cdot \frac{S \cdot b}{x_{\mathrm{vt}} - x_{\mathrm{c.g., aft}}} \tag{B.9}$$

In the above equations, x_{ht} and x_{vt} represent the longitudinal position of the aerodynamic center of the horizontal and vertical tails, respectively. $x_{\mathrm{c.g., aft}}$ is the x-coordinate of the most aft center-of-gravity position. The former two are set at 91% and 92% of the fuselage length, respectively. The statistical values for the tail volume coefficients are included in Table B.2.

The operational c.g. excursion determines $x_{\text{c.g., aft}}$ based on the position of the OEM c.g. location $x_{\text{c.g., OEM}}$, and the varying locations of payload and fuel. However, to obtain $x_{\text{c.g., OEM}}$, first, the longitudinal position of the wing has to be fixed. The latter position, defined by the leading edge of the MAC ($x_{\text{LE, MAC}}$), can be calculated from the masses of the main structural groups and their relative locations, as well as the assumed position of the OEM c.g. location with respect to the mean aerodynamic chord, $\xi_{\text{c.g., OEM}} = 0.25$. ξ is the longitudinal coordinate with respect to the mean aerodynamic chord ($\xi = \left(x - x_{\text{LE, MAC}}\right)/\bar{c}$). The wing position $x_{\text{LE, MAC}}$, measured from the fuselage nose point, is computed as follows:

$$\begin{aligned} x_{\text{LE, MAC}} &= x_{\text{c.g., FG}} + \bar{c} \cdot \left[\xi_{\text{c.g., WG}} \cdot \frac{m_{\text{WG}}}{m_{\text{FG}}} - \xi_{\text{c.g., OEM}} \cdot \left(1 + \frac{m_{\text{WG}}}{m_{\text{FG}}} \right) \right] \\ \text{where } x_{\text{c.g., FG}} &= \frac{x_{\text{fus}} m_{\text{fus}} + x_{\text{ht}} m_{\text{ht}} + x_{\text{vt}} m_{\text{vt}} + x_{\text{fe}} m_{\text{fe}}}{m_{\text{fus}} + m_{\text{ht}} + m_{\text{vt}} + m_{\text{fe}}}, \text{ and} \\ \xi_{\text{c.g., WG}} &= \frac{\xi_{\text{w}} m_{\text{w}} + \xi_{\text{eng}} m_{\text{eng}}}{m_{\text{w}} + m_{\text{eng}}} \end{aligned} \tag{B.10}$$

The parameter $\bar{c}$ is the absolute length of the mean aerodynamic chord in the above equations. The masses of the groups, being the wing (w), fuselage (fus), engines (eng), empennage (ht and vt), and fixed equipment (fe), result directly from the Class-II mass estimation (Section 3.1.2). The positions of the fuselage, empennage, and fixed equipment (fuselage group, FG) are expressed relative to the fuselage length, while the locations of the wing and engine masses (wing group, WG) are anchored to the MAC. The value of $x_{\text{LE, MAC}}$ allows to compute $x_{\text{c.g., OEM}}$ and $x_{\text{c.g., aft}}$, leading to the tail arms in Equations (B.8) and (B.9). The assumed relative positions in Equation (B.10) are gathered in Table B.2. The relative position of the engines with respect to the MAC (ξ_{eng}) has to be determined for the design under consideration since it is dependent on the wing and engine parameters.

Table B.2: Assumed parameters and design choices to determine the empennage geometry

	Narrow-body	**Wide-body**
$\overline{V}_{\text{ht}}$	1.1	0.70
$\overline{V}_{\text{vt}}$	0.085	0.060
$x_{\text{fus}}/l_{\text{fus}}$	0.45	
$x_{\text{ht}}/l_{\text{fus}}$	0.91	
$x_{\text{vt}}/l_{\text{fus}}$	0.92	
$x_{\text{fe}}/l_{\text{fus}}$	0.45	
ξ_{w}	0.40	

Table B.3: Fixed design parameters for horizontal and vertical tail surfaces

Parameter[Unit]	**Value**
Horizontal tail aspect ratio A_{ht} [-]	5.0
Vertical tail aspect ratio A_{vt} [-]	1.7
Horizontal tail taper ratio λ_{ht} [-]	0.4
Vertical tail taper ratio λ_{vt} [-]	0.6

B.4. NACELLES

The nacelles around the turbofan engines have a cylindrical shape in the current model. Although this is a simplification, it provides the necessary data to estimate the drag contribution. The diameter of the nacelles is based on the fan diameter, which is estimated from the mass flow entering the engine according to the following relation:

$$d_{\text{nac}} = 1.15 \cdot d_{\text{fan}} = 1.15 \cdot 2 \cdot \sqrt{\frac{A_{\text{fan}}}{\pi \cdot \left(1 - \text{ht}_{\text{fan}}^2\right)}} \quad \text{with} \quad A_{\text{fan}} = \dot{m}_{0,\text{TOC}} \cdot \frac{\sqrt{T_{t2}}}{p_{t2} \cdot \text{mfp}_2} \tag{B.11}$$

In the above equation, ht_{fan} is the fan hub-to-tip ratio (0.33), $\dot{m}_{0,\text{TOC}}$ is the total mass flow at top-of-climb conditions, T_{t2}, p_{t2}, and mfp_2 the total temperature, total pressure and mass flow parameter [105] at the fan inlet face. The latter is calculated from the total temperature at this station and an axial Mach number of 0.6 [107]. The length of the nacelle, in meters, is computed from the following statistical relation provided by Torenbeek and Berenschot [251]:

$$l_{\text{nac}} = 7.8 \left(\sqrt{\frac{\dot{m}_{0,\text{TO}}}{\rho_0 \cdot a_0} \cdot \frac{1 + 0.2 \cdot \text{BPR}_{\text{TO}}}{1 + \text{BPR}_{\text{TO}}}} + 0.10 \right) \tag{B.12}$$

In the case of turboprop engines, the nacelle is modeled as a rectangular prism around the cylindrically shaped engine core, allowing room for the support structure, accessories, and intake [146]. The dimensions of this prism are determined as functions of the engine dimensions in Equation (B.15).

$$l_{\text{tp,nacelle}} = \frac{3.3}{1.23} l_{\text{tp,eng}} \tag{B.13}$$

$$h_{\text{tp,nacelle}} = 1.5 d_{\text{tp,eng}} \tag{B.14}$$

$$w_{\text{tp,nacelle}} = 1.1 d_{\text{tp,eng}} \tag{B.15}$$

The engine diameter $d_{\text{tp,eng}}$ and engine length $l_{\text{tp,eng}}$, in meters, are determined statistically as follows [252]:

$$d_{\text{tp,eng}} = 0.20 \cdot \left(\frac{P_{\text{TO}}}{1000 N_{\text{eng}}} \right)^{0.18} \tag{B.16}$$

$$l_{\text{tp,eng}} = 0.10 \cdot \left(\frac{P_{\text{TO}}}{1000 N_{\text{eng}}} \right)^{0.4} \tag{B.17}$$

where P_{TO} is the total aircraft take-off power in Watt. The detailed design of the propeller is outside the scope of the conceptual level considered here. It is assumed that the number of blades will be 6 or 8, leading to the following approximation for the propeller diameter:

$$d_{\mathrm{prop}} = 0.55\left(P_{\mathrm{TO}}/1000\right)^{0.25} \tag{B.18}$$

The wetted area of a single turboprop nacelle is determined as follows:

$$S_{\mathrm{wet,\ tp,\ nacelle}} = 1.18\pi \cdot h_{\mathrm{tp,nacelle}} \cdot l_{\mathrm{tp,nacelle}} \tag{B.19}$$

C

OPTIMIZATION APPROACH AND CONVERGENCE INFORMATION

This appendix provides additional information on the optimization approach taken and presents the convergence of the optimizations. As stated in Chapter 3, the implemented MDAO frameworks use multiple-discipline feasible (MDF) scheme with Gauss-Seidel procedure. In this research, no other schemes are tested or compared. The MDF scheme is selected for its ease of implementation and because it does not require an optimization module to ensure consistent aircraft design, which would be the case for the individual discipline (IDF) scheme. Without the need for an optimization module, the code can also be easily run in a design of experiments without many implementation changes.

C.1. SINGLE-OBJECTIVE, KEROSENE

This appendix briefly discusses the optimization strategy employed to obtain the results in Section 3.3. The following three consecutive steps are carried out for the single-objective optimizations:

1. The design space is explored through design of experiments (DOE), using Latin Hypercube Sampling (LHS).
2. Global search algorithms are applied to the find design subspace which minimizes the objective under consideration. This helps with discrete steps in the design space, such as the formation condition of contrails. A genetic algorithm, or derived method, is used in this case.
3. The final step is to refine the optimal solution and ensure the solver converges. To achieve this, the Nelder-Mead algorithm is employed with a termination accuracy

---

Parts of this chapter have been published in Journal of Aircraft, **59**, 5, 2022, Proesmans and Vos [87] and CEAS Aeronautical Journal, 2024, Proesmans and Vos [154]. Appendix C.3 is being reviewed for a new publication in Journal of Aircraft.

of 1.0×10^{-4} on the objective value. Although gradient-based methods, such as SQP, also proved to be suitable for this step, the Nelder-Mead method appeared to be more robust.

The convergence in the final step is illustrated in Figure C.1 for the fuel mass objective. Note that in this case, the optimizer decided the initial point with which the objective function and design variable values are normalized. Furthermore, the constraints are formulated such that the value of g has to be non-negative. To obtain the Pareto front in Section 3.3.3 a multi-strategy algorithm named pilOPT is employed which is available in modeFRONTIER [1] software. This multi-objective algorithm automatically selects the best approach based on the problem formulation and DOE data, and continues until not enough strictly dominating designs are found anymore.

C.2. MEDIUM-RANGE, HYDROGEN AIRCRAFT

C.2.1. SINGLE-OBJECTIVE OPTIMIZATION

The single-objective optimization consists of two automated steps. First, a design of experiments (DOE) of the nine design variables is performed using Latin Hypercube Sampling (LHS). This DOE is subsequently used to start the optimization with the Simplex algorithm. The software modeFRONTIER is used to carry out both steps. The implemented Simplex algorithm is the Nelder-Mead approach, where constraints are handled through constraint domination. This algorithm is selected because it can solve nonlinear, constrained problems and because it is more robust than gradient-based methods for the problem under consideration. Two termination criteria are applied for the optimization algorithm, being the final termination accuracy (based on the difference of the objective function values in one simplex) of 1×10^{-5} and a maximum number of function evaluations of 2000. If the first termination accuracy is reached before the second criterion, the program automatically restarts at a different point in the design space. This feature helps with avoiding that the optimum found is a local minimum. Figure C.2 presents the convergence plots of the single-objective optimization of the hydrogen aircraft for minimal cash operating cost. These figures also show the automatic restarts.

C.2.2. MULTI-OBJECTIVE OPTIMIZATION

To carry out the multi-objective optimizations (as shown in Figures 5.6 and 5.10), the multi-strategy pilOPT algorithm is used. This method considers several optimization strategies and selects the most appropriate one based on the problem characteristics. The hypervolume indicator [191] is employed to verify the convergence of the multi-objective optimization. Figure C.4a shows the hypervolume convergence for the Pareto front in Figure 5.6. Figure C.4b shows the difference in hypervolume indicator between a Pareto front evaluated at design evaluation i and the Pareto front at design evaluation $i - 100$. After 6000 evaluations, this difference is smaller than 1.5×10^{-5}, indicating that further potential improvements in the Pareto-optimal set are limited.

---

[1] URL `https://engineering.esteco.com/modefrontier` accessed on 16 February 2022

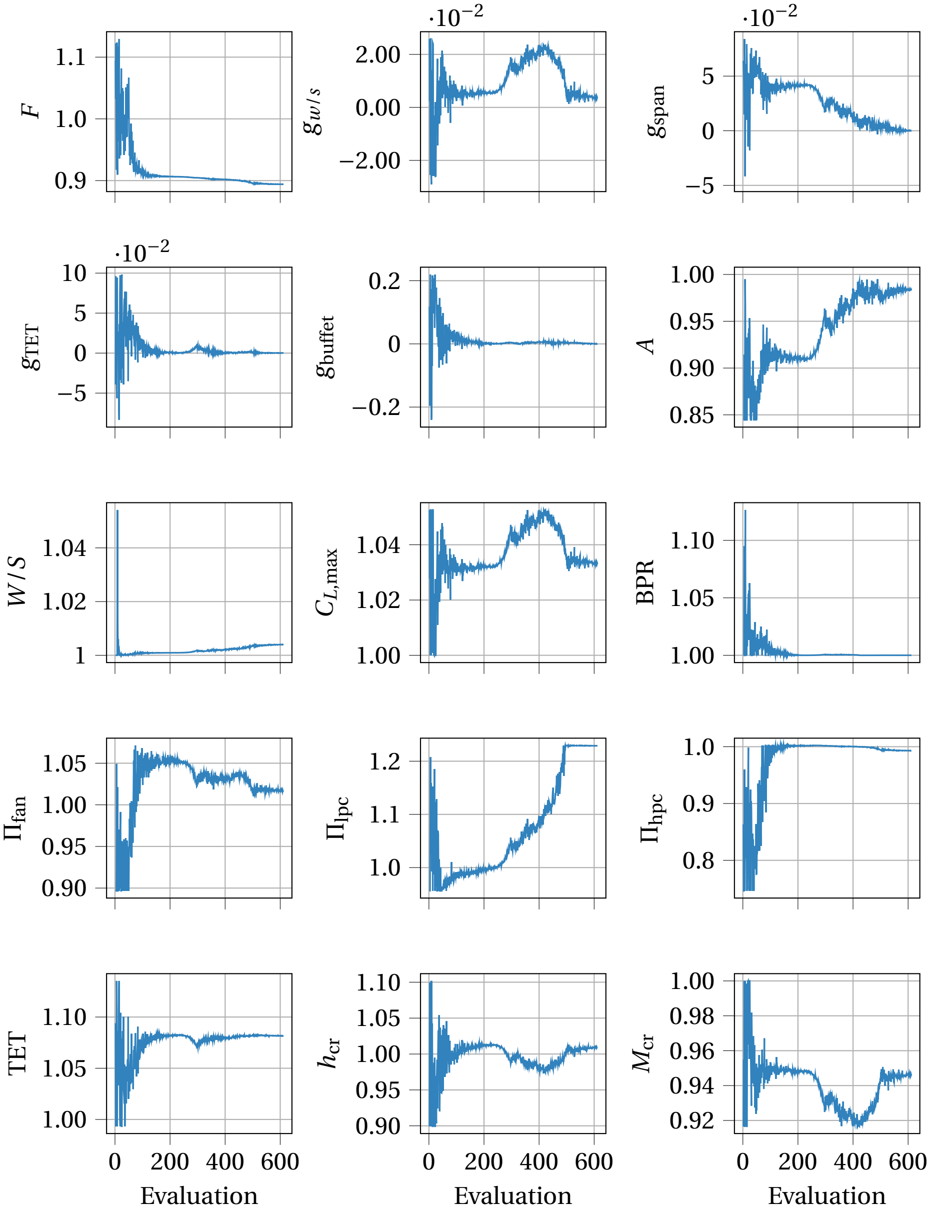

Figure C.1: Convergence plots of objective function, constraints, and design variables for fuel mass minimization

C.3. MULTI-OBJECTIVE FUEL COMPARISON

This appendix shows the convergence of the multi-objective optimizations with respect to the hypervolume indicator. This convergence is shown for the nine case in Figure C.5.

The hypervolume indicator is assumed to be converged when the difference with the parameter of 100 evaluations before, i.e. $H_i - H_{i-100}$, is smaller than 1.5×10^{-5}. However, this does not occur at the same design evaluation for ech case under investigation. Therefore, all multi-objective optimizations continue until 6000 evaluations are reached.

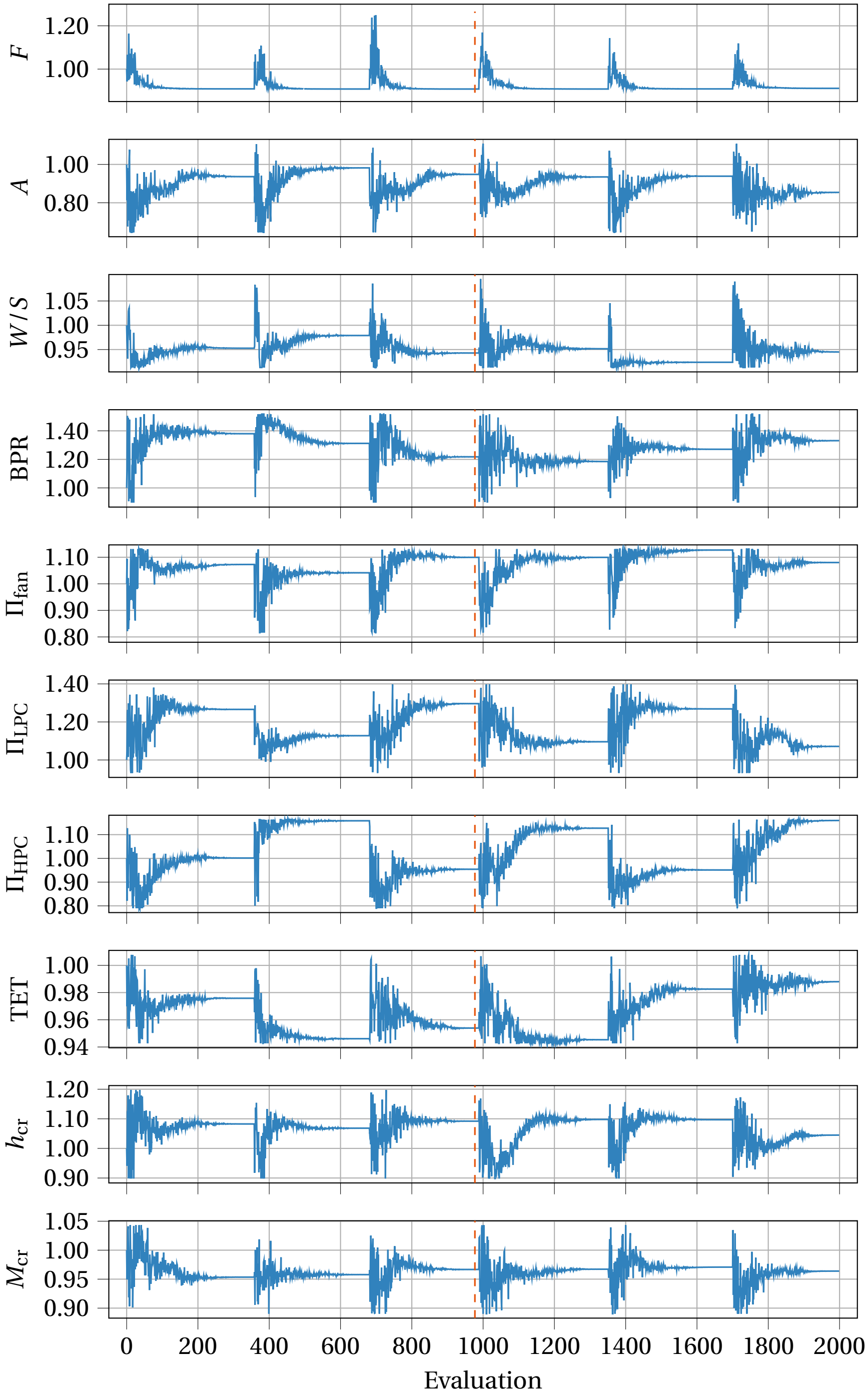

Figure C.2: Convergence plots of objective function and design variables for cash operating cost minimization of the hydrogen aircraft. The orange, dashed line indicates the optimum. The values are normalized with respect to the first evaluation.

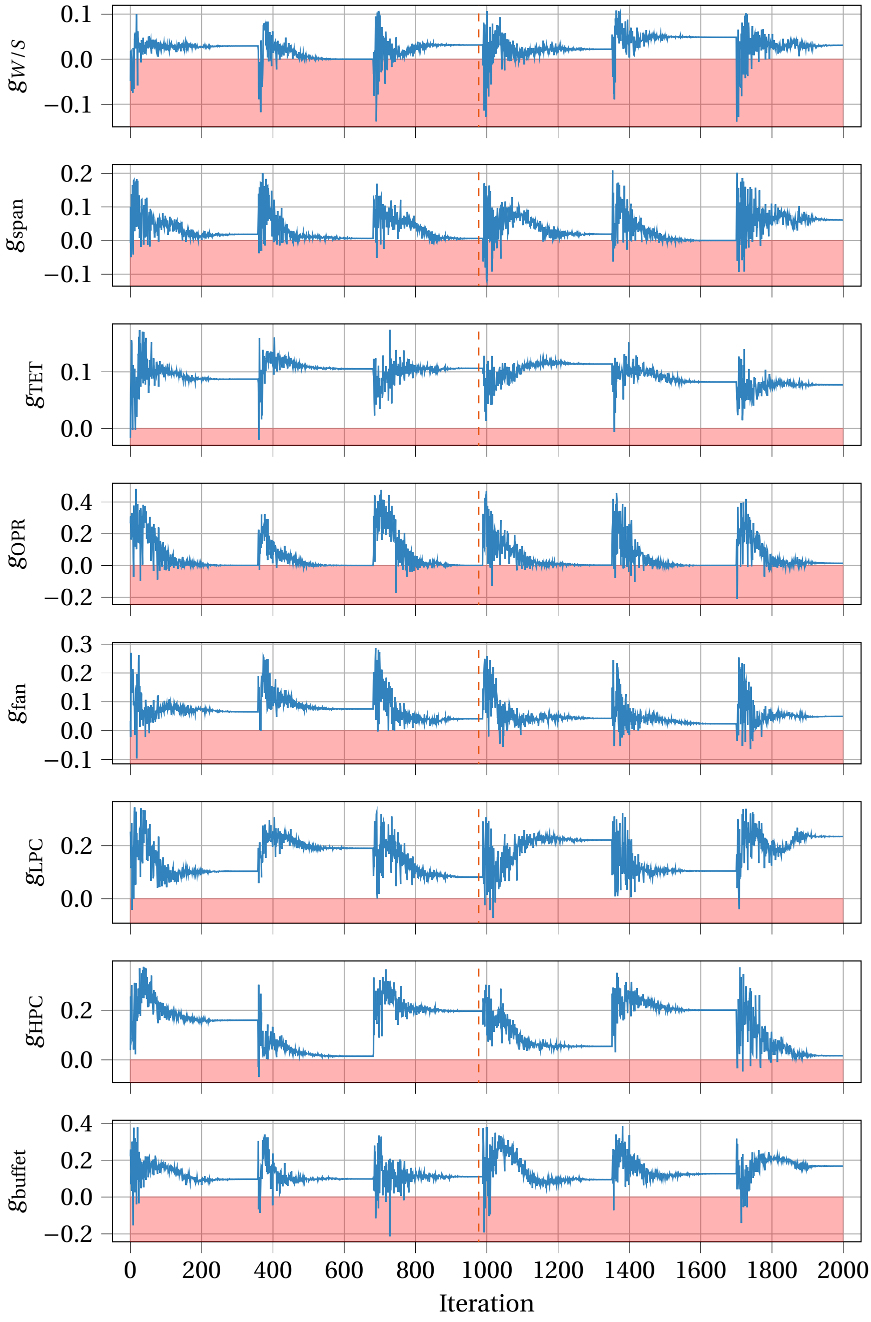

Figure C.3: Convergence plots of constraints for cash operating cost minimization of the hydrogen aircraft. The orange, dashed line indicates the optimum. The red shaded area indicates constraint violation.

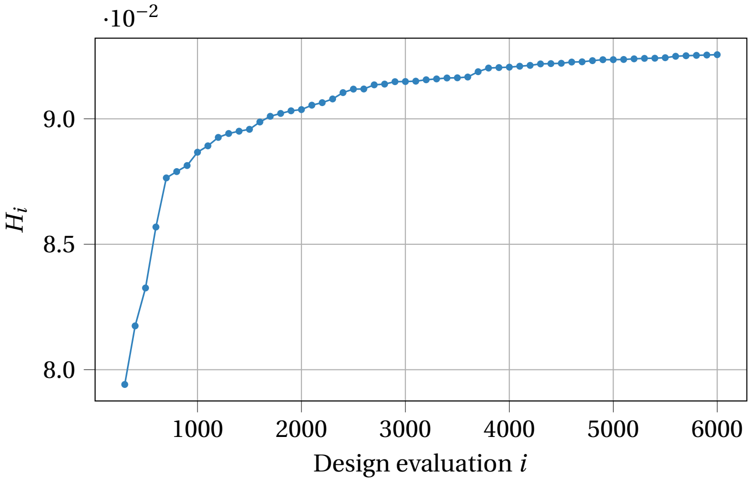

(a) Hypervolume indicator

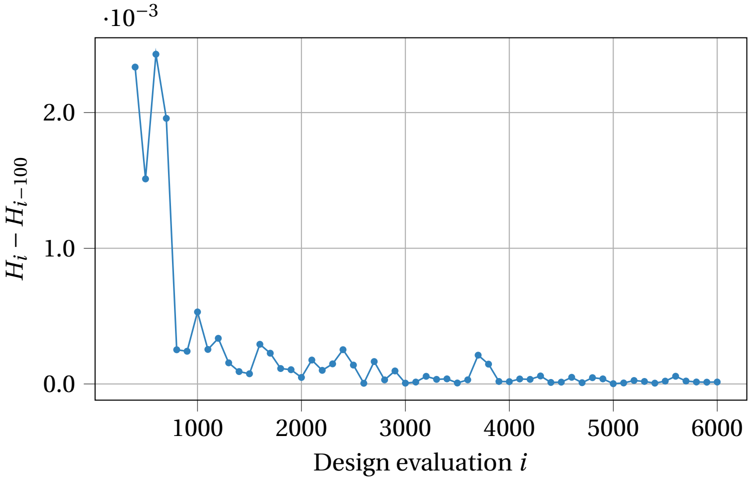

(b) Difference in hypervolume indicator

Figure C.4: Convergence plot hypervolume indicator H for the multi-objective optimization of the hydrogen aircraft. The hypervolume indicator is evaluated at each circular mark, with respect to the point $(1.1, 1.1)$.

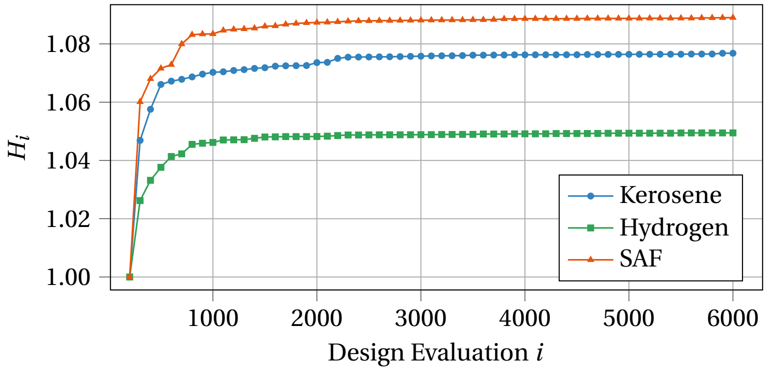

(a) Regional aircraft

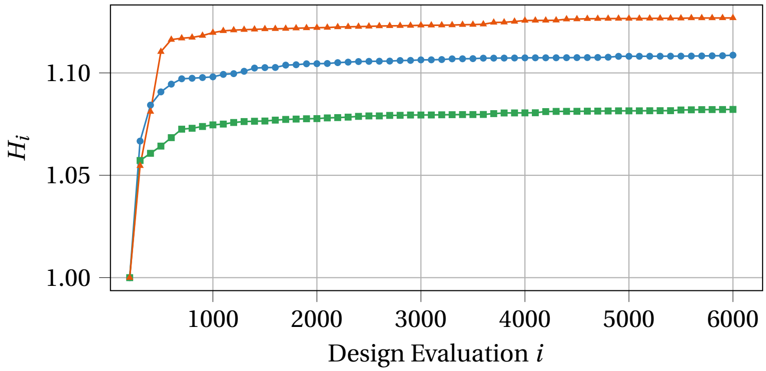

(b) Medium-range aircraft

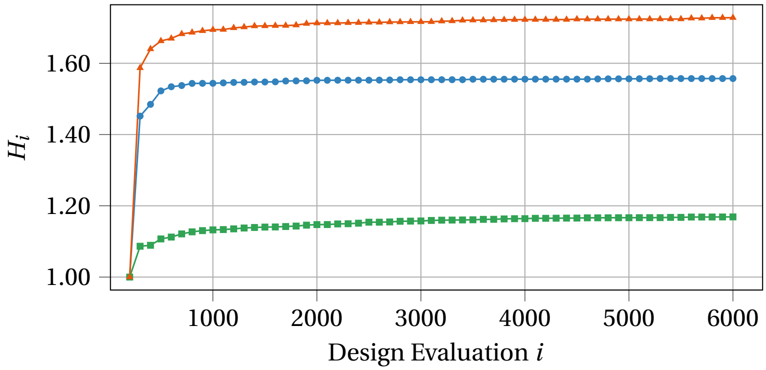

(c) Long-range aircraft

Figure C.5: Convergence of the hypervolume indicator H, evaluated at each mark with respect to point (1.5, 1.5), for the multi-objective optimizations presented in Sections 6.3.1 to 6.3.3. The hypervolume indicator is normalized with respect to the value after 200 evaluations (H_{200}).

D

ENGINE DESIGN DISCUSSION

This appendix elaborates upon the design choices of the turbofan engines and, in particular, the selection of the optimal turbine entry temperature. The discussion focuses on the following three observations:

1. When moving from the cost-optimal solution to the climate-optimal solution, both the overall engine efficiency and the thrust-specific fuel consumption decrease
2. The optimal TET decreases when moving from the cost to the climate objective
3. The TET selected by the optimization is higher than the TET which maximizes the overall engine efficiency

Figure D.1 shows the variation in overall engine efficiency $\eta_{\mathrm{ov,cr}}$ and thrust-specific fuel consumption, both in cruise, versus the design turbine entry temperature, for different design points. In this analysis, only the engine level is considered, disregarding any effects on the airframe. The first observation is that the maximum $\eta_{\mathrm{ov,cr}}$ is reached at the same TET as the minimum TSFC, for each engine design. The TET value at which this occurs corresponds to the point where the product of the thermal efficiency η_{th} and the propulsive efficiency η_{pr} is maximized. The former increases with increasing TET, while the latter decreases with TET. Hence, the fuel consumption is minimized when this product, i.e. the overall efficiency $\eta_{\mathrm{ov,cr}}$, is maximized.

Second, when switching from the cost design objective to the climate objective, three changes are identified that influence the engine performance: lower and slower cruise flight, reduced OPR, and a higher bypass ratio. The first change reduces the climate impact due to NO_x emissions and contrails, the second adjustment reduces the NO_x emission index, and finally, the increased BPR reduces overall fuel consumption which is important for the CO_2 emissions. Figure D.1 shows how these three differences influence the efficiency, TSFC, and the energy-optimal TSFC.

Reducing the OPR lowers the maximum achievable efficiency and increases the TSFC. The optimal TET shifts to the left in the diagram since the thermal efficiency is lower.

	BPR [-]	**OPR [-]**	$h_{\mathbf{cr}}$ **[km]**	$M_{\mathbf{cr}}$ **[-]**	**Comment**
—	8.43	59.9	9.74	0.80	COC optimal
●—	8.43	59.9	6.01	0.51	-
- - -	8.43	42.0	9.74	0.89	-
●- - -	8.43	42.0	6.01	0.51	-
■- - -	10.9	42.0	6.01	0.51	ATR$_{100}$ optimal

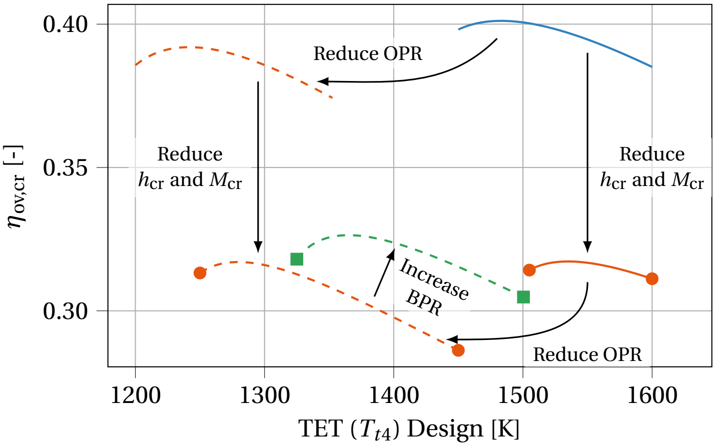

(a) Overall propulsion efficiency in cruise

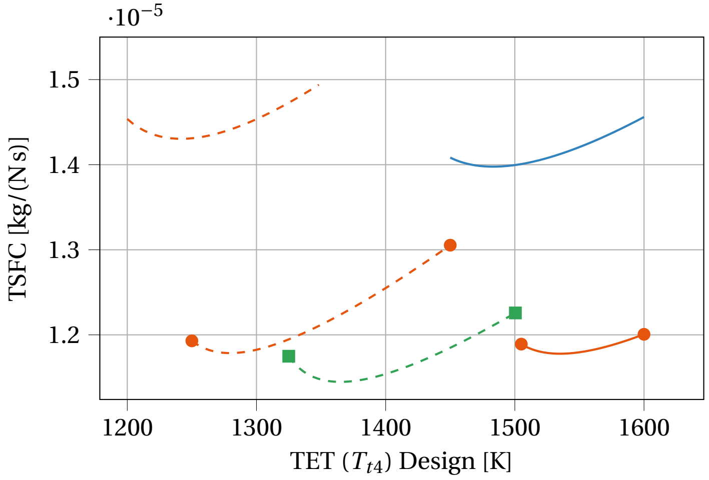

(b) Thrust-specific fuel consumption in cruise

Figure D.1: Turbofan overall propulsion efficiency and TSFC versus design turbine entry temperature in cruise. The arrows indicate the individual design steps which can be distinguished when moving from the cost-optimal to climate-optimal, medium-range, kerosene solution. The figure indicates that the optimal design TET decreases when moving from the cost to the climate objective.

The subsequent changes in flight altitude and Mach number reduce the efficiency and the TSFC, while slightly increasing the optimal TET. Finally, the increased BPR results in a higher efficiency and lower TSFC, but requires a higher TET to make sure enough power is available to move the increased mass flow through the bypass section.

As can be observed, when applying changes to the engine cycle such as OPR and BPR, the efficiency and TSFC move in the logical direction: the efficiency increases, and the fuel consumption per unit of thrust is decreased. However, when flying lower and slower, this trend is reversed and the TSFC still decreases but the efficiency is also lower. This shows that the operating conditions, and in particular the Mach number, perform an important role in the relation between these two objectives. The following equation shows the relation between the TSFC and efficiency:

$$\left.\begin{aligned} \mathrm{TSFC} &= \frac{\dot{m}_f}{F_N} \\ \eta_{\mathrm{ov,cr}} &= \frac{F_N \cdot v_0}{\dot{m}_f \cdot \mathrm{LHV}} \end{aligned}\right\} \Rightarrow \mathrm{TSFC} = \frac{v_0}{\eta_{\mathrm{ov,cr}} \cdot \mathrm{LHV}} = \frac{M_0 \cdot a_0}{\eta_{\mathrm{ov,cr}} \cdot \mathrm{LHV}} \tag{D.1}$$

This equation shows that TSFC indeed decreases with increasing $\eta_{\mathrm{ov,cr}}$, for example by increasing the OPR and/or BPR, but only if the freestream Mach number or velocity is kept constant. When the Mach number is lowered, the TSFC decreases, but also the efficiency decreases. Looking at the aircraft energy consumption, for example, it is observed that the overall mission fuel or energy consumption increases by applying these changes. Although the TSFC is lower, the thrust levels of the energy- and climate-optimal aircraft are similar, while the thrust has to be produced over a longer time in the case of the climate-optimized aircraft. This explains the increase in overall energy consumption, and it is therefore recommended to compare the aircraft using the overall engine efficiency $\eta_{\mathrm{ov,cr}}$ rather than the TSFC.

When comparing the optimal TET from Figure D.1 to the TET selected by the optimizer in Table 5.3 or Table 6.8, one can observe that these do not match exactly. The difference in chosen TET is indicated in Figure D.2 for the cost- and climate-optimal, kerosene engines. The explanation for this difference, according to the implemented design methods, is that an installation gain can be achieved from having a marginally higher TET than the energy-optimal value. While the energy curves in Figure D.2a show a plateau near the maximum energy value, with a small decrease in efficiency for a given TET change, the engine mass (Figure D.2b) and nacelle wetted area (Figure D.2d) are more sensitive to the chosen TET. This is because a higher TET results in a higher specific thrust and thus lower inlet mass flow. This positively affects the engine mass and dimensions. Hence, although the chosen TET does not deviate largely from the energy-optimal level, it is logical that the optimizer selects a marginally higher TET and trades some efficiency gain for reduced installation penalties. Of course, this trade depends on the implemented engine design methods.

Finally, Figure D.2c shows the design TET against the TET reach in take-off. The shaded area indicates constraint violation in the multidisciplinary design optimization. Although the optimizer selects a TET that is close to the energy-optimal value, this figure shows that for the climate-optimal aircraft, the constraint is almost active.

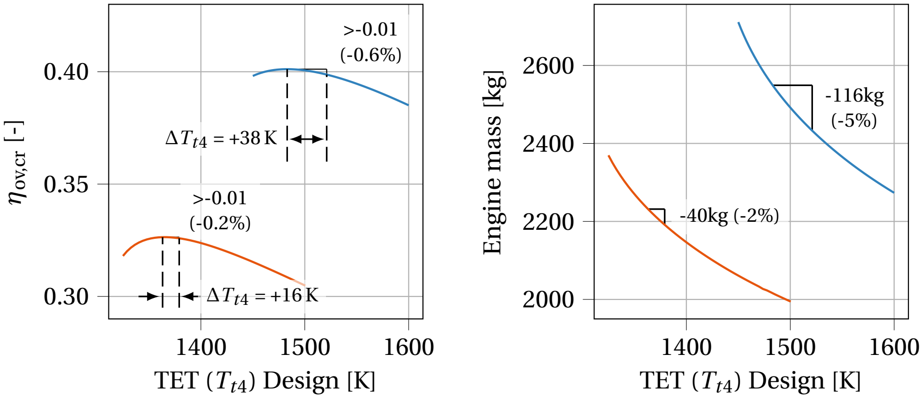

(a) Overall propulsion efficiency in cruise

(b) Engine bare mass

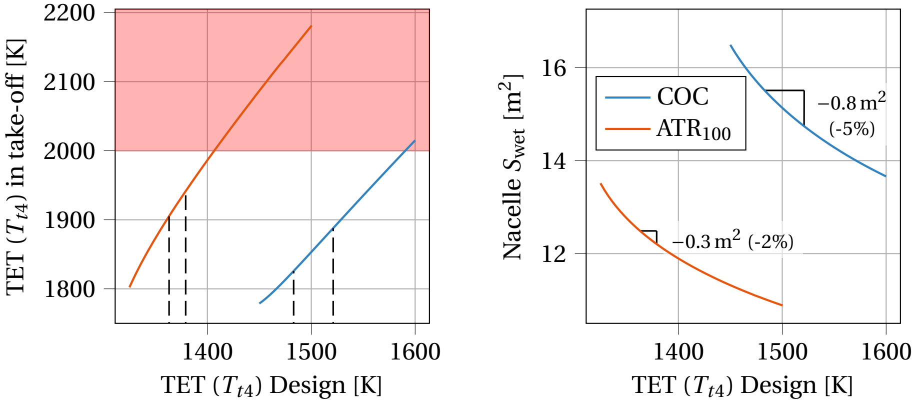

(c) TET at take-off conditions

(d) Wetted area of the nacelle

Figure D.2: Variation in (a) engine cruise efficiency, (b) engine mass, (c) TET at take-off, and (d) nacelle wetted area versus design TET at cruise (also known as T_{t4}). The trends are plotted for the cost- and climate-optimal, kerosene engines designed for the medium-range aircraft. ΔT_{t4} indicates the offset between the TET which maximizes the overall propulsion efficiency and the TET chosen by the optimizer. In Subfigures (a), (b), and (d), also the change in the parameter of interest is shown for the observed ΔT_{t4}, indicating that the relative changes in mass and wetted area are larger than the changes in efficiency.

E

OPTIMIZED AIRCRAFT DATA

This appendix presents data of the 27 optimized aircraft in Appendix E.1. This data is converted to inputs for the fleet allocation according to Figure 7.2 in Appendix E.2.

E.1. CHARACTERISTICS OF OPTIMIZED AIRCRAFT

This section presents more information about the optimal aircraft designs presented in Section 6.3. Tables E.1 to E.3 summarize that data for regional, medium-range, and long-range aircraft.

E.2. INPUTS FOR FLEET ALLOCATION

This section provides the input data for the fleet allocation for the nine fleet allocation case studies, based on the aircraft data presented in Appendix E.1.

Parts of this appendix have been published and presented at AIAA AVIATION 2022 Forum, Chicago, IL & Virtual, 2022, doi: 10.2514/6.2022-3288, and are currently being reviewed for publication in the AIAA Journal of Aircraft.

Table E.1: Performance and geometric data of optimized, regional aircraft. The performance data is computed for the reference mission with 67 passengers and a block range of 894 km.

	Kerosene			**Hydrogen**			**SAF - HEFA (50-50)**		
Variable [Unit]	**ATR$_{100}$**	**MO**	**COC**	**ATR$_{100}$**	**MO**	**COC**	**ATR$_{100}$**	**MO**	**COC**
MTOM [tons]	33.2	35.1	35.2	32.8	32.9	33.7	33.1	35.1	35.0
OEM [tons]	19.0	20.5	20.6	21.2	21.3	22.3	19.0	20.6	20.6
S [m^2]	61	66	67	59	58	64	66	66	68
b [m]	27.1	20.9	21.4	24.4	24.4	25.9	28.1	21.5	22.0
$\Lambda_{0.25}$ [-]	0.0	25.7	26.7	0.0	4.9	21.3	0.0	25.3	26.1
λ [-]	0.460	0.246	0.238	0.460	0.419	0.283	0.460	0.250	0.243
l_{fus} [m]	31.6	31.6	31.6	35.3	35.1	34.5	31.6	31.6	31.6
S_{ht} [m^2]	18	21	21	22	22	20	20	21	21
L/D_{cr} [-]	17.9	14.0	14.6	14.7	15.0	16.8	17.9	14.2	15.0
T/W_{TO} [-]	0.299	0.331	0.327	0.307	0.311	0.315	0.278	0.327	0.322
m_{eng} [tons]	1.12	1.28	1.26	1.29	1.26	1.27	1.03	1.30	1.25
d_{nac} [m]	0.97	1.14	1.17	1.04	1.09	1.17	0.94	1.14	1.17
l_{cowl} [m]	2.14	2.33	2.33	2.16	2.19	2.24	2.09	2.30	2.30
TSFC$_{\text{cr}}$ [10^{-5}kg/(N s)]	1.15	1.43	1.43	0.44	0.46	0.48	1.13	1.40	1.40
$\eta_{\text{ov,cr}}$ [-]	32.1%	39.1%	39.1%	35.7%	37.4%	38.6%	32.0%	39.2%	39.0%
SEC$_{\text{cr}}$ [10^{-4}MJ/(N s)]	4.93	6.16	6.15	5.32	5.48	5.73	4.95	6.10	6.10
Energy [MJ/(pax km)]	1.04	1.19	1.16	1.15	1.12	1.07	1.05	1.17	1.14
$N_{\text{AC, max}}$ [10^3]	5.4	4.4	4.4	4.9	4.7	4.5	5.4	4.4	4.4
t_{bl} [hrs]	2h44m	2h11m	2h12m	2h28m	2h22m	2h17m	2h44m	2h12m	2h12m

Table E.2: Performance and geometric data of optimized, medium-range aircraft. The performance data is computed for the reference mission with 130 passengers and a block range of 1852 km.

	Kerosene			**Hydrogen**			**SAF - HEFA (50-50)**		
Variable [Unit]	**ATR$_{100}$**	**MO**	**COC**	**ATR$_{100}$**	**MO**	**COC**	**ATR$_{100}$**	**MO**	**COC**
MTOM [tons]	65.1	68.3	68.4	62.1	63.7	65.5	64.5	68.0	68.4
OEM [tons]	36.2	39.2	39.5	40.1	41.8	43.8	35.8	39.0	39.7
S [m^2]	115	120	127	112	109	125	114	118	126
b [m]	36.0	30.2	31.3	33.9	35.0	35.8	35.9	29.9	31.6
$\Lambda_{0.25}$ [-]	0.0	25.7	27.0	0.0	7.0	23.0	0.0	25.6	26.9
λ [-]	0.460	0.246	0.235	0.460	0.402	0.269	0.460	0.247	0.236
l_{fus} [m]	37.5	37.5	37.5	44.7	44.4	43.7	37.5	37.5	37.5
S_{ht} [m^2]	30.8	30.5	31.0	44.7	42.4	41.2	30.6	30.0	30.1
L/D_{cr} [-]	19.0	16.0	16.7	16.4	16.4	17.9	19.1	15.9	16.9
T/W_{TO} [-]	0.288	0.327	0.315	0.283	0.301	0.295	0.289	0.332	0.317
m_{eng} [tons]	2.19	2.60	2.43	2.05	2.40	2.37	2.04	2.60	2.52
d_{nac} [m]	1.39	1.56	1.58	1.34	1.48	1.63	1.32	1.55	1.59
l_{cowl} [m]	2.80	2.98	2.96	2.69	2.79	2.90	2.74	2.97	2.94
TSFC$_{\text{cr}}$ [10^{-5}kg/(N s)]	1.15	1.40	1.41	0.44	0.45	0.48	1.14	1.38	1.38
$\eta_{\text{ov,cr}}$ [-]	32.6%	40.2%	39.9%	34.8%	38.1%	39.3%	32.1%	40.1%	40.2%
SEC$_{\text{cr}}$ [10^{-4}MJ/(N s)]	4.93	6.02	6.05	5.22	5.42	5.71	4.95	6.03	6.00
Energy [MJ/(pax km)]	0.82	0.88	0.85	0.90	0.87	0.83	0.82	0.88	0.84
$N_{\text{AC, max}}$ [10^3]	18.5	14.0	14.0	16.9	15.5	14.7	18.6	14.0	14.0
t_{bl} [hrs]	4h23m	3h19m	3h19m	4h1m	3h41m	3h29m	4h25m	3h19m	3h20m

Table E.3: Performance and geometric data of optimized, long-range aircraft. The performance data is computed for the reference mission with 253 passengers and a block range of 6060 km.

	Kerosene			**Hydrogen**			**SAF - HEFA (50-50)**		
Variable [Unit]	**ATR$_{100}$**	**MO**	**COC**	**ATR$_{100}$**	**MO**	**COC**	**ATR$_{100}$**	**MO**	**COC**
MTOM [tons]	269	266	268	228	233	234	265	264	265
OEM [tons]	126	132	134	143	149	152	126	131	134
S [m^2]	371	352	382	338	351	369	352	351	364
b [m]	64.8	60.3	58.8	63.7	64.1	65.1	65.0	59.7	59.6
$\Lambda_{0.25}$ [-]	0.0	23.2	26.6	0.0	8.7	20.4	0.0	22.9	25.4
λ [-]	0.390	0.197	0.170	0.390	0.318	0.221	0.390	0.200	0.179
l_{fus} [m]	65.3	65.3	65.3	89.7	90.1	87.3	65.3	65.3	65.3
S_{ht} [m^2]	97.4	77.7	86.4	109.3	114.7	104.0	90.6	78.9	80.1
L/D_{cr} [-]	20.9	20.5	20.2	19.7	18.8	20.3	21.2	20.3	20.6
T/W_{TO} [-]	0.252	0.285	0.273	0.249	0.251	0.250	0.261	0.283	0.280
m_{eng} [tons]	7.40	8.19	8.24	6.15	6.70	6.87	7.44	8.22	8.26
d_{nac} [m]	2.66	2.75	2.84	2.37	2.56	2.74	2.59	2.76	2.84
l_{cowl} [m]	4.83	5.01	4.94	4.37	4.46	4.54	4.81	4.99	4.97
TSFC$_{\mathrm{cr}}$ [10^{-5}kg/(N s)]	1.22	1.38	1.37	0.42	0.45	0.46	1.20	1.35	1.34
$\eta_{\mathrm{ov,cr}}$ [-]	34.6%	39.5%	40.8%	34.3%	38.2%	39.4%	34.7%	39.6%	40.4%
SEC$_{\mathrm{cr}}$ [10^{-4}MJ/(N s)]	5.25	5.93	5.88	5.09	5.46	5.57	5.23	5.89	5.84
Energy [MJ/(pax km)]	1.07	1.05	1.00	1.13	1.15	1.02	1.05	1.04	0.98
$N_{\mathrm{AC,\,max}}$ [10^3]	1.95	1.57	1.54	2.01	1.73	1.65	1.95	1.57	1.56
t_{bl} [hrs]	10h36m	8h32m	8h22m	10h58m	9h26m	9h00m	10h38m	8h33m	8h29m

Table E.4: Kerosene aircraft input data for fleet allocation

	ATR_{100}-optimal			**Multi-objective**			**COC-optimal**		
Variable [Unit]	**REG**	**SMR**	**LR**	**REG**	**SMR**	**LR**	**REG**	**SMR**	**LR**
h_{cr} [km]	6.00	6.00	6.37	8.63	8.32	7.30	9.63	9.74	8.70
M_{cr} [-]	0.50	0.51	0.58	0.79	0.79	0.75	0.80	0.80	0.79
MTOM [tons]	33.2	65.1	269	35.1	68.3	266	35.2	68.4	268
OEM [tons]	19.0	36.2	126	20.5	39.2	132	20.6	39.5	134
L/D_{cr} [-]	17.9	19.0	20.9	14.0	16.0	20.5	14.6	16.7	20.2
TSFC_{cr} [10^{-5}kg/(N s)]	1.15	1.15	1.22	1.43	1.40	1.38	1.43	1.41	1.37
$\eta_{\text{ov,cr}}$ [-]	32.1%	32.6%	34.6%	39.1%	40.2%	39.5%	39.1%	39.9%	40.8%
LTOT	0h19m	0h20m	0h27m	0h19m	0h20m	0h27m	0h19m	0h20m	0h27m
TAT	0h17m	0h41m	1h26m	0h17m	0h41m	1h26m	0h17m	0h41m	1h26m
C_{hours} [10^3 USD/hr]	2.01	2.89	7.60	2.10	3.04	7.27	2.10	3.05	7.33

Table E.5: Hydrogen aircraft input data for fleet allocation

	ATR_{100}-optimal			Multi-objective			COC-optimal		
Variable [Unit]	**REG**	**SMR**	**LR**	**REG**	**SMR**	**LR**	**REG**	**SMR**	**LR**
h_{cr} [km]	6.00	6.02	6.00	8.04	7.93	7.45	10.8	10.9	9.69
M_{cr} [-]	0.60	0.58	0.55	0.66	0.67	0.67	0.75	0.76	0.73
MTOM [tons]	32.8	62.1	228	32.9	63.7	233	33.7	65.5	234
OEM [tons]	21.2	40.1	143	21.3	41.8	149	22.3	43.8	152
L/D_{cr} [-]	14.7	16.4	19.7	15.0	16.4	18.8	16.8	17.9	20.3
TSFC_{cr} [10^{-5}kg/(N s)]	0.44	0.44	0.42	0.46	0.45	0.45	0.48	0.48	0.46
$\eta_{\text{ov,cr}}$ [-]	35.7%	34.8%	34.3%	37.4%	38.1%	38.2%	38.6%	39.3%	39.4%
LTOT	0h19m	0h20m	0h25m	0h19m	0h20m	0h26m	0h19m	0h20m	0h26m
TAT	0h17m	0h41m	1h26m	0h17m	0h41m	1h26m	0h17m	0h41m	1h26m
C_{hours} [10^3 USD/hr]	2.11	3.02	8.07	2.11	3.11	7.70	2.16	3.19	7.81

Table E.6: SAF (HEFA 50-50) aircraft input data for fleet allocation

	ATR$_{100}$-optimal			**Multi-objective**			**COC-optimal**		
Variable [Unit]	**REG**	**SMR**	**LR**	**REG**	**SMR**	**LR**	**REG**	**SMR**	**LR**
h_{cr} [km]	6.00	6.00	6.00	8.63	8.22	7.26	9.87	9.67	8.70
M_{cr} [-]	0.50	0.50	0.57	0.78	0.79	0.75	0.79	0.80	0.77
MTOM [tons]	33.1	64.5	265	35.1	68.0	264	35.0	68.4	265
OEM [tons]	19.0	35.8	126	20.6	39.0	131	20.6	39.7	134
L/D_{cr} [-]	17.9	19.1	21.2	14.2	15.9	20.3	15.0	16.9	20.6
TSFC$_{\mathrm{cr}}$ [10^{-5}kg/(N s)]	1.13	1.14	1.20	1.40	1.38	1.35	1.40	1.38	1.34
$\eta_{\mathrm{ov,cr}}$ [-]	32.0%	32.1%	34.7%	39.2%	40.1%	39.6%	39.0%	40.2%	40.4%
LTOT	0h19m	0h20m	0h27m	0h19m	0h20m	0h26m	0h19m	0h20m	0h27m
TAT	0h17m	0h41m	1h26m	0h17m	0h41m	1h26m	0h17m	0h41m	1h26m
C_{hours} [10^3 USD/hr]	2.00	2.87	7.60	2.10	3.04	7.23	2.10	3.06	7.32

F

DEMAND AND ALLOCATION OF REFERENCE NETWORK

Table F.1 presents the weekly passenger demand between origin-destination pairs considered in Chapter 7. Figures F.1a and F.1b present the initial and final, remaining demand of the reference network case, employing cost-optimal, kerosene aircraft. In Figure F.2, the allocation of the different cost-optimized aircraft is shown. Figure F.3 presents the allocation for the climate-optimal fleets.

The data presented in this chapter was gathered in collaboration with F. Morlupo, B.F. Santos, and R. Vos and have been published in Reference [200].

Table F.1: Reference network weekly passenger demand data per week

Origin Airport	Destination Airport	Destination Country	Demand
Atlanta (ATL)	Los Angeles (LAX)	USA	6442
Atlanta (ATL)	Minneapolis (MSP)	USA	5849
Atlanta (ATL)	Boston (BOS)	USA	5280
Atlanta (ATL)	Dallas-Fort Worth (DFW)	USA	4908
Atlanta (ATL)	Miami (MIA)	USA	4760
Atlanta (ATL)	Salt Lake City (SLC)	USA	4611
Atlanta (ATL)	San Francisco (SFO)	USA	4212
Atlanta (ATL)	New Orleans (MSY)	USA	4193
Atlanta (ATL)	Detroit (DTW)	USA	3932
Atlanta (ATL)	Denver (DEN)	USA	3658
Atlanta (ATL)	Seattle (SEA)	USA	3528
Atlanta (ATL)	Paris (CDG)	France	3438
Atlanta (ATL)	Phoenix (PHX)	USA	3406
Atlanta (ATL)	London (LHR)	UK	2896
Atlanta (ATL)	Columbus (CMH)	USA	2508
Atlanta (ATL)	Savannah (SAV)	USA	2273
Atlanta (ATL)	Cancun (CUN)	Mexico	2136
Atlanta (ATL)	Dublin (DUB)	Ireland	2084
Atlanta (ATL)	Buffalo (BUF)	USA	1943
Atlanta (ATL)	Amsterdam (AMS)	The Netherlands	1860
Atlanta (ATL)	Rome (FCO)	Italy	1689
Atlanta (ATL)	Portland (PDX)	USA	1577
Atlanta (ATL)	Albuquerque (ABQ)	USA	1327
Atlanta (ATL)	Munich (MUC)	Germany	1289
Atlanta (ATL)	Tucson (TUS)	USA	984
Atlanta (ATL)	Manchester NH (MHT)	USA	625
Atlanta (ATL)	Guadalajara (GDL)	Mexico	589
Atlanta (ATL)	Caracas (CCS)	Venezuela	455
Atlanta (ATL)	Georgetown (GCM)	Cayman Islands	422
Atlanta (ATL)	Quito (UIO)	Ecuador	392

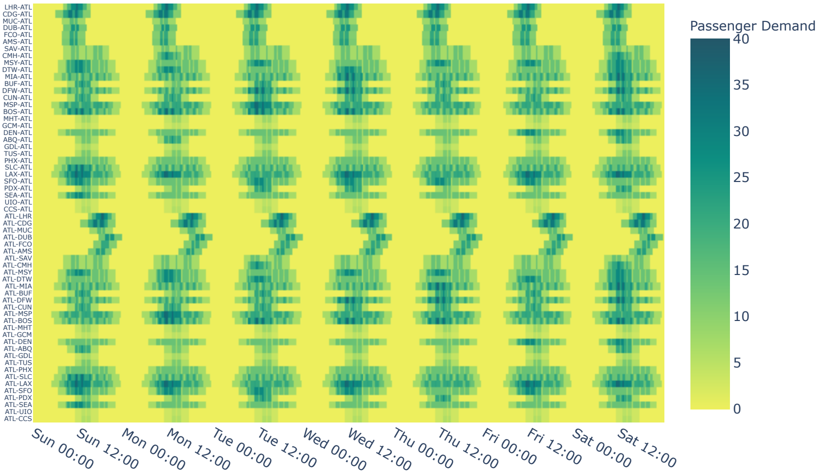

(a) Initial demand schedule (input)

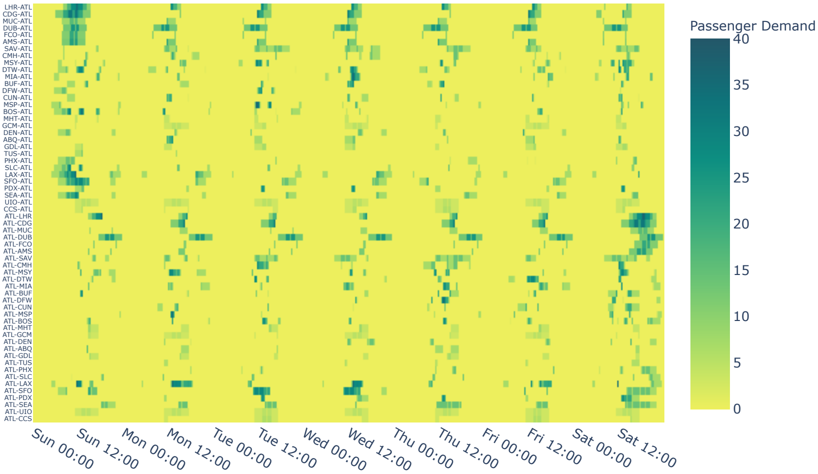

(b) Final remaining demand (after iterations converged)

Figure F.1: Passenger demand schedules between origin-destination pairs (y-axis) at all 20-minute time intervals (x-axis) throughout one week, for the kerosene fleet with cost-optimal aircraft discussed in Section 7.2

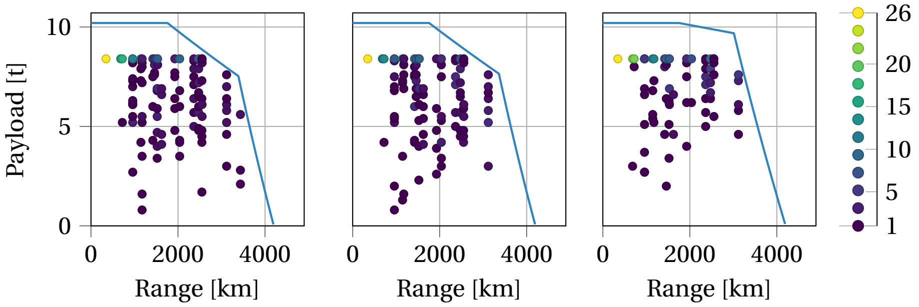

(a) Regional, kerosene (b) Regional, SAF (c) Regional, hydrogen

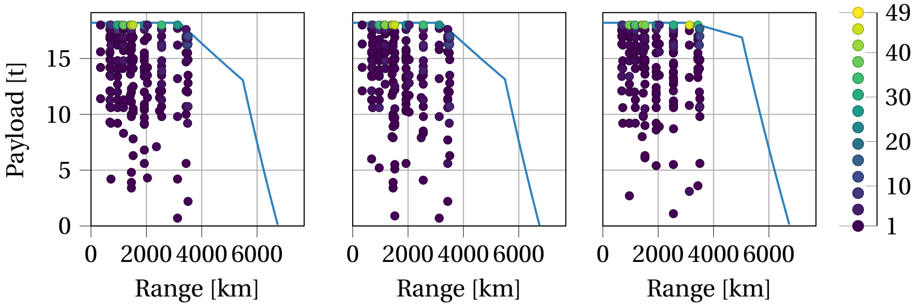

(d) Medium range, kerosene (e) Medium range, SAF (f) Medium range, hydrogen

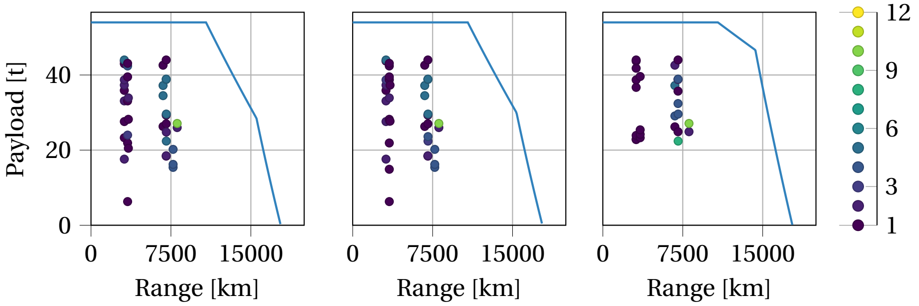

(g) Long range, kerosene (h) Long range, SAF (i) Long range, hydrogen

Figure F.2: Payload-range diagram and operated payload-range combinations for each aircraft type of the **cost-optimal** fleets. The colorbar indicates the flight frequency of a payload-range combination in one week.

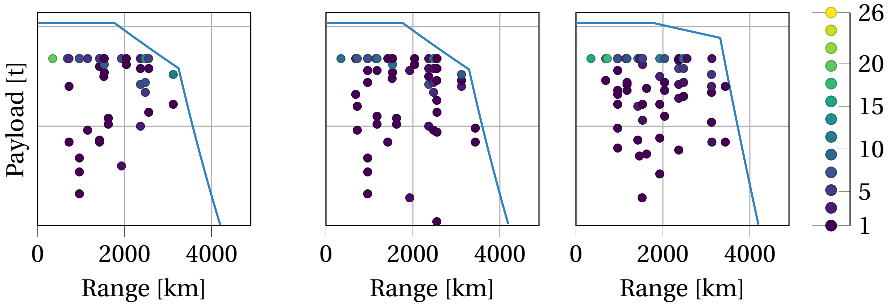

(a) Regional, kerosene

(b) Regional, SAF

(c) Regional, hydrogen

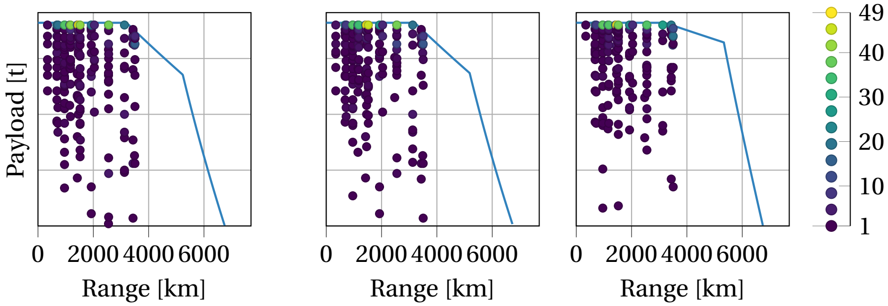

(d) Medium range, kerosene

(e) Medium range, SAF

(f) Medium range, hydrogen

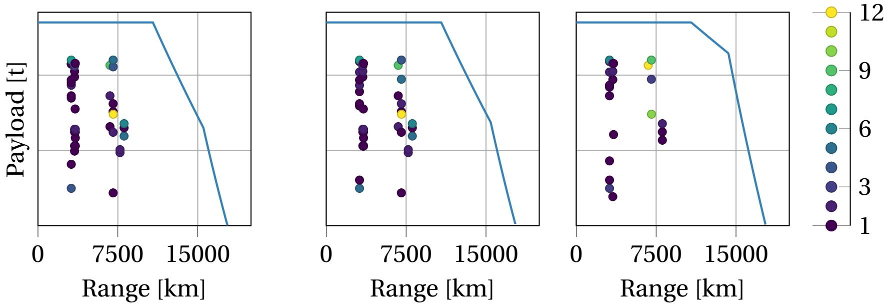

(g) Long range, kerosene

(h) Long range, SAF

(i) Long range, hydrogen

Figure F.3: Payload-range diagram and operated payload-range combinations for each aircraft type of the **climate-optimal** fleets. The colorbar indicates the flight frequency of a payload-range combination in one week.

G

SIMPLE TICKET PRICE ESTIMATION

The aim of this appendix to provide a simple estimation the relative ticket price increase as a function relative increase in direct operating cost (DOC), assuming the indirect operating cost (IOC) remains unchanged. Assuming the ticket price (P) is set based on the total operating cost (TOC=DOC+IOC) and a intended profit margin (PM), the ticket price can be computed as follows:

$$P = \text{TOC} + \text{PM} = \text{DOC} + \text{IOC} + \text{PM} \tag{G.1}$$

Since data is available on the relative contribution of DOC to TOC for kerosene aircraft, a factor f can be defined as follows:

$$f = \text{IOC}/\text{DOC} \tag{G.2}$$

Hence, if DOC typically contributes 45% to 60% of the total operating cost [230], the reference value of f_{ref} ranges between $2/3$ (≈ 0.67) and $11/9$ (≈ 1.22) for current cost-optimized aircraft. The profit margin can be assumed a fraction f_{PM} of the ticket price:

$$\text{PM} = f_{\text{PM}} \cdot P \tag{G.3}$$

This allows to rewrite Equation (G.1) as follows:

$$P = \text{DOC} \cdot \left(1 + f\right) + f_{\text{PM}} \cdot P \tag{G.4}$$

leading to

$$P = \text{DOC} \cdot \left(\frac{1 + f}{1 - f_{\text{PM}}}\right) \tag{G.5}$$

When considering climate-optimal aircraft or the application of novel fuels, the main parameter of interest is the relative ticket price increase with respect to a reference case, which in this thesis is the kerosene, cost-optimal aircraft. This allows to compute the following ratio between the ticket price of a new, climate-optimal aircraft and the reference aircraft (indicated by subscript "ref"):

$$\frac{P}{P_{\text{ref}}} = \frac{\text{TOC}}{\text{TOC}_{\text{ref}}} \cdot \frac{1 - f_{\text{PM}}}{1 - f_{\text{PM}}} = \frac{\text{DOC} + \text{IOC}}{\text{DOC}_{\text{ref}} \cdot \left(1 + f_{\text{ref}}\right)} \tag{G.6}$$

If it is assumed that the IOC remains constant in the case of climate-optimal design choices or novel fuels, the above ratio can be rewritten as

$$\frac{P}{P_{\text{ref}}} = \frac{\text{DOC} + f_{\text{ref}}\text{DOC}_{\text{ref}}}{\text{DOC}_{\text{ref}} \cdot \left(1 + f_{\text{ref}}\right)} = \frac{1}{1 + f_{\text{ref}}} \left(\frac{\text{DOC}}{\text{DOC}_{\text{ref}}} + f_{\text{ref}} \right) \tag{G.7}$$

This equation is used to plot the relation between the relative DOC increase and ticket price increase in Figure 8.5, for varying values of f_{ref}.

H

AIRCRAFT DESIGN CODE SETUP

The aircraft design and analysis disciplines discussed and employed in Chapters 3 to 6 are implemented in a modular Python [253] project. This Python code project can also be used independently from the modeFRONTIER software discussed in Appendix C. At the time of writing (July 2024), this project is stored in a repository on GitLab hosted by Delft University of Technology. The project is compatible with Python 3.7 or higher. This appendix elaborates upon the structure of the implemented code and how information is shared between disciplines.

H.1. SYNTHESIS AND OPTIMIZATION SETUP

The extended design structure matrix in Chapter 3 (Figure 3.2, Page 32) and the updates in the subsequent chapters are implemented by connecting modular, individual discipline functions in Python. The convergence of the design disciplines (blocks 1 to 4 in Figure 3.2) is assembled into one Synthesis function for which the pseudo-code is given in Listing H.1 where only the OEM and number of iterations are used as termination criteria. As can be seen, each discipline is a function with input and output file names as arguments. Some disciplines, such as the turbofan design, have an additional technology input file specifying parameters which do not change throughout the synthesis or optimization iterations but may vary between case studies.

Listing H.1: Synthesis function Python code

```

import os
from shutil import copyfile

mtom_path = "./aircraft/massBreakdown/mTo/design"
oem_path = "./aircraft/massBreakdown/oem"
mfuel_path = "./aircraft/massBreakdown/mFuel/design"
mpayload_path = "./aircraft/massBreakdown/mPayload/design"
```

```python


def synthesise(input_file,
               turbofan_tech_file,
               output_file=None,
               oem_max_rel_diff=1.,
               min_iterations=7,
               max_iterations=30,
               print_iterations=True,
               plot_iterations=True,
               plot_geometry=True,
               plot_payload_range=True,
               figure_path=None,
               figure_corners=None,
               validation_pr_file=None,
               ):
    # Define file names ------------------------------------------------
    folder_path = os.path.dirname(input_file)
    initialised_file = os.path.join(folder_path,
                                    "b_initialised.xml")
    itm_file = os.path.join(folder_path, "itm_0.xml")
    if output_file is None:
        output_file = os.path.join(folder_path,
                                   "z_output.xml")
    files_to_plot = [input_file, initialised_file]

    # Carry out iterations by running discipline modules -
    oem = read_xpath(file=initialised_file, xpath=oem_path)
    oem_new = oem * 0.9
    iteration = 0

    while (abs(percentage_difference(oem_new, oem))
           > oem_max_rel_diff) and (
             iteration < max_iterations) or (
             iteration < min_iterations):

        itm_file = os.path.join(
            folder_path,
            "itm_{:}.xml".format(iteration))
        itm_file_previous = os.path.join(
            folder_path,
            "itm_{:}.xml".format(iteration - 1))
        files_to_plot.append(itm_file)

        # Run class I weight estimation
        run_weight_1_estimation(
            input_file=itm_file_previous,
            output_file=itm_file)

        oem = read_xpath(file=itm_file, xpath=oem_path)

        # Run the loading diagram
        run_loading_diagram(input_file=itm_file,
                            output_file=itm_file)

        # Run drag estimation
        run_obert_drag_estimation(input_file=itm_file,
                                  output_file=itm_file)

        # Run class II weight estimation
        run_weight_2_estimation(input_file=itm_file,
                                output_file=itm_file)

        # Run the turbofan sizing
        run_turbofan_design(
            input_file=itm_file,
            output_file=itm_file,
            tech_input_file=turbofan_tech_file)

        # Run mission analysis
        run_commercial_jet_mission(
            input_file=itm_file,
            output_file=itm_file,
            tech_input_file=turbofan_tech_file)

        oem_new = read_xpath(file=itm_file,
                             xpath=oem_path)

        iteration += 1

    # Write output file -----------------------------------
    copyfile(src=itm_file, dst=output_file)
    files_to_plot.append(output_file)

    # Plot masses versus iteration -----------------------
    if plot_iterations:
        plot_iteration_variable_from_xml(
            xml_folder=files_to_plot,
            xpath=[mtom_path, oem_path, mfuel_path],
            tag_type="float",
            xlabel="Iteration",
            ylabel="Mass␣[kg]",
            labels=["MTOM", "OEM", "FM"],
            axes=None)

    # Plot payload range diagram ------------------------------------------
    if plot_payload_range:
        run_payload_range(
            input_file=output_file,
            output_file=output_file,
            validation_pr_file=validation_pr_file,
            tech_input_file=turbofan_tech_file)

    # Plot final geometry -------------------------------------------------
    if plot_geometry:
        plot_geometry_from_xml(
            input_file=output_file,
            figure=figure_path,
            figure_corners=figure_corners)

    return oem
```

The computational time of this synthesis function varies between the different multidisciplinary framework setups, aircraft categories, and fuel types considered in this thesis. For example, including the horizontal tail sizing discipline rather than assuming a fixed volume coefficient increases the computation time between the setups considered in Chapter 3 and later chapters. Also, the initial guesses for OEM and MTOM are better for the kerosene, cost- and fuel-optimal aircraft than for hydrogen and climate-optimal aircraft. This may require extra iterations before the design converges.

Table H.1 compares the computation time on a desktop computer [1] for the synthesis function for six cases in this dissertation. The time varies between approximately 4 and 29 seconds for one aircraft synthesis convergence. The times for kerosene- and SAF-powered aircraft are similar.

In each optimization evaluation step, first, the synthesis function is called. Subsequently, the cost and climate impact disciplines are run which have the same code implementation as the other disciplines. Finally, constraint functions are evaluated similarly. Each optimization evaluation starts with the same input file with top-level aircraft requirements, which don't change during the optimization, and adds the design vector to a copy of this file. This file is then passed to the synthesis, cost, climate, and constraint functions. The optimizer reads the objective from the populated data file and the constraint values to update the design vector and restart the process. In the current work, this process of calling the Python functions, evaluating the objective and constraints, and proposing a new design vector is handled by modeFRONTIER.

---

[1] Windows 10 Enterprise, Intel(R) Xeon(R) W-2223 CPU @ 3.60GHz, 32GB RAM, single-thread execution, Python 3.7, measured by cProfile profiler in PyCharm 2021.1.2, no intermediate plotting

Table H.1: Simple computation time comparison for different aircraft categories, tail sizing methods (fixed or optimized [opt.] horizontal tail volume coefficient $\overline{V}_{\mathrm{ht}}$), and fuel types

Case	**1**	**2**	**3**	**4**	**5**	6
Computational time [s]	± 3.5	± 15.3	± 20.6	± 15.2	± 12.3	± 29.1
Objective	V&V	Cost	ATR_{100}	Cost	Cost	ATR_{100}
Aircraft category	A320-200	SMR	SMR	SMR	LR	LR
$\overline{V}_{\mathrm{ht}}$ Sizing Method	Fixed	Opt.	Opt.	Opt.	Opt.	Opt.
Fuel Type	KER	KER	KER	LH2	KER	LH2

For one optimization evaluation, approximately 20 to 30 seconds of computational time are needed in addition the the synthesis call (approximate times in Table H.1) to call the cost, climate, and constraint functions, including all overhead for reading and writing .xml files and modeFRONTIER log files. This means that one optimization evaluation takes approximately 25 to 60 seconds, depending on the case and code version. The final multi-objective optimizations with up to 6000 evaluations, as discussed in Appendices C.2.2 and C.3, the full optimization takes up to 48 hours.

There is not an exact match between the evaluation times and total optimization time mentioned here because some evaluations are stopped prematurely when the engine variables result in an unachievable engine design. This happens when the turbine entry temperature is not high enough to support a high bypass and/or overall pressure ratio, resulting in an unfeasible pressure ratio between the nozzle and ambient conditions in the model, smaller than one.

H.2. DISCIPLINE SETUP

From a coding perspective, each discipline called in Listing H.1 is a Python function which has the same three-step approach:

1. it reads the necessary inputs from the input file (discussed in Appendix H.3)
2. it runs the underlying analysis or design methods (described in Chapters 3 to 6)
3. it writes the outputs to a copy of the input file

The general setup for such a discipline function is presented in Listing H.2. The benefit of this three-step approach is that calling the analysis and design calculations is separated from the file handling. The reading and writing steps can be adapted to different data or file structures without having to update the core technical analysis.

As introduced above, certain discipline functions require a technology or assumptions file with parameters that do not change with iterations. Examples of such files are the technology file for the turbofan design, containing polytropic efficiencies of the turbofan components, and cost assumptions such as the fuel price and salaries. Additionally, plotting options are available in some discipline functions, although no plots are made during the synthesis and optimization process.

Listing H.2: General descipline function Python code

```
def run_discipline(input_file,
                   tech_input_file,
                   output_file=None,
                   print_output=False):
    """
    Function to run the discipline in a workflow.
    """
    # 1. Read data
    input_dict, main_element = read_discipline_input(
        input_file=input_file,
        tech_input_file=tech_input_file)

    # 2. Call design and/or analysis function
    result = analysis_function(input_dict=input_dict)

    # Printing and/or plotting operations, if any
    if print_output:
        print("Performance", result["performance"])

    # 3. Write results
    output_dict = result
    # Here it is assumed that all results
    # should be written

    if output_file is None:
        output_file_path = input_file
    else:
        output_file_path = output_file

    write_discipline_output(output_file=output_file_path,
                            main_element=main_element,
                            info_dict=output_dict)

    return True
```

H.3. DATA STRUCTURE

The synthesis process starts with an aircraft input file which contains aircraft top-level requirements, as specified in for example Table 6.3. Subsequently, this file is further populated and updated by calling all disciplines and by iterating on the design. Once convergence is reached, a file with all aircraft design information is provided. By running the climate and cost modules, the file is finally completely populated.

The data files use Extensible Markup Language (XML) to store the aircraft data in a hierarchical structure. XML documents provide logic to the aircraft data, are flexible enough to update along with code updates, and can be interpreted by various computer programs. For example, the lxml Python package [2] allows reading specific slots in .xml through XPath evaluations. Examples of such XPaths are provided in lines 5 to 8 of Listing H.1. Furthermore, comments can be added to aid the user in filling out input files.

Figure H.1 presents the basic tree structure of such a .xml file. The file contains settings such as mass per passenger, which certification specification it should adhere to (e.g., CS25), whether some parameters, such as $C_{L_{\max}}$, are inputs or should be updated automatically, etc. Subsequently, the aircraft is defined in terms of its missions (passengers, cargo mass, and range), its mass breakdown, its components, any requirements impacting the wing and thrust loading, overall aerodynamic performance, cost, and climate impact.

The components block defines key parameters per component (fuselage, wing, empennage, and engines) that are of interest to the designer, the optimization, or which have to be exchanged between disciplines. For the fuselage component, geometric parameters such as length, cabin and outer diameters, and the wetted have to be exchanged. For the turbofan component, the design variables and their take-off counterparts, as well as the size of the engine are saved.

Rather than reading and writing a .xml file in every discipline call, which causes some overhead in computational time, one could also use a Python data structure such as a dictionary. This can also help with the parallelization of the code. Therefore, the use of a dictionary or other Python data structure (possibly from a non-native package) is recommended for further development.

---

[2] URL `https://lxml.de/index.html` accessed on 8 July 2024

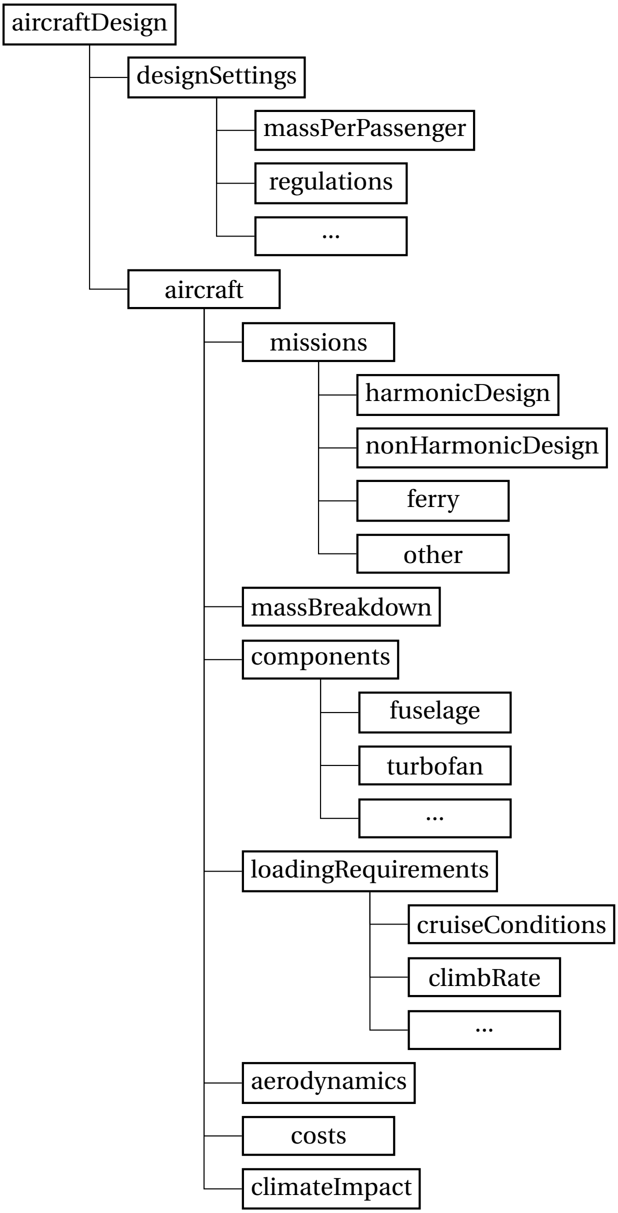
aircraftDesign
designSettings
massPerPassenger
regulations
...
aircraft
missions
harmonicDesign
nonHarmonicDesign
ferry
other
massBreakdown
components
fuselage
turbofan
...
loadingRequirements
cruiseConditions
climbRate
...
aerodynamics
costs
climateImpact

Figure H.1: Hierarchical aircraft design data format implemented in the XML input file

BIBLIOGRAPHY

[1] IPCC. “Summary for Policymakers”. In: *Climate Change 2022: Impacts, Adaptation, and Vulnerability. Contribution of Working Group II to the Sixth Assessment Report of the Intergovernmental Panel on Climate Change*. Ed. by H. O. Pörtner, D. C. Roberts, M. Tignor, E. S. Poloczanska, K. Mintenbeck, A. Alegría, M. Craig, S. Langsdorf, S. Löschke, V. Möller, A. Okem, and B. Rama. In Press. Cambridge, UK: Cambridge University Press, 2022, In Press.

[2] Lee, D., Pitari, G., Grewe, V., Gierens, K., Penner, J., Petzold, A., Prather, M., Schumann, U., Bais, A., Berntsen, T., Iachetti, D., Lim, L., and Sausen, R. “Transport impacts on atmosphere and climate: Aviation”. In: *Atmospheric Environment* 44.37 (2010), pp. 4678–4734. DOI: `10.1016/j.atmosenv.2009.06.005`.

[3] Lee, D. S., Fahey, D. W., Skowron, A., Allen, M. R., Burkhardt, U., Chen, Q., Doherty, S. J., Freeman, S., Forster, P. M., Fuglestvedt, J., Gettelman, A., De León, R. R., Lim, L. L., Lund, M. T., Millar, R. J., Owen, B., Penner, J. E., Pitari, G., Prather, M. J., Sausen, R., and Wilcox, L. J. “The contribution of global aviation to anthropogenic climate forcing for 2000 to 2018”. In: *Atmospheric Environment* 244 (2021), p. 117834. DOI: `10.1016/j.atmosenv.2020.117834`.

[4] Doganis, R. *Flying off course: The economics of international airlines*. Third Edition. Routledge, 2002.

[5] International Civil Aviation Organization via Airlines for America – processed by Our World in Data. *Available seat km*. Dataset. Processed by Our World in Data (2023) and retrieved from `https://ourworldindata.org/grapher/airline-capacity-and-traffic` on 25/01/2024. 2023.

[6] International Civil Aviation Organization via Airlines for America – processed by Our World in Data. *Passenger seat km*. Dataset. Processed by Our World in Data (2023) and retrieved from `https://ourworldindata.org/grapher/airline-capacity-and-traffic` on 25/01/2024. 2023.

[7] ATAG. *Fact Sheet # 3 - Tracking Aviation Efficiency*. Fact Sheet. Retrieved from `https://aviationbenefits.org/media/167219/fact-sheet_3_tracking-aviation-efficiency_3.pdf` on 25/01/2024. 2020.

[8] Ritchie, H. “Climate change and flying: what share of global CO_2 emissions come from aviation?” In: *Our World in Data* (2020). Published online at OurWorldInData.org. Retrieved from `https://ourworldindata.org/co2-emissions-from-aviation` on 22/02/2023.

[9] Airbus. *Global Market Forecast - Cities, Airports and Aircraft 2019-2038*. 5th ed. Blagnac Cedex: Airbus S.A.S., 2019. Chap. 1,3.

[10] Boeing. *Commercial Market Outlook 2019-2038*. Boeing, 2019.

[11] Lee, J. J., Lukachko, S. P., Waitz, I. A., and Schafer, A. “Historical and Future Trends in Aircraft Performance, Cost, and Emissions”. In: *Annual Review of Energy and the Environment* 26.1 (2001), pp. 167–200. DOI: 10.1146/annurev.energy.26.1.167.

[12] Delbecq, S., Fontane, J., Gourdain, N., Mugnier, H., Planès, T., and Simatos, F. *ISAE-SUPAERO Aviation and Climate: a literature review*. Tech. rep. 2022. DOI: 10.34849/a66a-vv58.

[13] Brasseur, G. P., Gupta, M., Anderson, B. E., Balasubramanian, S., Barrett, S., Duda, D., Fleming, G., Forster, P. M., Fuglestvedt, J., Gettelman, A., Halthore, R. N., Jacob, S. D., Jacobson, M. Z., Khodayari, A., Liou, K.-N., Lund, M. T., Miake-Lye, R. C., Minnis, P., Olsen, S., Penner, J. E., Prinn, R., Schumann, U., Selkirk, H. B., Sokolov, A., Unger, N., Wolfe, P., Wong, H.-W., Wuebbles, D. W., Yi, B., Yang, P., and Zhou, C. “Impact of Aviation on Climate: FAA’s Aviation Climate Change Research Initiative (ACCRI) Phase II”. In: *Bulletin of the American Meteorological Society* 97.4 (2016), pp. 561–583. DOI: 10.1175/BAMS-D-13-00089.1.

[14] Lefebvre, A. H. and Ballal, D. R. *Gas turbine combustion: Alternative Fuels and Emissions*. 3rd. CRC press, 2010. ISBN: 9781420086058.

[15] Wuebbles, D., Gupta, M., and Ko, M. “Evaluating the impacts of aviation on climate change”. In: *Eos, Transactions American Geophysical Union* 88.14 (2007), pp. 157–160. DOI: 10.1029/2007EO140001.

[16] Grewe, V. and Dahlmann, K. “Evaluating Climate-Chemistry Response and Mitigation Options with AirClim”. In: *Atmospheric Physics: Background – Methods – Trends*. Ed. by U. Schumann. Berlin, Heidelberg: Springer Berlin Heidelberg, 2012, pp. 591–606. DOI: 10.1007/978-3-642-30183-4_36.

[17] Schumann, U. “Influence of propulsion efficiency on contrail formation”. In: *Aerospace Science and Technology* 4.6 (2000), pp. 391–401. DOI: 10.1016/S1270-9638(00)01062-2.

[18] Schwartz, E. and Kroo, I. “Aircraft Design: Trading Cost and Climate Impact”. In: *47th AIAA Aerospace Sciences Meeting including The New Horizons Forum and Aerospace Exposition*. Orlando, FL: American Institute of Aeronautics and Astronautics, 2009. DOI: 10.2514/6.2009-1261.

[19] Dahlmann, K., Koch, A., Linke, F., Lührs, B., Grewe, V., Otten, T., Seider, D., Gollnick, V., and Schumann, U. “Climate-Compatible Air Transport System—Climate Impact Mitigation Potential for Actual and Future Aircraft”. In: *Aerospace* 3.4 (2016). DOI: 10.3390/aerospace3040038.

[20] Koch, A. “Climate Impact Mitigation Potential given by Flight Profile and Aircraft Optimization”. PhD thesis. Technischen Universität Hamburg - Harburg, 2013. DOI: 10.13140/RG.2.1.4896.9047.

[21] Torenbeek, E. *Advanced aircraft design: conceptual design, technology and optimization of subsonic civil airplanes*. Chichester: John Wiley & Sons, Ltd, 2013. DOI: 10.1002/9781118568101.

[22] Antoine, N. E. and Kroo, I. M. "Framework for Aircraft Conceptual Design and Environmental Performance Studies". In: *AIAA Journal* 43.10 (2005), pp. 2100–2109. DOI: `10.2514/1.13017`.

[23] Henderson, R. P., Martins, J. R. R. A., and Perez, R. E. "Aircraft conceptual design for optimal environmental performance". In: *The Aeronautical Journal* 116.1175 (2012), pp. 1–22. DOI: `10.1017/S000192400000659X`.

[24] Schwartz Dallara, E., Kroo, I. M., and Waitz, I. A. "Metric for Comparing Lifetime Average Climate Impact of Aircraft". In: *AIAA Journal* 49.8 (2011), pp. 1600–1613. DOI: `10.2514/1.J050763`.

[25] Jansen, P. W. and Perez, R. E. "Robust Coupled Optimization of Aircraft Design and Fleet Allocation for Multiple Markets". In: *AIAA/3AF Aircraft Noise and Emissions Reduction Symposium*. Atlanta, GA, 2014. DOI: `10.2514/6.2014-2735`.

[26] Jansen, P. W. and Perez, R. E. "Coupled Optimization of Aircraft Families and Fleet Allocation for Multiple Markets". In: *Journal of Aircraft* 53.5 (2016), pp. 1485–1504. DOI: `10.2514/1.C033646`.

[27] Perez, R. E. and Jansen, P. W. "Coupled aircraft design and staging assignment for long–range operations". In: *Journal of Aerospace Operations* 4.4 (2017), pp. 223–243. DOI: `10.3233/AOP-170064`.

[28] Moolchandani, K., Govindaraju, P., Roy, S., Crossley, W. A., and DeLaurentis, D. A. "Assessing Effects of Aircraft and Fuel Technology Advancement on Select Aviation Environmental Impacts". In: *Journal of Aircraft* 54.3 (2017), pp. 857–869. DOI: `10.2514/1.C033861`.

[29] Hwang, J., Roy, S., Kao, J., Martins, J. R. R. A., and Crossley, W. A. "Simultaneous aircraft allocation and mission optimization using a modular adjoint approach". In: *56th AIAA/ASCE/AHS/ASC Structures, Structural Dynamics, and Materials Conference*. 2015. DOI: `10.2514/6.2015-0900`.

[30] Bernardo, J. E., Zaidi, T., LeVine, M., Jimenez, H., and Mavris, D. "Rapid Integrated Interdependent Fleet-Level Environmental Model". In: *Journal of Aircraft* 54.3 (2017), pp. 939–954. DOI: `10.2514/1.C033572`.

[31] Govindaraju, P., Davendralingam, N., and Crossley, W. A. "A Concurrent Aircraft Design and Fleet Assignment Approach to Mitigate Environmental Impact through Fuel Burn Reduction under Operational Uncertainty". In: *Journal of Aerospace Operations* 4.4 (2017), pp. 163–184. DOI: `10.3233/AOP-170061`.

[32] Dahal, K., Brynolf, S., Xisto, C., Hansson, J., Grahn, M., Grönstedt, T., and Lehtveer, M. "Techno-economic review of alternative fuels and propulsion systems for the aviation sector". In: *Renewable and Sustainable Energy Reviews* 151 (2021), p. 111 564. DOI: `10.1016/j.rser.2021.111564`.

[33] Verstraete, D. "On the energy efficiency of hydrogen-fuelled transport aircraft". In: *International Journal of Hydrogen Energy* 40.23 (2015), pp. 7388–7394. DOI: `10.1016/j.ijhydene.2015.04.055`.

[34] Torenbeek, E. *Synthesis of Subsonic Airplane Design*. Dordrecht: Delft University Press and Kluwer Academic Publishers, 1982.

[35] Roskam, J. *Airplane Design. Part VIII: Airplane Cost Estimation: Design, Development, Manufacturing and Operating.* DARcorporation, 1985.

[36] Reekers, M. "Climate Effects of the Flying V". MSc thesis. Delft University of Technology (TU Delft), 2021.

[37] Ortuño, M. Á. S., Yin, F., Rao, A. G., Vos, R., and Proesmans, P. "Climate Assessment of Hydrogen Combustion Aircraft: Towards a Green Aviation Sector". In: *AIAA SCITECH 2023 Forum.* National Harbor, MD & Online, 2023. DOI: `10.2514/6.2023-2513`.

[38] Volker, G., Bock, L., Burkhardt, U., Dahlmann, K., Gierens, K., Hüttenhofer, L., Unterstrasser, S., Gangoli Rao, A., Bhat, A., Yin, F., Reichel, T., Paschereit, C., and Yeshayahou, L. "Assessing the climate impact of the AHEAD multi-fuel blended wing body". In: *Meteorologische Zeitschrift* 26 (2017), pp. 711–725. DOI: `10.1127/metz/2016/0758`.

[39] Gnadt, A. R., Speth, R. L., Sabnis, J. S., and Barrett, S. R. "Technical and environmental assessment of all-electric 180-passenger commercial aircraft". In: *Progress in Aerospace Sciences* 105 (2019), pp. 1–30. DOI: `10.1016/j.paerosci.2018.11.002`.

[40] Adu-Gyamfi, B. A. and Good, C. "Electric aviation: A review of concepts and enabling technologies". In: *Transportation Engineering* 9 (2022), p. 100134. DOI: `10.1016/j.treng.2022.100134`.

[41] de Vries, R. "Hybrid-Electric Aircraft with Over-the-Wing Distributed Propulsion: Aerodynamic Performance and Conceptual Design". PhD thesis. Delft University of Technology (TU Delft), 2022.

[42] Trainelli, L., Salucci, F., Comincini, D., Riboldi, C. E. D., and Rolando, A. "Sizing and Performance of Hydrogen-Driven Airplanes". In: *AIDAA XXV International Congress.* Rome, 2019.

[43] Yin, F., Grewe, V., and Gierens, K. "Impact of hybrid electric aircraft on contrail coverage". In: *Aerospace — Open Access Aeronautics and Astronautics Journal* 7.10 (2020), pp. 1–18. DOI: `10.3390/aerospace7100147`.

[44] Gierens, K. "Theory of Contrail Formation for Fuel Cells". In: *Aerospace* 8.6 (2021), p. 164. DOI: `10.3390/aerospace8060164`.

[45] Scholz, A. E., Trifonov, D., and Hornung, M. "Environmental life cycle assessment and operating cost analysis of a conceptual battery hybrid-electric transport aircraft". In: *CEAS Aeronautical Journal* 13.1 (2022), pp. 215–235. DOI: `10.1007/s13272-021-00556-0`.

[46] Wehrspohn, J., Rahn, A., Papantoni, V., Silberhorn, D., Burschyk, T., Schröder, M., Linke, F., Dahlmann, K., Kühlen, M., Wicke, K., and Wende, G. "A detailed and comparative economic analysis of hybrid-electric aircraft concepts considering environmental assessment factors". In: *AIAA AVIATION 2022 Forum.* Chicago, IL & Virtual: American Institute of Aeronautics and Astronautics, 2022. DOI: `10.2514/6.2022-3882`.

[47] IPCC. “Annex VII: Glossary [Matthews, J.B.R., V. Möller, R. van Diemen, J.S. Fuglestvedt, V. Masson-Delmotte, C. Méndez, S. Semenov, A. Reisinger (eds.)]” In: *Climate Change 2021: The Physical Science Basis. Contribution of Working Group I to the Sixth Assessment Report of the Intergovernmental Panel on Climate Change.* Ed. by V. Masson-Delmotte, P. Zhai, A. Pirani, S. Connors, C. Péan, S. Berger, N. Caud, Y. Chen, L. Goldfarb, M. Gomis, M. Huang, K. Leitzell, E. Lonnoy, J. Matthews, T. Maycock, T. Waterfield, O. Yelekçi, R. Yu, and B. Zhou. Cambridge, United Kingdom and New York, USA: Cambridge University Press, 2021, pp. 2215–2256. DOI: `10.1017/9781009157896.022`.

[48] Schumann, U. *Atmospheric Physics: Background–Methods–Trends.* Springer Science & Business Media, 2012. ISBN: 978-3-642-30182-7. DOI: `10.1007/978-3-642-30183-4`.

[49] Houghton, J. *Global warming: the complete briefing.* Second. Cambridge University Press, 1997. ISBN: 0521629322.

[50] Chaisson, E. J. “Long-Term Global Heating from Energy Usage”. In: *Eos, Transactions American Geophysical Union* 89.28 (2008), pp. 253–254. DOI: `10.1029/2008EO280001`.

[51] De Laat, A. “Current Climate Impact of Heating From Energy Usage”. In: *Eos, Transactions American Geophysical Union* 89.51 (2008), pp. 530–531. DOI: `10.1029/2008EO510005`.

[52] Zevenhoven, R. and Beyene, A. “The relative contribution of waste heat from power plants to global warming”. In: *Energy* 36.6 (2011). ECOS 2009, pp. 3754–3762. DOI: `10.1016/j.energy.2010.10.010`.

[53] Flanner, M. G. “Integrating anthropogenic heat flux with global climate models”. In: *Geophysical Research Letters* 36.2 (2009). DOI: `10.1029/2008GL036465`.

[54] Forster, P., Storelvmo, T., Armour, K., Collins, W., Dufresne, J.-L., Frame, D., Lunt, D., Mauritsen, T., Palmer, M., Watanabe, M., Wild, M., and Zhang, H. “The Earth’s Energy Budget, Climate Feedbacks, and Climate Sensitivity”. In: *Climate Change 2021: The Physical Science Basis. Contribution of Working Group I to the Sixth Assessment Report of the Intergovernmental Panel on Climate Change.* Ed. by V. Masson-Delmotte, P. Zhai, A. Pirani, S. Connors, C. Péan, S. Berger, N. Caud, Y. Chen, L. Goldfarb, M. Gomis, M. Huang, K. Leitzell, E. Lonnoy, J. Matthews, T. Maycock, T. Waterfield, O. Yelekçi, R. Yu, and B. Zhou. Cambridge, United Kingdom and New York, USA: Cambridge University Press, 2021, pp. 923–1054. DOI: `10.1017/9781009157896.009`.

[55] IPCC. *Aviation and the Global Atmosphere.* Ed. by J. Penner, D. Lister, D. Grigss, D. Dokken, and M. McFarland. Vol. In Press. Cambridge, United Kingdom and New York, USA: Cambridge University Press, 1999.

[56] Correa, S. M. “A Review of NOx Formation Under Gas-Turbine Combustion Conditions”. In: *Combustion Science and Technology* 87.1-6 (1993), pp. 329–362. DOI: `10.1080/00102209208947221`.

[57] Kyprianidis, K. G. and Dahlquist, E. “On the trade-off between aviation NOx and energy efficiency”. In: *Applied Energy* 185 (2017), pp. 1506–1516. DOI: 10.1016/j.apenergy.2015.12.055.

[58] Design Science and Technology Sub Group. “Air Travel – Greener by Design Mitigating the environmental impact of aviation: Opportunities and priorities”. In: *The Aeronautical Journal (1968)* 109.1099 (2005), pp. 361–416. DOI: 10.1017/S0001924000000841.

[59] Chandrasekaran, N. and Guha, A. “Study of Prediction Methods for NOx Emission from Turbofan Engines”. In: *Journal of Propulsion and Power* 28.1 (2012), pp. 170–180. DOI: 10.2514/1.B34245.

[60] Köhler, M. O., Rädel, G., Dessens, O., Shine, K. P., Rogers, H. L., Wild, O., and Pyle, J. A. “Impact of perturbations to nitrogen oxide emissions from global aviation”. In: *Journal of Geophysical Research: Atmospheres* 113.D11 (2008). DOI: 10.1029/2007JD009140.

[61] Stevenson, D. S., Doherty, R. M., Sanderson, M. G., Collins, W. J., Johnson, C. E., and Derwent, R. G. “Radiative forcing from aircraft NOx emissions: Mechanisms and seasonal dependence”. In: *Journal of Geophysical Research* 109.D17307 (2004). DOI: 10.1029/2004JD004759.

[62] Grewe, V. “Impact of Lightning on Air Chemistry and Climate”. In: *Lightning: Principles, Instruments and Applications: Review of Modern Lightning Research.* Ed. by H. D. Betz, U. Schumann, and P. Laroche. Dordrecht: Springer Netherlands, 2009, pp. 537–549. DOI: 10.1007/978-1-4020-9079-0_25.

[63] Fahey, D. W., Baughcum, S. L., Gupta, M., Lee, D. S., Sausen, R., and Velthoven, P. van. *Aviation and Climate: State of Science.* Tech. rep. ICAO, 2013, pp. 48–53.

[64] Grewe, V., Matthes, S., and Dahlmann, K. “The contribution of aviation NO_x emissions to climate change: are we ignoring methodological flaws?” In: *Environmental Research Letters* 14.12 (2019), p. 121003. DOI: 10.1088/1748-9326/ab5dd7.

[65] Myhre, G., Nilsen, J. S., Gulstad, L., Shine, K. P., Rognerud, B., and Isaksen, I. S. A. “Radiative forcing due to stratospheric water vapour from CH_4 oxidation”. In: *Geophysical Research Letters* 34.1 (2007). DOI: 10.1029/2006GL027472.

[66] Grewe, V. and Stenke, A. “AirClim: an efficient tool for climate evaluation of aircraft technology”. In: *Atmospheric Chemistry and Physics* 8.16 (2008), pp. 4621–4639. DOI: 10.5194/acp-8-4621-2008.

[67] Pletzer, J., Hauglustaine, D., Cohen, Y., Jöckel, P., and Grewe, V. “The climate impact of hydrogen-powered hypersonic transport”. In: *Atmospheric Chemistry and Physics* 22.21 (2022), pp. 14323–14354. DOI: 10.5194/acp-22-14323-2022.

[68] Ebbinghaus, A. and Wiesen, P. “Aircraft fuels and their effect upon engine emissions”. In: *Air & Space Europe* 3.1 (2001), pp. 101–103. DOI: 10.1016/S1290-0958(01)90026-7.

[69] Owen, B., Anet, J. G., Bertier, N., Christie, S., Cremaschi, M., Dellaert, S., Edebeli, J., Janicke, U., Kuenen, J., Lim, L., and Terrenoire, E. “Review: Particulate Matter Emissions from Aircraft”. In: *Atmosphere* 13.8 (2022). DOI: `10.3390/atmos1308-1230`.

[70] Kugele, A., Jelinek, F., and Gaffal, R. *Aircraft Particulate Matter Emission Estimation through all Phases of Flight*. Tech. rep. EEC/SEE/2005/0014. EUROCONTROL, 2005.

[71] Unterstrasser, S. “Properties of young contrails – a parametrisation based on large-eddy simulations”. In: *Atmospheric Chemistry and Physics* 16.4 (2016), pp. 2059–2082. DOI: `10.5194/acp-16-2059-2016`.

[72] Paoli, R. and Shariff, K. “Contrail Modeling and Simulation”. In: *Annual Review of Fluid Mechanics* 48.1 (2016), pp. 393–427. DOI: `10.1146/annurev-fluid-010814-013619`.

[73] Burkhardt, U., Bock, L., and Bier, A. “Mitigating the contrail cirrus climate impact by reducing aircraft soot number emissions”. In: *npj Climate and Atmospheric Science* 1.1 (2018), p. 37. DOI: `10.1038/s41612-018-0046-4`.

[74] Jeßberger, P., Voigt, C., Schumann, U., Sölch, I., Schlager, H., Kaufmann, S., Petzold, A., Schäuble, D., and Gayet, J.-F. “Aircraft type influence on contrail properties”. In: *Atmospheric Chemistry and Physics* 13.23 (2013), pp. 11965–11984. DOI: `10.5194/acp-13-11965-2013`.

[75] Rosenow, J., Hospodka, J., Lán, S., and Fricke, H. “Validation of a Contrail Life-Cycle Model in Central Europe”. In: *Sustainability* 15.11 (2023). DOI: `10.3390/su15118669`.

[76] Schumann, U., Mayer, B., Graf, K., and Mannstein, H. “A Parametric Radiative Forcing Model for Contrail Cirrus”. In: *Journal of Applied Meteorology and Climatology* 51.7 (2012), pp. 1391–1406. DOI: `10.1175/JAMC-D-11-0242.1`.

[77] Meerkötter, R., Schumann, U., Doelling, D. R., Minnis, P., Nakajima, T., and Tsushima, Y. “Radiative forcing by contrails”. In: *Annales Geophysicae* 17.8 (1999), pp. 1080–1094. DOI: `10.1007/s00585-999-1080-7`.

[78] Teoh, R., Schumann, U., Gryspeerdt, E., Shapiro, M., Molloy, J., Koudis, G., Voigt, C., and Stettler, M. E. J. “Aviation contrail climate effects in the North Atlantic from 2016 to 2021”. In: *Atmospheric Chemistry and Physics* 22.16 (2022), pp. 10919–10935. DOI: `10.5194/acp-22-10919-2022`.

[79] Rädel, G. and Shine, K. P. “Radiative forcing by persistent contrails and its dependence on cruise altitudes”. In: *Journal of Geophysical Research: Atmospheres* 113.D7 (2008). DOI: `10.1029/2007JD009117`.

[80] Burkhardt, U. and Kärcher, B. “Global radiative forcing from contrail cirrus”. In: *Nature climate change* 1.1 (2011), pp. 54–58.

[81] Megill, L., Deck, K., and Grewe, V. “Alternative climate metrics to the Global Warming Potential are more suitable for assessing aviation non-CO_2 effects”. In: *Commun Earth Environ* 5.249 (2024). DOI: `10.1038/s43247-024-01423-6`.

[82] Schwartz Dallara, E. “Aircraft Design for Reduced Climate Impact”. PhD thesis. Stanford University, 2011.

[83] IPCC. *Climate Change 2021: The Physical Science Basis. Contribution of Working Group I to the Sixth Assessment Report of the Intergovernmental Panel on Climate Change*. Vol. In Press. Cambridge, United Kingdom and New York, USA: Cambridge University Press, 2021. DOI: 10.1017/9781009157896.

[84] Seneviratne, S., Zhang, X., Adnan, M., Badi, W., Dereczynski, C., Di Luca, A., Ghosh, S., Iskandar, I., Kossin, J., Lewis, S., Otto, F., Pinto, I., Satoh, M., Vicente-Serrano, S., Wehner, M., and Zhou, B. “Weather and Climate Extreme Events in a Changing Climate”. In: *Climate Change 2021: The Physical Science Basis. Contribution of Working Group I to the Sixth Assessment Report of the Intergovernmental Panel on Climate Change*. Ed. by V. Masson-Delmotte, P. Zhai, A. Pirani, S. Connors, C. Péan, S. Berger, N. Caud, Y. Chen, L. Goldfarb, M. Gomis, M. Huang, K. Leitzell, E. Lonnoy, J. Matthews, T. Maycock, T. Waterfield, O. Yelekçi, R. Yu, and B. Zhou. Cambridge, United Kingdom and New York, USA: Cambridge University Press, 2021, pp. 1513–1766. DOI: 10.1017/9781009157896.013.

[85] Fox-Kemper, B., Hewitt, H., Xiao, C., Aðalgeirsdóttir, G., Drijfhout, S., Edwards, T., Golledge, N., Hemer, M., Kopp, R., Krinner, G., Mix, A., Notz, D., Nowicki, S., Nurhati, I., Ruiz, L., Sallée, J.-B., Slangen, A., and Yu, Y. “Ocean, Cryosphere and Sea Level Change”. In: *Climate Change 2021: The Physical Science Basis. Contribution of Working Group I to the Sixth Assessment Report of the Intergovernmental Panel on Climate Change*. Ed. by V. Masson-Delmotte, P. Zhai, A. Pirani, S. Connors, C. Péan, S. Berger, N. Caud, Y. Chen, L. Goldfarb, M. Gomis, M. Huang, K. Leitzell, E. Lonnoy, J. Matthews, T. Maycock, T. Waterfield, O. Yelekçi, R. Yu, and B. Zhou. Cambridge, United Kingdom and New York, USA: Cambridge University Press, 2021, pp. 1211–1362. DOI: 10.1017/9781009157896.011.

[86] IPCC. “Summary for Policymakers”. In: *Climate Change 2023: Synthesis Report. Contribution of Working Groups I, II and III to the Sixth Assessment Report of the Intergovernmental Panel on Climate Change*. Ed. by The Core Writing Team, H. Lee, and J. Romero. Geneva, Switzerland: IPCC, 2023. DOI: 10.59327/IPCC/AR6-9789291691647.001.

[87] Proesmans, P. and Vos, R. “Airplane Design Optimization for Minimal Global Warming Impact”. In: *Journal of Aircraft* 59.5 (2022), pp. 1363–1381. DOI: 10.2514/1.C036529.

[88] Dallara, E. S. and Kroo, I. “Aircraft Design for Reduced Climate Impact”. In: *49th AIAA Aerospace Sciences Meeting including the New Horizons Forum and Aerospace Exposition*. Orlando, FL: American Institute of Aeronautics and Astronautics, 2011. ISBN: 978-1-60086-950-1. DOI: 10.2514/6.2011-265.

[89] Grewe, V., Dahlmann, K., Flink, J., Frömming, C., Ghosh, R., Gierens, K., Heller, R., Hendricks, J., Jöckel, P., Kaufmann, S., Kölker, K., Linke, F., Luchkova, T., Lührs, B., Van Manen, J., Matthes, S., Minikin, A., Niklaß, M., Plohr, M., Righi, M., Rosanka, S., Schmitt, A., Schumann, U., Terekhov, I., Unterstrasser, S., Vázquez-Navarro, M., Voigt, C., Wicke, K., Yamashita, H., Zahn, A., and Ziereis, H. “Mitigating the

Climate Impact from Aviation: Achievements and Results of the DLR WeCare Project". In: *Aerospace* 4.3 (2017), p. 34. DOI: `10.3390/aerospace4030034`.

[90] Chai, X., Yu, X., and Wang, Y. "Tradeoff Study between Cost and Environmental Impact of Aircraft Using Simultaneous Optimization of Airframe and Engine Cycle". In: *International Journal of Aerospace Engineering* 2017 (2017), pp. 1–10. DOI: `10.1155/2017/2468535`.

[91] Egelhofer, R., Bickerstaff, C., and Bonnet, S. "Minimizing Impact on Climate in Aircraft Design". In: *SAE Technical Paper*. SAE International, 2007. DOI: `10.4271/2007-01-3807`.

[92] Wang, Y., Xing, Y., Yu, X., and Zhang, S. "Flight operation and airframe design for tradeoff between cost and environmental impact". In: *Proceedings of the Institution of Mechanical Engineers, Part G: Journal of Aerospace Engineering* 232.5 (2018), pp. 973–987. DOI: `10.1177/0954410017748967`.

[93] Schutte, J. and Mavris, D. N. "Evaluation of N+2 Technologies and Advanced Vehicle Concepts". In: *53rd AIAA Aerospace Sciences Meeting*. Kissimmee, FL, 2015. DOI: `10.2514/6.2015-0514`.

[94] Herbon, J., Aicholtz, J., Hsieh, S.-Y., Viars, P., Birmaher, S., Brown, D., Patel, N., Carper, D., Cooper, C., and Fitzgerald, R. *N+2 Advanced Low NOx Combustor Technology Final Report*. Tech. rep. NASA/CR-2017-219410. National Aeronautics and Space Administration (NASA), 2017.

[95] Reynolds, T., Barrett, S., Dray, L., Evans, A., Köhler, M., Vera-Morales, M., Schäfer, A., Wadud, Z., Britter, R., Hallam, H., and Hunsley, R. "Modelling Environmental and Economic Impacts of Aviation: Introducing the Aviation Integrated Modelling Project". In: *7th AIAA ATIO Conf, 2nd CEIAT Int'l Conf on Innov and Integr in Aero Sciences,17th LTA Systems Tech Conf; followed by 2nd TEOS Forum*. Belfast, 2007. DOI: `10.2514/6.2007-7751`.

[96] Bernardo, J. E., Zaidi, T., LeVine, M., Jimenez, H., and Mavris, D. "Rapid Integrated Interdependent Fleet-Level Environmental Model". In: *Journal of Aircraft* 54.3 (2017), pp. 939–954. DOI: `10.2514/1.C033572`.

[97] LeVine, M. J., Bernardo, J. E., Kirby, M., and Mavris, D. N. "Average Generic Vehicle Method for Fleet-Level Analysis of Noise and Emission Tradeoffs". In: *Journal of Aircraft* 55.3 (2018), pp. 929–946. DOI: `10.2514/1.C034368`.

[98] Vera-Morales, M. and Hall, C. A. "Modeling Performance and Emissions from Aircraft in the Aviation Integrated Modelling Project". In: *Journal of Aircraft* 47.3 (2010), pp. 812–819. DOI: `10.2514/1.44020`.

[99] Moolchandani, K., Govindaraju, P., Roy, S., Crossley, W. A., and DeLaurentis, D. A. "Assessing Effects of Aircraft and Fuel Technology Advancement on Select Aviation Environmental Impacts". In: *Journal of Aircraft* 54.3 (2017), pp. 857–869. DOI: `10.2514/1.C033861`.

[100] Jimenez, H., Pfaender, H., and Mavris, D. "Fuel Burn and CO_2 System-Wide Assessment of Environmentally Responsible Aviation Technologies". In: *Journal of Aircraft* 49.6 (2012), pp. 1913–1930. DOI: `10.2514/1.C031755`.

[101] McEnteggart, Q. and Whidborne, J. F. "Multiobjective Environmental Departure Procedure Optimization". In: *Journal of Aircraft* 55.3 (2018), pp. 905–917. DOI: 10.2514/1.C033132.

[102] Mori, R. "Fuel-Saving Climb Procedure by Reduced Thrust near Top of Climb". In: *Journal of Aircraft* 57.5 (2020), pp. 800–806. DOI: 10.2514/1.C035200.

[103] Lührs, B., Niklass, M., Froemming, C., Grewe, V., and Gollnick, V. "Cost-Benefit Assessment of 2D and 3D Climate And Weather Optimized Trajectories". In: *16th AIAA Aviation Technology, Integration, and Operations Conference*. Washington, D.C., 2016. DOI: 10.2514/6.2016-3758.

[104] Hwang, J. T., Jasa, J. P., and Martins, J. R. R. A. "High-Fidelity Design-Allocation Optimization of a Commercial Aircraft Maximizing Airline Profit". In: *Journal of Aircraft* 56.3 (2019), pp. 1164–1178. DOI: 10.2514/1.C035082.

[105] Mattingly, J. D., Heiser, W. H., and Pratt, D. T. *Aircraft Engine Design, Second Edition*. Reston, VA: American Institute of Aeronautics and Astronautics (AIAA), 2002. ISBN: 978-1-56347-538-2. DOI: 10.2514/4.861444.

[106] ICAO. *Annex 14 to the Convention on International Civil Aviation - Aerodromes - Volume I - Aerodromes Design and Operations*. Tech. rep. ICAO, 2018.

[107] Obert, E. *Aerodynamic Design of Transport Aircraft*. IOS press, 2009.

[108] Lambe, A. B. and Martins, J. R. "Extensions to the Design Structure Matrix for the Description of Multidisciplinary Design, Analysis, and Optimization Processes". In: *Structural and Multidisciplinary Optimization* 46.2 (2012), pp. 273–284. DOI: 10.1007/s00158-012-0763-y.

[109] Roskam, J. *Airplane Design. Part I: Preliminary Sizing of Airplanes*. DARcorporation, 1985. ISBN: 9781884885433.

[110] Obert, E. *Drag polars of nineteen jet transport aircraft at Mach number M = 0.40 - 0.60*. Tech. rep. A-XXX. Fokker, 2013.

[111] Proesmans, P. "Preliminary Propulsion System Design and Inegration for a Box-Wing Aircraft Configuration". MSc thesis. Delft University of Technology (TU Delft), 2019.

[112] Walsh, P. P. and Fletcher, P. *Gas turbine performance*. 2nd ed. Oxford: Blackwell Science Ltd, 2004. DOI: 10.1002/9780470774533.

[113] Greitzer, E. M., Bonnefoy, P., de la Rosa Blanco, E., Dorbian, C., Drela, M., Hall, D., Hansman, R., Hileman, J., Liebeck, R., Lovegren, J., Mody, P., Pertuze, J., Sato, S., Spakovszky, Z., Tan, C., Hollman, J., Duda, J., Fitzgerald, N., Houghton, J., Kerrebrock, J., Kiwada, G., Kordonowy, D., Parrish, J., Tylko, J., Wen, E., and Lord, W. *N+3 Aircraft Concept Designs and Trade Studies. Volume 2: Appendices - Design Methodologies for Aerodynamics, Structures, Weight, and Thermodynamic Cycles*. Tech. rep. NASA/CR-2010-216794/VOL2. National Aeronautics and Space Administration (NASA), 2010.

[114] Tong, M. T., Halliwell, I., and Ghosn, L. J. "A Computer Code for Gas Turbine Engine Weight and Disk Life Estimation ". In: *Journal of Engineering for Gas Turbines and Power* 126.2 (2004), pp. 265–270. DOI: 10.1115/1.1691980.

[115] Torenbeek, E. *The initial calculation of range and mission fuel during conceptual design*. Tech. rep. LR-525. Delft University of Technology (TU Delft), Faculty of Aerospace Engineering, 1987.

[116] Grewe, V. and Dahlmann, K. "How ambiguous are climate metrics? And are we prepared to assess and compare the climate impact of new air traffic technologies?" In: *Atmospheric Environment* 106 (2015), pp. 373–374. DOI: `10.1016/j.atmosenv.2015.02.039`.

[117] Sausen, R. and Schumann, U. "Estimates of the Climate Response to Aircraft CO_2 and NO_x Emissions Scenarios". In: *Climate Change* 44 (2000), pp. 27–58. DOI: `10.1023/A:1005579306109`.

[118] IPCC. *Climate Change 2007 - The physical science basis. Working group I. Contributions to the Fourth Assessment Report of the Intergovernmental Panel of Climate Change*. New York, USA: Cambridge University Press, 2007.

[119] Ponater, M., Pechtl, S., Sausen, R., Schumann, U., and Hüttig, G. "Potential of the cryoplane technology to reduce aircraft climate impact: A state-of-the-art assessment". In: *Atmospheric Environment* 40.36 (2006), pp. 6928–6944. DOI: `10.1016/j.atmosenv.2006.06.036`.

[120] Sonntag, D. "Important new values of the physical constants of 1986, vapour pressure formulations based on the ITS-90, and psychrometer formulae". In: *Zeitschrift für Meteorologie* 40.5 (1990), pp. 340–344.

[121] Grewe, V. *Aircraft Emissions and Climate Effects - Part 3: Contrails*. Lecture Notes. Delft University of Technology. 2020.

[122] Belobaba, P. "Airline Operating Costs and Measures of Productivity". In: *The Global Airline Industry*. John Wiley & Sons, Ltd, 2009. Chap. 5, pp. 113–151. DOI: `10.1002/9780470744734.ch5`.

[123] Airbus Media Relations. *2018 price adjustment across Airbus' modern product range reflects continuous investment and customer value*. 2018.

[124] The Boeing Company. *About Boeing Commercial Airplanes*. 2020.

[125] Visser, W. P. J. "Generic Analysis Methods for Gas Turbine Engine Performance: The development of the gas turbine simulation program GSP". PhD thesis. Delft University of Technology (TU Delft), 2015.

[126] Nicolai, L. M. and Carichner, G. E. *Fundamentals of Aircraft and Airship Design*. Vol. 1. Reston, VA: AIAA, 2010. ISBN: 978-1-60086-753-8. DOI: `10.2514/4.867538`.

[127] Jenkinson, L. R., Simpkin, P., and Rhodes, D. *Civil jet aircraft design*. Arnold London, 1999. DOI: `10.2514/4.473500`.

[128] Airbus S.A.S. Customer Services. *Airbus A320 Aircraft Characteristics Airport and Maintenance Planning*. Tech. rep. Airbus S.A.S. Customer Services, 2019.

[129] Boeing Commercial Airplanes. *Boeing 777-200/300 Airplane Characteristics and Airport Planning*. Tech. rep. Boeing Commercial Airplanes, 2002.

[130] Swelbar, W. S. and Belobaba, P. P. *Airline Data Project*. 2019.

[131] Husemann, M., Schäfer, K., and Stumpf, E. “Flexibility within flight operations as an evaluation criterion for preliminary aircraft design”. In: *Journal of Air Transport Management* 71 (2018), pp. 201–214. DOI: 10.1016/j.jairtraman.2018.04.007.

[132] Thijssen, R. “Propeller Aircraft Design Optimization for Climate Impact Reduction”. MSc thesis. Delft University of Technology (TU Delft), 2022.

[133] Stingo, L., Della Vecchia, P., Cerino, G., Nicolosi, F., and De Marco, A. “MDO applications to conventional and novel turboprop aircraft within agile European project”. In: *31st Congress of the International Council of the Aeronautical Sciences, ICAS 2018*. Belo Horizonte, 2018, pp. 1–10. ISBN: 9783932182884.

[134] Della Vecchia, P., Stingo, L., Nicolosi, F., De Marco, A., Cerino, G., Ciampa, P. D., Prakasha, P. S., Fioriti, M., Zhang, M., Mirzoyan, A., Aigner, B., and Charbonnier, D. “Advanced turboprop multidisciplinary design and optimization within AGILE project”. In: *2018 Aviation Technology, Integration, and Operations Conference*. Reston, VA: American Institute of Aeronautics and Astronautics, 2018, pp. 1–17. ISBN: 978-1-62410-556-2. DOI: 10.2514/6.2018-3205.

[135] Fuglestvedt, J. S., Berntsen, T. K., Godal, O., Sausen, R., Shine, K. P., and Skodvin, T. “Metrics of climate change: Assessing radiative forcing and emission indices”. In: *Climatic Change* 58.3 (2003), pp. 267–331. DOI: 10.1023/A:1023905326842.

[136] Hager, R. and Vrabel, D. *Advanced Turboprop Project*. NASA SP-495. Scientific and Technical Information Division, NASA, 1988.

[137] Guynn, M. D., Berton, J. J., Haller, W. J., Hendricks, E. S., and Tong, M. T. *Performance and Environmental Assessment of an Advanced Aircraft with Open Rotor Propulsion*. Tech. rep. NASA/TM-2012-217772. 2012. DOI: 10.13140/RG.2.1.4847.3687.

[138] Dron, S. “Toward ACARE 2020: Innovative Engine Architectures to Achieve the Environmental Goals?” In: *26th International Congress of the Aeronautical Sciences (ICAS)*. Anchorage, AK, 2008.

[139] Arnhem, N. van. “Unconventional Propeller-Airframe Integration for Transport Aircraft Configurations”. PhD thesis. Delft University of Technology (TU Delft), 2022. DOI: 10.4233/uuid:4d47b0db-1e6a-4f38-af95-aafd33c29402.

[140] European Union Aviation Safety Agency. “Certification Specifications and Acceptable Means of Compliance for Large Aeroplanes CS-25: Amendment 26”. In: (2020).

[141] ATR. *ATR 72-600 Fact Sheet*. Tech. rep. ATR, 2020.

[142] Vos, R. and Farokhi, S. *Introduction to Transonic Aerodynamics*. Vol. 110. Fluid Mechanics and Its Applications. Dordrecht: Springer Netherlands, 2015. ISBN: 978-94-017-9746-7. DOI: 10.1007/978-94-017-9747-4.

[143] Veldhuis, L. L. M. “Propeller wing aerodynamic interference”. PhD thesis. Delft University of Technology (TU Delft), 2005.

[144] Raymer, D. *Aircraft design: a conceptual approach*. American Institute of Aeronautics and Astronautics, Inc., 2012.

[145] IHS Markit. “P&WC PW100”. In: *Jane’s Aero-Engines*. IHS Markit, 2022.

[146] Vos, R., Melkert, J., and Zandbergen, B. *Aerospace Design and Systems Engineering Elements I: Wing and Propulsion System Design*. Lecture Notes. Delft University of Technology. 2016.

[147] Teeuwen, Y. “Propeller Design for Conceptual Turboprop Aircraft”. MSc thesis. Delft University of Technology (TU Delft), 2017.

[148] Marinus, B. G. and Quodbach, L. “Data and Design Models for Civil Turbopropeller Aircraft”. In: *Journal of Aircraft* 57.6 (2020), pp. 1252–1267. DOI: `10.2514/1.C035271`.

[149] Mattingly, J. *Elements of Gas Turbine Propulsion*. AIAA education series. American Institute of Aeronautics and Astronautics, 2005. ISBN: 9781563477782. DOI: `10.2514/4.861789`.

[150] Dinç, A. “Sizing of a turboprop unmanned air vehicle and its propulsion system”. In: *Journal of Thermal Sciences and Technology* 35 (2015), pp. 53–62. DOI: `10.23890/IJAST.vm01is01.0101`.

[151] Bombardier. *Dash 8 Series 400, Airport Planning Manual*. Tech. rep. Bombardier INC, 2014.

[152] Brasseur, G., Cox, R., Hauglustaine, D., Isaksen, I., Lelieveld, J., Lister, D., Sausen, R., Schumann, U., Wahner, A., and Wiesen, P. “European scientific assessment of the atmospheric effects of aircraft emissions”. In: *Atmospheric Environment* 32.13 (1998), pp. 2329–2418. DOI: `10.1016/S1352-2310(97)00486-X`.

[153] Wallace, J. and Hobbs, P. *Atmospheric Science: An Introductory Survey*. International geophysics series. Elsevier Academic Press, 2006. ISBN: 9780127329512. DOI: `10.1016/C2009-0-00034-8`.

[154] Proesmans, P. and Vos, R. “Hydrogen, medium-range airplane design optimization for minimal global warming impact”. In: *CEAS Aeronautical Journal* (2024). DOI: `10.1007/s13272-024-00734-w`.

[155] Gangoli Rao, A., Yin, F., and Werij, H. “Energy Transition in Aviation: The Role of Cryogenic Fuels”. In: *Aerospace* 7 (2020), p. 181. DOI: `10.3390/aerospace7120181`.

[156] Svensson, F., Hasselrot, A., and Moldanova, J. “Reduced environmental impact by lowered cruise altitude for liquid hydrogen-fuelled aircraft”. In: *Aerospace Science and Technology* 8.4 (2004), pp. 307–320. DOI: `10.1016/j.ast.2004.02.004`.

[157] Ström, L. and Gierens, K. “First simulations of cryoplane contrails”. In: *Journal of Geophysical Research: Atmospheres* 107.D18 (2002), AAC 2-1-AAC 2–13. DOI: `10.1029/2001JD000838`.

[158] Marquart, S., Ponater, M., Ström, L., and Gierens, K. “An upgraded estimate of the radiative forcing of cryoplane contrails”. In: *Meteorologische Zeitschrift* 14 (2005), pp. 573–582. DOI: `10.1127/0941-2948/2005/0057`.

[159] Khandelwal, B., Karakurt, A., Sekaran, P. R., Sethi, V., and Singh, R. “Hydrogen powered aircraft : The future of air transport”. In: *Progress in Aerospace Sciences* 60 (2013), pp. 45–59. DOI: `10.1016/j.paerosci.2012.12.002`.

[160] Brewer, G. D. *Hydrogen aircraft technology*. CRC Press, 1991. ISBN: 0849358388.

[161] Westenberger, A. “H2 Technology for Commercial Aircraft”. In: *Advances on Propulsion Technology for High-Speed Aircraft*. Neuilly-sur-Seine, 2008.

[162] Verstraete, D. “On the energy efficiency of hydrogen-fuelled transport aircraft”. In: *International Journal of Hydrogen Energy* 40.23 (2015), pp. 7388–7394. DOI: `10.1016/j.ijhydene.2015.04.055`.

[163] Onorato, G., Proesmans, P., and Hoogreef, M. “Assessment of hydrogen transport aircraft: Effects of fuel tank integration”. In: *CEAS Aeronautical Journal* 13.4 (2022), pp. 813–845. DOI: `10.1007/s13272-022-00601-6`.

[164] Boeing Commercial Airplanes. *Boeing 737 Airplane Characteristics and Airport Planning*. Tech. rep. Boeing Commercial Airplanes, 2013.

[165] Pinho Chiozotto, G. “Improving Aircraft Conceptual Design with Methods for Wing Loads, Aeroelasticity and Mass Estimation”. PhD. Göttingen: Technischen Universität Berlin, 2017.

[166] Mason, W. “Analytic models for technology integration in aircraft design”. In: *Aircraft Design, Systems and Operations Conference*. Dayton, OH, 1990. DOI: `10.2514/6.1990-3262`.

[167] Verstraete, D., Hendrick, P., Pilidis, P., and Ramsden, K. “Hydrogen fuel tanks for subsonic transport aircraft”. In: *International Journal of Hydrogen Energy* 35.20 (2010), pp. 11085–11098. DOI: `10.1016/j.ijhydene.2010.06.060`.

[168] Svensson, F. and Singh, R. “Effects of Using Hydrogen on Aero Gas Turbine Pollutant Emissions, Performance and Design”. In: *Turbo Expo: Power for Land, Sea, and Air*. Vienna, 2004, pp. 107–116. DOI: `10.1115/GT2004-53349`.

[169] Priyadarshini, M., Bhupendra, K., Vishal, S., and Riti, S. “Hydrogen as a Fuel for Gas Turbine Engines with Novel Micromix Type Combustors”. In: *47th AIAA / ASME / SAE / ASEE Joint Propulsion Conference & Exhibit*. San Diego, CA, 2011. DOI: `10.2514/6.2011-5806`.

[170] Warwick, N., P., G., Keeble, J., Archibald, A., Pyle, J., NCAS, and Shine, K. *Atmospheric implications of increased Hydrogen use*. Tech. rep. University of Cambridge and the National Centre for Atmospheric Sciences with the University of Reading, 2022.

[171] Clean Sky 2 JU and Fuel Cells and Hydrogen 2 JU. *Hydrogen-powered aviation: A fact-based study of hydrogen technology, economics, and climate impact by 2050*. Tech. rep. 2020. DOI: `10.2843/471510`.

[172] Marek, C., Smith, T., and Kundu, K. “Low Emission Hydrogen Combustors for Gas Turbines Using Lean Direct Injection”. In: *41st AIAA/ASME/SAE/ASEE Joint Propulsion Conference & Exhibit*. 2005. DOI: `10.2514/6.2005-3776`.

[173] Dahl, G. and Suttrop, F. “Engine control and low-NOx combustion for hydrogen fuelled aircraft gas turbines”. In: *International Journal of Hydrogen Energy* 23.8 (1998), pp. 695–704. DOI: `10.1016/S0360-3199(97)00115-8`.

[174] Hydrogen Council. *Path to hydrogen competitiveness: A cost perspective*. Tech. rep. 2020.

[175] Verstraete, D. "Long range transport aircraft using hydrogen fuel". In: *International Journal of Hydrogen Energy* 38.34 (2013), pp. 14824–14831. DOI: `10.1016/j.ijhydene.2013.09.021`.

[176] Hoelzen, J., Silberhorn, D., Zill, T., Bensmann, B., and Hanke-Rauschenbach, R. "Hydrogen-powered aviation and its reliance on green hydrogen infrastructure – Review and research gaps". In: *International Journal of Hydrogen Energy* 47.5 (2022), pp. 3108–3130. DOI: `10.1016/j.ijhydene.2021.10.239`.

[177] Wehrspohn, J., Rahn, A., Papantoni, V., Silberhorn, D., Burschyk, T., Schröder, M., Linke, F., Dahlmann, K., Kühlen, M., Wicke, K., and Wende, G. "A Detailed and Comparative Economic Analysis of Hybrid-Electric Aircraft Concepts Considering Environmental Assessment Factors". In: *AIAA AVIATION 2022 Forum*. 2022. DOI: `10.2514/6.2022-3882`.

[178] Adler, E. J. and Martins, J. R. "Hydrogen-powered aircraft: Fundamental concepts, key technologies, and environmental impacts". In: *Progress in Aerospace Sciences* 141 (2023). Special Issue on Green Aviation, p. 100922. DOI: `10.1016/j.paerosci.2023.100922`.

[179] Janić, M. "Greening commercial air transportation by using liquid hydrogen (LH2) as a fuel". In: *International Journal of Hydrogen Energy* 39.29 (2014), pp. 16426–16441. DOI: `10.1016/j.ijhydene.2014.08.011`.

[180] Brewer, G. D., Morris, R. E., Davis, G. W., Versaw, E. F., Cunnington Jr., G. R., Riple, J. C., Baerst, C. F., and Garmong, G. *Study of fuel systems for LH2-fueled subsonic transport aircraft, volume 1*. Tech. rep. NASA-CR-145369. 1978.

[181] Verstraete, D. "The Potential of Liquid Hydrogen for long range aircraft propulsion". PhD thesis. Cranfield University, 2009.

[182] Sethi, V. "Advanced Performance Simulation of Gas Turbine Components and Fluid Thermodynamic Properties". PhD thesis. Cranfield University, 2008.

[183] Klug, H. G. and Faass, R. "CRYOPLANE: hydrogen fuelled aircraft — status and challenges". In: *Air & Space Europe* 3.3 (2001), pp. 252–254. DOI: `10.1016/S1290-0958(01)90110-8`.

[184] Al-Shamma, O. and Ali, R. "A Comparative Study of Cost Estimation Models used For Preliminary Aircraft Design". In: *Global Journal of Researches In Engineering: B Automotive Engineering* 14.4 (2014).

[185] Kundu, A. K. *Aircraft Design*. Cambridge Aerospace Series. Cambridge University Press, 2010. DOI: `10.1017/CBO9780511844652`.

[186] Jong, S. de, Antonissen, K., Hoefnagels, R., Lonza, L., Wang, M., Faaij, A., and Junginger, M. "Life-cycle analysis of greenhouse gas emissions from renewable jet fuel production". In: *Biotechnology for Biofuels* 10.64 (2017). DOI: `10.1186/s13068-017-0739-7`.

[187] World Economic Forum. *Clean Skies for Tomorrow - Sustainable Aviation Fuels as a Pathway to Net-Zero Aviation*. Tech. rep. 2020.

[188] Prussi, M., Lee, U., Wang, M., Malina, R., Valin, H., Taheripour, F., Velarde, C., Staples, M. D., Lonza, L., and Hileman, J. I. “CORSIA: The first internationally adopted approach to calculate life-cycle GHG emissions for aviation fuels”. In: *Renewable and Sustainable Energy Reviews* 150 (2021), p. 111398. DOI: 10.1016/j.rser.2021.111398.

[189] Moore, R. H., Thornhill, K. L., Weinzierl, B., Sauer, D., D’Ascoli, E., Kim, J., Lichtenstern, M., Scheibe, M., Beaton, B., Beyersdorf, A. J., Barrick, J., Bulzan, D., Corr, C. A., Crosbie, E., Jurkat, T., Martin, R., Riddick, D., Shook, M., Slover, G., Voigt, C., White, R., Winstead, E., Yasky, R., Ziemba, L. D., Brown, A., Schlager, H., and Anderson, B. E. “Biofuel blending reduces particle emissions from aircraft engines at cruise conditions”. In: *Nature* 543.7645 (2017), pp. 411–415. DOI: 10.1038/nature21420.

[190] Voigt, C., Kleine, J., Sauer, D., Moore, R. H., Bräuer, T., Le Clercq, P., Kaufmann, S., Scheibe, M., Jurkat-Witschas, T., Aigner, M., Bauder, U., Boose, Y., Borrmann, S., Crosbie, E., Diskin, G. S., DiGangi, J., Hahn, V., Heckl, C., Huber, F., Nowak, J. B., Rapp, M., Rauch, B., Robinson, C., Schripp, T., Shook, M., Winstead, E., Ziemba, L., Schlager, H., and Anderson, B. E. “Cleaner burning aviation fuels can reduce contrail cloudiness”. In: *Communications Earth & Environment* 2.1 (2021). DOI: 10.1038/s43247-021-00174-y.

[191] Guerreiro, A. P., Fonseca, C. M., and Paquete, L. “The Hypervolume Indicator: Computational Problems and Algorithms”. In: *ACM Comput. Surv.* 54.6 (2021). DOI: 10.1145/3453474.

[192] Gierens, K., Braun-Unkhoff, M., Le Clercq, P., Plohr, M., Schlager, H., and Wolters, F. *Condensation trails from biofuels/kerosene blends scoping study*. Tech. rep. ENER /C2/2013-627. Deutsches Zentrum für Luft- und Raumfahrt (DLR), 2016.

[193] Wolters, F., Becker, R.-G., and Schaefer, M. “Impact of Alternative Fuels on Engine Performance and CO_2-emissions”. In: *28th International Congress of the Aeronautical Sciences (ICAS)*. Vol. 23. Brisbane, 2012.

[194] Cherubini, F., Bird, N. D., Cowie, A., Jungmeier, G., Schlamadinger, B., and Woess-Gallasch, S. “Energy- and greenhouse gas-based LCA of biofuel and bioenergy systems: Key issues, ranges and recommendations”. In: *Resources, Conservation and Recycling* 53.8 (2009), pp. 434–447. DOI: 10.1016/j.resconrec.2009.03.013.

[195] Moore, R., Thornhill, K., Weinzierl, B., Sauer, D., D’Ascoli, E., Kim, J., Lichtenstern, M., Scheibe, M., Beaton, B., Beyersdorf, A., et al. “Biofuel blending reduces particle emissions from aircraft engines at cruise conditions”. In: *Nature* 543.7645 (2017), pp. 411–415. DOI: 10.1038/nature21420.

[196] Unterstrasser, S. “Large-eddy simulation study of contrail microphysics and geometry during the vortex phase and consequences on contrail-to-cirrus transition”. In: *Journal of Geophysical Research: Atmospheres* 119.12 (2014), pp. 7537–7555. DOI: 10.1002/2013JD021418.

[197] Embraer S.A. *Embraer 175 Airport Planning Manual*. Tech. rep. Embraer S.A, 2021.

[198] Airbus S.A.S. Customer Services. *Airbus A350 Aircraft Characteristics Airport and Maintenance Planning*. Tech. rep. Airbus S.A.S. Customer Services, 2020.

[199] Regional Airline Association. *2021 The Year of Community*. Tech. rep. Regional Airline Association, 2021.

[200] Proesmans, P., Morlupo, F., Santos, B. F., and Vos, R. "Aircraft Design Optimization Considering Network Demand and Future Aviation Fuels". In: *AIAA AVIATION 2023 Forum*. San Diego, CA, 2023. DOI: 10.2514/6.2023-4300.

[201] Hillier, F. S. and Lieberman, G. J. *Introduction to operations research*. Tenth Edition. McGraw-Hill Education, 2001. ISBN: 978-1-259-25318-8.

[202] Seaone Álvarez, M. "Assessment of Climate Impact Mitigation Potential of Intermediate Stop Operations". MSc thesis. Delft University of Technology (TU Delft), 2021.

[203] Noorafza, M., Santos, B., Sharpanskykh, A., Zengerling, Z., Weder, C., Linke, F., and Grewe, V. "Airline Network Planning Considering Climate Impact: Assessing New Operational Improvements". In: *Applied Sciences, under review* (2023).

[204] Bellman, R. "On a routing problem". In: *Quarterly of applied mathematics* 16.1 (1958), pp. 87–90.

[205] Ford Jr, L. R. *Network flow theory*. Tech. rep. P-923. Rand Corp Santa Monica Ca, 1956.

[206] Stan, S. and Bob, L. *Global Market Forecast 2022*. Airbus S.A.S., 2022.

[207] Boeing. *Commercial Market Outlook 2022-2041*. Boeing, 2022.

[208] Jansen, P. W. and Perez, R. E. "Coupled Optimization of Aircraft Design and Fleet Allocation with Uncertain Passenger Demand". In: *2013 Aviation Technology, Integration, and Operations Conference*. 2013, pp. 2013–4392. DOI: 10.2514/6.2013-4392.

[209] Bos, P. "Impact of Uncertainties on the Climate-Optimized Aircraft Design". MSc thesis. Delft University of Technology (TU Delft), 2022.

[210] Radhakrishnan, K., Deck, K., Proesmans, P., Linke, F., Yin, F., Volker, G., Vos, R., Lührs, B., Niklaß, M., and Dedoussi, I. "Minimising the climate impact of the next generation aircraft using novel climate functions for aircraft design". In: *33rd International Congress of the Aeronautical Sciences (ICAS)*. Stockholm, 2022. DOI: 10.5281/zenodo.7674999.

[211] Dedoussi, I. C. "Implications of future atmospheric composition in decision-making for sustainable aviation". In: *Environmental Research Letters* 16.3 (2021), p. 031002. DOI: 10.1088/1748-9326/abe74d.

[212] Dedoussi, I. C. *AE4462-17 Aircraft Emissions and climate effects - Lecture 10*. Lecture Notes. Delft University of Technology. 2020.

[213] Turner, M. C., Jerrett, M., Pope, C. A. 3rd, Krewski, D., Gapstur, S. M., Diver, W. R., Beckerman, B. S., Marshall, J. D., Su, J., Crouse, D. L., and Burnett, R. T. “Long-Term Ozone Exposure and Mortality in a Large Prospective Study”. In: *American journal of respiratory and critical care medicine* 193.10 (2016), pp. 1134–42. DOI: 10.1164/rccm.201508-1633OC.

[214] Burnett, R., Chen, H., Szyszkowicz, M., Fann, N., Hubbell, B., Pope, C. A., Apte, J. S., Brauer, M., Cohen, A., Weichenthal, S., Coggins, J., Di, Q., Brunekreef, B., Frostad, J., Lim, S. S., Kan, H., Walker, K. D., Thurston, G. D., Hayes, R. B., Lim, C. C., Turner, M. C., Jerrett, M., Krewski, D., Gapstur, S. M., Diver, W. R., Ostro, B., Goldberg, D., Crouse, D. L., Martin, R. V., Peters, P., Pinault, L., Tjepkema, M., Donkelaar, A. van, Villeneuve, P. J., Miller, A. B., Yin, P., Zhou, M., Wang, L., Janssen, N. A. H., Marra, M., Atkinson, R. W., Tsang, H., Thach, T. Q., Cannon, J. B., Allen, R. T., Hart, J. E., Laden, F., Cesaroni, G., Forastiere, F., Weinmayr, G., Jaensch, A., Nagel, G., Concin, H., and Spadaro, J. V. “Global estimates of mortality associated with long-term exposure to outdoor fine particulate matter”. In: *Proceedings of the National Academy of Sciences* 115.38 (2018), pp. 9592–9597. DOI: 10.1073/pnas.1803222115.

[215] Quadros, F. D. A., Snellen, M., and Dedoussi, I. C. “Regional sensitivities of air quality and human health impacts to aviation emissions”. In: *Environmental Research Letters* 15.10 (2020), p. 105013. DOI: 10.1088/1748-9326/abb2c5.

[216] Eastham, S. D., Chossière, G. P., Speth, R. L., Jacob, D. J., and Barrett, S. R. H. “Global impacts of aviation on air quality evaluated at high resolution”. In: *EGUsphere* 2023 (2023), pp. 1–18. DOI: 10.5194/egusphere-2023-695.

[217] Yim, S. H. L., Lee, G. L., Lee, I. H., Allroggen, F., Ashok, A., Caiazzo, F., Eastham, S. D., Malina, R., and Barrett, S. R. H. “Global, regional and local health impacts of civil aviation emissions”. In: *Environmental Research Letters* 10.3 (2015), p. 034001. DOI: 10.1088/1748-9326/10/3/034001.

[218] Grobler, C., Wolfe, P. J., Dasadhikari, K., Dedoussi, I. C., Allroggen, F., Speth, R. L., Eastham, S. D., Agarwal, A., Staples, M. D., Sabnis, J., and Barrett, S. R. H. “Marginal climate and air quality costs of aviation emissions”. In: *Environmental Research Letters* 14.11 (2019), p. 114031. DOI: 10.1088/1748-9326/ab4942.

[219] ICAO. *Annex 16 to the Convention on International Civil Aviation, Volume II - Aircraft Engine Emission.* Tech. rep. ICAO, 2017.

[220] Proesmans, P., Snellen, M., and Dedoussi, I. C. *Deliverable 5.2 - Compliance of the Climate Optimized Aircraft Design with Additional Regulations.* Tech. rep. GLOWOPT, 2023.

[221] Lewis, A. C. “Optimising air quality co-benefits in a hydrogen economy: a case for hydrogen-specific standards for NOx emissions”. In: *Environ. Sci.: Atmos.* 1 (5 2021), pp. 201–207. DOI: 10.1039/D1EA00037C.

[222] Lighthill, M. J. “On sound generated aerodynamically I. General theory”. In: *Proceedings of the Royal Society of London. Series A. Mathematical and Physical Sciences* 211.1107 (1952), pp. 564–587.

[223] Vieira, A., Hoff, B. von den, Snellen, M., and Simons, D. G. "Comparison of Semi-Empirical Noise Models with Flyover Measurements of Operating Aircraft". In: *Journal of Aircraft* 59.6 (2022), pp. 1574–1587. DOI: 10.2514/1.C036387.

[224] Pereira, S. R., Fontes, T., and Coelho, M. C. "Can hydrogen or natural gas be alternatives for aviation? – A life cycle assessment". In: *International Journal of Hydrogen Energy* 39.25 (2014), pp. 13266–13275. DOI: 10.1016/j.ijhydene.2014.06.146.

[225] Bicer, Y. and Dincer, I. "Life cycle evaluation of hydrogen and other potential fuels for aircrafts". In: *International Journal of Hydrogen Energy* 42.16 (2017), pp. 10722–10738. DOI: 10.1016/j.ijhydene.2016.12.119.

[226] Lark, T. J., Hendricks, N. P., Smith, A., Pates, N., Spawn-Lee, S. A., Bougie, M., Booth, E. G., Kucharik, C. J., and Gibbs, H. K. "Environmental outcomes of the US Renewable Fuel Standard". In: *Proceedings of the National Academy of Sciences* 119.9 (2022), e2101084119. DOI: 10.1073/pnas.2101084119.

[227] Koroneos, C., Dompros, A., Roumbas, G., and Moussiopoulos, N. "Life cycle assessment of hydrogen fuel production processes". In: *International Journal of Hydrogen Energy* 29.14 (2004), pp. 1443–1450. DOI: 10.1016/j.ijhydene.2004.01.016.

[228] Suleman, F., Dincer, I., and Agelin-Chaab, M. "Comparative impact assessment study of various hydrogen production methods in terms of emissions". In: *International Journal of Hydrogen Energy* 41.19 (2016). Special Issue on Progress in Hydrogen Production and Applications (ICH2P-2015), 3-6 May 2015, Oshawa, Ontario, Canada, pp. 8364–8375. DOI: 10.1016/j.ijhydene.2015.12.225.

[229] Kossarev, K., Scholz, A. E., and Hornung, M. "Comparative environmental life cycle assessment and operating cost analysis of long-range hydrogen and biofuel fueled transport aircraft". In: *CEAS Aeronautical Journal* 14 (2023), pp. 3–28. DOI: 10.1007/s13272-022-00627-w.

[230] Doganis, R. *Flying Off Course: The Economics of International Airlines*. Third Edition. London: Routledge, 2002.

[231] Belobaba, P. "Fundamentals of Pricing and Revenue Management". In: *The Global Airline Industry*. John Wiley & Sons, Ltd, 2009. Chap. 4, pp. 73–111. DOI: 10.1002/9780470744734.ch4.

[232] Vasigh, B., Fleming, K., and Tacker, T. *Introduction to air transport economics: from theory to applications*. First Edition. Hampshire: Ashgate Publishing Limited, 2008.

[233] Belobaba, P. "Overview of Airline Economics, Markets and Demand". In: *The Global Airline Industry*. John Wiley & Sons, Ltd, 2009. Chap. 3, pp. 47–72. DOI: 10.1002/9780470744734.ch3.

[234] Hoogreef, M., Zuijderwijk, N., Scheers, E., Proesmans, P., and Santos, B. F. "Coupled Hybrid & Electric Aircraft Design and Strategic Airline Planning". In: *AIAA AVIATION 2023 Forum*. San Diego, CA, 2023. DOI: 10.2514/6.2023-3869.

[235] Mavromatidis, G., Orehounig, K., and Carmeliet, J. “Uncertainty and global sensitivity analysis for the optimal design of distributed energy systems”. In: *Applied Energy* 214 (2018), pp. 219–238. DOI: `10.1016/j.apenergy.2018.01.062`.

[236] Lee, D. S., Fahey, D. W., Forster, P. M., Newton, P. J., Wit, R. C., Lim, L. L., Owen, B., and Sausen, R. “Aviation and global climate change in the 21st century”. In: *Atmospheric Environment* 43.22 (2009), pp. 3520–3537. DOI: `10.1016/j.atmosenv.2009.04.024`.

[237] Meinshausen, M., Smith, S. J., Calvin, K., Daniel, J. S., Kainuma, M. L. T., Lamarque, J.-F., Matsumoto, K., Montzka, S. A., Raper, S. C. B., Riahi, K., Thomson, A., Velders, G. J. M., and Vuuren, D. P. van. “The RCP greenhouse gas concentrations and their extensions from 1765 to 2300”. In: *Climatic Change* 109 (2011), p. 213. DOI: `10.1007/s10584-011-0156-z`.

[238] Moss, R. H., Edmonds, J. A., Hibbard, K. A., Manning, M. R., Rose, S. K., Vuuren, D. P. van, Carter, T. R., Emori, S., Kainuma, M., Kram, T., Meehl, G. A., Mitchell, J. F. B., Nakicenovic, N., Riahi, K., Smith, S. J., Stouffer, R. J., Thomson, A. M., Weyant, J. P., and Wilbanks, T. J. “The next generation of scenarios for climate change research and assessment”. In: *Nature* 463 (2010), pp. 747–756. DOI: `10.1038/nature08823`.

[239] van Vuuren, D. P., Stehfest, E., den Elzen, M. G. J., Kram, T., van Vliet, J., Deetman, S., Isaac, M., Klein Goldewijk, K., Hof, A., Mendoza Beltran, A., Oostenrijk, R., and van Ruijven, B. “RCP2.6: exploring the possibility to keep global mean temperature increase below 2°C”. In: *Climatic Change* 109 (2011), p. 95. DOI: `10.1007/s10584-011-0152-3`.

[240] Thomson, A. M., Calvin, K. V., Smith, S. J., Kyle, G. P., Volke, A., Patel, P., Delgado-Arias, S., Bond-Lamberty, B., Wise, M. A., Clarke, L. E., and Edmonds, J. A. “RCP4.5: a pathway for stabilization of radiative forcing by 2100”. In: *Climatic Change* 109 (2011), p. 77. DOI: `10.1007/s10584-011-0151-4`.

[241] Masui, T., Matsumoto, K., Hijioka, Y., Kinoshita, T., Nozawa, T., Ishiwatari, S., Kato, E., Shukla, P. R., Yamagata, Y., and Kainuma, M. “An emission pathway for stabilization at 6Wm^{-2} radiative forcing”. In: *Climatic Change* 109 (2011), p. 59. DOI: `10.1007/s10584-011-0150-5`.

[242] Riahi, K., Rao, S., Krey, V., Cho, C., Chirkov, V., Fischer, G., Kindermann, G., Nakicenovic, N., and Rafaj, P. “RCP 8.5—A scenario of comparatively high greenhouse gas emissions”. In: *Climatic Change* 109 (2011), p. 33. DOI: `10.1007/s10584-011-0149-y`.

[243] Zaman, K., McDonald, M., Mahadevan, S., and Green, L. “Robustness-based design optimization under data uncertainty”. In: *Structural and Multidisciplinary Optimization* 44 (2011), pp. 183–197. DOI: `10.1007/s00158-011-0622-2`.

[244] Deb, K., Pratap, A., Agarwal, S., and Meyarivan, T. “A fast and elitist multiobjective genetic algorithm: NSGA-II”. In: *IEEE Transactions on Evolutionary Computation* 6.2 (2002), pp. 182–197. DOI: `10.1109/4235.996017`.

[245] Campolongo, F., Cariboni, J., and Saltelli, A. “An effective screening design for sensitivity analysis of large models”. In: *Environmental Modelling & Software* 22.10 (2007). Modelling, computer-assisted simulations, and mapping of dangerous phenomena for hazard assessment, pp. 1509–1518. DOI: `10.1016/j.envsoft.2006.10.004`.

[246] Ponater, M., Pechtl, S., Sausen, R., Schumann, U., and Hüttig, G. “Potential of the cryoplane technology to reduce aircraft climate impact: A state-of-the-art assessment”. In: *Atmospheric Environment* 40.36 (2006), pp. 6928–6944. DOI: `10.1016/j.atmosenv.2006.06.036`.

[247] Bruggeman, A., Nikitin, M., La Rocca, G., and Bergsma, O. “Model-Based Approach for the Simultaneous Design of Airframe Components and their Production Process Using Dynamic MDAO Workflows”. In: *AIAA SCITECH 2024 Forum*. Orlando, FL, 2024. DOI: `10.2514/6.2024-1530`.

[248] IHS Markit. “General Electric GE90”. In: *Jane’s Aero-Engines*. IHS Markit, 2019.

[249] York, M. A., Hoburg, W. W., and Drela, M. “Turbofan Engine Sizing and Tradeoff Analysis via Signomial Programming”. In: *Journal of Aircraft* 55.3 (2018), pp. 988–1003. DOI: `10.2514/1.C034463`.

[250] IHS Markit. “General Electric CF34”. In: *Jane’s Aero-Engines*. IHS Markit, 2021.

[251] Torenbeek, E. and Berenschot, G. *De berekening van het omspoeld gondelroppervlak van enkel- en dubbelstroom straalmotoren voor civiele vliegtuigen*. Tech. rep. M-445. Delft University of Technology (TU Delft), Faculty of Aerospace Engineering, 1983.

[252] Mahieu, T. “Regional Aircraft Design Space Exploration”. MSc thesis. Delft University of Technology (TU Delft), 2016.

[253] Van Rossum, G. and Drake, F. L. *Python 3 Reference Manual*. Scotts Valley, CA: CreateSpace, 2009. ISBN: 1441412697.

ACKNOWLEDGMENTS

Based on my PhD experience, it is unfair to only put one name on the cover of this dissertation. The work presented herein is the sum of meetings, coffee breaks, lunches, parties, and holidays with amazing colleagues, friends, and family who have supported me in the past years. Therefore, I would like to thank these people now.

First of all, I would like to thank my promotors Roelof Vos and Leo Veldhuis for their support and technical insights over the past years. Thank you for teaching me how to think more critically, to present my ideas more clearly, and to be more confident.

Roelof, thank you for all the interesting aircraft design discussions and side stories. You gave me a lot of freedom to explore different research topics, supervise extra MSc students, join the PhD council, etc., while still steering me to complete the PhD in just over 4 years. Leo, thanks for all the "shooting from the hip" questions and "playing the devil" during my progress meetings. You made me think more critically and zoom out from time to time.

Above all, I would like to thank Roelof and Leo for being role models in two aspects: first, showing how to have a healthy work-life balance while performing interesting research. Academia does not have to be a 24/7 business to be successful. Second, you both abundantly exhibit the most important characteristic for a PhD promotor which, in my humble opinion, is being kind to people.

I would also like to express my gratitude towards Gianfranco La Rocca, my MSc thesis supervisor, who surprisingly triggered my interest in starting a PhD. Thank you to all FPP colleagues for your insights and coffee breaks in the past years. I would like to thank Federico and Bruno from ATO for their support with the fleet allocation research (sponsored partially by the CHYLA project) and for sparking a curiosity for airline operations.

Thank you to the "senior" FPP PhD candidates and their partners, Reynard and Ale, Adam and Max, Nitish, Nando, Summit, Carmine, Akshay and Spoorti, Anne-Liza and Maurice, Tomas and Sonia, Andre and Elisa, for "adopting" me early 2020 right before the pandemic. We had some amazing nights around Delft and abroad. You are amazing friends, and I hope we will have many more food-and-drink gatherings. Thank you to all "roommates" in office 7.15 for the interesting discussions, proving that fewer people in the office leads to lower productivity levels. And special thanks to Reynard, Ale, Roberto, Ligaya, Beto, and Bea for showing me that Fiesta Macumba is a lifestyle, not just a party.

Then a big thank you to all my colleagues whom I got to know over these four years: Robert, Jatinder, Ramon, Sarah, Fernanda, Nitish, Rishikesh, Martijn, Jente, Kaushal, Hugo, Kilian, Nikki, Daaman, Turhan, Ankit, Aaron, Dabo, and many more. Thanks for all the discussions, coffee breaks, PhD drinks, and parties!

In the first three years of my PhD, I participated in the GLOWOPT project focusing on climate functions for aircraft design which could speed up multidisciplinary design optimizations for minimal global warming impact. Thank you to the GLOWOPT colleagues, Kaushik, Kathrin, Feijia, Irene, Florian, Volker, and Mirjam for the fruitful discussions and interesting research.

I greatly enjoyed my time as a PhD Council member. So, thank you, Agnes, Ata, Bieke, Christoph, Eva, Gitte, Luc, Stavrow, Victor, Sven, Laurike, and Piero for all the interesting discussions and for representing the PhD candidates (not students!) at our faculty. I hope we managed to bring the PhD community together after the COVID pandemic and to make a small contribution to a more smooth PhD experience for the next generations.

Another aspect I truly enjoyed was supervising and learning from Master students. Thank you Roel and Peter, for your research which also contributed directly to this dissertation (Chapter 4 and Section 8.5) and for improving the aircraft design code. Thank you Maurice, Bruno, and Roelof for taking me along in the thesis projects of Giuseppe, Noa, Elise, Sofia, and Rowan, whose research greatly expanded my knowledge base.

There is also a group of friends in the Netherlands and abroad, whom I have known for many years and who regularly check in on me. Thank you, Lander, Co, Wouter, Lukas, Janne, Aviva, Amaury, Hanne, and Nina for all the messages, talks, visits, workouts, and fun activities! I am sorry for my long response time on WhatsApp sometimes.

I would also like to mention a couple of people and places in Delft who unknowingly provided great times to relax and reflect on life outside the PhD. Thank you, Sil and your crew at BAR SIL, for the best pizzas in town. And special thanks to Menno, also known as Barber Nozem, in Delft for the most ridiculous jokes during my haircuts, as well as conversations about the most important aspects of life.

Finally, an extremely big thank you to my whole family! I haven't found the right way yet to thank my Mum and Dad for everything they have done for me. Thanks for always being there when I needed you, for all the long conversations (and bottles of wine) at the dinner table, and for offering "hotel-like" service whenever I came to Belgium. My apologies for the moments when I was a grumpy nerd, complaining about my research and seemingly not present in the moment because some optimization was running on the computer and in the back of my mind.

Life is unpredictable, not everything is in our control.
But as long as you're with the right people, you can handle anything.

Amy Santiago in Brooklyn 99

CURRICULUM VITÆ

Pieter-Jan PROESMANS

17-08-1995	Born in Brasschaat, Belgium

EXPERIENCE

2024	Researcher Air Transport & Operations, Aerospace Engineering Delft University of Technology, Delft, The Netherlands
2020–2024	PhD in Flight Performance & Propulsion, Aerospace Engineering Delft University of Technology, Delft, The Netherlands *Thesis:* Climate-Optimal Aircraft Design and Fleet Allocation *Promotors:* Dr. ir. R. Vos & Prof. dr. ir. L.L.M. Veldhuis *Project:* GLOWOPT
2018	Trent 900 Lifecylce Engineer (Internship) Rolls-Royce plc., Derby, United Kingdom
2017	Business Operations Assistant Eoluz, Kapellen, Belgium
2016	Engineering Assistant (Summer Intern) ENGIE Fabricom Belgium, Grimbergen, Belgium
2012–2016	E-business Assistant (Part-time Student Jobs) OZ - Onafhankelijk Ziekenfonds, Wilrijk, Belgium

EDUCATION

2020–2024	PhD in Aerospace Engineering, Doctoral Education Program Delft University of Technology, Delft, The Netherlands
2016–2019	Master in Aerospace Engineering Delft University of Technology, Delft, The Netherlands
2015	Minor in Economics and Finance Queensland University of Technology, Brisbane, Australia
2013–2016	Bachelor in Aerospace Engineering Delft University of Technology, Delft, The Netherlands
2007–2013	Secondary School, Ancient Greek and Mathematics College van het Eucharistisch Hart, Essen, Belgium

AWARDS

2023	AIAA/IEEE Electric Aircraft Technologies Symposium Best Paper for Aircraft with Maurice Hoogreef, Noa Zuijderwijk, Elise Scheers, and Bruno F. Santos
2023	AIAA Electrified Aircraft Technology Committee Best Paper Award with Maurice Hoogreef, Noa Zuijderwijk, Elise Scheers, and Bruno F. Santos
2022	AIAA Aircraft Design Best Paper Award with Roelof Vos
2017	First Prize Fokker KBE Final with Lukas Müller
2016	Anthony Fokker Prize with Tom Gulikers, Daan van Hoogstraten, Radu Iordache, Imke Kleinbekman, Mike Koch, Dave Kroezen, Lukas Müller, Marleen Otting, and Marc Pieters

LIST OF PUBLICATIONS

JOURNAL ARTICLES

4. P. Proesmans and R. Vos, *Comparison of Future Aviation Fuels to Minimize the Climate Impact of Commercial Aircraft*, Journal of Aircraft. (Under review)

3. P. Proesmans and R. Vos, *Hydrogen, Medium-Range Airplane Design Optimization for Minimal Global Warming Impact*, CEAS Aeronautical Journal, 2024, doi:10.1007/s13272-024-00734-w.

2. G. Onorato, **P. Proesmans** and M. Hoogreef, *Assessment of hydrogen transport aircraft: Effects of fuel tank integration*, CEAS Aeronautical Journal **13**, 813–845, 2022, doi: 10.1007/s13272-022-00601-6.

1. P. Proesmans and R. Vos, *Airplane Design Optimization for Minimal Global Warming Impact*, Journal of Aircraft **59.5**, 1361-1381, 2022, doi:10.2514/1.C036529.

CONFERENCE PAPERS

7. P. Proesmans, F. Morlupo, B.F. Santos, and R. Vos, *Aircraft Design Optimization Considering Network Demand and Future Aviation Fuels*, AIAA Aviation 2023 Forum, San Diego, CA, 2023, doi:10.2514/6.2023-4300.

6. M.F.M. Hoogreef, N.R. Zuijderwijk, E. Scheers, **P. Proesmans**, and B.F. Santos, *Coupled Hybrid & Electric Aircraft Design and Strategic Airline Planning*, AIAA Aviation 2023 Forum, San Diego, CA, 2023, doi:10.2514/6.2023-3869.

5. M. Sáez Ortuño, F. Yin, A. Gangoli Rao, R. Vos, and **P. Proesmans**, *Climate Assessment of Hydrogen Combustion Aircraft: Towards a Green Aviation Sector*, AIAA Scitech 2023 Forum, National Harbor, MD & Online, 2023, doi:10.2514/6.2023-2513.

4. K. Radhakrishnan, K. Deck, **P. Proesmans**, F. Linke, F. Yin, V. Grewe, R. Vos, B. Lührs, M. Niklaß, and I. Dedoussi, *Minimizing the Climate Impact of the Next Generation Aircraft using Novel Climate Functions for Aircraft Design*, 33rd Congress of the International Council of the Aeronautical Sciences, Stockholm, 2022, doi:10.5281/zenodo.7674998.

3. R. Thijssen, **P. Proesmans**, and R. Vos, *Propeller Aircraft Design Optimization for Climate Impact Reduction*, 33rd Congress of the International Council of the Aeronautical Sciences, Stockholm, 2022.

2. P. Proesmans and R. Vos, *Comparison of Future Aviation Fuels to Minimize the Climate Impact of Commercial Aircraft*, AIAA AVIATION 2022 Forum, Chicago, IL & Virtual, 2022, doi: 10.2514/6.2022-3288.

1. P. Proesmans and R. Vos, *Airplane Design Optimization for Minimal Global Warming Impact*, AIAA Scitech 2021 Forum, Virtual, 2021, doi:10.2514/6.2021-1297.

PROJECT REPORTS

3. P. Proesmans, M. Snellen, and I. Dedoussi, *Deliverable 5.2 - Compliance of the Climate Optimized Aircraft Design with Additional Regulations*, 2023.

2. P. Proesmans and R. Vos, *Deliverable 4.2 - Global Warming Optimised Aircraft Design and Technology Evaluation*, 2023.

1. P. Proesmans and R. Vos, *Deliverable 4.1 - Reference Aircraft Design*, 2022.